



**US Army Corps
of Engineers**

Construction Engineering
Research Laboratories

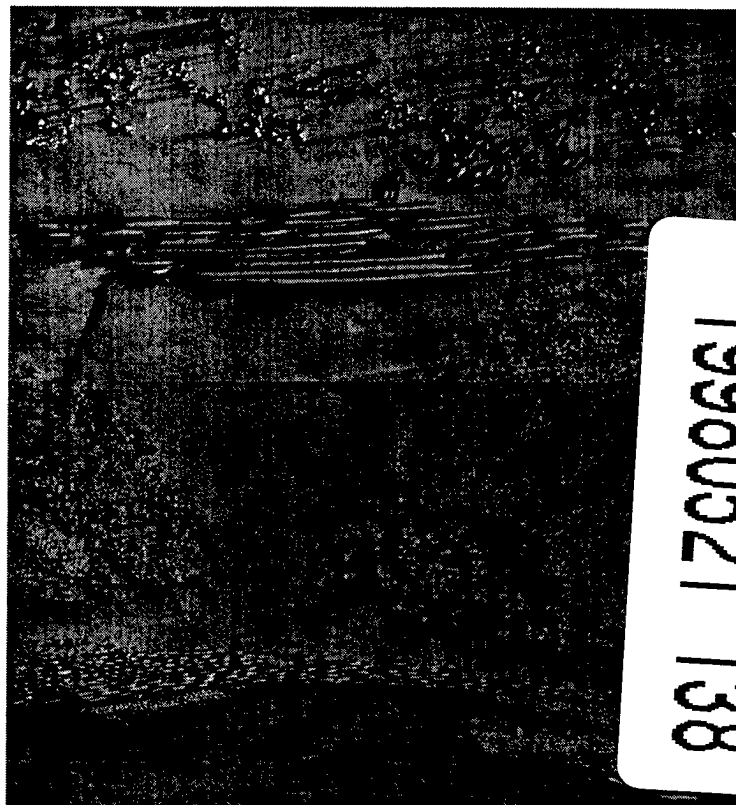
USACERL Technical Report 98/22
April 1998

Investigation of Active Tagged Composites for Army Infrastructure Applications

by
R.F. Quattrone, J.B. Berman, Z. Chaudhry, V. Giurgiutiu, C.A. Rogers, and S.R. White

Deterioration of reinforced concrete structures due to corrosion of the reinforcing steel is a very expensive infrastructure decay problem. Advanced composites, such as fiber-reinforced plastics (FRP), can eliminate many problems related to steel reinforcement because of their excellent fatigue resistance, corrosion resistance, and their very high specific strength. Acceptance of composites in retrofit applications and new construction creates the need for in-service monitoring techniques to ensure material performance and serviceability, but conventional nondestructive evaluation (NDE) methods are not applicable. Particle tagging technology can enhance the inspectability of advanced composites. Tagging involves embedding micron-size particles into materials to make them an integral part of the host material. When interrogated by suitable instrumentation, the embedded particle sensors interact with their host structures and generate certain types of measurable signatures. The signatures can then be correlated with material and structural conditions.

The objective of this research is to understand the physics and mechanisms involved in using the tagging method for in-situ NDE of composite materials for infrastructure applications. Several tagging methods have been proposed, modelled theoretically and evaluated experimentally. Ferromagnetic and



**Micrograph of a magnetostrictive composite
showing magnetostrictive tags in top layer.**

magnetostrictive tagging methods were found to have high potential for in-service QC/QA inspection of infrastructure structural composites.

The contents of this report are not to be used for advertising, publication, or promotional purposes. Citation of trade names does not constitute an official endorsement or approval of the use of such commercial products. The findings of this report are not to be construed as an official Department of the Army position, unless so designated by other authorized documents.

DESTROY THIS REPORT WHEN IT IS NO LONGER NEEDED

DO NOT RETURN IT TO THE ORIGINATOR

USER EVALUATION OF REPORT

REFERENCE: USACERL Technical Report 98/22, *Investigation of Active Tagged Composites for Army Infrastructure Applications*

Please take a few minutes to answer the questions below, tear out this sheet, and return it to USACERL. As user of this report, your customer comments will provide USACERL with information essential for improving future reports.

1. Does this report satisfy a need? (Comment on purpose, related project, or other area of interest for which report will be used.)

2. How, specifically, is the report being used? (Information source, design data or procedure, management procedure, source of ideas, etc.)

3. Has the information in this report led to any quantitative savings as far as manhours/contract dollars saved, operating costs avoided, efficiencies achieved, etc.? If so, please elaborate.

4. What is your evaluation of this report in the following areas?

a. Presentation: _____

b. Completeness: _____

c. Easy to Understand: _____

d. Easy to Implement: _____

e. Adequate Reference Material: _____

f. Relates to Area of Interest: _____

g. Did the report meet your expectations? _____

h. Does the report raise unanswered questions? _____

i. General Comments. (Indicate what you think should be changed to make this report and future reports of this type more responsive to your needs, more usable, improve readability, etc.)

5. If you would like to be contacted by the personnel who prepared this report to raise specific questions or discuss the topic, please fill in the following information.

Name: _____

Telephone Number: _____

Organization Address: _____

6. Please mail the completed form to:

Department of the Army
CONSTRUCTION ENGINEERING RESEARCH LABORATORIES
ATTN: CECER-TR-I
P.O. Box 9005
Champaign, IL 61826-9005

REPORT DOCUMENTATION PAGE

Form Approved
OMB No. 0704-0188

Public reporting burden for this collection of information is estimated to average 1 hour per response, including the time for reviewing instructions, searching existing data sources, gathering and maintaining the data needed, and completing and reviewing the collection of information. Send comments regarding this burden estimate or any other aspect of this collection of information, including suggestions for reducing this burden, to Washington Headquarters Services, Directorate for Information Operations and Reports, 1215 Jefferson Davis Highway, Suite 1204, Arlington, VA 22202-4302, and to the Office of Management and Budget, Paperwork Reduction Project (0704-0188), Washington, DC 20503.

1. AGENCY USE ONLY (Leave Blank)		2. REPORT DATE April 1998		3. REPORT TYPE AND DATES COVERED Final	
4. TITLE AND SUBTITLE Investigation of Active Tagged Composites for Army Infrastructure Applications				5. FUNDING NUMBERS 4A161102 AT23 EE7	
6. AUTHOR(S) J.B. Berman, Z. Chaudhry, V. Giurgiutiu, R.F. Quattrone, C.A. Rogers, and S.R. White					
7. PERFORMING ORGANIZATION NAME(S) AND ADDRESS(ES) U.S. Army Construction Engineering Research Laboratories (USACERL) P.O. Box 9005 Champaign, IL 61826-9005				8. PERFORMING ORGANIZATION REPORT NUMBER TR 98/22	
9. SPONSORING / MONITORING AGENCY NAME(S) AND ADDRESS(ES) Headquarters, U.S. Army Corps of Engineers ATTN: CEMP-ET 20 Massachusetts Ave. NW Washington, DC 20314-1000				10. SPONSORING / MONITORING AGENCY REPORT NUMBER	
11. SUPPLEMENTARY NOTES Copies are available from the National Technical Information Service, 5285 Port Royal Road, Springfield, VA 22161.					
12a. DISTRIBUTION / AVAILABILITY STATEMENT Approved for public release; distribution is unlimited.				12b. DISTRIBUTION CODE	
13. ABSTRACT (Maximum 200 words) <p>Deterioration of reinforced concrete structures due to corrosion of the reinforcing steel is a very expensive infrastructure decay problem. Advanced composites, such as fiber-reinforced plastics (FRP), can eliminate many problems related to steel reinforcement because of their excellent fatigue resistance, corrosion resistance, and their very high specific strength. Acceptance of composites in retrofit applications and new construction creates the need for in-service monitoring techniques to ensure material performance and serviceability, but conventional nondestructive evaluation (NDE) methods are not applicable. Particle tagging technology can enhance the inspectability of advanced composites. Tagging involves embedding micron-size particles into materials to make them an integral part of the host material. When interrogated by suitable instrumentation, the embedded particle sensors interact with their host structures and generate certain types of measurable signatures. The signatures can then be correlated with material and structural conditions.</p> <p>The objective of this research is to understand the physics and mechanisms involved in using the tagging method for in-situ NDE of composite materials for infrastructure applications. Several tagging methods have been proposed, modelled theoretically and evaluated experimentally. Ferromagnetic and magnetostrictive tagging methods were found to have high potential for in-service QC/QA inspection of infrastructure structural composites.</p>					
14. SUBJECT TERMS fiber-reinforced plastics (FRP) particle tagging corrosion control composite materials				15. NUMBER OF PAGES 192	
				16. PRICE CODE	
17. SECURITY CLASSIFICATION OF REPORT Unclassified	18. SECURITY CLASSIFICATION OF THIS PAGE Unclassified	19. SECURITY CLASSIFICATION OF ABSTRACT Unclassified		20. LIMITATION OF ABSTRACT SAR	

Foreword

This research was conducted for the Directorate of Military Programs, Headquarters, U.S. Army Corps of Engineers under Project 4A161102AT23, "Basic Research/Military Construction"; Work Unit FM-EE7, "Smart Tagged Composites for Infrastructure." The technical monitor was Charles Gutberlet, Jr., CEMP-ET.

The work was performed by the Materials Science and Technology Division (FL-M) of the Facilities Technology Laboratory (FL), U.S. Army Construction Engineering Research Laboratories (USACERL). The USACERL Principal Investigator was Dr. Robert F. Quattrone. Dr. Ilker R. Adiguzel is Division Chief, CECER-FL-M; Mr. Donald F. Fournier is Lab Operations Chief, CECER-FL; and Dr. Alan W. Moore is Technical Director. The USACERL technical editor was Gordon L. Cohen, Technical Resources Team.

A portion of this work was performed under contract by Dr. C.A. Rogers, Dr. Z. Chaudhry, Dr. V. Giurgiutiu, and Dr. S.R. White.

Matching funds and manufacturing of all composite samples were provided by the Composites Institute, a Division of the Society of the Plastics Industry, Inc. The following Composites Institute companies assisted in this research: Clark-Schwebel, Creative Pultrusions, DSB Associates, Interplastics, Owens-Corning, PPG, Reichhold, and TPI.

COL James A. Walter is the Commander of USACERL and Dr. Michael J. O'Connor is the Director.

Contents

SF298	1
Foreword	2
List of Figures and Tables	5
1 Introduction	15
Background	15
Objectives	16
Approach	17
Mode of Technology Transfer	17
Nomenclature	17
2 Review of the History of Particle Tagging	21
3 Particle Tagging Technology	24
Candidate Tagging Particles	24
Instrumentation	26
Excitation Methods in Active Tagging	27
Limitations	27
4 Applications of Particle Tagging Techniques	29
Application Overview	29
Applications in Fiber-Reinforced Polymers for Infrastructures in Civil Engineering ...	29
5 Recent Studies In Tagging	33
Manufacture of Tagged Epoxy Specimens	33
Experiments Involving Particle Tagging	34
Experimental Results and Discussion	35
6 Ferromagnetic Active Tagging (Theory)	39
Background	39
Determination of Active Magnetomotive Force	39
Modeling of Tagging Particles	43
Solution of the Tagging Particle Model	44
Numerical Examples and Discussion	46

7	Ferromagnetic Active Tagging (Experiment)	49
	Experimental Program	49
	Equipment Requirements	49
	Test Descriptions and Principles	50
	Description of Tagging Materials	52
	Fabrication of Specimens	52
	Specimen Testing Procedure	53
	Results and Discussion	54
8	Magnetostrictive Active Tagging (Theory)	57
	Background	57
	Particle Magnetization	58
	Magnetic Induction Field of a Particle Dipole	59
	Residual Induction-Based NDE Approach	60
	Signal Strength Estimation	61
9	Magnetostrictive Active Tagging (Experiment)	63
	Background	63
	Literature Review	64
	CIMSS Experimental Program	66
	University of Illinois Experimental Program	70
	Summary	87
10	Piezoelectric Active Tagging (Theory and Experiment)	89
	Interrogation Schemes	89
	Experimental Testing	92
	Percolation Limits	98
	Efficiency	100
11	Conclusions	104
	Conclusions on Theoretical Analysis	105
	Conclusions on Experimental Work	105
	References	180

List of Figures and Tables

Figures

1	Schematic illustration of explosive tagging using phosphor particles (Ryan and Miller, 1973)	107
2	Illustration of using an ultraviolet lamp or magnet to locate tagged explosives (Ryan and Handke, 1978)	107
3	Schematic drawing showing the method of tagging units of production of a substance with color-coded particles (Lee, 1977)	108
4	Schematic illustration of the concept of active tagging (Clark and Junker, 1990)	108
5	Correlations between the Eddy Current Response and the Ferrite content (weight ratio) in deionized water (Clark et al., 1990)	109
6	Comparison of the Eddy Current Response in an aluminum plate (3.2 mm) and a glass plate (2.5 mm) (Clark et al., 1990)	109
7	Comparison of the cured and uncured microwave response of the Ferrite particle-tagged polymer (Clark and Shannon, 1990)	110
8	The Eddy Current Response vs. the state-of-cure of a cement (Clark, 1991)	110
9	Schematic representation of a tagged adhesive system set-up (Clark, 1991)	111
10	Schematic illustration of the principle of Eddy Current Testing (Shaffer, 1994; Clark, 1991)	111
11	Schematic illustration of an active tagging system using a magnetic excitor	112
12	Effect of particle weight ratio on bonding strength (Clark et al., 1990)	112

13	Skin-effect in a ferromagnetic material with an applied magnetic field . . .	113
14	Photograph of the experimental set-up for manufacturing a tagged epoxy	113
15	Schematic drawing of an experimental setup for active tagging using magnetic excitation	114
16	Experimental set-up for active tagging using magnetostrictive particles and mechanical excitation	114
17	Experimental set-up for inspecting the state-of-cure of a tagged bonding layer	115
18	Changes ($\Delta\omega$) in the resonant frequency reflect the state-of-cure of the tagged adhesives	115
19	Dynamic model for a tagged epoxy system under magnetic excitation	116
20	Comparison of the structural response of the tagged material at different tagging levels (3 % and 5 %)	116
21	Comparison of the power spectrum intensity of the tagged material for different bias levels of the magnetic field	117
22	Experimental results obtained using magnetostrictive particle tagging . . .	117
23	Experimental set-up for active tagging with ferromagnet particles and magnetic excitation	118
24	Schematic drawing showing a dynamic model for ferromagnetic particle tagging	119
25	Numerical results showing the three structural excitation force components	120
26	Numerical results show that a high value of C_p/C can suppress the signature distortion caused by the second harmonic excitation	120
27	Numerical results show that the force response is proportional to the embedded particle contents	121
28	The active tagging particle technique in inspecting the bonding integrity of an adhesive joint	121

29	The experimental configuration used to measure the dynamic response of the specimen using magnetic excitation	122
30	Experimental set-up used to test the dynamic response of the specimen using magnetic excitation	122
31	Illustration of the connections between a test specimen and a force gage	123
32	Transfer function of time domain to frequency domain transform	123
33	Schematic drawing showing magnetic fields of a bar magnet in zero applied field: (a) magnetic intensity, H , field, and (b) magnetic flux density, B , fieldThe vectors in the center indicate the values of these quantities at the center of the magnet	124
34	Power spectrum analysis of magnetomotive force for active tagging with ferromagnetic particles	124
35	Output power spectrum of the frequency response of (a) 3% magnetite tagging specimen; (b) 5% MnZn ferrite tagging specimen; (c) 8% MnZn ferrite tagging specimen	125
36	Frequency response function of polymer composite tagged with 8% MnZn ferrite subjected to magnetic excitation	126
37	Magnetostrictive particle tagged specimen stressed by mechanical loading	126
38	Schematic illustration of a single domain of a magnetostrictive particle	127
39	Schematic illustration of the magnetic induction outside a magnetic dipole	127
40	Schematic drawing showing the flux lines due to the attraction between unlike poles under mechanical loading	128
41	Schematic drawing showing a surface magnetic flux leakage due to a residual induction of a discontinuity	128
42	Magnetostriction effect	129
43	Magnetic domains	129

44	Schematic drawing showing the magnetostrictive tagged specimen experimental set-up	130
45	Schematic drawing showing a hysteresis loop in the magnetostriction of magnetostrictive material	130
46	Schematic drawing showing a saw-cut crack on specimen B, where A and B are the locations of a gaussmeter probe to pick up the crack-free signal and the crack signal, respectively	131
47	Test results of specimen A with the magnetostrictive active tagging method for experimental validation of the theoretical model	131
48	Test results of specimen B with the magnetostrictive active tagging method for defect detection	132
49	Glass/silicone rubber mold used for unreinforced specimens	132
50	Plexiglas mold used for reinforced specimens	133
51	Schematic representation of micrographs M1-M4	133
52	Terfenol-D "chaining" observed in a vinyl-ester polymer (no magnetic field, 40X)	134
53	Significant terfenol-D "chaining" observed in a vinyl-ester polymer (965 Gauss magnetic field, 40X)	134
54	Terfenol-D "chaining" observed in a vinyl-ester polymer (127 Gauss magnetic field, 40X)	135
55	Sparse terfenol-D "chaining" observed in a vinyl-ester polymer (52 Gauss magnetic field, 40X)	135
56	Uniform terfenol-D distribution is achieved by adding the particles to a partially gelled vinyl-ester polymer (no magnetic field, 40X)	136
57	Terfenol-D particles settling in a glass/vinyl-ester composite (no magnetic field, 40X)	136
58	Significant terfenol-D "chaining" observed in a glass/vinyl-ester composite (965 Gauss magnetic field, 40X)	137

59	Terfenol-D "chaining" observed in a glass/vinyl-ester composite (127 Gauss magnetic field, 40X)	137
60	Processing issues affect terenol-D distribution in a partially gelled (6 minute gel time) glass/vinyl-ester composite (no magnetic field, 40X) ...	138
61	Uniform terfenol-D distribution is acheived by adding the particles to a partially gelled (15 minute gel time) glass/vinyl-ester composite (no magnetic field, 40X)	138
62	Terfenol-D "chaining" observed in a glass/vinyl-ester composite (965 Gauss magnetic field, 40X)	139
63	Terfenol-D "chaining" observed in a glass/vinyl-ester composite (127 Gauss magnetic field, 40X)	139
64	Single terfenol-D particle (<45mm) embedded in a glass/vinyl-ester composite (the absence of radial cracks or debonds shows that a good interface has developed between tag and polymer, 400X)	140
65	Terfenol-D particles (<100mm) interacting with glass fibers in a glass/vinyl-ester composite (400X)	140
66	Principles of Magnetic Force Microscopy (MFM)	141
67	MFM image showing the domain structure of a 0.8 μ thick amorphous terfenol-D film grown on Si/SiO ₂ (Su et al., 1995)	141
68	MFM image of a specimen cured under 52 Gauss field in a direction perpendicular to the image. No postcure field was applied to the specimen. The terfenol particle appears as a white region in the middle-right portion of the image. No magnetic domain features can be detected	142
69	MFM image of a specimen cured under 965 Gauss field in a direction perpendicular to the image. No postcure field was applied to the specimen. The terfenol particle extends from the lower-right corner to about half way across the diagonal of the image. Some magnetic domain features are detectable with a gradual shading across the particle and faint lines radiating out from the lower-right corner	143

70	MFM image of a specimen cured under 52 Gauss field in a direction perpendicular to the image. A postcure field of 1307 Gauss was applied to the specimen for 30 minutes, again in a direction perpendicular to the image. The entire image is the central portion of a terfenol particle. Now distinct magnetic domains are present, primarily in a vertical orientation to the image	144
71	Same as Figure 70 with increased contrast to differentiate the domain walls	145
72	Typical terfenol tagged polyester specimen after strain gaging	146
73	Transverse and axial probe guides	147
74	Mechanical loading experimental set-up	148
75	Photograph of mechanical loading experimental set-up	149
76	Specimen loaded in mechanical grips at the start of a test. The Gauss probe is supported by a clamp and stand while the tip of the probe is housed in the plexiglas template next to the specimen surface	150
77	Magnetic field loading experimental test set-up	151
78	Magnetic loading experiment test set-up. Specimen is placed in the central core of the electromagnet and magnetic field lines are oriented along the length of the specimen	152
79	Typical axial field response curve [series D, specimen T1-P21]	153
80	Typical transverse field response curve [series D, specimen T1-P21] ...	153
81	Normalized and smoothed data for specimen T1-P21	154
82	Effect of tag volume fraction on axial response curves	155
83	Effect of tag size on axial response curve	156
84	Effect of glass reinforcement on axial response curves	157
85	Effect of matrix material on axial response curves	157
86	Series G axial field response curves	158
87	Data summary for mechanical loading studies	159

88	Series B (specimen #T1-P9) showing residual axial field response after specimen failure	160
89	Normal loading-unloading curves showing no residual axial field response [series G, specimen #T1-P16]	160
90	Axial field distribution along the length of the delamination [0=edge, <0 inside the delam]	161
91	Loading curves for woven glass/vinyl ester series specimens and the delamination specimen at a position far from the edge of the delamination	162
92	Piezoelectric tagged 0-3 composite material	163
93	Laminated electrode interrogation method	164
94	Laser excitation interrogation method	165
95	Poling apparatus used in the experiments	166
96	Diametral compression test set-up for PTC specimens	166
97	Summary plot of normalized voltage <i>versus</i> applied load	167
98	Percolation curves for 0.5 μ m Ag powder-filled silicone rubber composites (Rushau et al., 1992)	167
99	Critical volume fraction for electrical conductivity as a function of fiber aspect ratio	168
100	Geometry of a PTC plate	168

Tables

1	Parameters of the typical specimens in the experiments	169
2	Comparison of test results and Finite Element calculation results	169
3	Parameters of tagging particles and polymer	169
4	Parameters of the coils and the yoke	170
5	Equipment list	170
6	Comparison of test data and predicted values for ferromagnetic active tagging	170
7	Parameters of a tagged circular beam made of Shell Epon 828 resin	171
8	Parameters of Terfenol-D particles	171
9	Comparison of test results and predicted values of specimen A with magnetostrictive tagging particles	172
10	Comparison of signals of flux leakage field and crack-free field of specimen B with magnetostrictive tagging particles	172
11	Mixing ratios for matrix resins	173
12	Materials used in this study	173
13	Polishing routine for microscopy samples	174
14	Equipment used in mechanical loading experiment	174
15	Results of magnetite specimen tensile tests	175
16	Specimens for volume fraction study	175
17	Specimens for tag size study	176
18	Piezoelectric voltage constants for several materials	176
19	Properties of PZT-5A-169G (24 h after poling)	177

20	Materials used in this study	177
21	Piezoelectric tagged composite specimens manufactured	178
22	Poling conditions for PTC specimens	179

1 Introduction

Background

The Army maintains an aging inventory of more than 130,000 facilities representing a \$4.6 billion high priority unfinanced maintenance and repair. No adequate structural health monitoring capability now exists, so damage or deterioration of building structural elements and concealed structures often occurs without being noticed. External stimuli such as earthquake motion, high winds, and cyclic loading of pressure vessels can accelerate structural damage. Moreover, locations of existing damage due to structural overload are often nonintuitive, making internal damage difficult to detect. According to the Civil Engineering Research Foundation (CERF), effective condition evaluation "is an essential step in the assessment of the safety and remaining service life of civil engineering structures. There is a need to develop and improve diagnostic technologies in which the structure (or component) senses and reports aberrant performance and possibly corrects it" (CERF 1991).

Deterioration of reinforced concrete structures due to corrosion of the reinforcing steel is one of the most expensive types of infrastructure decay across the nation, costing billions of dollars annually. In the United States, thousands of bridges and miles of highway subjected to adverse environmental conditions need to be repaired or replaced with new construction. In fact, 42% of all bridges in the United States are considered to be deficient (Meier 1992). Advanced composites such as fiber-reinforced plastics (FRP) can eliminate many problems associated with metal corrosion because of their excellent fatigue and corrosion resistance as well as their very high strength and ratio of strength to mass density (Kim and Meier, January 1991). Acceptance of advanced composites in both new and retrofit construction applications necessitates quality assurance/quality control (QA/QC) and in-service monitoring techniques to assure the performance and serviceability of the composites. However, conventional nondestructive evaluation (NDE) methods are not very effective for in-field or in-process inspection. One technology that enhances inspectability of advanced composites is the *particle tagging* technique.

The concept of particle tagging involves embedding micron-size sensor particles into materials, such as composites, concrete, or adhesive layers, to make them an integral part of the host material. When interrogated by suitable instrumentation, the embedded particle sensors interact with their host structures and generate certain types of measurable signatures. These signatures can then be correlated with the material and structural conditions, such as internal material strength, distribution uniformity of critical constituents, state of cure, location of voids, etc.

When the tagging approach is used for NDE, it may be classified into two categories: active tagging and passive tagging. *Active tagging* requires an external energy source to energize the embedded tagging particles. *Passive tagging* directly uses an NDE technique, for example, eddy current probe, ultraviolet lamp, magnetic pick-up, or x-ray, to inspect the presence, the amount, and the distribution of the particles.

Although the concept of passive tagging to locate explosives dates to 1973 (Livesay 1973; Ryan and Handke 1973) and active tagging was proposed for NDE in 1990 (Clark and Junker 1990), the physics and mechanism of the particle tagging technique are not well known. For example, the fundamental mechanics and electromagnetics of particle excitation is unclear. Still in the engineering trial-and-error stage is the current knowledge of how to select particle materials and particle size, how to establish proper correlations between particle response and excitation input, and, most importantly, how to interpret the measured signature and relate the response to the structural integrity of tagged materials. For this reason, particle tagging—a novel prospective NDE technique—has not been widely used for in-field and in-process inspection of reinforced structures and composites.

The U.S. Army Construction Engineering Research Laboratories (USACERL) has completed a basic research investigation of selected active tagging technologies, conducted as part of the USACERL Smart Structural Systems Capability Package.

Objectives

The objective of this work was to investigate the active tagging of polymeric composites as a nondestructive evaluation technology to inspect Army infrastructure for internal and external structural problems.

Approach

An overview of materials-tagging technology is presented, including patents, publications, and results of other previous work. This section includes a historical review of tagging techniques, a detailed description of the tagging systems used for *in-situ* NDE of composites, and the experimental results to date. The current and potential applications of the tagging technique are also addressed, and an assessment of future development and research trends in this area is included.

An investigation of active tagging through theoretical modeling was conducted. A theoretical development of active tagging techniques using either embedded ferromagnetic, magnetostrictive, or piezoelectric particles is presented. Modeling methods for tagged systems are proposed to characterize the dynamic behavior of the particles. The sensory signature from a tagged polymer is extracted as a result of the interaction between embedded particles and their host matrix. Relationships between the response of tags and important physical and structural parameters are investigated based upon the electromagnetic theory and material constitutive equations to interpret material conditions or adhesive joint integrity. Numerical examples are provided in this report to demonstrate the feasibility of the use of active tagging for NDE applications. The theoretical assumptions are also discussed in detail. Experimental validations of both the ferromagnetic, magnetostrictive, and piezoelectric tagging techniques are presented in full detail and the results of the experiments are compared to the theoretical models.

Mode of Technology Transfer

This work feeds directly into the AT41 work unit Tagged Composite Construction Elements. The Tagged Construction Elements program at USACERL, along with the Composites Institute, is currently developing full-scale tagged specimens. The specimens will be evaluated for damage using the tagged composites testing technique. Standards will be drafted for the manufacturing and in-service evaluation of parts using this technique, and submitted to the American Society for Testing and Materials (ASTM, Philadelphia, PA).

Nomenclature

a	length of polymer specimen
a	radius of coil
a _p	radius of magnetostrictive tag

\bar{a}	estimated average radius of tags
A	cross-sectional area of the yoke
B	magnetic induction
C	mechanical property of interest
C_m	mechanical property of matrix
C_m	alternating magnetic field coefficient
C_p	mechanical property of particle
C_s	static magnetic field coefficient
d	piezomagnetic constant
D	flexural stiffness
DF	dissipation factor
E	Young's modulus
E	RMS electric field
f	operational frequency
f_r	resonant frequency
F_i	active magnetomotive force component (time domain)
F_i	piezoelectric force component
F_m	total active magnetomotive force
F_{mi}	force on individual magnetic tag
h	thickness
H	magnetic field inside yoke
H	equilibrium magnetic field
H	total magnetic field intensity
H_a	applied magnetic field of the yoke
H_i	magnetic field intensity of dipole
H_m	alternating magnetic field function
H_s	static magnetic field function
H_0	unit vector of magnetic field
I	excitation current
I_{ms}	magnitude of (direct) current (dc)
k^*	effective medium property
k_p	particle property
K_s	equivalent stiffness of host polymer
L	axial length of coil
L	distance between the yoke poles
L	length of plate
m	real mass of polymer specimen
m	generalized modal mass of the tags
m	magnetic dipole moment
m_i	mass of tag
M	magnetization vector

M_s	equivalent specimen mass
N	coil turns
N_d	demagnetization factor
p	pole strength of the end of yoke
p	number of points of contact between particles
P	acoustic power density
P_{cb}	probability for bond to exist
P_{cs}	probability for sites to exist
P_d	power dissipated through dielectric loss
P_h	hydrostatic pressure upon packing
Q_E	inverse of dissipation factor
Q_i	active magnetomotive force component (frequency domain)
Q_M	mechanical damping factor
r	distance from the magnetic dipole (end of yoke)
r_0	unit vector of radial direction
s^H	elastic compliance
S	strain
t	time
t	thickness of plate
T	kinetic energy of tagged specimen
U	strain energy of tagged specimen
V	applied field strength
V_i	volume of particle
V_p	volume of magnetostrictive tag
V_p	critical volume fraction
w	displacement function
W	width of plate
W_1	weight of tagging material
W_2	weight of polymeric host material
z	displacement response of tag
\underline{Z}	displacement of equivalent mass
\bar{Z}	average distance of tag to N-pole on yoke
α	shape factor
γ	particle/matrix coupling constant
δ	dirac-delta function
ϵ	permittivity
η	loss factor of host polymer
η	transducer material efficiency
θ	angle between domain magnetic vector and magnetic field
κ	electromechanical coupling coefficient
σ_0	amplitude of applied alternating mechanical stress

μ_r	resultant effective magnetic permeability
μ_{app}	apparent magnetic permeability
ν	Poisson's ratio
ν	packing factor
ν_f	particle volume fraction
ξ	Halpin-Tsai factor
ρ	mass density of the polymer host
ρ_p	mass density of tagging material
σ	stress
σ	Poisson's ration of the particle
ϕ	particle volume fraction
$\chi\sigma$	magnetic susceptibility of yoke
ψ_r	mode shape of structure
Ψ	phase angle
ω	frequency
ω_n	fundamental natural frequency
$\hat{\omega}_i$	frequency of the equivalent system
Ω_i	magnetic scaler potential of a dipole
$(\vec{i}, \vec{j}, \vec{k})$	unit vector in cartesian coordinates
$(\vec{r}, \vec{\theta}, \vec{\phi})$	unit vector in spherical coordinates

2 Review of the History of Particle Tagging

The concept of adding particles into other materials in order to provide a distinctive information label for the material was first proposed by Ryan and Miller in a U.S. Patent in 1973 (Ryan and Handke 1973). In this study, a small amount of inorganic phosphor was mixed with explosive material so it could be readily located with an ultraviolet lamp, either before or after detonation of the explosive. The phosphor emission spectra were correlated with data known about the explosive when it was manufactured. Figure 1* is an illustration showing the concept of tagging explosives. Ryan and Vodoklys then suggested in a 1976 U.S. Patent that different emission types of inorganic fluorescent materials be combined together for tagging explosives to reduce expensive coding of the phosphor (Ryan and Vodoklys 1976). A patent for this tagging technique was reissued in 1977 (Ryan and Handke 1977), and one year later, Ryan and Handke further suggested the inclusion of magnetic particle materials in explosives (Ryan and Handke 1978). In this case, ferromagnetic particles combined with phosphor grains were mixed with explosives and easily detected by visual luminescent response, magnetic pickup, or both, as illustrated in Figure 2. This is perhaps the earliest reported work on magnetic particle tagging.

In 1973 (the same year the patent was issued to Ryan and Miller), Livesay (1973) developed an approach to tagging individual units of production of a substance by fabricating micro-particles into the substance. The recovery of a single micro-particle would then be sufficient to provide an indication regarding the unit of production of the substance. The phrase *tagging with micro-particles* was first used in the literature in reference to this approach. Further refinements of this particle tagging system were disclosed in U.S. Patent No. 3,897,284 (Livesay 1975). The idea of tagging was again applied to identify the explosive after it had been detonated. A specific description of the micro-particle was given in the patent: the particle has a spherical shape with a diametrical dimension between 1 micrometer and 250 micrometers, and its weight fraction is at least 0.1% of the total weight. Another U.S. Patent (No. 4,053,433) issued to Lee (1977) further suggested that individual units of production of a substance can be tagged with color-coded micro-

* All figures and tables are presented immediately following Chapter 11.

particles for the purpose of visual retrospective identification, as shown in Figure 3.

U.S. Patent No. 4,944,185 (Clark and Junker 1990) discloses a method for nondestructively inspecting adhesive joints using the particle tagging technique. The concept of particle tagging was thus extended to monitor the structural integrity of an adhesive joint, the interface integrity of a matrix-reinforcement composite material, and the state-of-cure of a resin. In this case, a small amount of fine ferromagnetic particles are dispersed throughout materials to be inspected. An electromagnetic field coil and an actuator are suggested to activate the tagging particle such that the structural resonance in the tagged material can be induced. The structural response of the material is measured with an appropriate probe and related to the material conditions. Obviously, this approach requires external energy input to energize the tagging particle; thus, the concept of active tagging, as demonstrated in Figure 4, was introduced. Most of the experimental work done by Clark and others has been focused on the development of the passive tagging technique using an eddy current probe (Clark, Sadhir, and Junker 1990; Clark and Shannon 1990; Clark 1991; Clark 1992).

The earliest publication of Clark's work about passive particle tagging appeared in the first issue of *Material Evaluation* in 1990 (Clark, Sadhir, and Junker 1990). Experimental results were presented to demonstrate the feasibility of a ferrite-particle tagging inspection system. An eddy current probe was used to detect the presence of the tagged adhesive. A good correlation between the eddy current signal amplitude and the ferrite content in deionized water was observed at several specific frequencies: 100 Hz, 500 Hz, and 1000 Hz, as displayed in Figure 5. The ferrite tagging particles included ferromagnetic iron lignosulfonate (GPC, Bellingham, WA). The tagged subjects used an adhesive of EPON 828 and Jeffamine T403 (EPON, Houston, TX), an aluminum plate (3.2 mm in thickness), and a glass plate (2.5 mm in thickness), as shown in Figure 6. This concept was further applied in tagging cement and plaster (Clark and Shannon 1990). Furthermore, in the research a microwave response of the tagged polymer was used to inspect the polymer's state-of-cure, as shown in Figure 7. Further efforts demonstrated that the eddy current response of the tagged cement could also be correlated with the state-of-cure of the cement (Clark 1991), as shown in Figure 8. A simple eddy current system for inspecting tagged adhesives, as illustrated in Figure 9, demonstrated a practical utility for the application of the tagging technique.

Since 1994, renewed interest in tagging of polymeric materials has been generated by USACERL and the Composites Institute. Both organizations have pooled their efforts to explore the feasibility of incorporating "smart" tagging components into

polymer composites for advanced infrastructure health monitoring. Early efforts produced some interesting results with piezoelectric tagged composites (White 1994). More recent studies have focused on ferromagnetic tagging (Rogers, Zhou, and Chaudhry 1994; Rogers, Zhou, and Chaudhry 1995; Rogers, Chen, and Giurgiutiu 1996) and magnetostrictive tagging (Rogers, Zhou, and Chaudhry 1995; Rogers, Chen, and Giurgiutiu 1996; White and Albers 1996). Future work will explore piezoelectric, ferromagnetic, and magnetostrictive tagging in more detail and will seek to incorporate self-repairing tagging components (White et al. 1996) into the research.

3 Particle Tagging Technology

The application of advanced composite materials in infrastructure necessitates in-service monitoring techniques to ensure reliability. However, conventional NDE methods involving radiography, ultrasonics, and eddy current are not capable of providing a reliable inspection of a composite's material integrity. The ultrasonic technique is unable to transmit high-frequency sound waves across an interface; eddy current inspection fails when it is applied to nonmetallic adhesives, rubber, and cements; and radiography cannot detect bonding quality or defects in bonds. Particle tagging technology can address these problems and provide a unique nondestructive testing and evaluation capability.

The use of the particle tagging method for in-field NDE usually involves several critical issues, including selection of acceptable sensory particles (material, size, and quantity), using the proper excitation technique, and determining the corresponding instrumentation. The following sections' discussions focus on these issues.

Candidate Tagging Particles

The particles listed below have been proposed or tested as embedded sensors for use with the tagging technique.

Ferromagnetic Particles

Ferromagnetic particles have been widely used in both active tagging and passive tagging because of their good overall performance. For example, they are easily detectable with existing instrumentation, available at low cost, extremely fine (50-200 Å), and have little chance of chemical interaction with the matrix. However, they are not suitable for tagging ferromagnetic material. For passive tagging, the fine particles (less than 1 micron diameter) of small weight percentage (0.1%) were sufficient to obtain the signature. For active tagging, relatively rough particles (10-20 microns) with a weight ratio of 3%-5% were successfully tested (Zhou et al., February 1993; Sun et al., February 1993). Further efforts may be needed to qualify finer particles for use in both passive and active tagging.

Phosphor Particles or Other Inorganic Particles

These particles have so far only been used for passive tagging. Phosphors have distinctive emission spectra providing a vast number of possible combinations of emission. This is especially useful in identifying different tagged subjects. Particles with a size of 1-250 μm diameter and at least 0.1% weight ratio were suggested in Livesay's work (Livesay 1973).

Dyed or Pigmented Organic Particles

These particles could be visually identified in a unit of production (Lee 1977). The use of micro-particles encoded with an orderly sequence of visually distinguishable colored segments can improve the retrospective identification of the substance. Decoding of the micro-particles can be accomplished with a microscope or other magnifying device.

Piezoelectric Particles

When a mechanical stress is applied to a piezoelectric material, it creates an electrical charge, and in turn, a measurable voltage. Piezoelectric particles might be embedded in a composite structure and used as sensors to detect the internal stress status in the composite.

Magnetostrictive Particles

Embedded magnetostrictive particles may be used for health monitoring of composite materials. When the tagged material is subjected to stress, the *in situ* particles generate small, detectable magnetic fields because of the magnetostrictive effect. The variation in the magnetic field in different locations might be used to locate abnormal stress conditions resulting from damage or delamination.

Electrostrictive Particles

The principle of using electrostrictive particles as embedded sensors is similar to that of using piezoelectric particles. The measurable signature is created by an induced electrical field.

Instrumentation

Conventional NDE instrumentation can be used with various tagging methods.

Eddy Current Probe

An eddy current probe has been most commonly used as a sensor in passive ferromagnetic particle tagging. Figure 10 schematically shows the principle of eddy current testing. The eddy current probe is placed close to or in contact with the tagged material to be tested. A primary coil generates a magnetic field that penetrates the material, creating eddy currents. A secondary coil measures the eddy current flow and records changes caused by defects in the material composition. The magnitude of the eddy current response could be correlated to the presence, the amount, the distribution of the tagging particles, or the tagged material conditions such as state-of-cure, etc.

Magnetic Excitor

A magnetic excitor, which includes alternating electromagnetic coils and static electromagnetic coils, is used to energize the tagging particles, as shown in Figure 11. A force gage or accelerometer sensor can be used to measure the resulting dynamic response of the material.

Ultraviolet Lamp

An ultraviolet lamp is used to locate phosphor particles and to identify the phosphor emission spectra, which are correlated to data known about the material (e.g. explosive) when it is manufactured.

Microwave Device

A microwave device can be used to heat tagged polymers. Heat generation in the tagged material is a function of the microwave properties of the particles, the tagging level, the particle-to-matrix interface, and the properties of the tagged material. The microwave response of tagged materials may be applied to inspect the material integrity, such as the state-of-cure, as shown in Figure 7.

Force Gage or Accelerometer

A force gage or an accelerometer is a conventional transducer that can be used to pick up the dynamic response of tagged materials. In active tagging, when a force

gage is exposed in an active magnetic field, a force gage with a nonferromagnetic housing is usually required, and could be customized to minimize the interference caused by the magnetic excitation on the gage itself.

Magnets

Magnets are simple devices used in passive tagging to locate and recover ferromagnetic tagging particles. The recovery and identification of specific ferrite particles in a spot can provide the detailed tagging or coding information embedded into tagged materials such as explosives or cements.

Acoustic Emission Detector

An acoustic emission detector can be used to receive the acoustic emission of excited tagged structures, and the acoustic emission may be correlated with the emission to determine structural integrity.

X-ray Radioscopy

X-ray radioscopy can be used to visualize embedded tagging particles and to locate the presence and distribution of the tagging particles.

Excitation Methods in Active Tagging

Active particle tagging requires external energy input to energize the tagging particles. The excitation methods may include:

1. magnetic excitation for ferrite particles and magnetostrictive particles
2. microwave excitation for ferrite particles
3. electrical excitation for piezoelectric particles and electrostrictive particles
4. acoustical wave excitation for particles with specific acoustic impedance
5. mechanical (stress or strain) excitation for magnetostrictive, piezoelectric, and electrostrictive particles.

Limitations

Limited testing has shown that a relatively high percentage of ferrite tagging particles may have an impact on the shear strength of tagged adhesives, as shown in Figure 12. However, this result is not considered conclusive (Clark, Sadhir, and

Junker 1990). Therefore, further efforts are needed to quantitatively evaluate the potential impact of tagging particles on the properties of tagged materials.

The skin-effect in the surface of a ferrous material caused by magnetic field excitation poses a limitation on the use of eddy current probes for ferromagnetic material tagging, as shown in Figure 13. The eddy current response from tagged ferromagnetic materials can prevent the inspection of ferrite particles. Active tagging using ferromagnetic particles and magnetic excitation may have the same problem because of the difficulty identifying the presence and distribution of the ferrite particles from the structural response of the tagged ferromagnetic materials. In this case, acoustic excitation may be an option.

Finally, the linear resolution of the eddy current mapping capability is a function of the size of the eddy current probe being used. A smaller-diameter probe would produce less distortion, while a relatively large diameter probe might cause a serious distortion. However, this limitation could be eliminated with the use of advanced manufacturing technology for small and sensitive eddy current probes.

4 Applications of Particle Tagging Techniques

Application Overview

The use of particle tagging techniques has resulted in many applications in research settings because of their unique advantage over conventional sensory techniques. Some of the current and potential applications of the tagging techniques include:

- locating explosives either before or after detonation
- correlating a specific particle emission spectrum with information about an explosive, such as identity of manufacturer and date of manufacture
- identifying individual units of production of a substance by tagging the substance
- assessing the material integrity of tagged asphalt paving materials or cement materials
- permitting assessments of bonding quality, by assessing voids, state-of-cure, uniformity, etc.
- measuring important properties of polymers, such as damping and Young's modulus and their variation
- providing a means to easily excite nonconductive and nonmagnetic materials
- quality control of powder blending processes in industry, ultimately resulting in in-process control
- examining coating quality by energizing tagged coating material mixed with ferrite particles.

Applications in Fiber-Reinforced Polymers for Infrastructures in Civil Engineering

Highway agencies worldwide have been facing a growing problem with deteriorating bridges and structures. In the United States, thousands of bridges and miles of highway subjected to aggressive environments need to be repaired or replaced with new construction. Therefore, structural rehabilitation is the most promising area for initial market introduction of fiber-reinforced polymers (FRP) in civil engineering. In fact, column-wrapping systems with glass/epoxy sheet have already

been used in bridge columns in San Francisco and San Diego (McConnell 1992). In addition, new bridges employing advanced fibrous composites are under construction (Meier 1992).

In both retrofit applications and new construction, it is necessary to use NDE methods for ensuring the performance and serviceability of FRP. However, conventional NDE techniques are not very effective for in-field or in-process inspection. In addition, the diverse properties of the epoxy matrix and reinforcement fibers prevent the use of conventional test methods that utilize signal differentiation to reveal defects in the materials. The quality assurance of advanced composites—both before and during service—has been a formidable challenge.

To enhance the inspectability of FRP, the use of sensors embedded into composites is particularly attractive for the measurement of various parameters and the detection of internal structural defects. The particle-tagging technique, which is considered a logical extension of advanced composites engineering, can offer a convenient, cost-effective, and rapid method of material assessment. Tagging can make FRP sensible in a manner of distributed sensing, which is not possible with many types of sensors. It can also provide inherent information about the in-service state of advanced composites. Potential applications of passive tagging and active tagging in advanced composite materials for structural rehabilitation and new construction are addressed below.

Cure Monitoring

The mechanical properties of FRP composites are, to a great extent, dictated by how well the resin is cured. Many techniques have been applied for quality assurance of resin materials. The simplest and most commonly used cure-monitoring devices are thermocouples. However, used chiefly to control the temperature profile of the cure, they provide little direct information about the cure itself (Strong 1989). Very few direct measurement methods can be used successfully to monitor the mechanical properties as a function of the degree of curing during manufacturing and in the in-service environment (Jang, Hsieh, and Shelby 1989). Tagging offers a new option for inspecting the state-of-cure characterization of the epoxy in FRP. These particle sensors will allow not only monitoring of curing, but also internal sensing during the construction phase and in the manufacturing and environment. The proof-of-concept tests demonstrate that active tagging-based dynamic analysis can directly obtain information about the dynamic mechanical properties as a function of cure time and temperature. The frequency response function (FRF) is found to be sensitive to the state-of-cure of tagged epoxies. Clark and Shannon (1990) also showed in their experiments that cured and uncured samples of silicone-

rubber tagged with ferrite particles have significantly different responses to microwave heating. The microwave response of the tagged silicone-rubber depends on both particle amounts and material's state-of-cure.

Assessment of Bonding Integrity

The use of composites in structural rehabilitation usually requires reliable bonding between FRP and conventional materials such as concrete. Glass/epoxy systems are suggested to wrap bridges or highway columns and piers, not only to strengthen the structures but also for seismic protection (McConell, 1992). Glass/vinyl ester reinforcement bar (rebar) is another choice in repair of bridges. Coated or surface-prepped composite rebar can facilitate bonding to concrete and be effectively used in repair or new construction of bridge decks. In these cases, NDE methodology for inspecting joint integrity must be taken into account, including assessment of defects (voids and inclusions, etc.), postcracking behaviors, and long-term degradation in bonding layers. Unfortunately, no reliable inspection methods can be used to accurately establish adhesive joint conditions. Feasibility studies conducted independently by Clark et al. (1986) demonstrated the potential of particle tagging to assess bond quality in adhesive joints. When the tagged adhesives at the interface are scanned by a proper eddy current probe or actuated by a magnetic field, the presence and distribution of the particles can be closely correlated to interpret defects in the joint, such as voids or inclusions. For example, the response of tagging particles can show the distribution of voids: no ferrite, would indicate the lack of adhesive and hence, no bond. The variation of localized particle amounts can also report the adhesive thickness and coverage of joints.

Damage Detection

Damage of FRP can occur during any phase of its use: manufacturing, handling, transportation, field construction, or normal operation. Examples are delaminations, cracks, abrasions, dents, etc. The first step toward preventing the development of damage and structural failure is to determine the type and location of the damage. Conventional NDE methods include visual inspection, ultrasonics, acoustic-ultrasonic, acoustic emission, radiography, thermography, etc. As discussed earlier, no single NDE technique stands out as a comprehensive solution for FRP inspection. Tagging designed for embedded sensing can provide a new nondestructive testing and evaluation capability for advanced composites. Preliminary tests show the feasibility of using magnetostrictive particles in the inspection of delaminations in glass-reinforced composites. Under a certain loading, the samples with embedded particles produce a measurable magnetic field due to inverse magnetostriction. The variation of the signature picked up by a gaussmeter

or similar hall-effect device can be used to determine whether delamination has occurred in the composite.

5 Recent Studies In Tagging

Early exploratory work at The Center for Intelligent Material Systems and Structures (CIMSS) at Virginia Tech first demonstrated the concept and capability of embedded macro-scale sensors and actuators for structural control and sensing (Rogers et al. September 1988). Since then, efforts have focused on critical issues concerning the development of micro-particle tagging techniques (Sun et al. February 1993; Zhou et al., February 1993; Silimon 1994). Some of the ferromagnetic tagging experimental and theoretical contributions in this area can be summarized as follows. Researchers:

- experimentally demonstrated the feasibility of active tagging using a conventional magnetic excitor and a force gage for the first time in 1992
- theoretically explored the excitation mechanism of magnetic tagging particles and developed a fundamental system model for active tagging in 1992
- experimentally and theoretically investigated the correlations between the measured structural response and the integrity of the tagged structure (the presence and distribution of the particles, and the complex Young's modulus of the tagged material) in 1992
- experimentally showed the concept of using magnetostrictive tagging particles to detect delamination in FRP in 1993
- experimentally demonstrated the utility of the active tagging technique to inspect the state-of-cure of tagged adhesive joints in 1993
- experimentally demonstrated the utility of the passive tagging technique to determine the presence and distribution of the particles and the defects of the tagged epoxy in 1994.

Manufacture of Tagged Epoxy Specimens

The first problem in manufacturing a tagged specimen was uniformly distributing the ferromagnetic particles throughout the specimen. To solve this problem, the specimen was allowed to rotate horizontally while curing, as shown in Figure 14. This prevented the particles from settling to the bottom. A typical specimen contained Epon Curing Agent V-40, Epon Resin 828 (EPON, Houston, TX), and MI-Glow 106 (Circle Systems Inc., Hinckley, IL) ferromagnetic particles. The resin,

curing agent, and particles were mixed and poured into a glass tube of 48 mm diameter, 150 mm long. After the specimen had cured, it was taken out of the glass tube and cut into 0.25 in. samples with a band saw.

Experiments Involving Particle Tagging

Figure 15 shows one of the experimental setups for active tagging testing. The specimen, consisting of the host epoxy and the tagging particles, is located in an alternating magnetic field. A magnetic excitor, consisting of a silicon steel yoke and two coils, is used to activate the distributed particles in the epoxy matrix. One coil generates a static magnetic field to magnetize the particles or turn them into tiny magnetic dipoles, while the other creates an alternating magnetic flux to vibrate the magnetized particles. The proper static magnetic flux bias can maximize the excitation.

In the experiments, a piezoelectric force gage is employed to detect the excitation force imposed on the specimen by an alternating field. It is customized with a nonferromagnetic housing to minimize interference caused by the magnetic excitation itself. The gage sits on a very rigid plastic stand so that the dynamic driving force will act on the gage without significant "inertial attenuation" within the frequency range of interest. In addition, a Hall-effect sensor is placed near the specimen to monitor the magnetic flux density in the air gap. In the excitation experiment at a sampling frequency of 10,000 Hz, a random signal was input to the system to excite the embedded particles.

The experiments were first conducted in 1992 using particles with a high weight fraction (15% and 25%) to demonstrate the concept of active magnetic particle tagging. Further refined tests used the lower weight ratio particles (3% and 5%). Table 1 lists the parameters of the typical specimens.

Figure 16 shows another experimental setup for active tagging using magnetostrictive particles and mechanical stress excitation. The goal of this test was to demonstrate the concept of embedding magnetostrictive particles in composites for structural health monitoring. A beam specimen was made of carbon-fiber-reinforced composites, and two individual beams were bonded together with an adhesive layer tagged with magnetostrictive particles. A specimen was clamped at both ends on a hydraulic actuator and excited at a certain frequency. When the tagged specimen was subjected to the mechanical stress, the embedded particles generated a small, detectable magnetic field due to a mechanomagnetic effect. A gaussmeter was used to pick up the magnetic signature, which could then be

correlated to the in-field material conditions. Four specimens were tested in the experiments. Three were deliberately damaged (i.e., delaminated) and one had no defects. This proof-of-concept experiment showed that discontinuities in the magnetic field resulting from damage or delamination could be located using active magnetostrictive tagging.

Figure 17 demonstrates the concept of using active tagging to inspect the state-of-cure of adhesive joints. Two plastic plates were bonded with the ferrite-tagged adhesive material. When the bonding layer was exposed to a magnetic field, the particles were excited; in turn, the plastic plates were actuated. The structural resonance of the plates was measured with a small piezoelectric patch. The changes ($\Delta\omega$) in the resonant frequency could be correlated with the state-of-cure of the tagged adhesives, as shown in Figure 18.

Experimental Results and Discussion

The structural response of a tagged material obtained from the tests described above can be used to inspect the amount and distribution of critical constituents and to infer the material conditions. The following analysis will provide a brief description to determine the complex Young's modulus of the tagged material. The detailed development of this approach can be found in a separate reference (Zhou et al., February 1993).

Figure 19 shows an equivalent dynamic model of a polymeric material with embedded ferromagnetic particles. The particles are uniformly distributed in the host polymer. As a medium of applying force, the particles transfer the magnetomotive force into a uniformly distributed load to the epoxy matrix and excite the epoxy specimen. Several vibrational modes of the specimen may be obtained in the excitation test, where the fundamental resonant frequency is utilized to identify the Young's modulus of the epoxy matrix.

The equivalent one-degree-of-freedom dynamic model for a measured polymeric specimen, as shown in Figure 19, can be described by

$$M_s \ddot{Z} + (K_s + j\eta K_s)Z = F_m \quad [\text{Eq 1}]$$

where M_s is the equivalent mass of the specimen; K_s is the equivalent stiffness or real part of the complex stiffness of the host polymeric material; η is the damping or loss factor of the polymer; Z is the displacement of the equivalent mass; and F_m

is the active magnetomotive force. Solving Equation 1 yields the phase angle Ψ between the output force measured by the force gage and the input magnetic excitation field,

$$\psi = \tan^{-1} \frac{\eta \left(\frac{\omega}{\omega_n} \right)^2}{1 - \left(\frac{\omega}{\omega_n} \right)^2 + \eta^2} \quad [\text{Eq 2}]$$

where the fundamental natural frequency is $\omega_n = K_s/M_s$.

By means of the Rayleigh energy method, the relationship between Young's modulus and fundamental resonant frequency of the polymer specimen can be established. The governing equations of kinetic energy, T , and strain energy, U , of a plate are described as follows:

$$T = \frac{\rho h}{2} \int_s \left(\frac{\partial w}{\partial t} \right)^2 dx dy \quad [\text{Eq 3}]$$

and

$$U = \frac{D}{2} \int_s \left(\left(\frac{\partial^2 w}{\partial x^2} \right)^2 + \left(\frac{\partial^2 w}{\partial y^2} \right)^2 + 2\nu \left(\frac{\partial^2 w}{\partial x^2} \right) \left(\frac{\partial^2 w}{\partial y^2} \right) + 2(1-\nu) \left(\frac{\partial^2 w}{\partial x \partial y} \right)^2 \right) dx dy \quad [\text{Eq 4}]$$

where h is the thickness of the plate; ρ is the mass density of the plate; s is the surface area of the plate; $w(x,y,t)$ is the displacement function; ν is Poisson's ratio; and D is the flexural stiffness of the plate, $D = Eh^3 / 12(1-\nu^2)$.

The appropriate displacement function, $w(x,y,t)$, may be chosen considering the first vibrational mode of the epoxy specimen and the geometric boundary condition of the sample. Utilizing the equivalent energy relations of kinetic energy and strain energy of the plate, the mass, M_s , and the stiffness, K_s , of the equivalent system can be derived:

$$\begin{cases} K_s = \frac{12352}{35301} \frac{Eh^3}{a^2(1-\nu^2)} \\ M_s = \frac{22304}{58835} m \end{cases} \quad [\text{Eq 5}]$$

where m is real mass of the polymer specimen and a is the length of the plate.

In an excitation experiment at a known value of frequency, ω , the equivalent complex stiffness of a polymer specimen can be obtained from the magnitude frequency response of the equivalent system at the fundamental resonant frequency:

$$\begin{cases} K^* = K' + jK'' \\ K' = K_s = \omega_n^2 M_s \\ K'' = K_s \eta \end{cases} \quad [\text{Eq 6}]$$

The complex Young's modulus of the polymeric material can thus be determined from the following equations:

$$\begin{cases} E^* = E' + jE'' \\ E' = qK' \\ E'' = \eta E' \end{cases} \quad [\text{Eq 7}]$$

where the coefficient, q , determined by Equations 5 and 6, depends on the geometric parameters.

The loss factor of the polymer can be given at the resonant frequency by utilizing the phase frequency characteristics in Equation 2:

$$\begin{cases} \omega = \omega_n \\ \eta = \frac{1}{\tan \psi} \end{cases} \quad [\text{Eq 8}]$$

Figure 20 shows the structural response of the tagged epoxy sample. The resonance frequencies have been identified as the frequencies of the epoxy plate rather than the vibrational frequencies of the embedded ferromagnetic particles by comparison of the results with the finite element (FE) calculations, as listed in Table 2. The epoxy plate structure was modeled with 198 linear quadrilateral shell elements. It should be noted that the model for finite element calculation is established without any embedded particles in the polymer. Thus, the data agreements in Table 2 indicate that a portion of extremely fine sensory particles mixed with polymers does not significantly change the resonant frequencies of the polymeric matrix. Considering the importance of variations of frequency in structural dynamic analysis, the conclusion derived above implies that embedding fine sensory particles into various nonferromagnetic materials may not worsen the dynamic performance of the host materials.

Furthermore, Figure 20 demonstrates that the intensity of the power spectrum of the excited system is proportional to the level of the embedded particles. The higher the weight fraction of the particles in the host epoxy, the more intensive the magnitude frequency response of the tagged epoxy. Especially at the fundamental frequency, a big difference in the signal intensity exists. Thus, this observation can be utilized to report in-field amount and distribution of critical constituents in ferromagnetic particle-reinforced polymeric composites. In addition, in an adhesive joint with embedded particles, localized particle levels will vary with bond thickness and coverage of the joint. The state-of-cure of adhesives is also correlated with variations in their complex Young's modulus. Thus, analyses of signal intensity and variation of modulus during *in situ* inspection can provide a quantitative evaluation of bond integrity.

Figure 21 shows the variation of the magnitude frequency response of a polymer tagged at different bias levels. The amplitude of the frequency response is amplified while increasing the static bias magnetic field. The signal-to-noise ratio of the magnitude frequency response is further improved so that the low fraction of the embedded sensory particles can generate a sufficient signal intensity.

In summary, the preliminary theoretical analyses and experimental results have demonstrated the feasibility of using particle tagging techniques to measure the complex Young's modulus of host polymers. Furthermore, as a feature parameter of polymers, the complex Young's modulus will provide the critical information needed to evaluate in-service or in-process performance of polymeric material systems. The tests also show that the amplitude of the power spectrum of the excited system is proportional to the embedded particle levels. Thus, the amount and distribution of important constituents of ferromagnetic particle-reinforced polymer composites can be quantitatively evaluated. The adhesive thickness, coverage, and state-of-cure of adhesive joints could also be reported when the localized particle levels or structural resonances vary.

Figure 22 shows the experimental results of four active tagging tests using magnetostrictive particles. These tests demonstrate that embedded magnetostrictive tagging particles can be used for NDE and health monitoring of composite materials.

6 Ferromagnetic Active Tagging (Theory)

Background

Although the concept of active tagging with ferromagnetic particles for NDE applications was proposed in 1990 (Clark and Junker 1990), the fundamental mechanisms and electromagnetics involved in the particle tagging are unclear. In particular, there appears to be little in the literature on the theoretical development of active tagging. The previous studies (Sun et al., February 1993; Zhou et al., February 1993) demonstrated the feasibility and applications of the active tagging for improved material diagnostics; however, such experimental engineering trial-and-error approaches are not sufficient for the development of a new particle sensory technique.

This chapter presents a theoretical analysis to provide a fundamental understanding of mechanisms and principles of active tagging using magnetic excitation and ferromagnetic particles (Zhou et al., April 1995). The sensing signature will be extracted as a result of the interaction between embedded particles and their host material. The overall interaction force will be measured using a sensitive force gauge under a tagged specimen. The signature is then correlated to the particle contents, which in turn, can report the presence of defects and material conditions of a tagged polymer or adhesive layer. A dynamic model will be proposed to characterize the dynamic behavior of tagging particles. A transduction relationship between an active magnetic field and the dynamic response of particles will be derived based upon electromagnetic field theory. In addition, the signature distortion and extraction associated with the magnetic excitation will be discussed from theoretical formulations.

Determination of Active Magnetomotive Force

When ferromagnetic particles embedded in a polymer specimen are exposed to a static magnetic field, the particles are magnetized and become magnetic dipoles. Under the excitation of an alternating magnetic field, the particles are driven by the magnetomotive force (mmf) and apply a distributed loading on the surrounding matrix material. The mmf is thus transformed through the particles into a

structural excitation force to drive the nonmagnetic host polymer. To estimate the excitation force of the particle and understand the principle involved in the particle excitation, the magnetomotive force applied on the particle should first be determined.

Figure 23 shows a sketch of an experimental setup for active tagging with ferromagnetic particles. A resultant exciting magnetic field is generated by alternating current (AC) and direct current (DC) in different solenoidal coils, respectively. The DC coils create a static bias field to magnetize the particles and maximize the excitation, while the AC coils create an alternating magnetic flux to vibrate the particles. A ferromagnetic yoke is used as a concentrator of flux lines to create a relatively uniform excitation field. It is assumed that the yoke material is isotropic and linear. Considering the demagnetization factor (N_d), the magnetic field inside the yoke may be expressed by the following (Bray and Stanley 1989; Cheng 1989)

$$H = \frac{H_a}{1 + N_d \chi} \quad [\text{Eq 9}]$$

where χ is the magnetic susceptibility of the yoke and H_a is the applied magnetic field for the magnetization of the yoke. The pole strength at the end of the yoke may be determined by (Jackson 1962; Bray and Stanley 1989)

$$p = \frac{\chi AN}{4\sqrt{a^2 + l^2}} \frac{I}{(1 + N_d \chi)} H_0 \quad [\text{Eq 10}]$$

where $I = I_m \sin \omega t$ is the exciting current; N is a coil of turns; a and l are the radius and the axial length of the coil, respectively; A is the cross section area of the yoke; and H_0 is a unit vector. Consequently, the excitation magnetic field at a distance of r from the end of the yoke is expressed as:

$$H_m = \frac{p}{4\pi} \frac{1}{r^2} r_0 \quad [\text{Eq 11}]$$

Considering a relatively uniform excitation field along the Z axis direction, as shown in Figure 23, Equation 11 yields:

$$H_m = \frac{NA\chi}{16\pi\sqrt{a^2 + l^2}} \frac{1}{(1 + N_d \chi)} \frac{I}{Z^2} \vec{k} = \frac{C_m}{Z^2} \sin \omega t \vec{k} \quad [\text{Eq 12}]$$

in which C_m denotes a simplified coefficient and \vec{k} is a unit vector along the Z direction. Similarly, the static magnetic field, H_s , is expressed as

$$H_s = \frac{\chi AN_s}{8\pi\sqrt{a_s^2 + l_s^2}} \frac{1}{(1+N_d\chi)} \frac{I_{ms}}{Z^2} \vec{k} = \frac{C_s}{Z^2} \vec{k} \quad [\text{Eq 13}]$$

where the subscript s refers to the parameters of a DC solenoidal coil and I_{ms} is the magnitude of a DC current.

When the particles are magnetically driven by the exciting field, the exciting force acting on a particle may be expressed by the following (Bray and Stanley 1989, p 13):

$$F_{mi} = \alpha\mu_0 V_i [(H_m + H_d) \cdot \nabla] (H_m + H_d) \quad [\text{Eq 14}]$$

where the subscript i denotes the parameters of a single particle; V_i is the volume of the particle; $\mu_0 = 4\pi \times 10^{-7}$ H/m is the permeability in free space; and the coefficient α depends on the shape of the particle, and for a spherical particle, $\alpha = 3$. If a particle has an elongated shape, the value of α will rise, which could benefit the magnetization and excitation of particles in ferromagnetic particle tagging. The gradient function, ∇ , expressed in Equation 14, is defined by:

$$\nabla = \frac{\partial}{\partial X} \vec{i} + \frac{\partial}{\partial Y} \vec{j} + \frac{\partial}{\partial Z} \vec{k} \quad [\text{Eq 15}]$$

Substituting Equations 12, 13, and 15 into Equation 14 and considering the resultant mmf acting of the both N-pole and S-pole of the yoke on the particle (see Figure 23b) yields the active magnetomotive force:

$$F_{mi} = \mu_0 \alpha V_i (C_m^2 + 2C_s^2 + 4C_m C_s \sin \omega t - C_m^2 \cos 2\omega t) \left[-\frac{1}{Z^5} + \frac{1}{(L-Z)^5} \right] \vec{k} \quad [\text{Eq 16}]$$

The overall mmf applied on the particles can be obtained by a collection of the whole particles:

$$F_m = \sum F_{mi} = \Delta N F_{mi} \Delta V \quad [\text{Eq 17}]$$

in which ΔN denotes the number of the particle in a unit volume and ΔV denotes an area exposed to the excitation field. For a certain tagging particle level, the weight ratio, ΔW , is defined as:

$$\Delta W = \frac{W_1}{W_1 + W_2} \quad [\text{Eq 18}]$$

where W_1 and W_2 denote the weight of the particles and polymer material, respectively. The number of particles in a unit volume is estimated by:

$$\Delta N = \frac{N}{V} = \frac{3}{4\pi} \frac{\Delta W \rho}{\bar{a}^3 \rho_p} \quad [\text{Eq 19}]$$

in which V is the volume of the tagged polymer; N is the total number of the particles in the specimen; \bar{a} is the estimated average radius of the particles; ρ and ρ_p are the mass density of the polymer and particle material, respectively. Substituting Equations 16 and 19 into 17 and considering the average distance from the particle to the N-pole of the yoke to be \bar{Z} , yields:

$$F_m = \mu_0 \alpha \Delta W V \frac{\rho}{\rho_p} \left[-\frac{1}{\bar{Z}^5} + \frac{1}{(L-\bar{Z})^5} \right] (C_m^2 + 2C_s^2 + 4C_m C_s \sin \omega t - C_m^2 \cos 2\omega t) k \quad [\text{Eq 20}]$$

In Equation 20, the magnetomotive force includes three components. The first constant component, $(C_m^2 + 2C_s^2)$, is the static excitation used for the magnetization of the particles. The second component, $4C_m C_s \sin \omega t$, is the major alternating portion in the particle excitation, in which the static bias field has the same contribution as the alternating field to this major part of the excitation. The third component, i.e., $C_m^2 \cos 2\omega t$, is a double frequency portion evolved from the original excitation field ($C_m \sin \omega t$) and could cause the serious distortion of the excitation signature. Obviously, this second harmonic term is proportional to the alternating excitation field. One way to suppress the second harmonic term, in turn, the signature distortion in experiments, is to reduce the magnitude of the alternating current excitation (C_m). The other way is to maintain the static bias field (C_s) at a level much higher than the alternating excitation. A coefficient, C_s/C_m , thus, is an important indication to determine the influence of the signature distortion. This issue will be discussed in numerical examples later.

It is also noticed in Equation 20 that when a specimen is located in the middle of the two ends of the yoke, the overall magnetomotive force of particles cancels out. The specimen has the minimum excitation, which was observed in a laboratory experiment.

Modeling of Tagging Particles

Figure 24a shows a polymer specimen tagged with randomly dispersed ferromagnetic particles. When subjected to the excitation of magnetomotive force, the particles interact with their host matrix material which applies a viscoelastic constraint force on the particle, as shown in Figure 24b. The motion of the tagging particle may be characterized by a one-degree-of-freedom mass-complex spring system, as shown in Figure 24c. The governing equation is described by

$$m_i \ddot{z} + K'(1+j\eta)z = F_{mi} \quad [\text{Eq 21}]$$

where the lowercase z indicates the displacement response of the particle; m_i denotes the mass of the particle; K' and η are the real part of the complex stiffness and the loss factor of the tagged polymer, respectively.

In response to the active mmf, F_{mi} , the particle vibrates. The governing equations for the steady-state displacement response of the particle can be expressed as three portions corresponding to the excitation of the three components of the magnetomotive force:

$$m_i \ddot{z}_1 + K'(1+j\eta)z_1 = \mu_0 \alpha V_l \left[-\frac{1}{\bar{z}^5} + \frac{1}{(L-\bar{z})^5} \right] (C_m^2 + 2C_s^2) \quad [\text{Eq 22a}]$$

$$m_i \ddot{z}_2 + K'(1+j\eta)z_2 = 4\mu_0 \alpha V_l \left[-\frac{1}{\bar{z}^5} + \frac{1}{(L-\bar{z})^5} \right] C_m C_s \sin \omega t \quad [\text{Eq 22b}]$$

and

$$m_i \ddot{z}_3 + K'(1+j\eta)z_3 = -\mu_0 \alpha V_l \left[-\frac{1}{\bar{z}^5} + \frac{1}{(L-\bar{z})^5} \right] C_m^2 \cos 2\omega t \quad [\text{Eq 22c}]$$

The structural excitation force caused by the particle motion may be expressed in the form of a viscoelastic force:

$$F_i = (K' + K'\eta j)z_i \quad [\text{Eq 23}]$$

where the displacement response z_i ($i=1,2,3$) can be solved from Equation 22. The overall excitation force applied from the particles to the matrix is thus expressed by:

$$F_1 = \mu_0 \alpha V \Delta W \frac{\rho}{\rho_0} \left[\frac{1}{(L-\bar{Z})^5} - \frac{1}{\bar{Z}^5} \right] (C_m^2 + 2C_s^2) \quad [\text{Eq 24a}]$$

$$F_2 = \frac{\mu_0 \alpha V \Delta W \sqrt{1+\eta^2}}{\sqrt{1-(2\omega/\omega_n)^2+\eta^2}} \frac{\rho}{\rho_p} \left[\frac{1}{\bar{Z}^5} - \frac{1}{(L-\bar{Z})^5} \right] C_m^2 \cos(2\omega t - \phi_2) \quad [\text{Eq 24b}]$$

and

$$F_3 = \frac{4\mu_0 \alpha V \Delta W \sqrt{1+\eta^2}}{\sqrt{1-(\omega/\omega_n)^2+\eta^2}} \frac{\rho}{\rho_p} \left[\frac{1}{(L-\bar{Z})^5} - \frac{1}{\bar{Z}^5} \right] C_m C_s \sin(\omega t - \phi_3) \quad [\text{Eq 24c}]$$

where the phase between the excitation field and the force output of the particle is described by:

$$\phi_2 = \tan^{-1} \frac{\eta(2\omega/\omega_n)^2}{1-(2\omega/\omega_n)^2+\eta^2} \quad [\text{Eq 25a}]$$

and

$$\phi_3 = \tan^{-1} \frac{\eta(\omega/\omega_n)^2}{1-(\omega/\omega_n)^2+\eta^2} \quad [\text{Eq 25b}]$$

in which $\omega_n = K'/m_i$ is the natural frequency. The overall excitation force applied by the particles is obtained by a linear superposition of the three parts in Equation 24:

$$F = F_1 + F_2 + F_3 \quad [\text{Eq 26}]$$

Solution of the Tagging Particle Model

Neglecting polymer inertial effects, the motion of ferromagnetic particles embedded in a polymer matrix is equivalent to that of a single-degree-of-freedom spring system when only the first mode of the structural vibration is dominant. Then, the governing equation of the equivalent system can be rewritten in the frequency domain:

$$-\omega^2 mX + KX = F(\omega) \quad [\text{Eq 27}]$$

where m is the generalized modal mass of the tagging particles; $K=K'(1+j\eta)$ is the generalized modal stiffness of the system; and η is the modal damping of the system. The generalized force, $F(\omega)$, is defined from the relation:

$$F(\omega) = F_m(\omega) \int_s \psi_i(\vec{r}) ds \quad [\text{Eq 28}]$$

where $\psi_i(\vec{r})$ is the mode shape of the structure and $F_m(\omega)$ is the Fourier Transform of $F_m(t)$ of Equation 26. Substituting the Fourier Transform of Equation 26 in Equation 28 yields:

$$F(\omega) = [F_{m1}\delta(\omega - \omega_n) + F_{m2}\delta(\omega - 2\omega_n)] \int_s \psi_i(\vec{r}) ds \quad [\text{Eq 29}]$$

where

$$F_{m1} = 4\mu_0\alpha V\Delta w \frac{\rho}{\rho_p} \left[\frac{1}{(L-\bar{Z})^5} - \frac{1}{\bar{Z}^5} \right] C_m C_s \quad [\text{Eq 30b}]$$

$$F_{m2} = \mu_0\alpha V\Delta w \frac{\rho}{\rho_p} \left[\frac{1}{(L-\bar{Z})^5} - \frac{1}{\bar{Z}^5} \right] C_m^2 \quad [\text{Eq 30a}]$$

and δ is Dirac's δ -function. The solution of Equation 27 is:

$$X = \frac{F(\omega)}{K'} \frac{(1 - \frac{\omega^2}{\omega_i^2}) - j\eta}{(1 - \frac{\omega^2}{\omega_i^2})^2 + \eta^2} \quad [\text{Eq 31}]$$

where $\omega_i^2 = \frac{K'}{m} = \frac{M+m}{m} \omega_i^2$ is the frequency of the equivalent system, and ω_i is the frequency of the original system.

When the mass of the polymeric matrix is neglected, the interactive force between the matrix and the particle can be represented by:

$$\begin{aligned}
 Q(\omega) &= KX \\
 &= F(\omega) \frac{(1 - \frac{\omega^2}{\omega_l^2}) - j\eta}{(1 - \frac{\omega^2}{\omega_l^2})^2 + \eta^2}
 \end{aligned}
 \tag{Eq 32}$$

Substituting Equation 29 in Equation 32 yields:

$$Q(\omega) = Q_{01}\delta(\omega - \omega_n) + Q_{02}\delta(\omega - 2\omega_n) \tag{Eq 33}$$

where

$$Q_{01} = F_{m1} \frac{1 - \frac{\omega_n^2}{\omega_l^2} \frac{1}{\Delta\omega}}{(1 - \frac{\omega_n^2}{\omega_l^2} \frac{1}{\Delta\omega})^2 + \eta^2} \int \psi_n(\tau) d\tau
 \tag{Eq 34a}$$

is the amplitude of the $\sin(\omega t)$ signal, and

$$Q_{02} = F_{m2} \frac{1 - \frac{4\omega_n^2}{\omega_l^2} \frac{1}{\Delta\omega}}{(1 - \frac{4\omega_n^2}{\omega_l^2} \frac{1}{\Delta\omega})^2 + \eta^2} \int \psi_n(\tau) d\tau
 \tag{Eq 34b}$$

is the amplitude of the $\cos(2\omega t)$ signal.

It should be noted that in Equation 33, the interactive force has two components of different frequencies. The first component, of frequency ω , is the major component in the particle excitation, in which the static bias field has the same contribution as the alternating field shown in Equation 29. The second component, of the double frequency 2ω , is proportional to the square of the alternating excitation field and could be the cause of serious distortion of the excitation signature.

Numerical Examples and Discussion

In an excitation experiment at a known value of ω , the overall structural excitation force can be measured using a force gage. This dynamic force signature can then be utilized to evaluate material conditions of a tagged polymeric material, such as

the complex Young's modulus (Zhou et al., February 1993). As mentioned above, however, the double frequency component of the magnetomotive force (Equation 24b) causes a second-order harmonic distortion in the structural excitation, which in turn, influences the inspection and interpretation of material conditions of a tagged host matrix. In addition, many other physical parameters will affect the extraction and analysis of the dynamic signature in the active tagging. Included parameters are the location on the specimen, the shape and weight ratio of particles, and the optimization of the static bias field. The following case studies will provide a quantitative analysis to assist in understanding these effects and mechanisms involved in the active tagging with ferromagnetic particles and magnetic excitation.

In numerical examples, the ratio of the bias field and alternating field, C_s/C_m , is used as an index to evaluate the impact of the nonlinear component on the structure excitation. This coefficient is a pure constant associated with physical parameters of a resultant magnetic excitation field, such as the turns, radius, and length of static and alternating excitation coils, as well as the size and magnetic susceptibility of the yoke (as expressed in Equations 12 and 13). It will be clearly shown through this coefficient (C_s/C_m) that a bias static field plays a key role in the suppression of the nonlinearity of a tagged system caused by the double harmonic component. Table 3 shows the fundamental parameters of particles and host matrix material used in the case study. Table 4 lists the physical parameters of excitation coils and a yoke.

Suppose that the excitation frequency is 300 Hz. Figure 25 shows the structural excitation force corresponding to the three components of the magnetomotive force. The overall excitation force in this case is dominated by the major frequency portion ($C_m \sin \omega t$). The double frequency portion is significantly attenuated and the nonlinear distortion does not appear in the excitation force due to a high value of C_s/C_m (i.e., $C_s/C_m=10$). In an active tagging experiment, the dynamic force output, (F_2+F_3) , is more interesting than the constant force (F_1). Following discussion, thus, will focus on the variation of the dynamic force output with physical parameters.

Figure 26 shows that when a static bias field decreases from $C_s/C_m=2$ to $C_s/C_m=0.2$, the second-order harmonic excitation is amplified, which causes a serious distortion in the excitation force. Therefore, in an active tagging using a magnetic excitation, a static bias field at a certain level must be imposed on the embedded particles such that the excitation force signature can effectively be extracted with the minimum distortion, and then used for the inspection of material conditions of tagged polymers.

Figure 27 shows that the excitation force of the particles is proportional to the weight fraction (ΔW) of tagging particles, which was verified in preliminary experiments (Sun et al., February 1993; Zhou et al., February 1993; Zhou et al., April 1995). This observation is useful in reporting the bonding integrity that is associated with localized particle levels. Figure 28 demonstrates the concept of the inspection of a bonding layer. The local particle contents vary with the bond coverage. The presence of a void or inclusion yields a smaller detectable response than the normal signature, while a stronger signature indicates the *in situ* particle concentration. If tagging particles are mixed with other critical powders in the same blending process, the ferrite concentration implies the concentration of the other powders, providing a tool to inspect the quality of a powder blending process.

Figure 28 also shows the concept of using the active tagging technique to inspect the state-of-cure of polymers or adhesive bonds. The mechanical properties of FRP are, to a great extent, dictated by how well a resin matrix is cured. However, few direct measurement methods can effectively be used to monitor the degree of curing in an in-service environment (Jang, Hsieh, and Shelby 1989; Strong 1989). Active tagging offers a new option for inspecting the curing state of polymers. With the ferromagnetic particle tagging, the degree of curing of polymers or bonds can be estimated from their force response. A fully cured sample yields a higher fundamental structural resonance and smaller damping than those of an uncured sample.

In addition, active tagging with ferromagnetic particles can be used to inspect the complex Young's modulus and loss factor, which are important characteristic properties of polymer-matrix composites. In a tagging excitation test, the structural response of a tagged material can be obtained using a force gage, and the fundamental resonant frequency is utilized to identify the Young's modulus of the tagged polymeric specimen. The loss factor is also estimated from the phase frequency function between the excitation field and the force output. A brief description is given in this report, whereas the detailed development of this approach can be found in a separate reference (Zhou et al., February 1993).

It should be pointed out that a high percentage of particles is good for improving the signature intensity of the dynamic force, but the effect of particle concentration on material properties of tagged composites needs further investigation.

7 Ferromagnetic Active Tagging (Experiment)

Experimental Program

An experimental study was aimed at validating the theoretical model presented in the previous chapter. The experiments sought to confirm the relationship between the response of a tagged polymer specimen and the dynamic behavior of the particles. To accomplish this, several tasks are required:

1. fabrication of specimens with different concentrations of particles
2. demonstration of the nonlinear distortion caused by the double harmonic term in the excitation force
3. measurements of the mmf using a force gage, and comparison of the mmf with that predicted by Equation 26 (see Chapter 6)
4. demonstration of the influence of different parameters of particles, such as particle concentration and materials, on mmf
5. experimental validation of the relationship between the response of a tagged polymer specimen and the dynamic behavior of the particles.

Equipment Requirements

Figure 29 shows an illustration of the experimental configuration for the measurement system. Figure 30 shows a schematic drawing of the experimental setup for the measurement system. Table 5 presents the list of equipment used in the experiments. The magnetic exciter consists of a high-permeability silicon steel yoke and two energizing coils. One coil is driven by an AC power amplifier (Crown-CT-400) to generate an alternating magnetic field, while the other coil is powered by a DC source (HP 6268B) to establish a constant magnetic field (Figure 30). A schematic of this principle is shown in Figure 23. The constructive parameters of the magnetic exciter are presented in Table 4. The ferromagnetic yoke is used as a concentrator of magnetic flux lines to create a relatively uniform excitation field. It is assumed that the yoke material is linear and isotropic. The specimen is bolted to a piezoelectric force gage (PCB 208M100) whose housing is made of a 300 series stainless steel, which does not respond to a magnetic field. The assembly sits on the

top of a very stiff plastic stand with its first natural frequency beyond 10,000 Hz. It can be assumed that the specimen is essentially still when excited. Figure 31 is an illustration showing the connection between the specimens and the force gage and the base. The Hall probe of a Gaussmeter (Type MG-5D, Walker Scientific, Inc.) is placed near the specimen in the magnetic field to register the magnetic flux density. A frequency analyzer (Zonic WCA) is employed to process the test data to obtain the frequency response function (FRF).

Test Descriptions and Principles

The test is designed to compare the changes in the natural (resonant) frequencies and damping ratio of the specimens with damage. These are dynamic properties of the structure and do not depend on the position of excitation. More attention has been devoted to the natural frequency measurements than to the damping measurements since the natural frequency measurements are known to have a smaller margin. The current experiments concentrated on the first natural frequency, i.e., the fundamental frequency of vibration of the specimen. Using this technique, the time record of response of a structure to excitation was converted to the corresponding frequency spectrum. The frequencies of the test specimen were readily identified from the peaks of the frequency spectrum. These experiments used the real component of the frequency response of the force signal. The general theory of experimental vibration analysis (Buzdugan 1986) shows that, at resonance, the real part of the force signal goes through a peak, while the imaginary part crosses the zero axis. Equation 32 gives the general expression of the force response in the base of the experimental setup. Examination of Equation 32 reveals that, at resonance ($\omega = \hat{\omega}$), only the imaginary part of the expression for $Q(\omega)$ remains nonzero. The damping was determined by the half-power bandwidth technique (assuming that linear damping was present). A block diagram of the transform from the time domain into the frequency domain used to obtain the natural frequency and damping of the specimen is shown in Figure 32.

When particles embedded in a polymer specimen are exposed to a magnetic field, the particles are magnetized and become magnetic dipoles. Under the excitation of an alternating magnetic field, the particles are driven by the magnetomotive force (mmf) and apply a distributed loading on their matrix materials. Since the distributed loading was assumed uniform and was made equivalent to an overall magnetomotive force, the single-degree-of-freedom analysis could be employed. In theory, tagging particles should possess as high a permeability as possible in order to obtain a larger excitation for a given tagging level. In practice, however, almost no correlation was noticed between the magnetic permeability of the particle and

the resulting excitation force on the specimen. The reason for this apparent paradox is that when a ferromagnetic particle is magnetized, a demagnetization field, acting in the opposite direction to the magnetization field, is spontaneously established. A detailed explanation of this phenomenon was given by Cullity (1972). For example, suppose that a bar is magnetized by a field which is applied from left to right and subsequently removed. A north pole, N, is formed at the right end of the bar, while a south pole, S, is formed on the left end (Figure 33). After removing the external field, the bar remains magnetized. Outside the bar, the magnetic flux lines travel from N to S through the surrounding air on curved paths. Inside the bar, the magnetic flux lines travel again from N to S, but this is in the opposite direction to the magnetization field that was initially applied, and hence it tends to demagnetize the material. The combination of these two effects gives rise to a resulting internal field intensity much lower than its adjacent field or apparent field. Cullity (1972, pp 49-61) and Bray and Stanley (1989) give a detailed explanation of this phenomenon and analytical expressions for calculating its effects. Since these details are not directly bearing on this investigation, they are not presented here.

Due to the demagnetization effect, the resultant effective permeability, or apparent permeability, μ_{app} , is also much lower than the material permeability, μ_r (Sun et al., February 1993). The relationship between μ_r , μ_{app} , and the demagnetization factor, N_d , is:

$$\frac{1}{\mu_r} = \frac{1}{\mu_{app}} - N_d \quad [\text{Eq 35}]$$

where N_d is solely determined by the particle's geometry. If μ_r is sufficiently large, e.g., larger than 500 (this is the case for nearly all of the ferromagnetic materials operating at a medium field intensity; the medium field could be air, fluid, polymer, etc.) the approximation can be made:

$$\mu_{app} \approx \frac{1}{N_d} \quad [\text{Eq 36}]$$

Equation 36 states that the apparent permeability of a ferromagnetic particle is virtually independent of its properties and is solely determined by its geometry. For a sphere, $N_d = 1/3$ and $\mu_{app} = 3$, and for a particle with a l/d ratio of 2, μ_{app} rises to 5.8. The relationship of the demagnetization factor, N_d , and the shape coefficient, α , is referred to by Cullity (1972) and Bray and Stanley (1989). From Equations 35

and 36, one can conclude that it is more effective to select elongated particles than to search for a high-permeability tagging material in order to increase the activation force. This allows one more alternative in selecting particles when other factors, such as their chemical reactivity or interfacial adhesion to the matrix, are important issues.

Description of Tagging Materials

Five tagging materials (from three manufacturers) were initially proposed to be used: Iron (II,III) oxide (or *magnetite*) and MnZn ferrite. Details about these materials are as follows:

Iron (II,III) Oxide (Fe_3O_4).

Two different companies were used each with a different magnetite particle size. Fisher Scientific's magnetite was used in powder form with a size less than $44\text{ }\mu\text{m}$, where Aldrich Chemical's magnetite was used in powder form with a size less than $5\text{ }\mu\text{m}$.

MnZn ferrite ($\text{MnO}_x\text{ZnO}_y(\text{Fe}_2\text{O}_3)_{1-x-y}$).

This material is a polycrystalline compound of:

Manganese ferrite: $\text{MnO}-\text{Fe}_2\text{O}_3$ 45-70% by weight,

Zinc ferrite: $\text{ZnO}-\text{Fe}_2\text{O}_3$ 25-55% by weight,

Iron ferrite: $\text{FeO}-\text{Fe}_2\text{O}_3$ 0-5% by weight.

It is manufactured by Steward, Inc., Chattanooga, TN, and was used in powder form with a size less than $1.5\text{ }\mu\text{m}$.

Fabrication of Specimens

The tagging material, in powder form, was mixed with the matrix material in proportions of 3%, 5% and 8%, by weight. As the matrix material, we used a HTP-402 polyester resin (100 pbw*) (Resin Services, Inc., Sterling Heights, MI) and methyl ethyl retone (MEK) peroxide hardener (1.5 pbw). The parameters of the particles and the polymer are listed in Table 3 (previous chapter). The tagging material was stirred thoroughly into the resin until a uniform distribution into the mass of the polyester resin was obtained. The matrix was observed to enter the gel

* pbw = parts by weight.

stage after approximately 8 minutes at room temperature. This quick gelling time reduced the risk of particle accumulation at the bottom of the specimen due to gravity action. A few trials were performed with curing in an oven at 170 °F. The gel time was observed to reduce significantly with the rise in temperature. However, the room temperature cure was considered sufficient and was adopted for subsequent specimen fabrication, especially in view of its simplicity.

The influence of particle size on specimen fabrication was studied. It was found that the heavier size particles (magnetite less than 44 μm , powder) had the tendency to accumulate at the bottom of the specimen leading to a nonuniform distribution. Subsequently investigation was focused on the finer size particles (magnetite less than 5 μm ; and MnZn ferrite, less than 1.5 μm). The use of fine-size particles ensured that a uniform distribution of tagging particles inside the matrix was obtained.

The tagged matrix was poured into 2-in. diameter containers with a thickness of 0.5 in. After cure of the resin, test specimens were fabricated in a rectangular shape 1.26 in. \times 1.42 in. \times 0.0785 in. (32 mm \times 36 mm \times 2 mm), with a 0.1905-in. (4.84 mm) diameter fixing hole in the middle.

Specimen Testing Procedure

The experimental setup used for specimen testing was previously shown in Figure 29. The rectangular specimens were mounted on top of the force gage using a fixing bolt. Figure 31 shows the connection between the specimens and the force gage and the base. The force gauge and the specimen were placed between the poles of the excitation electromagnet. Figure 30 illustrates the principles used to connect the instruments. The instruments comprise three main components: exciting instruments, measuring instruments, and signal processing instruments. The exciting instruments include a generator, filters, and power amplifiers. As for the excitation, though harmonic forces were most often used, broadband excitation is routinely used to determine the frequencies contributing to the interested frequency range, especially to identify natural frequencies. Both types of excitation were used. The excitation magnetic field is generated by both an alternating current and a direct current in the different solenoidal coils of the electromagnet (as previously shown in Figure 23). The DC coils create a static bias flux density to magnetize the particles and maximize the excitation to improve signal-to-noise ratio and suppress the nonlinear second-order frequency component; the AC coils create an alternating magnetic flux density on a broad frequency band to produce vibrations of the

particles. The alternating component is frequency-dependent, as it is proportional to the energizing current.

The effective impedance of the coil increases with frequency. The current experiments were conducted under constant voltage excitation, and hence the excitation current decreases with frequency. The measuring instruments were termed "measuring transducers", which accomplish the conversion of the change of the physical quantity into the change of an electrical quantity. In the experiment, the specimen was interrogated with the electromagnetic field, and its mechanical response was measured. For this case, a Hall probe of a gaussmeter and a force gage were used. The input data of the experiment was the magnetic field excitation. This was measured with a Hall probe of a gaussmeter placed in close proximity of the specimen. The output data was the force gage signal, which was captured through a charge amplifier signal conditioner. According to Equation 32, the force gage signal, $Q(\omega)$, is proportional to the magnetomotive force, $F(\omega)$, applied on the tagging particles. After conversion and conditioning of the physical data, test data could either be displayed using oscilloscopes, or recorded and stored on floppy disks, for signal post-processing. Both input and output signals were passed to the frequency analyzer. Processing of these signals yielded frequency response curves. From the frequency response curves, the inherent characteristics of the specimen, the natural frequencies and damping ratios, could be ascertained. In the experiment, a signal generator, a filter, and a fast-Fourier-transform (FFT) analyzer were integrated in a computer.

Results and Discussion

Figure 34 shows a typical power spectrum analysis of the magnetomotive force recorded during the experiment. It should be noted that, besides the dominant first harmonic peak at about 1700 Hz, a smaller, second harmonic peak was noticed at about 3400 Hz. This distortion of the magnetic excitation was observed while a sinusoidal current was applied to the AC coils at a lower value of coefficient C_s/C_m associated with the physical parameters of the resultant magnetic excitation field. These phenomena match the theoretical prediction resulting from the nonlinearity of the magnetomotive force caused by the higher harmonic component. Figure 26 shows that variation of the coefficient (C_s/C_m), representing the relative magnitude of the bias static field, plays a key role in the suppression of the nonlinearity of the magnetic exciting force caused by the higher harmonic component. The nonlinear distortion of the excitation force decreases with increases in the coefficient C_s/C_m . The presence of the nonlinear portion of the excitation force makes the interrogation of defects of the examined specimens difficult. This problem has been solved by

means of increasing the bias magnetic field. It has also been found that the first-order harmonic component is much greater than the second-order harmonic component, while the excitation frequency is equal to the fundamental frequency of the specimen. This follows that the magnetomotive force goes through maximum at the excitation frequency equal to the fundamental frequency of the specimen. And at this frequency, the signal-to-noise ratio is better, too. Higher volume fractions of particles in the composite yield a stronger frequency response. For comparison, the output power spectrums of the specimens with different percentages of particles are shown in Figure 35a—c. Specimens with low levels of tagging, for example 3%, 5% and 8%, are found to be clearly actuated by the magnetic field.

The results shown in Figure 36 present the frequency response function (FRF) of 8% MnZn tagged specimens subjected to magnetic excitation. The sensory signature of the FRF from the tagged specimen could be extracted as a result of the interaction between the embedded particles and their host matrix. Relationships between the response of the tagging particles and their dynamic behavior have been experimentally studied to facilitate understanding of the fundamental physics and mechanisms involved in using the active tagging method.

Table 6 shows a comparison of the theoretical and experimental results. Good agreement is obtained in the frequency values, but a significant error is found in the phase angle response. The measurements of natural frequency are known to have a smaller margin of error since frequencies are easy to identify at the resonance peaks of the frequency response curve. However, when a system passes a resonance peak, its phase angle jumps abruptly from phase=0 degrees to phase=180 degrees and tends to be sensitive to the type of damping. According to Equations 25a and 25b, the phase angles are directly related to the damping at the resonance of the system.

This abrupt jumping causes an error of the measurement that cannot be ignored. It is appropriate to consider the possible limitations to this measurement. First, it must be noted that the estimates of both damping and phase angle depend heavily on the accuracy of the maximum FRF level, and this is not a quantity that can be readily measured with great accuracy. Most of the errors in measurements are concentrated around the resonance region, and special precautions must be taken with lightly-damped structures where the peak value may rely entirely on the validity of a single point in the FRF spectrum (Ewins 1984). The second most serious limitation generally arise because the single-degree-of-freedom assumption is not strictly applicable. It should be pointed out that the dynamic behavior of the test specimen is of a multifrequency elastic vibration. It is often found that the

neighboring frequencies do contribute a noticeable amount to the total response at the resonance of the frequency being analyzed, which may affect the peak value of the FRF greatly. This is also one reason why the phase angle cannot be measured accurately. However, enough information can be extracted from frequency alone, and phase discrepancies can be ignored in a first-order analysis. It is also observed that, when driven by the magnetic field, the embedded particle sensors interact with their host matrix and generate measurable signatures of the structural response, and these can be interpreted as structural information.

The results of this phase of the research indicate that the active tagging method with ferromagnetic particles is feasible and demonstrates potential for its application in nondestructive evaluation of basically nonconducting and nonmagnetic composite materials.

8 Magnetostrictive Active Tagging (Theory)

Background

Magnetostrictive materials are a subclass of ferromagnetic materials in that they are ferromagnetic, but they also can change their volume and shape due to the magnetostriction effect when a magnetic field is applied. The magnetostriction effect is reversible such that it generates a measurable magnetic field if a mechanical stress is applied to a magnetostrictive material. This material magnetization due to mechanical loading can be used as an effective sensing means to improve material diagnostics. In this section, a preliminary theoretical model will be proposed to establish a relationship between the response of magnetostrictive particles and important physical and structural parameters. The goal of this phase of the research is to provide a framework for understanding the physics and mechanics involved in active tagging with magnetostrictive particles.

Magnetostrictive materials are currently provided in the form of circular or cubic rod. There are several different methods of material fabrication. One of the methods is called a horizontal zone method (Savage, Abbundi, and Clark 1979), in which a supporting "cold finger" is used to hold the zone in place. The zone is passed through an originally arc-cast material at a slow rate of 1 cm/min. The resulting sample has an elliptical shape and possesses a grain structure with a strong preferential orientation, but this method does not yield a homogeneous boule. Another method is to drop a boron nitride crucible containing the melt through a temperature at a rate of 0.2 cm/min. The boule obtained is almost single crystal in nature. This fabrication method can yield a large, relatively homogeneous boule.

The first problem encountered in the use of the magnetostrictive particle tagging for NDE applications is the need to obtain micron-sized particles, and micron-sized magnetostrictive particles are not commercially available. One of the proposed solutions is to grind a rod in an inert atmosphere to manufacture the particles. In this situation, therefore, some assumptions need to be clearly stated, which make it possible to treat magnetostrictive particles correctly. The following assumptions are employed in the development of the model:

1. A magnetostrictive particle is adequately characterized by a single domain of magnetostrictive material. The magnetostriction after grinding still effectively exists and domain constitutive equations for the material magnetization can be applied to particles.
2. Under a certain level of an external mechanical loading, a magnetostrictive particle becomes a dipole. The magnetization vector rotates to or aligns with the orientation of the external stress field.
3. The interaction between particles is ignored in the modeling.
4. Tagged polymeric materials do not affect the local and external magnetic field generated by the particles because of a very small permeability of the polymers.
5. The particles are uniformly dispersed in the tagged material such that the magnetic response of the particle sensors mainly depends on the local stress level.

Particle Magnetization

Figure 37 shows a polymer specimen tagged with magnetostrictive particles. Under an external mechanical loading, F , which is applied at the ends of the sample, a mechanical stress is produced on the embedded particles. The average applied stress is $\sigma = F/A$, where A is the cross-section of the sample. Under this condition, the magnetization in the particle is developed in response to the imposed stress field due to the inverse magnetostrictive effect. As mentioned above, the assumption of a single domain is made to characterize the response of the particle. Stressed by the mechanical loading, the particle acting as a dipole rotates to or aligns with the direction of the applied stress field. Figure 38 shows an idealized single domain (Mermelstein 1986). The domain is characterized by a magnetization vector, M , which has an angle θ with respect to the anisotropy axis characterized by the anisotropy field H_A . The domain constitutive equations for the magnetization and strain modes may be described by (Mermelstein 1986):

$$\begin{pmatrix} S \\ M \end{pmatrix} = \begin{pmatrix} s^H & d \\ \mu_0^{-1}d & \chi^0 \end{pmatrix} \begin{pmatrix} \sigma \\ H \end{pmatrix} \quad [\text{Eq 37}]$$

where S is the strain; χ^0 is the magnetic susceptibility at zero stress; $(\sigma=0)d$ is the piezomagnetic constant and is a function of equilibrium magnetic field (H); s^H is the elastic compliance measured with coil leads open circuit ($H=0$); μ_0 is the permeability in free-space. When the magnetostrictive material subjected to a mechanical loading is used as a sensor with open-circuited coil leads ($H=0$), Equation 37 can be reduced to:

$$S = s^H \sigma \quad [\text{Eq 38a}]$$

$$M = \frac{d}{\mu_0} \sigma \quad [\text{Eq 38b}]$$

Equation 38b describes a simple relationship between the magnetization and the amplitude of mechanical stress. The macroscopic magnetization generates a magnetic dipole. The magnetic moment of the dipole is determined by (Bray and Stanley 1989):

$$m = V_p M = \frac{4\pi a_p^3}{3\mu_0} d \sigma \quad [\text{Eq 39}]$$

where the subscript p denotes the parameters of the particle (e.g., the dipole). V_p is the volume; and a_p is the radius of the particle.

Magnetic Induction Field of a Particle Dipole

Outside of the particle, the strength of the magnetic field in air can be estimated based on classic electromagnetic theory of magnetic dipole. Figure 39 shows a schematic of magnetic field due to a magnetic dipole. First, the magnetic scalar potential at a point Q is determined by

$$\Omega_i = -\frac{m}{4\pi r^2} \cos\theta \quad [\text{Eq 40}]$$

where the subscript i denotes the parameters of a single dipole; r is the distance from the dipole to the point Q . Then, the magnetic field intensity of the dipole at the point Q is found by

$$H_i = -\nabla \Omega_i \quad [\text{Eq 41}]$$

where the gradient function ∇ given in a spherical coordinate is

$$\nabla = \frac{\partial}{\partial r} \mathbf{r} + \frac{1}{r} \frac{\partial}{\partial \theta} \bar{\theta} + \frac{1}{r \sin \theta} \frac{\partial}{\partial \phi} \bar{\phi} \quad [\text{Eq 42}]$$

Substituting Equations 40 and 42 into Equation 41, the value of H at the point Q can be determined from $H=(H_r^2+H_\theta^2)^{1/2}$:

$$H_r = \frac{m}{4\pi r^3} (3\cos\theta + 1)^{1/2} \quad (A/m) \quad [\text{Eq 43}]$$

It is noted that the size of the particle is relatively small when compared to the distance r such that only horizontal component of the field is considered. Equation 43 is thus reduced to:

$$H_r = \frac{m}{4\pi r^3} \quad (A/m) \quad [\text{Eq 44}]$$

Residual Induction-Based NDE Approach

Magnetostrictive dipoles, subject to a certain level of mechanical stress, rotate to or align with the orientation of the stress. Different particles attract each other between unlike poles, which form flux lines inside a tagged polymer, as shown in Figure 40. The magnetic field outside the tagged specimen is generated by a collection of the particle sensors subjected to a localized stress in a small area. The sum of the particle contributes to magnetic flux is given by

$$H = \sum_{i=1}^N H_i = \frac{1}{3\mu_0} \sum_{i=1}^N \left(\frac{\bar{a}_p}{r_i} \right)^3 d\sigma \quad [\text{Eq 45}]$$

Considering an average size of the particles and the distance (r) yields:

$$H = \frac{\Delta N \Delta v}{3\mu_0} \left(\frac{\bar{a}_p}{\bar{r}} \right)^3 d\sigma \quad [\text{Eq 46}]$$

where the bar symbolizes an average value; Δv is a small area representing local stress state; ΔN is the particle number in a unit volume, and,

$$\Delta N = \frac{\Delta W \rho_p}{V_p \rho} \quad [\text{Eq 47}]$$

Substituting Equation 47 into Equation 46 gives:

$$H = \frac{\Delta v}{3\mu_0} \frac{\Delta W \rho_p}{V_p \rho} \left(\frac{\bar{a}_p}{\bar{r}} \right)^3 d\sigma \quad [\text{Eq 48}]$$

Such fields can be detected and measured with flux-sensitive sensors, such as a gaussmeter or a flux gate:

$$B = \mu_0 H = \frac{\Delta W}{3} \frac{\Delta v \rho_p}{V_p \rho} \left(\frac{\bar{a}_p}{r} \right)^3 d \sigma_0 e^{j\omega t} \quad [\text{Eq 49}]$$

where σ_0 is the amplitude of an applied alternating mechanical stress.

If a magnetometer is placed on the surface above a normally stressed region, it picks up a background field, as shown in Figure 41. This background field may fluctuate because of the non-uniformity of distribution of the particles and surface noise caused by local permeability variations, etc. Figure 41 shows that if a discontinuity, such as internal cracking or a void, is present inside the tagged sample, the local stress level above and below the flaw is higher in comparison to the other. A higher field, similar to a magnetic flux leakage field, is eventually produced. The signal level will be much higher than the other region. The diversion of flux caused by the localized stress amplitude along the length of the sample can give a signature showing the presence and location of the flaws inside the sample. It is also noted that there is a common problem encountered in nondestructive inspection: the flux expressed in Equation 49 decreases rapidly with the depth of the flaw. Hence, a possibility exists for the background field or the surface noise to obscure the small flaw signals. In this case, the applied mechanical loading should be increased to obtain an adequate magnetic induction. In addition, a mechanical or magnetic bias field combined with the use of noise reduction flux sensors, can help to improve the signal-to-noise ratio (Bray and Stanley 1989).

Signal Strength Estimation

A case study is conducted to estimate the signal strength of magnetostrictive particles due to the magnetization. A circular beam tagged with Terfenol-D particles is considered in the case study. The parameters of the tagged beam and the particles are listed in Table 7 and Table 8, respectively. Equation 49 is used to estimate the external magnetic induction of the particles. Substituting the values from Table 7 and Table 8 into Equation 49 yields:

$$B = 2.6 \times 10^{-8} \text{ T} \quad (\text{Gauss}) \quad [\text{Eq 50}]$$

Suppose that a very modest stress of the 10^4 N/m^2 is applied to the magnetostrictive particle-tagged specimen. The magnetic induction outside the particles is raised to:

$$B = 2.6 \times 10^{-4} \quad (\text{Gauss})$$

[Eq 51]

This order of the magnetic signal can be sensed and measured with conventional and inexpensive detectors, such as gaussmeters, coils, or flux gates. Thus, active tagging with magnetostrictive particles appears to have the potential for use in the inspection of internal flaws in advanced composites, such as cracking, voids, and debonding.

9 Magnetostrictive Active Tagging (Experiment)

Background

The preliminary theoretical model developed in Chapter 8 establishes a relationship between the response of magnetostrictive particles and important physical and structural parameters, providing a framework for understanding the physics and mechanics involved in active tagging with magnetostrictive particles.

Magnetostrictive materials are similar to ferromagnetic materials except that they also change their volume and shape under the action of an applied magnetic field. This behavior is due to the magnetostrictive effect. The magnetostrictive effect is reversible such that it generates a measurable magnetic field if mechanical loading is applied to a magnetostrictive material. This magnetization of the material due to mechanical loading can be used as an effective sensing means to improve material diagnostics. Figure 37 shows a polymer specimen tagged with magnetostrictive particles. Under an external mechanical loading, F , which is applied at the ends of the specimen, a mechanical stress is produced on the embedded particles. In this condition, the magnetization in the particle is developed in response to the imposed stress field due to the inverse magnetostrictive effect. Stressed by the mechanical loading of the particles, acting as dipoles, rotate to or align with the orientation of the principal stress direction. Different particles attract each other between unlike poles, forming flux lines inside a tagged polymer as shown in Figure 41. Such a magnetic field can be detected and measured with flux-sensitive sensors, for example, a probe or a flux gate. The flux density is:

$$B = \frac{\Delta w}{3} \frac{\Delta v}{V_p} \frac{\rho_p}{\rho} \left(\frac{\bar{a}_p}{r} \right)^3 \sigma \quad [\text{Eq 52}]$$

where V_p is the volume of the tagged polymer; Δw is the weight ratio of particles; Δv is a small area representing the local stress state; ρ and ρ_p are the mass density of the polymer and particle material, respectively; \bar{a}_p is the average radius of the

particle; \bar{r} is the distance from a magnetic dipole to a magnetic potential point; d is the piezomagnetic constant; and σ is the applied stress.

If a probe is placed on the surface just above a normally stressed region, it picks up a crack-free field, as shown in Figure 41. Equation 52 indicates that if a discontinuity is present in the tagged specimen, a greater magnetic flux leakage is eventually produced since the local stress level above and below the flaw is higher. The signal level will depend on the size of the flaw. A common problem encountered in MS tagging nondestructive inspection, arises with a decrease in magnetic flux sensitivity with flow depth. Thus, it is possible for the background field or the surface noise to obscure the small flaw signal. In this case, the applied mechanical loading should be increased to obtain an adequate magnetic induction. In addition, a mechanical or magnetic bias field, combined with the use of noise reduction flux sensors, is helpful to improve the signal-to-noise ratio (Bray and Stanley 1989).

Literature Review

There is a limited volume of literature devoted to the constitutive modeling and theoretical aspects of magnetostriction compared to the large number of papers dealing with experimental results. Constitutive modeling will be discussed first, followed by recent experimental results.

Magnetostriction is defined as the change in any dimension of a magnetic material caused by a change in its magnetic state. This concept is shown in Figure 42 (Hathaway and Clark 1993). The magnetostriction constant L is given as the change in length over a gage length. Dimensional change happens via the realignment of magnetic domains. These domains are small regions in the material in which the atomic dipole moments are all aligned in one direction due to strong interaction fields arising from the neighboring dipoles (see Figure 43, Rao 1987). In the absence of an external magnetic field, the magnetizations in various domains are randomly oriented for a single crystal. The net magnetization on a macroscopic level is therefore zero. When a weak magnetic field is applied, the volumes of the domains in which the original magnetizations are parallel to the applied field grow at the expense of other domains. This is called *domain wall motion*. In the presence of a strong magnetic field, domain rotation can occur—the realignment of the magnetizations of the individual domains. Irreversibility of domain wall movement leads to magnetic hysteresis.

Broadly speaking, magnetostrictive materials may be divided into two forms based on microstructure: crystalline and amorphous. The former—mainly metallics and

rare-earths—display relatively large saturation strains, especially the so-called "giant" magnetostrictive materials. Therefore, they are ideally suited for actuating purposes. Most of the current interest in this type of magnetostrictive is in Terfenol-D, and most of the papers on crystalline material modeling described below deal with Terfenol-D.

Bergquist and Engdahl extended the classical Preisach model to include the stress dependence of the magnetic field (Bergquist and Engdahl 1991). This paper essentially tries to model the field and stress hysteresis curves for magnetostrictive materials. Comparisons with experimental results for Terfenol-D give excellent agreement.

Engdahl and Svensson (1988) and Engdahl and Kvarnsjö (1990) developed a dynamic simulation model for the behavior of Terfenol-D rods under magnetic and mechanical excitations. Maxwell's equations, the equations of motion, and the nonlinear stress-strain and field relations comprise the constitutive equations. A one-dimensional analysis was used, and they did not account for hysteresis. A commercial software package was used to solve the differential equations. This type of analysis was extended to two dimensions by Kvarnsjö and Engdahl and combined with a Preisach hysteresis model by Bergqvist and Engdahl (Bergqvist and Engdahl 1991; Kvarnsjö and Engdahl 1991). Adly et al. presented a generalized Preisach model for Terfenol-D (Adly, Mayergoyz, and Bergqvist 1991).

Benbouzid et al. proposed a nonlinear finite element method for modeling Terfenol-D (Benbouzid, Reyne, and Meunier 1993). The equations are the same as those used by Kvarnsjö and Engdahl, but a variational formulation is introduced. Commercial packages were used to solve the finite element problem.

Jiles and Thoelke (1991) extended the rotational model presented earlier by Clark et al. (1986) to include a full three-dimensional case. The extension is based on calculating the free energy minima under different stress and field conditions. The change in the minima with loading in the [112] direction, which is typically the axial direction in Terfenol-D rods, is presented in the paper, and the critical field strengths were found and compared to experimental data. Clark's paper is the special case where the loading is only in the [111] directions and rotations of the magnetic moments are permitted only in the [110] plane.

Bagdassaryan and Danoyan (1992) derived a solution for a thin, infinite plate with different constraints on one edge and made up of two layers of magnetostrictive materials subjected to a dynamic magnetic field. The mathematical formulation is complicated and only the simplest cases (homogeneity, elastic isotropy, etc.) can be

solved. The equations of magnetoelasticity are combined with the Kirchhoff thin plate theory.

Note that the response of Equation 52 is only in the range of linear material behavior. It has been shown (Clark, Spano, and Savage 1983; Carman and Mitrovic September 1995) that the piezo-magnetic relation of the magnetostrictive materials is only linear for low values of strain and magnetic field. Outside the linear range, significant saturation takes place and the strain-field curve becomes increasingly flatter. As presented earlier, the nonlinearity threshold depends on the amount of prestress.

Most experimental papers deal with using monolithic magnetostrictive rods or discs to produce an actuation. However, Mitrovic et al. recently reported the results of some analytical and experimental work involving magnetostrictive composite materials (Mitrovic, Robert and Carman 1995). A nonlinear constitutive relation for magnetostrictive materials was developed that includes coupling between temperature/preload and magnetic field strengths. Mitrovic et al. manufactured directional (1-3) magnetostrictive specimens using epoxy and Terfenol-D powder. Chains were induced using permanent magnets with a magnetic field H of about 1.26 kOe. The particulate volume fraction was unknown, but was less than 30 percent. The epoxy was cured for 60 minutes at approximately 149 °C with the magnetic field perpendicular to the direction of gravity. Specimens were 25 mm x 6.35 mm. Some of these specimens were then strain gaged and placed in a magnetic field. Results show a longitudinal strain of nearly 100 microstrain for a field of $H = 0.72$ kOe. The derived constitutive equations and experimental data showed reasonable correlation.

CIMSS Experimental Program

In this experimental investigation, the goal of the research was to validate the theoretical model in Equation 52, and to understand the physics and mechanics involved in active tagging with magnetostrictive particles. Therefore, the following work was performed:

1. fabrication of specimens with and without cracks
2. demonstration of the reverse magnetostrictive effect
3. measurements of magnetic flux density of the magnetic induction field due to mechanical loading
4. defect detection of a specimen embedded with magnetostrictive particles.

Equipment Requirements

Figure 44 shows a schematic diagram of the experimental setup for the measurement system, consisting of the loading force from the testing machine, the fixture for testing, the tagged specimen and the gaussmeter probe (magnetometer flux gate). A model 810 MTS machine applied a mechanical force, which can be a constant or a harmonic loading, on the ends of the test specimen. The gaussmeter was used to record the magnetic flux density due to the mechanical loading.

Test Descriptions and Principles

The theory of magnetostriction states that under an external mechanical loading, magnetization occurs in a magnetostrictive material because the magnetization vectors rotate to or align with the orientation of the external stress field and form a magnetic induction field.

The first consideration in the experiment is the generation of a suitable magnetic field within the specimen. In ferromagnetic materials, beginning with the magnetizing field, the flux density, B , rises in a nonlinear fashion for small increases in the intensity, H , during magnetizing until saturation occurs. Also when a magnetostrictive material is subjected to a magnetic field, the variation of flux density, B , with intensity, H , traces out a hysteresis loop. Figure 45 shows a typical hysteresis loop of a magnetostrictive material (Cullity 1972). If the magnetic intensity, H , initially zero, is increased, the B-H relationship will trace out the curve OA. This is called the magnetization curve of the material. If the magnetic intensity, H , is decreased, the B-H relationship does not follow back down the curve AO, but instead moves along the new curve AR. The magnetization, once established, does not disappear with the removal of H ; in fact, it takes a reversed magnetic intensity to reduce the magnetization to zero. If H continues to build up in the reverse direction, then B will establish itself in reversed direction, and Figure 45 begins to show a certain symmetry. Finally, when H once again increases, the operating point follows the lower curve of Figure 45. Thus the B-H curve for increasing H is entirely different from that for decreasing H , resulting in a B-H curve hysteresis. If the mechanical loading is proportional to the flux density applied to the magnetic saturation region, the maximum possible value of the flux density can be achieved. In general, the magnitude of the magnetization should be chosen to maximize the flaw leakage field with respect to other field sources that might interfere with flaw detection; the optimum magnetization is usually difficult to determine in advance of a test and is often approached by the trial-and-error method. Ideally, the direction of the field should be perpendicular to flaw dimension to maximize the effect of the flaw on the leakage field.

Description of Tagging Materials

Four size classifications of tagging material Terfenol-D ($\text{Tb}_x\text{Dy}_{1-x}\text{Fe}_2$, where $0.27 < X < 0.3$, $0 < Y < 0.5$) were initially proposed to be used: less than 45-micron; 45-75 micron; 75-100 micron and 150-250 micron. Since heavier particles (for example, more than 45-micron) were obviously observed concentrating on the bottoms of containers during fabrication, only the particles less than 45-micron were used. Table 8 lists the parameters of Terfenol-D particles.

Fabrication of Specimens

The tagging material, in powder form, was mixed with the matrix material in proportions of 8% and 15%, by weight. The matrix material of HTP-402 polyester resin (Resin Services, Inc., Sterling Heights, MI) (100 pbw) and MEK peroxide hardener (1.5 pbw). The tagging material was stirred thoroughly into the resin until a uniform distribution into the mass of the polyester resin was obtained. The matrix was observed to enter the gel stage after approximately 8 minutes at room temperature. This quick gelling time reduced the risk of particle accumulation at the bottom of the specimen due to gravity action.

The influence of particle size upon specimen fabrication was studied. It was found that the heavier particles had the tendency to accumulate at the bottom of the specimen, leading to a nonuniform distribution. Subsequently, only the finer-size particles (less than 45 micron) were used.

The tagged matrix was poured into 2.5 x 5.0 in. containers, at a thickness of 1/2-in. After final cure of the resin, test specimens were fabricated. One of test specimens had a rectangular cross section of 0.394 in. x 0.204 in. (10 mm x 5.17 mm), was labeled specimen A (without defect), and was embedded with 8% of the tagging particles. The other test specimen had a rectangular cross-section of 0.469-in. x 0.206-in. (11.92 mm x 5.23 mm), was labeled specimen B (with a saw-cut crack), and was embedded with 15% of the tagging particles. The saw-cut crack was cut in a wedge pattern and was located on the surface in the middle of the specimen (shown in Figure 46).

Specimen Testing Procedure

The experimental setup used for specimen testing is shown in Figure 44. Specimens were secured to a Model 810 MTS machine, which applied axial loadings of compressive or tensile force to the test specimen. A static compressive force up

to 450 lb was applied. The magnetization was obtained in response to the applied mechanical loading. Magnetic flux density was measured with a gaussmeter probe.

Test Results and Discussions

It was observed from the experiments that the magnetostrictive properties of the powdered Terfenol-D material was preserved even after the bulk material was mechanically ground into small particles. This is the first documented case of Terfenol-D retaining mechanical properties below 100 micron powder form.

The data in Table 9 (specimen A) represents the normal component of the magnetic induction flux density close to the specimen under compressive load. It was found that at a low stress field, the flux density measured was less than that predicted in Equation 52 when the magnetostrictive particles were not completely magnetized. It was also found that the magnetic flux density increased with the stress field until it reached saturation. However, the values predicted in the theoretical model increased proportionally as the mechanical stresses increased, as indicated by Equation 52. Figure 47 shows that theory and experiment differ at high stress. This discrepancy was due to the assumption of a linear relationship between the magnetization and the mechanical stress. However, such an assumption simplifies the problem dramatically. Observation of Figure 47 indicates that the linear relationship between load and magnetic flux, as given in Equation 52, was only applicable at low load/flux levels. In the current experiments, the critical threshold force value of the linear behavior is $F_{cr}=100$ lb (critical stress $\sigma_{cr}=1243.8$ psi). Above the threshold critical value, increasingly nonlinear behavior was observed. For $F=200$ lb, the error between the theoretical linear model and the experimental nonlinear behavior was 33%. This error increased to 113% at $F=400$ lb. These observations indicate that the linear model for magnetostrictive tagging is only valid for predicting low stress/field ranges of behavior. At higher stress/field values, the response will be lower than the linear prediction. This nonlinear behavior does not render the method ineffective, but only signals to the user not to expect proportionality at high load/field values. The experimental curves also showed the tendency for a saturation limitation, which was in agreement with other magnetostriction theories (Cullity 1972). Clark observed this phenomenon (Clark, Spano, and Savage 1983).

Above a certain threshold, a correction to Equation 52 must be introduced. In these experiments, the critical threshold force value of the linear behavior appears to be $F_{cr} = 100$ lb (critical stress $\sigma_{cr} = 1243.8$ psi). The correction consisted of the following formula:

$$B_{corrected}(F) = \alpha \cdot B_{th}(F) + \beta \cdot B_{th}(F_{cr})$$

[Eq 53]

where $B_{corrected}$ is the corrected field prediction formula, B_{th} is the theoretical field predicted by Equation 52, and $\alpha=20\%$ and $\beta=120\%$ are correction factors. Figure 47 shows that the corrected theory given by Equation 53 fits the experimental results quite well.

For defect detection, a saw-cut crack was simulated on the surface of Specimen B. The data shown in Table 10 were obtained by measuring the normal component of the magnetic flux leakage field at the surface of the crack. The crack-free field was also measured in the vicinity of the crack. The signal difference between the saw-cut crack and the crack-free field was significant. It was also noted that at low stress field, the signal difference was small. The reason may be that the background field or the surface noise obscures the small flaw signals at a low stress field. It was also noted that the test values dropped after a 350 lb force (Figure 48). This was caused by bending of the strip specimen during the testing. Figure 48 also shows that the field near the crack tip seems to be smaller than the crack-free field. This contradicts the theoretical model, which predicts that the field near the crack tip will be larger than the crack-free field. The difference may be the result of the existence of an additional bias field in the lab environment. The test figure houses a large ferromagnetic fixture that could focus the environmental magnetic field. A bias field of the opposite sign to the field generated in the experiment through the piezomagnetic effect would shift the data line and could result in the observed effect. Although the environmental magnetic field was not measured at the time of the experiment, its existence appears to be a plausible explanation of the observed data. However, the presence of the environmental field does not modify the conclusions of this experiment, which indicate that the magnetic field generated near the crack tip through the piezomagnetic effect in a tagged composite is sufficiently different from the crack-free field to detect cracks. Hence, the prediction of the theoretical model was experimentally confirmed. In future practical applications, care should be taken to measure any environmental magnetic field and to remove any ambient electromagnetic noise.

Because the defect detection was based on the comparison of signals between the crack and the crack-free field, it can be concluded that the experiments were successful in demonstrating a potential application for active tagging with magnetostrictive particles in nondestructive evaluation.

University of Illinois Experimental Program

Magnetostrictive specimens were manufactured with variations in the volume fraction of tags, particle size distribution of tags, magnetic field during cure, and

matrix material. These specimens were sectioned and polished for optical microscopy to determine tag volume fraction and distribution, and to characterize the tag/polymer interface. Several specimens were also analyzed using an atomic force microscope (AFM) under magnetic force mode (MFM) to determine the magnetic domain alignment of tags subjected to various magnetic postcure field levels. Mechanical test specimens were fabricated and loaded in uniaxial tension while monitoring the induced magnetic field next to the specimen surface. Several specimens were then subjected to magnetic field loading while monitoring the induced surface strains. The sections that follow describe the manufacturing procedure, microscopy results, experimental setup, and experimental results for Terfenol-D tagged composites.

Specimen Manufacturing

A series of experiments was performed to serve as the basis for a feasibility study of the concepts discussed above. Magnetite and Terfenol-D specimens were manufactured with varying matrix material, fiberglass reinforcement, particle volume fraction, and particle size. In all, 30 magnetite and 75 Terfenol-D specimens were made. Several specimens were sectioned and used for microscopy, while others were used for mechanical loading and magnetic field loading experiments.

Materials. Magnetostrictive ingots were obtained from Etrema Products, Inc., (Ames, IA). The ingots were ground and classified into four different particle diameter ranges: 0-45 μ , 45-75 μ , 75-100 μ , and 100-150 μ . Grinding was carried out under a nitrogen atmosphere to prevent oxidation. Magnetite powder (<5 μ) was used for preliminary manufacturing as a proof-of-concept. Two different matrix materials were used—an isophthalic modified polyester and a bisphenol epoxy vinyl ester. These resins were cured at room temperature in relatively short times using two catalysts (dimethylaniline and cobalt naphthenate) and an initiator (methyl ethyl ketone peroxide). Table 11 shows the mixing ratios for different cure times. The fiberglass reinforcements were both plain weaves using 60 x 56 (woven 2113) and 50 x 20 (pseudo unidirectional 1297) counts. Table 12 lists all the materials used in this study and the supplier for each.

Specimen preparation. Specimens were made using combinations of polyester or vinyl ester, magnetite or Terfenol-D, and woven or pseudo unidirectional fiberglass. Different volume fractions and size ranges of Terfenol tags were used and various magnetic field levels were applied during cure. The nomenclature below represents key specimen parameters and identifiers:

Example: T1-P10A

<i>T (or M):</i>	Terfenol-D (or magnetite) used
<i>first number:</i>	volume fraction of resin of tags (1% in example)
<i>hyphen [-], W, or U</i>	- : no reinforcement
	W : woven fiberglass
	U : pseudo unidirectional fiberglass
<i>P (or V):</i>	polyester matrix (or V for vinyl ester)
<i>second number:</i>	specimen number (#10 in example)
<i>A (A-H possible):</i>	specimen series designation

Specimens were manufactured using either a glass/silicone rubber mold (unreinforced specimens) or a Plexiglas mold (reinforced specimens). The glass/silicone rubber molds were made using a pyrex glass Wheaton slide staining dish (Fisher Scientific, Itasca, IL) and Airtech Aircast 3700 RTV silicone rubber (Coast-Line International Distributing, Lindenhurst, NY), shown in Figure 49. The Plexiglas mold is shown in Figure 50 and was made by the UIUC Dept. of Theoretical and Applied Mechanics (TAM) Machine Shop. This mold was used with reinforced specimens so that a compaction pressure of approximately 0.186 MPa could be applied to the specimen during cure.

Unreinforced specimens were manufactured using the following procedure:

1. Polyester or vinyl ester resin was weighed using a Denver Instruments (Arvada, CO) XL-300 precision electronic balance (± 0.001 g).
2. Weight percentage calculations of magnetite or Terfenol-D and the catalysts and initiator were made. Magnetite specimens used the 60-minute cure vinyl ester mix; Terfenol-D specimens used the 15-minute cure mix (see Table 11).
3. Particles and catalysts were weighed (using disposable glass pipettes for the liquids to avoid contamination) and mixed using an electric mixer (Arrow Engineering Co., Hillside, NJ) for 2-3 minutes.
4. Initiator was weighed and the resin and particles were mixed again—for 3 minutes for polyester and 10-15 minutes for vinyl ester.
5. Mixture was then poured into a glass/silicone rubber mold and allowed to cure for 1 hour for polyester, and between 2 and 12 hours for the vinyl ester. All specimens were allowed to stand at least 48 hours at room temperature before testing.
6. If a magnetic field was to be applied during cure, two large permanent magnets (Adams Magnetic Products Co., Melrose Park, IL) were placed below and above the mold. The magnets are 152.4 x 101.6 x 25.4 mm and have a strength of approximately 1200 Gauss. Various field levels were obtained by controlling the magnet separation with plexiglas spacers.

Reinforced specimens were manufactured using a slightly different procedure:

1. The plexiglas mold was coated with carnauba wax (Trewax, City of Commerce, CA) and the specimen removal holes were sealed with Airtech GS43MR vacuum bag sealant tape (Coast-Line International).
2. Plies of woven or pseudo unidirectional fiberglass were cut, enough to provide approximately 50% fiber volume fraction composites (45 plies for woven, 59 plies for pseudo unidirectional).
3. The matrix resin was mixed according to steps 1, 2, and 3 above.
4. Alternate layers of resin mixture and fiberglass were placed in the mold. The woven fiberglass was stacked and laid-up in small packs of 10 plies; the pseudo unidirectional fiberglass was laid-up as individual plies. The resin mixture was stirred during fiber placement to avoid settling of Terfenol-D particles. For the delamination specimen (T1WV11), a 38.1 x 12.7 mm piece of 0.1 mm thick Teflon[®] film (Airtech A4000R, Coast-Line International) was placed in the specimen between the 22nd and 23rd plies to provide the delamination site.
5. The mold top was placed on the specimen, air was squeezed from the mold, and a nonmetallic weight was placed on top.

All specimens were then surface milled in the TAM machine shop to dimensions of 76.2 x 12.7 x 4.76 mm.

Microscopy Studies

Some representative specimens were prepared for microscopy and domain visualization. A small (1 cm) section of the specimen was removed from its center using a radial arm saw and diamond blade. This small sample was then placed in a mold—a phenolic ring with a 31.75 mm outer diameter (Buehler Ltd., Lake Bluff, IL). The sample was then set in EPO-KWICK[™] Fast Cure Epoxy and allowed to cure according to the instructions. The sample was then polished on a Buehler Ecomet 3 variable speed grinder-polisher with an Automet 2 power head. The polishing machine was set for 150 rpm, 15 lb force, counterclockwise rotation, and a water lubrication system was used. The polishing routine is shown in Table 13, as suggested by Buehler. Fresh abrasive discs were used for each set of three samples to avoid smearing the sample surface with contaminants. All micrographs were taken using a trinocular 1600X microscope (Edmund Scientific, Barrington, NJ), a Nikon HFX-II Polaroid[®] System (Fryer Co., Inc., Huntley, IL), and Polaroid[®] Series 52 film.

Effect of curing magnetic field. Fourteen micrographs were taken. Micrographs M1 through M12 are 40X magnification; micrographs M13 and M14 are 400X. All micrographs were of a cross-section through the thickness near the center of the specimen. Figure 51 is a schematic representation of results associated with the micrographs shown in Figures 52–55. A guide to the micrographs follows:

Figure 52—Specimen T1-V1. In the absence of a magnetic field, particles of Terfenol-D can be seen to have settled at the bottom of the specimen. This type of behavior was not seen with magnetite tags, owing to the large difference in density of the two materials (magnetite specific gravity = 5.47; Terfenol-D specific gravity = 9.25).

Figure 53—Specimen T1-V2. Magnetic field $B = 965$ Gauss. The Terfenol-D particles can be seen to form "chains" along the magnetic field lines, from top to bottom. The intensity of the applied field forms very heavy, thick chains; nearly all the Terfenol-D is aggregated into relatively few chains. The chains are extended through the entire thickness.

Figure 54—Specimen T1-V3. Magnetic field $B = 127$ Gauss. Again, one can see chaining of the particles, but they are not as heavy as with the stronger magnetic field. Although there are more chains, they do not extend completely through the thickness.

Figure 55—Specimen T1-V4. Magnetic field $B = 52$ Gauss. The chains have now become very sparse and there are many of them. They do not extend through the entire thickness. For magnetic fields lower than 52 Gauss, the Terfenol-D settles as with no magnetic field, although the particles remain in chains oriented along magnetic field lines.

Figure 56—Specimen T1-P1. To achieve a suspension and uniform distribution of the Terfenol-D particles in the specimen, a short gelation time was desired in the absence of a magnetic field. The polyester resin was formulated to gel in six minutes. This micrograph shows a uniform distribution of the Terfenol tags in polyester achieved with a short gel time. Similar behavior was obtained for vinyl ester resin.

Figure 57—Specimen T1WV1. No magnetic field; four plies of woven fiberglass. It can be seen that, as in Figure 52, the Terfenol-D settles with gravity. However, the plies have kept the particles from settling to the bottom because the particles are much larger than the openings between the fibers.

Figure 58—Specimen T1WV2. Magnetic field $B = 965$ Gauss. Four plies. Again, as in Figure 53, heavy chaining has occurred throughout the thickness and through the fiberglass plies.

Figure 59—Specimen T1WV3. Magnetic field $B = 127$ Gauss. Four plies. Similar behavior as noted in Figure 54.

Figure 60—Specimen T1WP1. No magnetic field. Forty-five plies. In an attempt to create a suspension of Terfenol-D within the composite specimens, the six minute cure polyester was attempted. The cure time did not allow sufficient time to properly place all the plies in the mold; the result is very wavy plies and many voids.

Figure 61—Specimen T1WV4. No magnetic field. Forty-five plies. This is a micrograph of the prototype composite Terfenol-D/fiberglass specimen. Using a 15 minute cure formulation of the vinyl ester resin, sufficient time was allowed for proper placement of the fiberglass plies within in the mold. As a result, it can be seen that the Terfenol-D particles are uniformly distributed between the plies.

Figure 62—Specimen T1UV2. Magnetic field $B = 965$ Gauss. Four plies. Once again heavy chaining is evident, but now the chains can continue through the loosely woven pseudo unidirectional plies by separation of the individual reinforcing fibers.

Figure 63—Specimen T1UV3. Magnetic field $B = 127$ Gauss. Four plies. Similar results as discussed in Figure 59.

Figure 64—Specimen T1-V1. Terfenol-D particles with size range less than 45μ . Close-up view of a single particle surrounded by matrix showing no debond or radial cracks around particle. This is a typical result for this series of specimens.

Figure 65—Specimen T1WV4. Terfenol-D particles with size range less than 100μ . Close-up view of particle/fiberglass interactions in high fiber volume fraction specimen.

These micrographs show the experimental progression from particle settling to uniform suspension in both unreinforced and reinforced specimens. The study also shows some of the variety of particle distributions that can be achieved using different magnetic fields and matrix cure times. The chaining phenomenon could be useful for specific tagging purposes; it may be possible to enhance the response

through the thickness as a result of the chaining phenomena, making detection easier.

Effect of postcure magnetic field. Three specimens were used to investigate the effect of a postcure magnetic field and domain alignment. The intent was to apply a large magnetic field after curing the material to induce magnetic domain alignment in the direction of the field. Alternatively, a large magnetic field could be applied during cure, although particle chaining would also occur. Specimens that have been magnetically aligned would have enhanced (effective) magnetostrictive behavior. If domains are not aligned, then some particles tend to cancel or balance the induced fields of other particles in their neighborhood, reducing overall detection sensitivity.

Two specimens were not subjected to a postcure magnetic field. The first of these was cured under a 52 Gauss magnetic field; the second was cured under a field of 965 Gauss. A third specimen was cured at 52 Gauss and then subjected to a postcure field of 1307 Gauss for 30 minutes.

Specimens were then taken to an AFM at the Beckman Institute (University of Illinois at Urbana-Champaign) to perform magnetic force microscopy (MFM). In MFM imaging a very small cantilever probe is brought close to the sample surface (see Figure 66). The probe tip is magnetized and it responds to magnetic forces near the surface of the sample. The images that follow were obtained using a noncontact oscillatory mode. In this mode the cantilever is driven at resonance and changes in the resonant amplitude of deflection is measured. Samples are scanned across the surface and magnetic forces are monitored and stored in the computer. The strength of the magnetic force is imaged as a greyscale or color code on a digital image displayed on the computer monitor.

Some background information is useful to make sense of the images that follow. The objective is to visualize the magnetic domains of Terfenol particles. A single-domain particle will appear as one color on the MFM image since the magnetic force is nearly constant across the surface. Alternately, a random orientation of magnetic domains in a particle will also produce a single color on the MFM image, again with little change in magnetic force across the sample surface. However, if multiple domains are present and oriented, then as the probe reaches a domain wall, the force will change dramatically and the domain wall can be visualized. This phenomenon is shown in the work of Su et al. in Figure 67 (Su et al. 1995). Here the domain walls appear as black lines on the image. The presence of these lines indicates that extremely uniform domain alignment was obtained.

Figure 68 shows a single particle in a specimen subjected to a 52 Gauss curing field but not to a postcure magnetic field. The embedding polymer appears as black surrounding the Terfenol particle, which appears as white. There are no features evident in the particle, which indicates no alignment of the magnetic domains. Many particles were scanned and the result shown is typical.

Figure 69 shows a single Terfenol particle for the specimen cured at 965 Gauss field strength and no postcure field. The magnetic features are difficult to distinguish in the image; some alignment was obtained but the level was minimal. Figure 70 shows the kind of features indicative of domain alignment. The entire image comprises the central portion of a large particle for a specimen subjected to 1307 Gauss postcure magnetic field. In this sample a rich texture is evident with several clear domain walls. Figure 71 is the same image with increased contrast. Now the domain walls are clearly evident and the image corresponds closely to that published in the work of Su and others. A preliminary image analysis was carried out on Figure 70; fractal analysis indicates a mean feature size of about 1 micron. This is also in agreement with the work of Su and others in which they measured domain sizes on the order of 1μ .

The primary conclusion that can be drawn from the MFM images is that domain alignment is possible under a postcure magnetic field. In the current testing this alignment was accomplished at 1307 Gauss.

Loading Tests

Two sets of experiments were performed in this study. The mechanical loading experiment consisted of placing a tagged specimen in a loading frame and applying a tensile load. During the test, the load, longitudinal strain, transverse strain, and induced axial and transverse magnetic fields were recorded. In magnetic field loading experiments a magnetic field was applied to a specimen and the resulting longitudinal and transverse strains were recorded.

Specimen preparation. For both experiments, strain gages were applied to the specimens. Two types of gages were used, both from the Micro-Measurements Division of Measurements Group, Inc., Raleigh, NC: EA-18-125VA-350, a biaxial, 350 Ω general-purpose gage; and H06A-AC1-125-700, a stacked rosette, magnetically shielded 700 W strain gage. Two H-series gages were used on specimens T1WV9, T1WV10, T1UV8, T1UV9, and T1WV11Delam. All other specimens used the EA-series gages.

The strain gaging procedure was the same for all gages. All supplies were obtained from Micro-Measurements:

1. Area to be strain gaged was dry-sanded with SCP-3 400 grit sandpaper.
2. Surfaces were then cleaned with isopropyl alcohol and gauze sponges.
3. Centerline of gage was marked on the surface.
4. Gage was transferred to specimen using PCT-2A cellophane tape.
5. Gage was then bonded to the specimen using M-Bond 200, according to instructions.
6. Lead wires were cut and stripped (326-DFV).
7. Leads were held in place by PDT-1 drafting tape and soldered using 361-20R solder and a Weller WC100 soldering iron. Two wires were soldered to one of the terminals to facilitate either a two- or three-wire bridge.
8. Connectivity was checked using a hand-held multimeter.
9. The strain gages and leads were then coated and protected with M-Coat A, a xylene-thinned air-drying polyurethane.

Figure 72 is a photograph of a typical specimen after strain gaging.

A special effort was made with some of the specimens (T1WV9, T1WV10, T1UV8, T1UV9, and T1WV11Delam) to provide protection for the strain gages from the magnetic field they would experience in the electromagnet. Suggestions from *Noise Control in Strain Gage Measurements* (Measurements Group Tech Note TN-501-2, 1992) were followed as closely as possible. In addition to using the H-series shielded gages, woven cable called Inter-8 Weave (Magnetic Shield Division, Perfection Mica, Bensenville, IL) was used, effectively cancelling magnetic fields both parallel and perpendicular to the cable length. Attention was given to the attachment of these woven lead wires: they were soldered directly to the strain gage tabs (no auxiliary terminals) and the solder area and area between the two leads was kept small to minimize susceptible loop area. With these precautions it was expected that strain signals would be relatively noise-free even in a high magnetic field.

Mechanical loading test procedure. Throughout the tension testing of the specimens, four signals were recorded simultaneously: axial and transverse strain, load, and axial or transverse magnetic field. To accomplish this task two separate data acquisition systems were used—one for the strain data and one for magnetic field data. Table 14 shows the equipment used in this experiment.

In addition to the equipment listed in Table 14, several other items were needed. Long sets of wires were needed to connect the strain gage lead wires to the strain

gage conditioners; BNC-to-wire connectors were needed to connect both the gaussmeter and the machine load output to the Omega data acquisition system. A system for holding the transverse Hall probe at a fixed and repeatable position near the specimen during testing was needed. A small stand with an adjustable angle three-prong clamp was used to hold the base of the probe stationary. To keep the probe tip near the specimen two probe guides were made, one each for the axial and transverse probe positions (see Figure 73). Each one is made from four pieces of Plexiglas bonded together with toluene. The guides were attached to the specimen using dental rubber bands, and the probe was inserted and adjusted for position before the test.

For each specimen, both axial and transverse magnetic field data were collected. Both sets of data could not be obtained during the same test, so the axial field data was first obtained, then the transverse field data. The specimen was allowed to relax for at least 24 hours between tests. It is assumed that this time period is sufficient to fully relax the specimen after the first test due to the rapid stress relaxation properties of neat polyester and vinyl ester. The reinforced specimens were tested only for axial magnetic field because of the poor transverse field response.

The experimental test setup is shown schematically in Figure 74. The appropriate probe guide was attached to the specimen. The mechanical grips were flat and mechanically clamped (screws), and the specimen was aligned in the grips using a guide to ensure proper alignment. The grips were tightened evenly and the strain gage lead wires attached to the appropriate connecting wire in a two-wire quarter-bridge configuration. The two-wire quarter-bridge box was in turn connected to two strain gage conditioners and a power supply. These were fed into the Instron data acquisition system and on to a Power Macintosh®; where control was provided by LabView*. This system also recorded the output from the load cell and the position of the hydraulic piston.

Next, the Hall probe was inserted into the probe guide in the appropriate orientation with the support stand placed so the base of the probe was supported in the proper position. The probe was attached to the gaussmeter, and the analog voltage output from the gaussmeter was fed into the Omega data acquisition system. To correlate the two separate data acquisition systems the output from the load cell was also recorded here. Both of these voltage outputs were fed into the

* LabView is a registered trademark of National Instruments, Austin, Texas.

OM-912 general voltage input module of the system. The Omega data acquisition system was controlled by a Gateway 2000® computer using Labtech Notebook Pro*.

Before testing was attempted on the Terfenol-tagged specimens, several magnetite specimens were tested to failure to determine ultimate strength and failure load. Table 15 shows the results of these tests. Since the same specimens were to be used for both the mechanical loading and the magnetic field loading tests it was important to keep these specimens intact. Therefore, it was decided to test the unreinforced specimens to a load of 1 kN (about 16.5 MPa) and the reinforced specimens to a load of 5.5 kN (woven) or 5 kN (pseudo unidirectional) (about 86.8 MPa).

For the tension test a single position-controlled ramp was used, at a rate of 0.005 mm/sec for the unreinforced specimens and 0.01 mm/sec for the reinforced specimens. This gave a testing time of about 2.5 minutes. Data were recorded for the Instron system every 0.4 sec; for the Omega system, every 0.5 sec. The Omega system was triggered to begin taking data before the test was started to record the initial magnetic field and load. The test was then begun and allowed to continue until the limit load was reached. The Instron machine was then stopped, and the specimen unloaded. The Omega system was allowed to continue for a brief time after this to record the final unloaded magnetic field. The specimen was removed from the grips and the next specimen prepared.

Figure 75 shows the experimental setup before mechanical testing and Figure 76 shows a specimen loaded in the test frame immediately before the test.

Magnetic field loading test procedure. Because it was desirable to be able to saturate Terfenol-D at room temperature, an electromagnet capable of a field of at least $B = 2513$ gauss was needed (Clark 1980). After checking with other companies, the Ogallala Division of Arnold Engineering (Ogallala, NE) was contracted to manufacture an electromagnet. The model P/N 41C1375 water-cooled electromagnet has a maximum field strength of 3100 Gauss at 7 amps, pole pieces of 60.96 mm in diameter, and a gap of 77.47 mm. To power this electromagnet a Sorensen (San Diego, CA) Model DCS 150-7 programmable DC power supply was used, configured to operate on an input of 110 volts AC and outputs approximately 30 volts at 7 amps.

For the magnetic field loading tests only three signals had to be recorded: axial strain, transverse strain, and magnetic field. The Omega OM-900 data acquisition

* Labtech Notebook Pro is a registered trademark of Laboratories Technologies Corp., Wilmington, Massachusetts

system was utilized with an OM-912 general input voltage module for the gaussmeter (as in the tension testing) and an OM-941 strain gage conditioner for the two strain gages. The strain gage resistance, gage factor, lead wire resistance, etc., were input into the OM-941 via the Labtech program. For the biaxial, EA-Series gages, a three-wire quarter bridge configuration was used. For the magnetically shielded, H-Series gages, a full Wheatstone bridge was used. This was accomplished by using another similar gage and wiring the circuit as if there were four $350\ \Omega$ instead of two $700\ \Omega$ gages. This was necessary to accommodate the capabilities of the OM-941 module.

The test setup for the magnetic field loading experiment is shown in Figure 77. The specimen was held suspended in the center of the electromagnet using a thick, Plexiglas, L-shaped holder and an adhesively-backed nylon wire clip #RTA6 (Serv-A-Lite Products, Inc., East Moline, IL). The Hall probe was positioned near the center of the specimen in an axial orientation using a stand and clamp as in the tension testing. The lead wires from the strain gages were connected to the OM-941 module in the appropriate configuration, and the gaussmeter was connected to the OM-912 module. The electromagnet coolant water was turned on and the power supply allowed to warm up. Then the data acquisition program (2 Hz frequency) was triggered and the magnetic field slowly increased by using the current control on the power supply. The magnetic field was increased to approximately 1300 Gauss and then ramped down at the same rate. The data acquisition was then stopped and the specimen removed. Figure 78 shows the electromagnet test setup with a specimen loaded and ready to be connected to the data acquisition system.

Mechanical Loading Results

In this section the extensive mechanical loading results are presented and discussed. Several different effects were investigated, such as Terfenol volume fraction and particle size. Each of these effects is presented in separate sections with a full data summary of the experiments presented at the conclusion of the chapter.

Typical results and data reduction. Most of the mechanical loading experimental results are similar in form. Two curves for each specimen were produced from the raw test data: axial field response and transverse field response. Two examples are shown in Figures 79 and 80.

The axial field response curves are fairly linear throughout the test. Some nonlinearity is present in the strain data for neat resin specimens. Transverse field response curves were undetectable for all specimens, and were about one order of

magnitude smaller in scale. A Gauss probe with increased sensitivity might have been able to detect the transverse field signal response.

For each test the raw data for axial field response was corrected by subtracting the zero-stress field signal. Next, a weighted (0.67 weighting) smoothing operation was performed on the data using Kaleidagraph (Synergy Software, Reading, PA) a data processing software package v3.05. These operations yield the curves in Figure 81 for specimen T1-P21. The test results for each series of specimens were combined in one database and reduced in the same manner to produce smoothed response curves for each series.

Effect of volume fraction. Four levels of Terfenol-D volume fraction were used in the manufacturing of mechanical test specimens: 0.5, 1, 2, and 4% by volume of resin. Table 16 lists the series designations and specimen descriptions for these tests. Equal amounts of the three size groupings of particles were used to fabricate the specimens.

Overall, the axial field response is increased with increasing volume fraction of Terfenol-D tagging. There was a curious drop in response between 0.5 and 1% tag volume fraction. However, when examining the results of other testing, for instance series E (1% tag volume fraction with 45 and 75 μ tag size), the response curves at 1% volume fraction were elevated from those shown in Figure 82 for series D. This result may be an anomaly in the data for this particular series of specimens, or it may indicate a sensitivity to tag size.

Effect of tag size. Three different size ranges of Terfenol tags were used in this study: <45 μ , 45-75 μ , and 75-100 μ . The size distributions were said to be Gaussian, but no characterization experiments were performed to confirm this. Table 17 lists the series designations and specimen descriptions for these tests and Figure 83 shows the results for this series of tests.

Most of the response curves are within the experimental scatter of the tests except for series B (75 μ tags) and series D (all tag sizes mixed), in which the response is significantly lower than for the rest. There is no clear trend indicated by the data. The 45 μ and 100 μ curves nearly overlay, while the 75 μ curve is significantly lower. When different size ranges were mixed, the response did not follow a mixture of the single size curves. For example, the response of series E containing both 45 μ and 75 μ size ranges is slightly higher than all other tests, while series D containing all three tag size ranges is the lowest. The results of the effect of volume fraction have already indicated that the response curve of series D is suspect. Particle size effects seem to reinforce that view. There are a number of effects that could have

influenced any single series of testing. As an example, background magnetic fields (noise) near the test equipment could have contributed to a shift in response from one day to the next during testing.

The primary conclusion from these tests is that particle size has little effect on magnetostrictive response at these volume fractions (1%) and in this size range (45-100 μ). However, there could be a particle size effect if samples are subjected to a strong postcure magnetic field in order to obtain magnetic domain alignment. If particles are too small, domain reorientation may be restricted or prevented. The results of MFM imaging have indicated that domain sizes on the order of 1 μ are typical for Terfenol-D. Thus, a lower bound on tag size would be on the order of several microns.

Effect of reinforcement. Two series of specimens were fabricated incorporating glass fiber reinforcement in the form of a plain weave fabric (Style 2113, Clark-Schwebel) or a pseudo unidirectional fabric (Style 1297, Clark-Schwebel). Approximately 50% volume fraction of glass reinforcement was used for all specimens. The tag volume fraction was 1% (*of resin*) for all specimens and tag sizes were an equal mixture of 45, 75, and 105 μ size ranges.

The results are shown in Figure 84 together with a representative test for the neat vinyl ester resin. Two observations are immediately evident. First, the total change in axial field is dramatically increased, since the composite specimens are more highly stressed. Second, the response to a given change in stress level is reduced from the neat resin specimens. Up to 20 MPa the neat resin samples develop 0.008 Gauss axial field whereas the unidirectional and woven specimens are 25-50% of that level. Obviously, some of this effect is caused by stress shielding of the Terfenol-D as a result of the glass reinforcement. Additionally, the volume fraction of Terfenol-D has dropped to about 0.5% of the *total* volume.

The increased transverse stiffness of the woven specimens seems to contribute to a reduction in axial field response compared to the unidirectional specimens. Poisson's effects are thought to be a significant factor in the total axial field response of Terfenol-tagged specimens. Increasing the transverse stiffness of specimens has the effect of reducing the transverse contraction and associated domain switching/rotation.

Effect of matrix. One series of specimens was fabricated with neat vinyl ester resin to ascertain the effect of changing the matrix properties on induced magnetostrictive response. The results in comparison to data for polyester are shown in Figure 85.

Both series of data were obtained from specimens with 1% volume fraction of tags using the 45 μ size range. There is a measurable degradation in response for the vinyl ester specimens. Here, the increased stiffness of vinyl ester could contribute to this reduction, similar to the effect of glass reinforcement. In fact, the vinyl ester data lies between those for neat polyester and unidirectionally reinforced glass/vinyl ester.

Effect of postcure magnetic field. Series G specimens (2% Terfenol-D loading, polyester matrix) were subjected to a postcure magnetic field after initial testing was completed. The specimens were placed in the electromagnet in an orientation transverse to the applied field (through thickness). The field was slowly increased to 1307 Gauss and held constant for 30 minutes. Afterwards, the specimens were tested in uniaxial tension to obtain the axial and transverse field response under load. After this series of tests, the same specimens were again placed in the electromagnet in an orientation parallel to the applied field. Once again, a field of 1307 Gauss was applied for 30 minutes. The specimens were subsequently removed and retested to obtain axial and transverse field response. The results of this set of experiments is shown in Figure 86.

In no case could transverse field response be detected. Remarkably both of the postcure curves show a reduced axial field response. The no-postcure and the transverse-postcure field cases show nearly the same behavior. There is some dropoff at high stress, but the reduction is small. Based on these results it was not clear that any domain reorientation was obtained. Thus, a second series of tests was performed, this time with the postcure field oriented parallel to the axial direction of the specimens. The results for these specimens showed that the axial field response was significantly lowered. From these results it is deduced that some domain alignment was, in fact, obtained. The lowering of axial field response for an axial postcure field is intuitively consistent with domain switching under an applied axial stress. If the magnetic domains are all aligned with the applied stress, no switching occurs and the overall magnetostrictive coefficient is zero.

However, the lack of increase in axial field response for a transverse postcure field is puzzling. One explanation could be that domain alignment through the thickness direction will have little influence on response because the through-thickness stress (and strains) are very small. Most of the switching and rotation that occurs is driven by transverse stresses *in the plane* of the specimen. Thus, a postcure field oriented in the transverse direction (through the width) of the specimen may increase the axial field response. If magnetic domains are aligned through the width direction, then as the applied stress is increased, the Possion's effect can act to switch and rotate domains. In this case the postcure magnetic field acts in the

same way as the prestress in magnetostrictive actuators (Hathaway and Clark 1993).

Data summary. All of the data series have been plotted on the same graph in Figures 86 and 87. Of all the samples tested, series G showed the highest sensitivity and largest total change in axial field (0.025 Gauss). These specimens were neat resin polyester with 2% volume fraction of Terfenol-D tags of mixed particle size (45-105 μ m). The unidirectional glass/vinyl ester specimens also performed well, developing 0.024 Gauss at 85 MPa.

The most important conclusion to draw from all of the testing is that a *definite* and *measurable* response is obtained for all of the specimens. *The concept of using a small amount of magnetostrictive tags to measure a state of health in a structural component is clearly demonstrated.* Now, thorough analysis and comprehensive testing can be undertaken in order to maximize sensitivity and understand the mechanisms that contribute to field development. An important question that must be examined is, "Can the same type of behavior be obtained using other (lower cost) magnetostrictives?" The giant magnetostrictives, of which Terfenol-D is one, have magnetostrictive coefficients three orders of magnitude larger than more common (and less costly) materials. However, this giant magnetostriction may not be necessary to ascertain important information about structural health. A sacrifice in sensitivity may be warranted if there is a sufficient benefit in cost reduction.

Damage Detection Response

One of the most exciting aspects of these studies has been the clear indication of a damage detection capability for magnetostrictive tagging. Two types of experiments are discussed in the following sections. The first is the axial field response after tensile failure and the second is the spatial variation in magnetic field for a delamination specimen.

Tensile failure experiment. During the course of mechanical testing several specimens failed, and an interesting response was observed in the post-failure axial magnetic field. Figure 88 shows the response curve for specimen T1-P9 (series B). The induced axial field is normal throughout the loading curve and increases to approximately 0.01 Gauss at 17 MPa. At this point the specimen failed in tension. The load immediately drops to zero, but the induced field does not. In fact, the post failure field is significantly higher and stabilizes around 0.16 Gauss. This type of response can be compared to the unloading curves for specimens which did not fail. Figure 89, for example, shows the loading and unloading curves for specimen T1-P16 (series C).

For the unfractured specimens, the axial field response curve returns to zero after unloading. Thus, it may be concluded that the failure process in specimen T1-P9 has resulted in a change in the residual stress field that can be detected. It should be noted that the 0.16 Gauss residual field in Figure 88 is a relative field, i.e., a normalized change in response at zero stress.

This result is extremely promising. It indicates that the damage state of a structural component could be correlated to the "zero-stress" field response. Thus, a component could be scanned to create a "field signature" before placing it into service. At periodic intervals during the service life of the component, a scan could be performed (under the same load conditions) and compared to the original signature to ascertain the structural health.

Delamination experiment. An artificial delamination was introduced at the midplane of a woven glass/vinyl ester specimen during fabrication by placing a Teflon® film between layers of glass fabric at the mid-plane. The delamination extended to the center of the specimen gage section. This specimen was then tested in uniaxial tension and the response curves at various positions along the delamination were obtained during mechanical loading.

The results of this set of tests are shown in Figure 90. The normalized axial field is plotted versus position along the delamination at several different stress levels. The origin (0 in) corresponds to the edge of the delamination. Positions less than zero are inside the delamination area and positions greater than zero are ahead of the delamination.

The largest response is at the edge of the delamination (0 in.) which also corresponds to the largest stresses. There is a clear correlation of field intensity with distance from the edge of the delamination. Also, the response levels are highly elevated from normal testing. The maximum field is nearly 0.1 Gauss at the edge of the delamination at 70 MPa. The maximum field measured in normal testing was only 0.025 Gauss. Interestingly, positions far away from the delamination (0.5 in. position) gave very similar data to previous tensile testing. Figure 91 shows the axial response curve for the woven glass/vinyl ester series overlaid on the data for delamination test at 0.5 in. position. The data very nearly overlays exactly and it is well within the experimental scatter.

At positions within the delamination some interesting features are evident. The induced field changes sign about halfway through the delamination (at the -0.25 in. position) and increases to about 0.05 Gauss at -0.375 in. at 70 MPa. Stress fields near the surface layers within the delamination are dramatically different than the

stress field near the edge of the delamination. Obviously, the sign of the stress as well as the stress level itself will play a role in the strength and direction of the induced magnetic field. These results give further confirmation to the idea that the damage state of a structure can be detected using magnetostrictive tagging at modest tagging levels (1% volume fraction in this case).

Magnetic Field Loading Experiments

Magnetic field loading experiments were envisioned to measure the inverse response of the tagged specimens; after applying a magnetic field to the specimen, the induced surface strains were to be measured.

The results of this test series were inconclusive. No detectable surface strains were measured up to 1300 G applied magnetic field. There are two possible reasons for this result.

First, the induced strains may simply be too small to detect with currently available measurement equipment. This series of experiments was intended to measure the actuation capability of a Terfenol/polymer composite with 1% volume fraction of actuator phase. The actuation capabilities of such a composite are very small. Even assuming that the Terfenol-D phase strains by 0.2% (at saturation) for the composite with 1% volume fraction, only 20 microstrain would be detected. This level of strain actuation is too small to detect using resistance strain gages in a normal Wheatstone bridge setup.

Second, the strain gages themselves interfere with the magnetic field in the neighborhood of the measurement area. Specially shielded gages and electrical wiring were used to minimize this effect, but when attempting to obtain such precise strain measurements, it was found that even small magnetic interference could overwhelm signals produced by the magnetostrictive effect.

Summary

The experimental results for magnetorestrictive tagging strongly support the concept of structural health monitoring of composites through the use of embedded magnetostrictive tags. In all mechanical loading experiments, a detectable change in axial magnetic field was obtained. The response was almost always linear and highly repeatable. High tag volume fractions and low transverse stiffness both contribute to enhancing the response under mechanical stress. The use of a large

postcure magnetic field to achieve magnetic domain alignment was demonstrated using MFM imaging and should prove to be beneficial in enhancing response levels.

Perhaps the most significant results were produced in tests in which damage detection was demonstrated. Tensile failure of mechanical test specimens induced a step discontinuity in axial field level that remained after unloading. This effect is thought to be the result of a change in the residual stress field near the measurement location. Furthermore, the stress concentration around an artificial delamination was clearly observed in the axial magnetic field distribution. Both results strongly suggest that the damage state of a composite structure could be monitored and characterized by measuring the magnetic field signature at various times during the service life.

10 Piezoelectric Active Tagging (Theory and Experiment)

Interrogation Schemes

In the context of this research, piezoelectric tagged composites (PTCs) are polymers or polymer composites that contain particles of piezoelectric materials distributed in either a random or an oriented fashion throughout the host material.

The piezo particles are most commonly spherical, but other geometries can be used as well. The literature commonly refers to such systems as *0-3 composites* where the two numeric designations describe the connectivity of the piezoelectric phase and the host phase, respectively. For 0-3 composites the piezoelectric phase has 0-dimensional connectivity (i.e., it is not continuous in any direction) and the host material is continuous in all directions (designated as 3-orthogonal directions). Some recent research shows that 1-3 connectivity can be induced by using the dielectrophoretic effect in piezoelectric particle-filled composite systems (Newnham 1997). Thus, in the sections that follow, both 0-3 and 1-3 particle-filled composite systems are discussed.

For this approach three main interrogation schemes are feasible. Each is based on the direct piezoelectric effect. Many of the fundamental mechanics and processing issues are common among all three techniques, so advances in this area of research may apply equally to each scheme.

Direct Piezo Interrogation

The first interrogation technique applies to isotropic 0-3 systems or 1-3 composite systems in which polarization of the piezoelectric phase is in the thickness direction. This technique will be very difficult for even marginally thick structures. However, lamination of poled thin layers or the incorporation of prepoled particles and single-domain particles should overcome these limitations.

Figure 92 illustrates the interrogation scheme in which a piezoelectric particle is encapsulated by a host material. An external stress applied to the host material will in turn transfer stresses to the piezo particle. These stresses are transduced

to a voltage through the direct piezoelectric effect. A material's efficiency in this transducing is defined by, g , in volts/meter/Pascal. Table 18 lists some common values of g for several piezoelectric materials. Note that since piezoelectric materials are anisotropic, their response is directionally dependent. Thus, the piezoelectric constants are defined using double subscripts. The first indicates the direction in which the electrodes are placed and the second designates the direction of applied stress.

The piezoelectric constants for a PTC will be much lower than the values listed in Table 18. Hossack and Auld (1992) present a unified model to predict the effective medium properties for 0-3 composites. This model may be used as a first approximation to calculate a typical g_{31} coefficient for a PTC material. Equation 54 is the final form of their prediction and is composed of terms describing the particle geometry, mechanical, and electrical properties, and the packing efficiency of the PTC system:

$$k^* = k_p \left(\frac{\phi p}{\pi} \right)^{2/3} \left(\frac{3P_M[1 - \sigma^2]}{E} \right)^{1/3} \quad [\text{Eq 54}]$$

where k^* is the effective medium property and the various quantities are defined in the nomenclature in Chapter 1.

Assuming 50% volume fraction of particles, 6 points of contact (a range of 6 to 9 has been reported by experimental observation) and atmospheric pressure during compaction, a typical g_{31} value of -0.14×10^{-3} Vm/N is obtained for a PTC. This value can be used to calculate the open circuit voltage for a model geometry and loading case. Consider a PTC specimen in which a uniform tensile stress is applied in the x-direction. Assuming that the PTC modulus of elasticity is 53 GPa (a typical value for a 50% piezoelectric volume fraction PTC) the field strength is 7000 V/m up to the elastic limit of the material. Thus, a 10 mm thick specimen will develop a field of 70 V across the thickness. Larger thicknesses reduce the field strength, but more importantly, poling of the PTC becomes a serious problem. Incredibly large electric fields are required to pole the piezo phase during manufacturing. This effectively limits the maximum thickness that can be fabricated in one step. For example, field strengths of 100-150 kV/cm are necessary to pole PbTiO₃/Eccogel PTC systems (Newnham et al. 1984). A discussion of poling conditions and alternative techniques can be found in the next section. The lamination technique commonly used in the fabrication of composite structures lends itself well to this problem. It will be much easier to pole (continuous poling is also possible) relatively thin plies of PTC that are then laid up onto a mold surface to form the structural

part. As long as intimate contact can be obtained across the ply interfaces, the direct piezoelectric effect should be maintained across the entire structure.

Laminated Electrode Interrogation

The second technique is shown schematically in Figure 93. In this case 0-3 or 1-3 PTC plies are laminated to form composite structures. Between the individual plies an electrode or array of electrodes is incorporated. Once the entire structure is fabricated individual plies can be interrogated by monitoring the charge that develops across successive electrodes. There are many interesting possibilities for such a structure. For example, an electrical pulse can be given to the structure through one electrode and the response measured through all or some of the remaining electrodes. This is really just taking the ultrasonic NDE technique to a much more refined level. In this case the electrical pulse given to one electrode would be transduced as a coupled stress/electric field wave (highly magnified) throughout the structure. By monitoring the other electrodes, the time of flight and attenuation and/or piezoelectric stress-induced electric field can be determined in a spatial fashion. There are questions that remain to be answered before a conclusive statement can be made about the feasibility of such a technique. How far the stress wave will permeate throughout the structure remains to be seen. However, the attenuation should be much lower than for typical composite systems since the piezoelectric "transducers" are integrally dispersed throughout the material. Even if attenuation poses a problem, successive electrodes can be pulsed one after the other across the entire thickness to obtain complete structural characterization.

This interrogation technique could feasibly give the information necessary to construct a mapping of distributed mechanical properties over the entire structure. It is an interesting point of conjecture whether such a technique could also give information on crack locations, sizes, and distributions. To characterize damage, the electrodes deposited at the ply interfaces would probably need to be discontinuous, i.e., many small electrodes deposited in some pattern over the ply interface. This approach would provide control over which ply is excited, but the planar location as well. With this control, a truly three-dimensional mapping of response could be attempted. There are undoubtedly numerous control system issues to address for these types of structures. The number of electrodes could easily reach several thousand for a typical structure. The sheer number of calculations required to process the data from such a structure is daunting. However, if the resolution on crack size is not overly restrictive, the number of required electrodes could be reduced and may prove to be feasible.

Laser Excitation Interrogation

The third interrogation technique is shown in Figure 94. In this case a localized heat source is used to change the internal stress field in the structure. A single particle embedded in the host material acted upon by a localized heat source will be subject to a "hydrostatic" tensile stress acting upon the particle. This in turn is transduced to a voltage that can be monitored. However, the novelty here is that spatially resolved response can be obtained without the need for complex electrode placement at the ply interfaces. A laser pulse would be sufficient to induce a thermal wave emanating from a particular location in a PTC structure. This thermal pulse is coupled to a stress wave that propagates from the point of heating. A similar technique is already used in the NDE of metals. It is also being actively pursued for graphite-reinforced composites. For PTC material the laser pulse serves the same purpose as the electrical pulse in the laminated electrode interrogation. Obviously, with a laser source, only the surface of the structure can be heated whereas in the laminated electrode technique the excitation can be internal. This limitation may be a problem in that attenuation across the thickness of the structure may dampen the signature too severely.

Experimental Testing

A series of experiments was performed to serve as a feasibility study of the concepts discussed above. PTC specimens (both 0-3 and 1-3 connectivity) were manufactured and interrogated using the direct piezo interrogation technique. The results of this study are fundamental for all three interrogation techniques. Ultimately, the efficiency of all three techniques is dependent on the efficiency of the fundamental transductance of mechanical energy to electrical energy by a 0-3 or 1-3 PTC material.

Materials

Piezoelectric powder was obtained from Morgan Matroc, Inc. (Bedford, OH). It is a PZT-5A-169G ceramic and has "as-poled" properties as listed in Table 19. This powder also has a small amount of organic processing aids in its as-received condition. An unsaturated polyester polymer was used as the matrix material for all testing. Graphite reinforcement was obtained by grinding AS-4 graphite fibers (Hercules Inc. Wilmington, DE) with a mortar and pestle. This process produced a fine "powder" consisting of short fiber segments typically 50-100 microns in length. The diameter of fibers was approximately 7 microns. Continuous E-type glass fibers were also used for some specimens. These fibers were typically 15

microns in diameter. Table 20 lists all the materials used in this study and the supplier for each.

Specimen Preparation

Table 21 lists the various types of PTC specimens that were manufactured. Several are composites of piezoelectric ceramic/polymer matrix while others include other types of reinforcements. Both 0-3 and 1-3 connectivity systems were made. The specimens were disc-shaped with a diameter of 16.0 mm and thicknesses between 1.0 and 1.3 mm. For all specimens the following fabrication procedure was used:

1. Silicone rubber molds were drilled with a 16 mm hole cutter. The mold thickness was 1.59 mm. These molds were taped to a release-coated (Teflon® film) aluminum plate.
2. Samples of the various components were weighed using a Fisher XL-3000 (Fisher Scientific Springfield, NJ) precision electronic balance (± 0.001 g).
3. Unsaturated polyester resin was mixed with an appropriate quantity of resin-hardening agent in a small graduated beaker for 3-5 minutes.
4. If graphite reinforcement was used, it was then mixed with the matrix material until uniformly dispersed (< 1 minute).
5. The ceramic powder was then mixed with the matrix until a fine dispersion was obtained (typically < 5 minutes).
6. If glass fiber reinforcement was used, these materials were laid into the mold in a random orientation (within the plane).
7. The ceramic/polymer mix was then poured into the mold and allowed to settle. In some cases the mixture was squeezed into the mold using a spatula. Care was taken to remove entrapped air bubbles during this step.
8. Once all the molds had been filled, a heat lamp was placed over the mold to cure the specimens. Approximately 30 minutes was needed for full cure. All specimens were allowed an additional 48-72 hours at room temperature before testing.
9. Once the specimens had been removed from the mold they were sanded to obtain smooth, flat, parallel surfaces. Final thicknesses of specimens ranged from 1.0 to 1.3 mm.
10. The surfaces of the specimens were then electroded by painting them with silver print conductive paint (GC Electronics, Rockford, IL).

It was particularly difficult to work with highly loaded systems. Once the ceramic powder volume fraction reached about 50%, the mixture consistency was essentially that of a paste. It was difficult getting these pastes to flow into the mold, remove entrapped air, or infiltrate fiber networks (for the glass fiber composite specimens).

Two solutions to this problem could be used. First, a solvent could be mixed with the matrix before infiltration to reduce the viscosity. This solvent would be driven off during the cure cycle. Second, elevated pressure could be used to squeeze the mixture into a mold cavity. This same principle is used in autoclave and resin transfer molding operations.

The 1-3 composite specimens were prepared somewhat differently from the procedure described above. For these specimens the polyester matrix was poured into the mold and allowed to cure while 0.9 mm diameter rods were held in place using a wire mesh stretched over the mold surface. These rods were later removed after the polyester had cured. The resulting holes were then filled with a piezoelectric ceramic/polyester matrix paste (50% volume fraction). After the paste had cured these specimens were then sanded and electroded. The resulting specimens essentially mimic the effect of putting piezoelectric rods oriented through the thickness of a polyester matrix.

Poling and Testing

After their manufacture, specimens were poled in the thickness direction. The poling setup is shown in Figure 95. A high-voltage power supply (Bertran High Voltage Corp., Hicksville, NY) Model 205B-10R) with 10,000 V capability was connected to a poling fixture. The high-voltage lead was connected to a probe that rested on the upper electrode of the disk specimens. The bottom electrode rested on the bottom fixture and was connected to ground. All specimens were poled in the range 95-110 °C for approximately 5 minutes. Table 22 shows the poling conditions for each specimen. None of the specimens was able to be poled at 10,000 V at 100 °C. The voltage levels used were dictated by the limitations of the specimen before electric discharge occurred. In each case the voltage level was slowly increased until discharge occurred. The voltage level was then reduced slightly and poling of the specimen was allowed to occur for 5 minutes. The particular temperature of the silicone oil bath was chosen for two reasons. First, higher bath temperatures make it easier to polarize the ceramic phase, but it also accentuates the electrical discharge problem. Second, the temperature had to be above the glass transition temperature of the matrix so reorientation of the ceramic phase could occur unimpeded.

After the specimens were poled they were mechanically tested to failure in diametral compression. Electrical leads were attached to each surface of the specimen to monitor the direct piezoelectric effect throughout the test. Figure 96 is a schematic of the test setup. An MTS 880 servohydraulic test frame was used with an Instron 8000 controller run with LabView at a loading rate of 0.002 mm/sec.

A special test fixture was needed for these tests. The bottom fixture is a block of aluminum with a 1.5 mm groove scalloped out of the center. The groove has a radius of curvature of 100 mm so that the specimens would align themselves in the center of the fixture. Shims were used to align specimens that were significantly thinner than 1.5 mm. The top fixture is an 18 mm circular aluminum rod with faces machined for parallelism. Once the specimen was loaded into the bottom fixture, the top fixture was brought down to the top of the specimen and the test was begun.

Results

Several plots for load versus crosshead displacement, piezoelectric voltage versus crosshead displacement, and load versus piezoelectric voltage can be found in the literature (White, September 1995).

Group 1. Specimens in group 1 were loaded with 50% piezoelectric powder. Specimen 1-2 showed a direct piezoelectric effect. The effect was nearly linear up to about 60 N. Thereafter, the voltage seemed to saturate and remain constant after about 100 N. This type of behavior was repeated for many different types of specimens. Specimen 1-1 seemed to breakdown after about 20 N load. The piezoelectric voltage was linear up to this point, then it dropped and remained constant thereafter up to failure. This type of behavior was also repeated for other types of specimens. Specimen 1-3 and 1-4 showed inconclusive behavior. In the case of specimen 1-3 the piezoelectric voltage started to increase negatively then turned around at about 40 N and began to increase positively up to failure. Specimen 1-4 did not show any effect throughout the test. It is interesting to note that specimen 1-2 was not poled (it short-circuited during poling), yet it showed the best results. It appears that a significant fraction of the powder particles are single-domain, and as such are already polarized.

Group 2. Specimens in group 2 were loaded with 30% piezoelectric powder. Specimen 2-1 showed the best results. There was a direct linear relationship between load and piezoelectric voltage all the way to failure (about 450 N). Specimens 2-2 and 2-3 saturated between 50 and 100 N. Specimen 2-4 started linearly and remained so up to 75 N, but breakdown occurred afterwards.

Group 3. These specimens were loaded with only 10% powder. At this volume fraction there is little chance of a connecting network across the thickness of the specimen. As a result, four of the five specimens did not show any discernible piezoelectric effect. However, specimen 3-4 showed a remarkably typical direct effect proceeding to saturation after about 200 N.

Group 4. Group 4 specimens (50% piezo powder) were loaded with 1.5% graphite fiber to increase conductivity of the polymer matrix so that poling was more effective. All four specimens in this group showed a measurable direct piezoelectric effect and taken as a whole, exhibited better behavior than group 1. Specimen 4-1 showed an interesting behavior: an initial linear effect followed by saturation between 20 and 100 N and finally another linear effect thereafter. Examination of the loading curve shows that at about 125 N the load drops. This is indicative of cracking and other types of damage being induced in the specimen. It is at this point when the direct piezoelectric effect begins to register again. This result is especially encouraging as a means of monitoring structural damage. There are several different types of specimens that showed this linear-saturation-linear response.

Group 5. These specimens can be compared directly with group 2 specimens, the only difference being the 1.5 % graphite loading for group 5. Again, the overall response is improved with the addition of graphite in the matrix. All four specimens showed a measurable effect during loading. Note that specimens 5-1 and 5-2 showed an increasingly *positive* voltage during loading as compared to specimens 5-3 and 5-4 which showed increasingly *negative* voltage. The polarization direction was obviously switched between these specimens during the testing. Specimen 5-3 exhibited the best response (over 1.3 mV change up to 150 N).

Group 6. Group 6 specimens had 10% piezo powder and 1.5% graphite. The results were consistently poor. No specimen showed a direct piezoelectric effect over the entire range of loading.

Group 7. These specimens were loaded with approximately 10% glass fiber reinforcement along with 1.5% graphite and 30% piezo powder. Specimen 7-1 did not exhibit any significant behavior. Specimen 7-2 progressed from a small linear region, to saturation, to a large linear region, and to final saturation up to failure. Again, examination of the loading curve indicates that the second linear region corresponds to the beginning of cracking in the specimen (the load drops immediately before the second linear region). Specimen 7-3 showed a typical linear-saturation response, with saturation occurring relatively early (about 10 N). The results for specimen 7-4 are inconclusive.

Group 8. Here the fiberglass loading was increased to approximately 30%. Only specimen 8-3 exhibited a useful piezoelectric effect. The response was nearly linear up to about 100 N followed by saturation thereafter.

Group 9. Group 9 specimens were loaded with 10% glass fiber and 30% piezo powder. For comparison purposes, note that group 7 specimens are the same with the addition of 1.5% graphite. Only two specimens were suitable for testing—specimens 9-2 and 9-4. The other specimens were too thin and failed in bending during the test setup.

Specimen 9-2 shows a linear effect up to about 20 N followed by saturation. Four separate tests were run on this specimen to examine the repeatability of testing. A summary plot of all tests on this specimen is included in Figure 97. To make this plot, the piezoelectric voltages for each test are normalized with respect to the initial voltage at zero load. The results are overlaid on the same plot and they show repeatable response. Test #2 showed a second linear region that, again, correlates to specimen damage. The subsequent tests on this specimen showed saturation after the initial linear region without the second linear region. Specimen 9-4 did not show a direct effect.

Group 10. Specimens in group 10 were loaded with 5% fiberglass and 30% piezo powder. Of all the groups of 0-3 composite systems, these exhibited the best behavior. All four specimens showed a direct piezoelectric effect all the way to failure. Specimens 10-2 and 10-4 were both quite remarkable. In the case of specimen 10-4, nearly 6 mV of charge was developed during the test (up to 400 N). Specimen 10-2 was almost perfectly linear throughout the entire test with roughly the same slope as specimen 10-4 (approximately 16 mV/N).

Group 11. These specimens were not tested since nearly all (4 of the 5) experienced a graphite-induced short-circuit during poling.

Group 12. These specimens were loaded with a large (3%) graphite content to help reduce the poling voltage requirement. Only specimens 12-1 and 12-3 exhibited a direct effect. Again, the single-domain behavior of the powder was demonstrated by the results of specimen 12-1 since this specimen short-circuited during poling.

Group 13. These specimens were the first of three groups of 1-3 composite systems. In this group 20 "rods" of 50% piezo powder were embedded in a polyester matrix. The total volume fraction of piezo powder in the specimen was only 6%. The results are astounding for specimens 13-1 and 13-2. These specimens developed nearly 35 mV within 300-500 N loading. In this case the relationship between load and voltage is nonlinear, probably due to interaction with the matrix nonlinearities. These results are truly remarkable. Of all the 0-3 specimens, only specimen 10-4 could even approach 15% of these results. The results for specimen 13-3 are disappointing and unexplainable.

Group 14. There were 10 "rods" embedded in the matrix for group 14 specimens (a total of 3% piezo loading). The results are significantly reduced from group 13. Specimens 14-1 and 14-2 show the best results, with a total charge developed of between 0.6 and 1 mV up to 500 N.

Group 15. Here, only 3 "rods" are embedded (1% total piezo powder). Remarkably, specimen 15-1 does show a measurable direct effect. It develops nearly 1.5 mV up to 500 N load. Specimens 15-2 and 15-3 did not show any piezoelectric effect.

Summary of results. The results of this preliminary study are quite promising. The direct effect was demonstrated for both 0-3 and 1-3 composite systems. There was evidence that structural damage has a measurable effect on the piezoelectric effect. One of the composite specimens (10-4) showed the best response for 0-3 systems. The results on 1-3 systems were extremely exciting, with group 13 specimens showing the best overall response of all the groups tested.

Many interesting results have been generated, and a more detailed analysis of these tests as well as further tests on specific types of specimens should prove to be very beneficial in developing analytical models to predict the direct effect, the influence of microcracking, and the influence of the matrix nonlinearities.

Percolation Limits

Percolation theory can be applied to describe the influence of particle volume fraction, size, and distribution on connectivity. Excellent reviews of percolation theory are given by Zallen (1983) and Stauffer (1985). Essentially, a percolation model describes the physical space as an interconnecting network of bonds and lattice sites. One starts with a large (preferably infinite) regular lattice. A site or bond is then assigned at random with a probability P to each site or bond. For values of P between zero and P_{cs} (for sites) and P_{cb} (for bonds) the physical space is adequately described as a collection of finite clusters. At exactly P_{cs} or P_{cb} an infinite cluster is formed. Because there is now a percolation path across the entire lattice, connectivity is established. This type of modeling has been used to define critical conditions for conductive composites (McLachlan, Blaszkiewicz, and Newnham 1990; Ruschau, Yoshikawa and Newnham 1992). The critical volume fraction can be determined from P_{cs} as

$$V_p = vP_{cs} \quad [\text{Eq 55}]$$

where V_p is the critical volume fraction and v is the packing factor. Short fiber networks have also been analyzed to predict electrical conductivity (De Bondt, Froyen, and Deruyttere 1983; Taya and Ueda 1987). Monte Carlo simulations are also used in which a given lattice geometry is filled randomly (Ruschau, Yoshikawa, and Newnham 1992).

A typical result for a particle-filled polymer system is shown in Figure 98. There exists a volume fraction percolation limit above which a conductive pathway is established (in this case about 0.05). Particle size, geometry, and size distribution will have a dramatic effect on this limit. For example, Carmona et al. (1980, 1987) found that the critical volume fraction for connectivity in carbon particle/epoxy composites was about 0.16. When carbon fibers of the same size were used (length/diameter = 100) this limit decreased to about 0.0055. A similar type of result is shown in Figure 99.

These results are important for two reasons. First, a conductive path is needed for the piezoelectric phase so that the direct piezoelectric effect can be measured. Second, the graphite reinforcement is added to increase the electrical conductivity of the matrix to more closely match that of the piezoelectric ceramic. However, the percolation threshold must not be exceeded because poling of the PTC will no longer be possible (graphite shorts out the specimens above a certain volume fraction).

There are several results to draw from in the literature to predict a percolation limit for the piezoelectric particles. McLachlan and others showed that a percolation limit of 50% was obtained for a GeAl cermet. In another result they found that a carbon particle/epoxy matrix system was conductive after about 7.4% volume fraction. The same model predicts a percolation limit of about 42.1% for graphite particles in epoxy. Ruschau and others studied Ag powder-filled silicone rubber composite systems. They show that conductivity is obtained after about 7% volume fraction of 0.5 micron Ag powder. This limit increases to 20% for 9.0 micron powders. They also show that specimen thickness has a direct effect on percolation limits: thin specimens required larger volume fractions (25%) than thicker specimens (18%). Synthesizing all of the available data is difficult. The resistivity of PZT-5A is about $10^{11} \Omega\text{-m}$ compared to $10^{-4} \Omega\text{-m}$ for Ag and $8.7 \Omega\text{-m}$ for graphite. Thus, the percolation limits for the current PZT-filled systems will be larger than those predicted for Ag- or graphite-filled systems. However, the effect will not be as large as one might expect. The percolation limit is primarily affected by geometry and packing, not the electrical properties of the composite phases. In this work three volume fractions were used—10, 30, and 50%. There is some evidence to suggest that 15-16% volume fraction is a universal percolation limit (Ruschau, Yoshikawa, and Newnham 1992) for particle-filled systems. The 10% systems used

here were chosen to see if any direct effect could be monitored. The 30% system was chosen to provide a baseline. The 50% system represents an upper limit on PTC behavior.

The addition of graphite short fiber reinforcements can lead to reduced poling voltages and/or lower poling temperatures. However, the addition of graphite over the percolation limit leads to electrical shorting of the specimens. Since the current follows the path of least resistance, most of the electric field is lost by direct conduction through the graphite. The graphite particle results of McLachlan and co-workers predicts a percolation limit of 42.1%. However, when viewed at 200x power under an optical microscope the ground fiber powders used here exhibited an aspect ratio between 50-200. Taya and Ueda (1987) studied the conductivity of short fiber composites using percolation and effective medium theories. For random fiber orientations (as in the current experimental PTC systems) an aspect ratio of 50 yields a percolation limit of about 4%. This limit decreases to about 2% for an aspect ratio of 100. Newnham used 1.5% graphite powder to reinforce an Eccogel (W.R. Grace & Co., Boca Raton, FL) polymer to make PTC systems at low poling conditions. Three levels of graphite loading were chosen—1.5, 3, and 5%. The largest graphite loading before percolation should yield the best possible poling conditions.

Efficiency

The efficiency of PTC materials is not easily defined. There are several types of energy losses to consider. In addition, the efficiency is highly dependent on the geometry of the structure and the type of external loading. One of the unique features of the proposed interrogation schemes is that they are all based on the direct piezoelectric effect. Thus, one measure of their efficiency is just the mechanical-electrical coupling coefficients, g and d .

$$\begin{aligned}
 g_{33} &= \frac{\text{electric field developed with the 3 - direction}}{\text{applied stress with the 3 - direction}} \\
 g_{31} &= \frac{\text{electric field developed with the 3 - direction}}{\text{applied stress with the 1 - direction}} \\
 d_{33} &= \frac{\text{strain developed with the 3 - direction}}{\text{applied field with the 3 - direction}} \\
 d_{31} &= \frac{\text{strain developed with the 3 - direction}}{\text{applied field with the 1 - direction}}
 \end{aligned}
 \tag{Eq 56}$$

For a composite system the effective coupling coefficients will be some fraction of the piezoceramic coefficients. For lack of a better approximation, the Halpin-Tsai mixture rules can be applied (Tsai and Hahn 1980).

$$C = C_m \frac{1 + \xi \gamma V_f}{1 - \xi V_f} \quad [\text{Eq 57a}]$$

where

$$\xi = \frac{\left(\frac{C_p}{C_m} - 1 \right)}{\left(\frac{C_p}{C_m} + \gamma \right)} \quad [\text{Eq 57b}]$$

$$\gamma \approx 1 - 2$$

Here, C represents the property of interest. The subscripts in Equation 57a refer to the piezoelectric particle (p) and the host material (m). For the direct piezoelectric effect, maximum coupling coefficients are optimal. This necessitates a high volume fraction of ceramic phase, maximized coupling coefficients for the piezoceramic phase, and optimal bonding at the particle/host interface (which is reflected in the coupling constant, γ , in Equation 55a).

With predictions of the composite coupling coefficients in hand, the next step is to model PTC structures. Consider the PTC plate shown in Figure 100 where the polarization direction is through the thickness. The static displacement of the plate (under an applied field) is given by

$$\begin{aligned} \Delta W &= \frac{d_{31} V W}{t} \\ \Delta L &= \frac{d_{31} V L}{t} \\ \Delta t &= d_{33} V \end{aligned} \quad [\text{Eq 58}]$$

where V is the applied field strength. The static voltage developed by an applied force is given by

$$\begin{aligned} V &= \frac{g_{31} F_1}{W} \\ &= \frac{d_{31} F_2}{L} \\ &= \frac{g_{33} F_3 t}{L W} \end{aligned} \quad [\text{Eq 59}]$$

where the form of the equation depends on the type of force applied, i.e., F_1 represents a force applied in the 1-direction, etc. Obviously, the direct effect is maximum when the coupling coefficients d_{31} , d_{33} , g_{31} , and g_{33} are maximized.

When PTC materials are used under dynamic conditions, efficiency calculations are much more complex. The acoustic power density of a piezoelectric material is given by

$$P = 2\pi f E^2 \kappa^2 \epsilon_{33}^T Q_M \quad [\text{Eq 60}]$$

where P is the power density, f , is the resonant frequency, E is the rms electric field, κ is the electromechanical coupling coefficient, ϵ is the permittivity, and Q_M is the mechanical damping factor. The power dissipated through dielectric losses can be expressed as

$$P_d = 2\pi f E^2 \epsilon_{33}^T (D.F.) \quad [\text{Eq 61}]$$

where f is the operational frequency and $D.F.$ is the dissipation factor ($=1/Q_E$). Thus, the efficiency of the transducer material is given by

$$\eta = \frac{\kappa^2}{\kappa^2 + \frac{1}{Q_M Q_E}} \quad [\text{Eq 62}]$$

where η is the efficiency. For a PTC material the dielectric constant is drastically affected by the matrix properties and volume fraction. For example, a typical PZT-type material has a dielectric constant of about 1800. Most polymers are 2-3 orders of magnitude less, in the range 3-6. Newnham et al. (1984) measured the dielectric constants for several PTC systems and found them to be in the range 20-120. The mechanical and electric damping factors will also be affected, but these effects have yet to be investigated in PTC systems. Obviously, mechanical damping will be larger than the ceramic alone, and the electric damping should be relatively unaffected by the matrix properties. However, the way volume fraction of matrix, particle size and geometry, and matrix physical properties influence the damping factors is not clear and should be investigated in the future.

Assuming that the electromechanical coupling coefficients and the dielectric constant are affected similarly, a typical k_{33} for a PTC system would be 0.14. Using best estimates of Q_E and Q_M , the transducer efficiency is calculated to be 83%. Thus, a large portion of the electrical/mechanical energy is converted to mechanical/electrical energy under dynamic conditions. However, there is significant attenuation of mechanical energy in composite materials. In most cases this attenuation is so great that transmission is fully damped within about 6-8 mm of the source. So, while the efficiency is large at the particle/host interface, in practical terms the signal strength at the measurement location will be a small fraction of the input signal. A typical attenuation coefficient for a graphite/epoxy

material is about 0.1. For PTC materials there may be an amplification of the source signal by interactions with surrounding particles. At any rate, the attenuation through one ply is not expected to be too large, so the laminated electrode interrogation method should work reasonably well.

11 Conclusions

Applications of advanced composites in retrofit and new construction in civil engineering make it necessary to develop nondestructive evaluation (NDE) methods that will ensure the performance and reliability of structural members. The embedded particle tagging method is a unique potential sensing technique that may be used for in-field or in-process NDE of advanced composites in infrastructure applications. Through particle tagging, sensing capabilities can be given to composites during manufacturing or construction. As a logical extension of advanced composites technology, particle tagging can offer a convenient, cost-effective, and rapid method of material or structural assessment. The most important characteristic of the tagging technique is distributed sensing, which is not possible with many types of conventional sensors. Using this technique, the inspectability and quality assurance of the composites both before and during service can be improved.

Preliminary experimental work and basic theoretical studies have demonstrated the concepts of tagging and the feasibility of using this method for NDE of advanced composites. In fact, the use of particle tagging techniques has promise for many application environments. Examples are the detection of defects (voids, inclusions, etc.), the monitoring of the state-of-cure of the epoxy-matrix, and the inspection of damage (delamination, etc.) during manufacturing, construction, or service of advanced composites. Potential applications include the inspection of coating (thickness, coverage, etc.), quality control of powder blending processes in industry, and in-process quality assurance of the manufacturing process for the composites.

Active tagging with ferromagnetic and magnetostrictive material provide the greatest promise for Army application. Piezoelectric tagging suffers from the requirement of a conductive composite (therefore, it may be successfully applied to carbon fiber composites) or a high volume fraction if the composite is nonconductive.

Conclusions on Theoretical Analysis

This report has presented a theoretical analysis concerning the development of active tagging with ferromagnetic, magnetostrictive and piezoelectric particles, respectively.

Ferromagnetic

A dynamic model of an active tagged system was developed to help understand the fundamental mechanisms and physics involved with active tagging using ferromagnetic particles and magnetic excitation. The structural excitation force applied by embedded particles is extracted as a result of interaction between the particles and their host matrix, which in turn, is correlated to material conditions and defects in bonding layers or polymers. The important role of a static bias field in magnetizing the particles and suppressing the signature distortion in the active magnetic particle tagging is also recognized.

Magnetostrictive

Preliminary theoretical studies were conducted for active tagging with magnetostrictive particles. A single-domain theory was applied to magnetostrictive particles to establish a fundamental relationship between the response of the particles and internal stress states.

Piezoelectric

A brief theoretical discussion of the volume fraction requirements of piezoelectric tagged composites using percolation theory was presented. Models also were presented to evaluate the mechanical properties of piezoelectric tagged composites and the efficiency of the piezoelectric powder.

The experimental results presented in this report strongly support the concept of structural health monitoring of composites.

Conclusions on Experimental Work

The experimental results using ferromagnetic, magnetostrictive and piezoelectric particles, respectively, are described below.

Ferromagnetic

Laboratory tests were conducted on a large number of ferromagnetically tagged composite materials. Experiments confirmed the ferromagnetic testing technique can be used as a repeatable damage-detection NDE systems for structural composites. This technique also uses low volume fractions (near 1%).

Magnetostrictive

In all mechanical loading experiments, a detectable change in axial magnetic field was obtained. The response was almost always linear and highly repeatable. High tag volume fractions and low transverse stiffness both contribute to enhancing the response under mechanical stress. The use of large postcure magnetic field to achieve magnetic domain alignment was demonstrated using magnetic force microscopy imaging, and this technique should prove to be beneficial in enhancing response levels.

Perhaps the most significant results were those tests in which damage detection was demonstrated. Tensile failure of mechanical test specimens induced a step discontinuity in axial field level that remained after unloading. This effect is thought to be the result of a change in residual stress field near the measurement location. Furthermore, the stress concentration around an artificial delamination was clearly observed in the axial magnetic field distribution. Both results strongly suggest that the damage state of a composite structure could be monitored and characterized by measuring the magnetic field signature at various times during the service life.

Piezoelectric

In addition to the conductivity problems associated with piezoelectric composite tagging, the direct effect was demonstrated for both 0-3 and 1-3 composite systems. There was evidence that structural damage has a measurable effect on the piezoelectric effect.

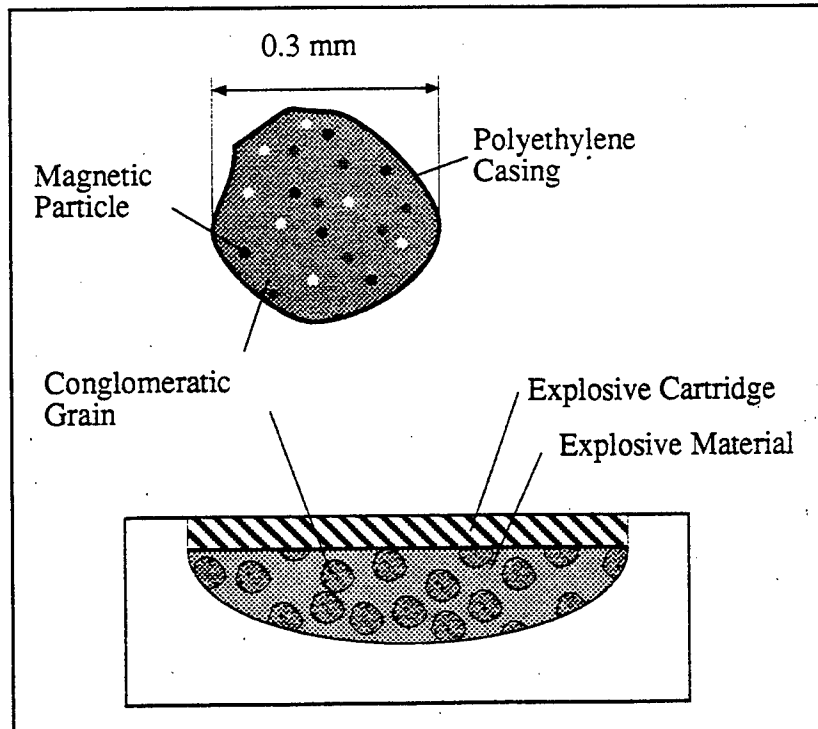


Figure 1. Schematic illustration of explosive tagging using phosphor particles (Ryan and Miller, 1973).

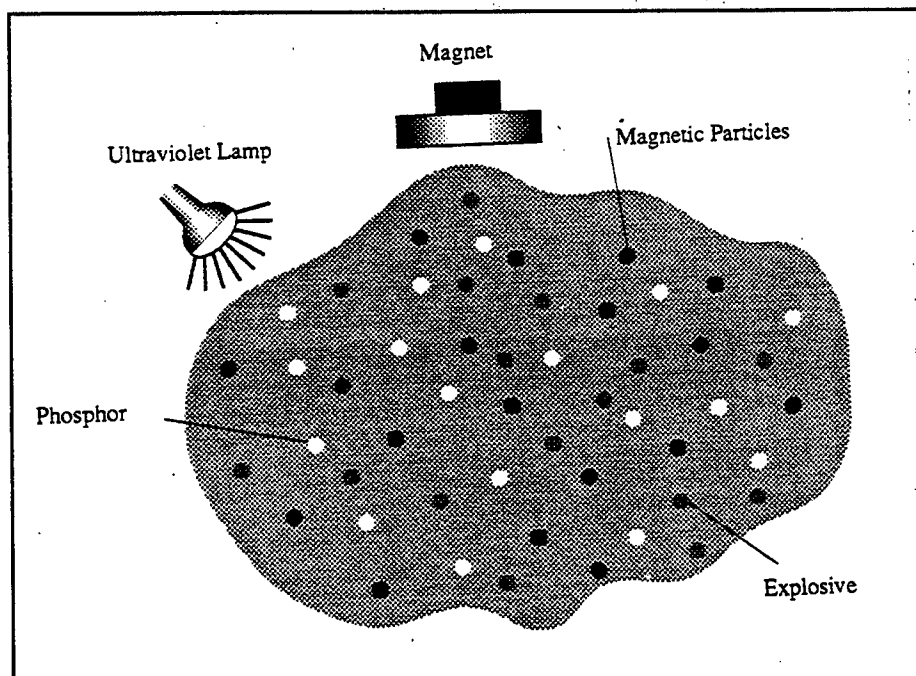


Figure 2. Illustration of using an ultraviolet lamp or magnet to locate tagged explosives (Ryan and Handke, 1978).

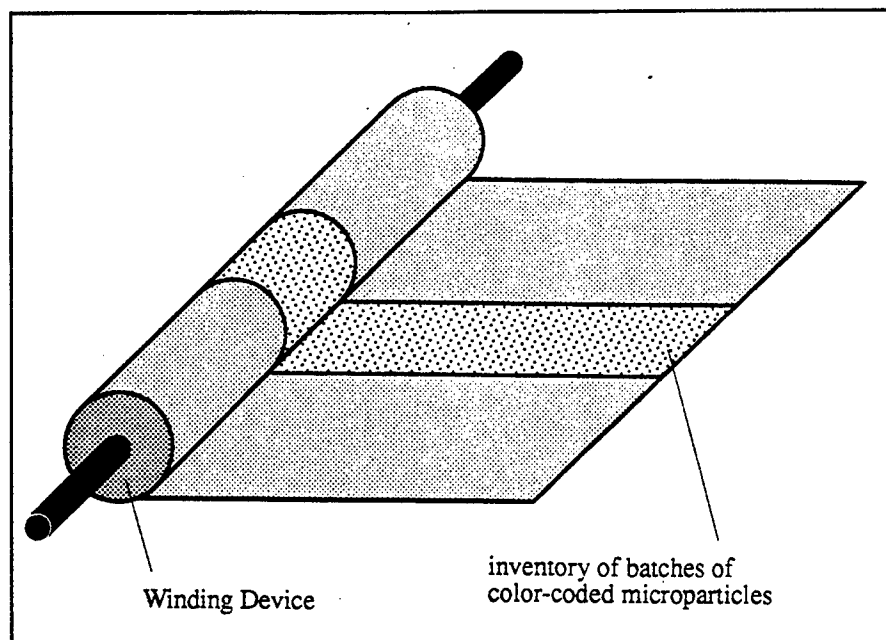


Figure 4. Schematic drawing showing the method of tagging units of production of a substance with color-coded particles (Lee, 1977).

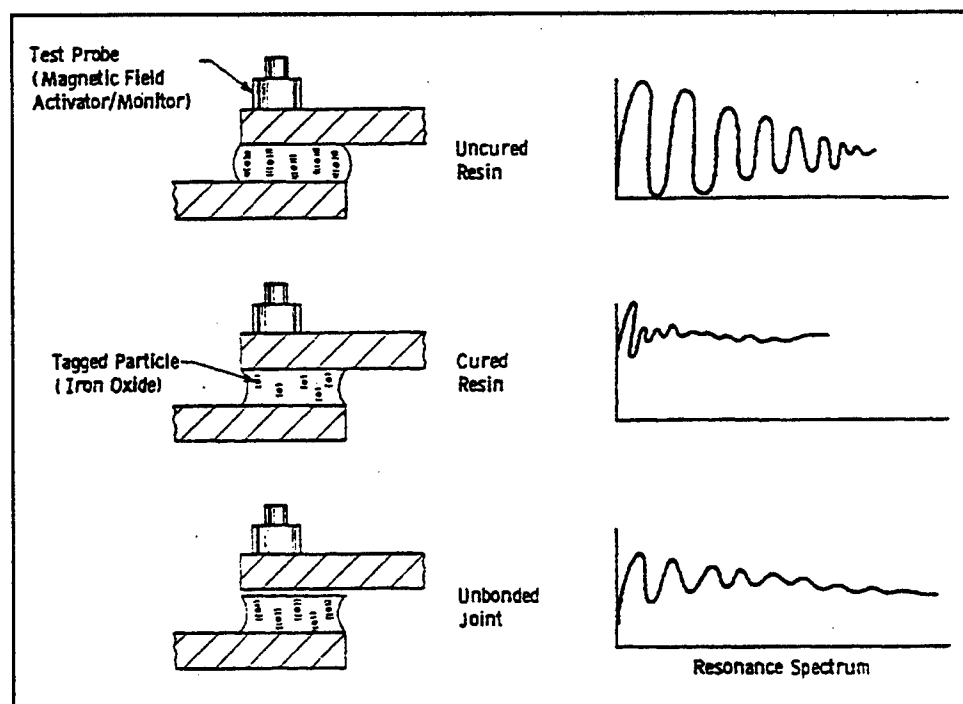


Figure 5. Schematic illustration of the concept of active tagging (Clark and Junker, 1990).

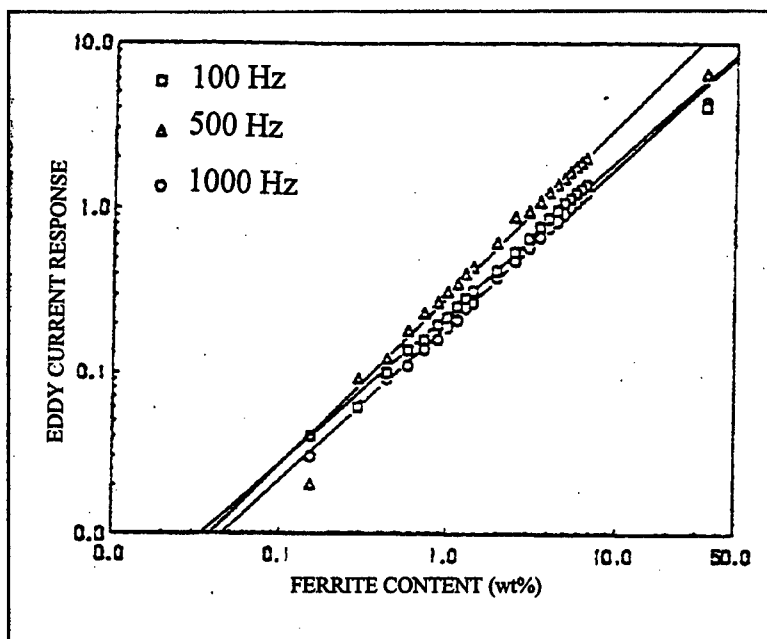


Figure 5. Correlations between the Eddy Current Response and the Ferrite content (weight ratio) in deionized water (Clark et al., 1990).

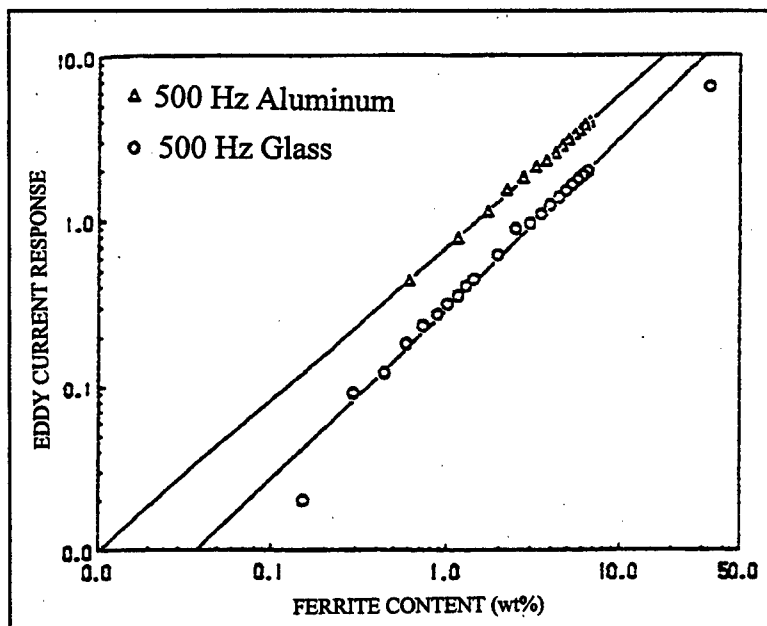


Figure 6. Comparison of the Eddy Current Response in an aluminum plate (3.2 mm) and a glass plate (2.5 mm) (Clark et al., 1990).

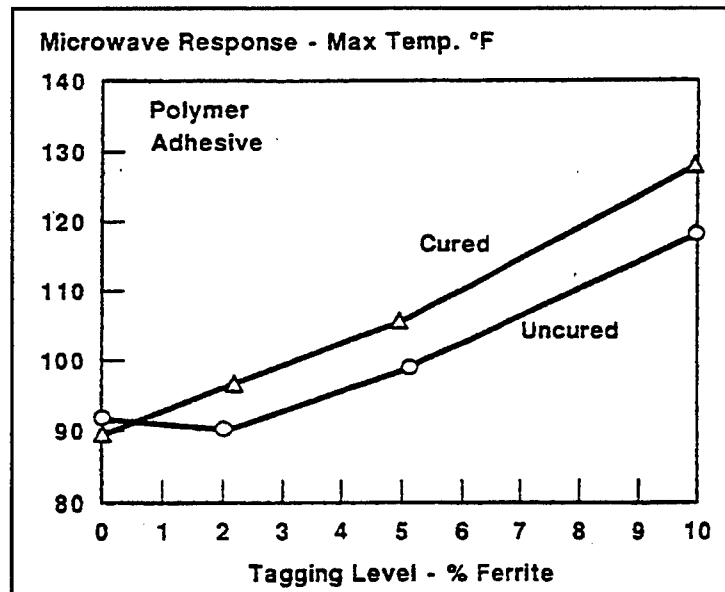


Figure 7. Comparison of the cured and uncured microwave response of the Ferrite particle-tagged polymer (Clark and Shannon, 1990).

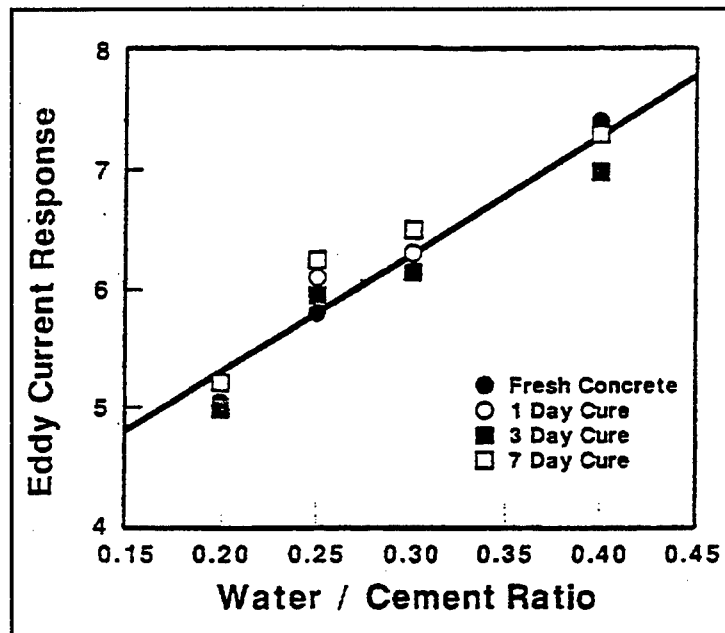


Figure 8. The Eddy Current Response vs. the state-of-cure of a cement (Clark, 1991).

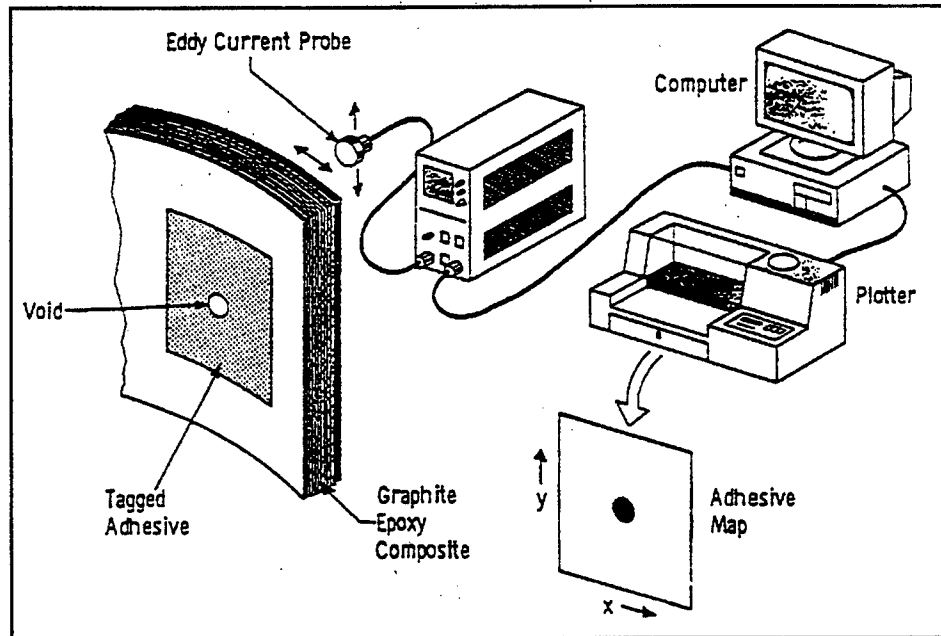


Figure 9. Schematic representation of a tagged adhesive system set-up (Clark, 1991).

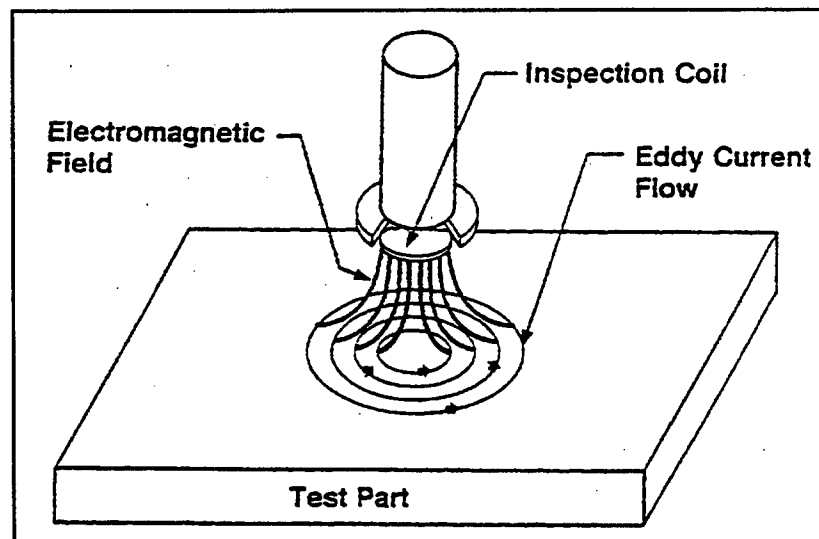


Figure 10. Schematic illustration of the principle of Eddy Current Testing (Shaffer, 1994; Clark, 1991).

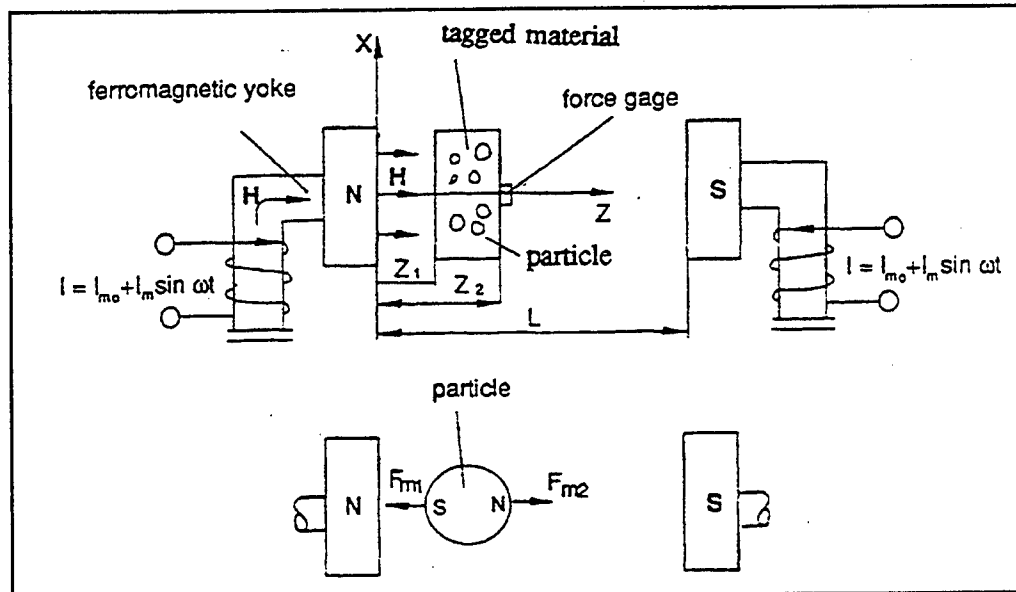


Figure 11. Schematic illustration of an active tagging system using a magnetic excitor.

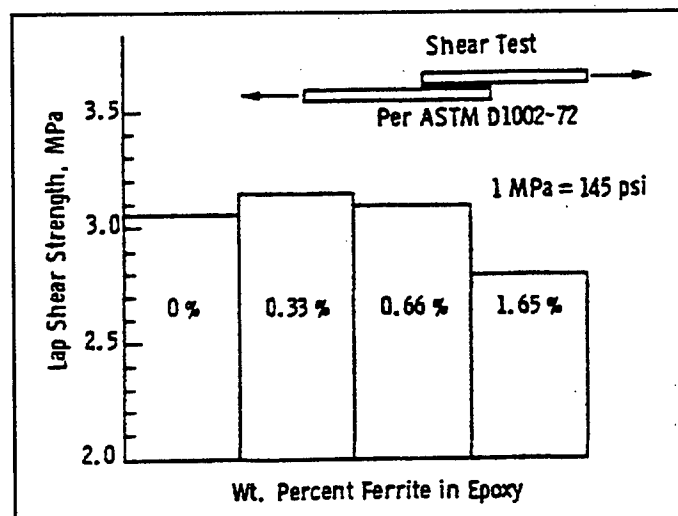


Figure 12. Effect of particle weight ratio on bonding strength (Clark et al., 1990).

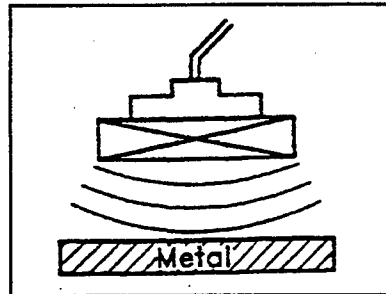


Figure 13. Skin-effect in a ferromagnetic material with an applied magnetic field.

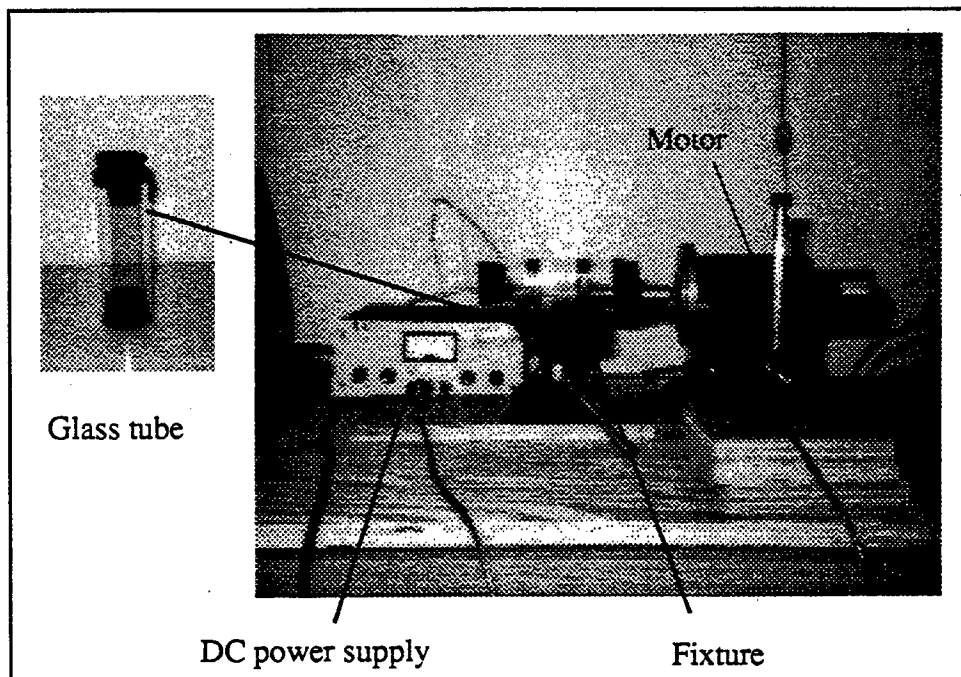


Figure 14. Photograph of the experimental set-up for manufacturing a tagged epoxy.

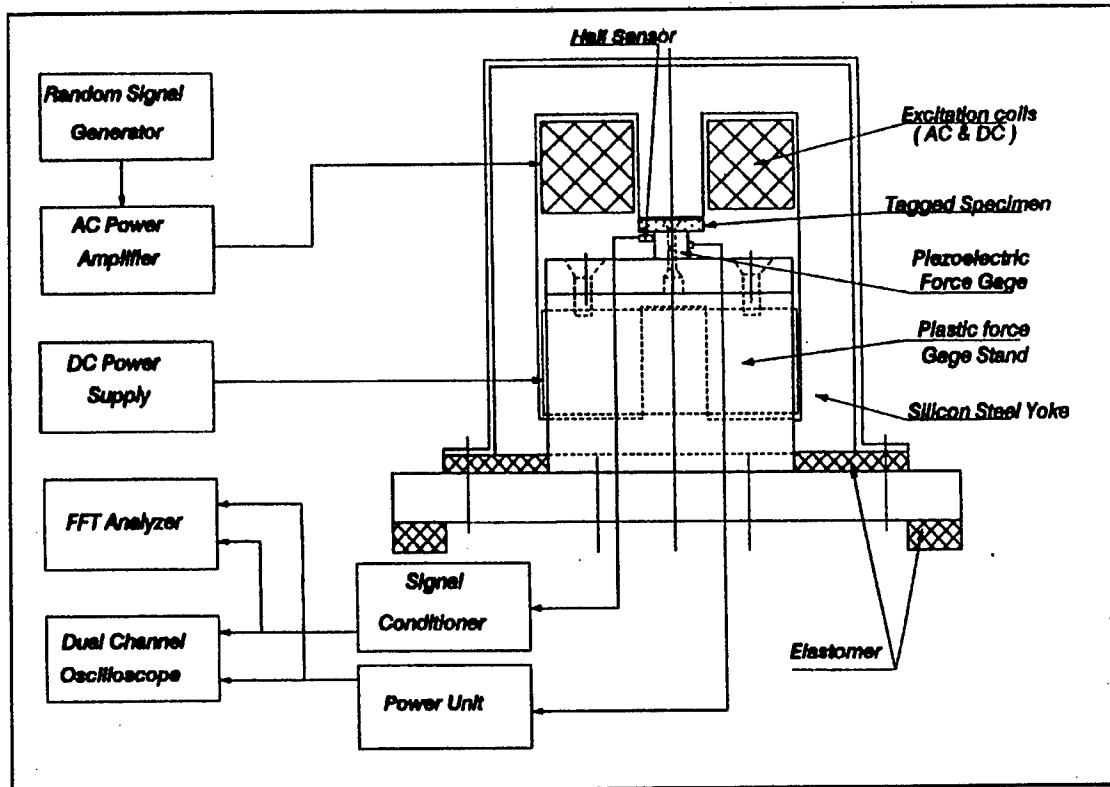


Figure 15. Schematic drawing of an experimental setup for active tagging using magnetic excitation.

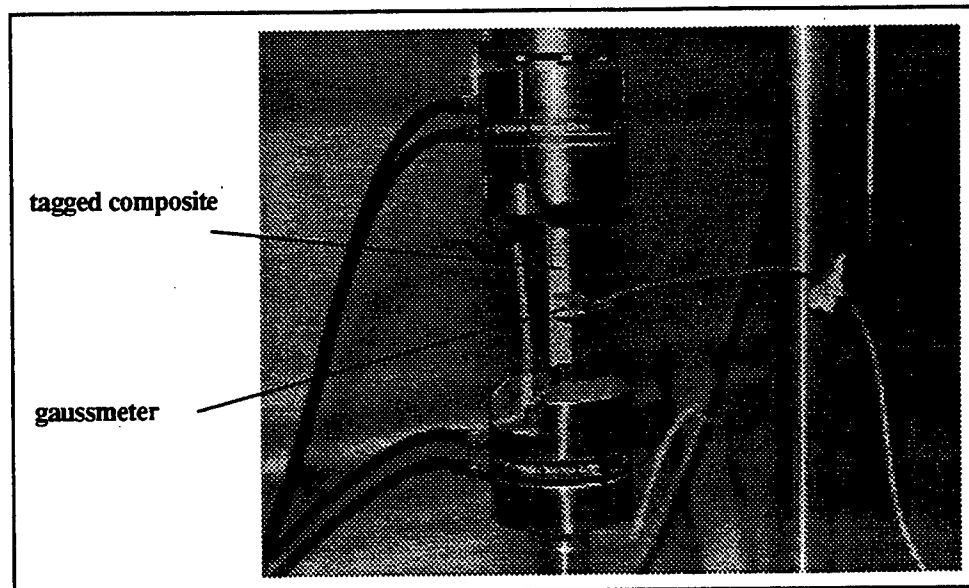


Figure 16. Experimental set-up for active tagging using magnetostrictive particles and mechanical excitation.

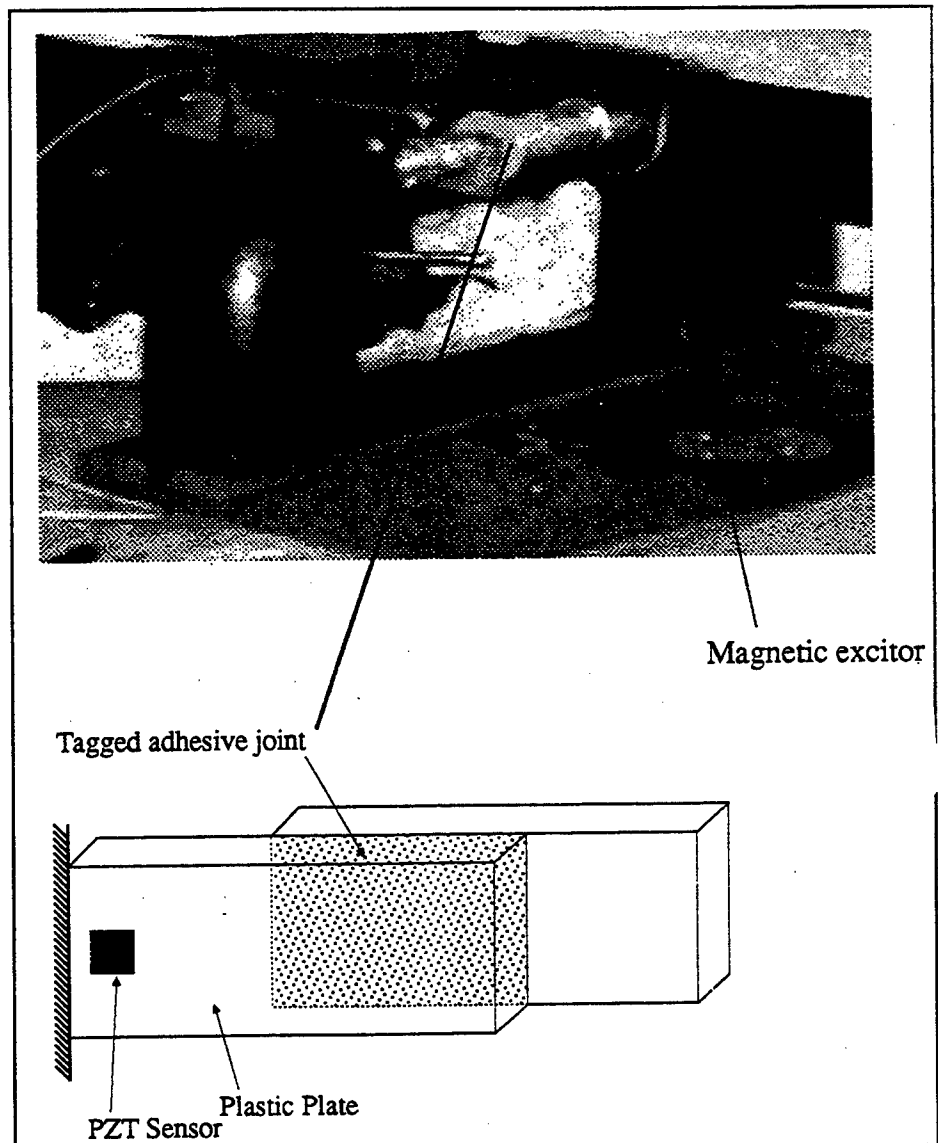


Figure 17. Experimental set-up for inspecting the state-of-cure of a tagged bonding layer.

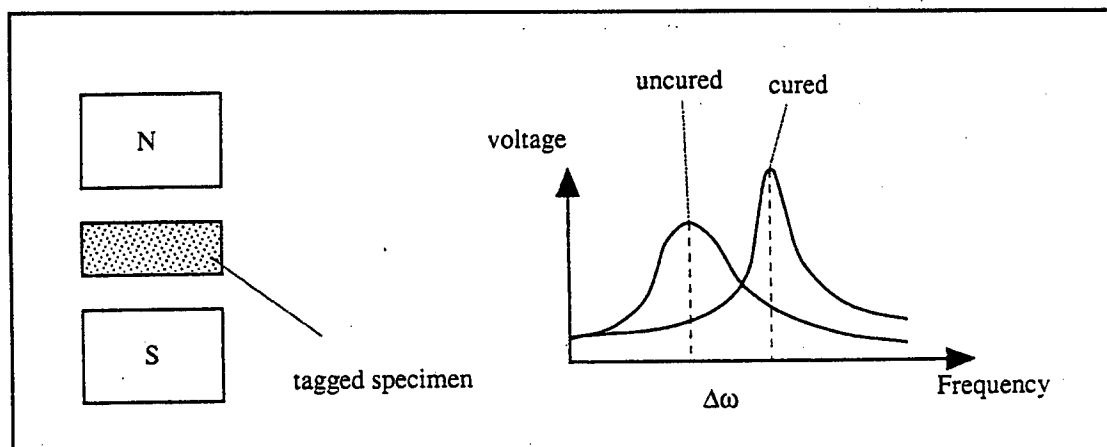


Figure 18. Changes ($\Delta\omega$) in the resonant frequency reflect the state-of-cure of the tagged adhesives.

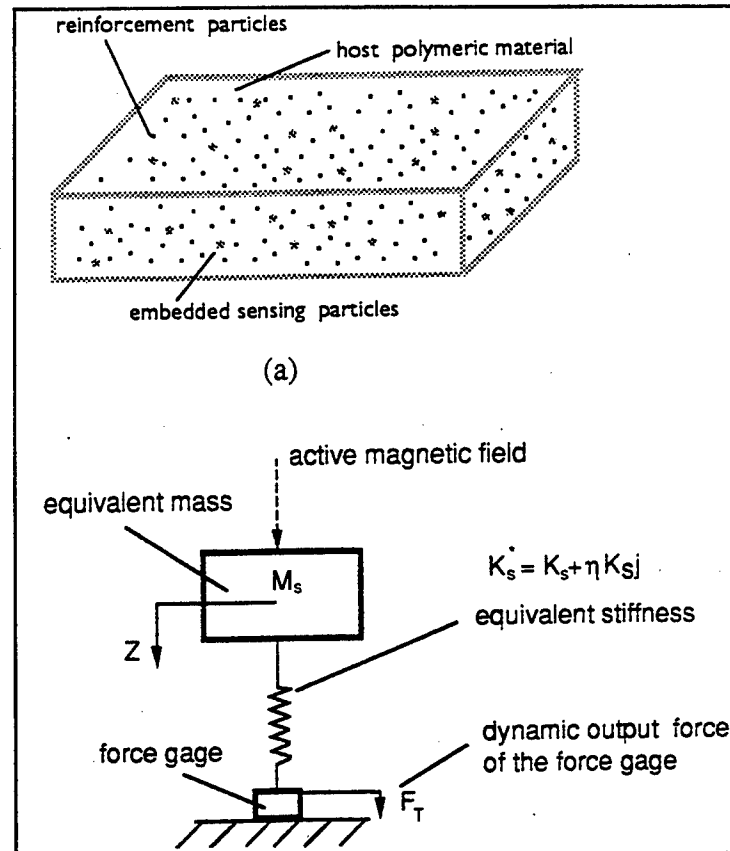


Figure 19. Dynamic model for a tagged epoxy system under magnetic excitation.

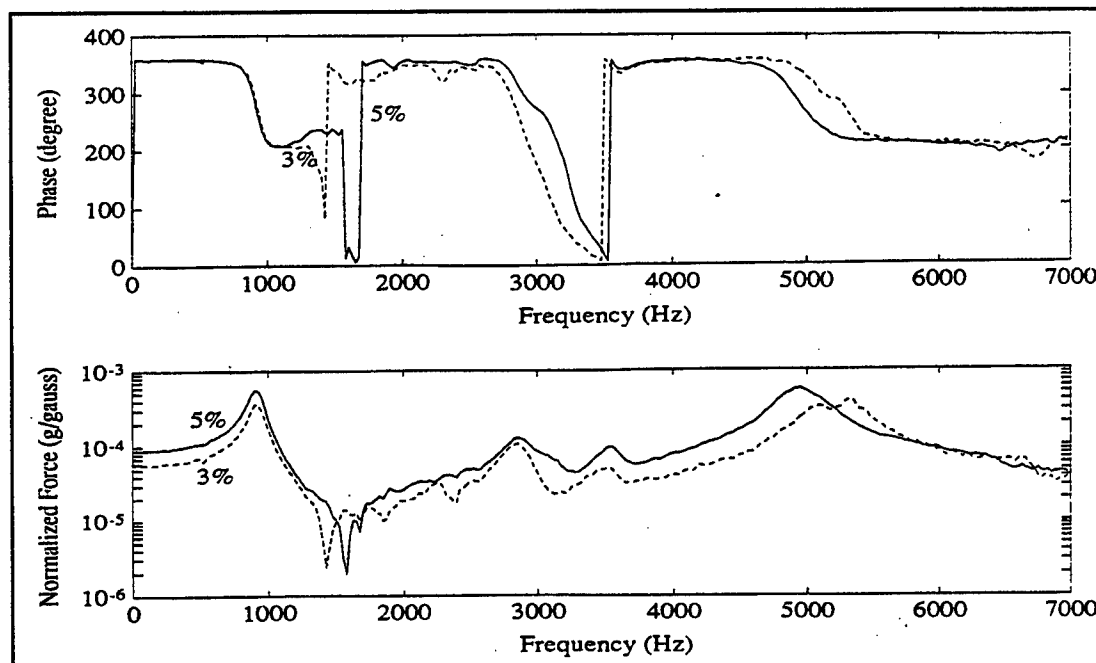


Figure 20. Comparison of the structural response of the tagged material at different tagging levels (3 % and 5 %).

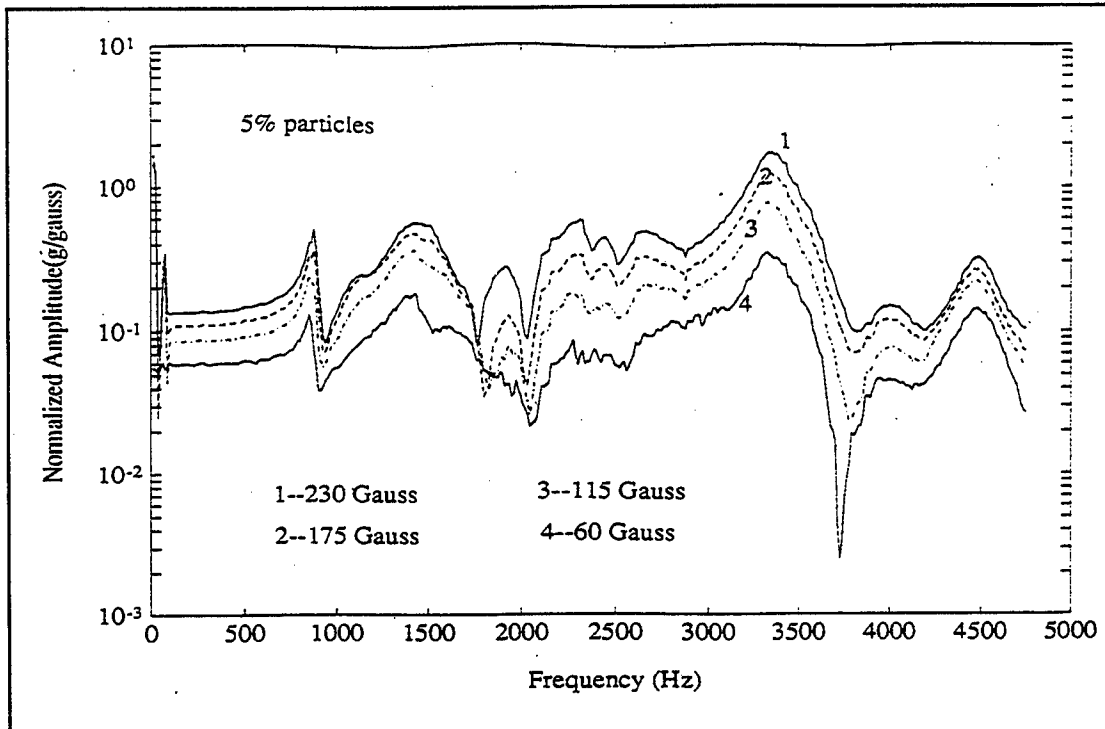


Figure 21. Comparison of the power spectrum intensity of the tagged material for different bias levels of the magnetic field.

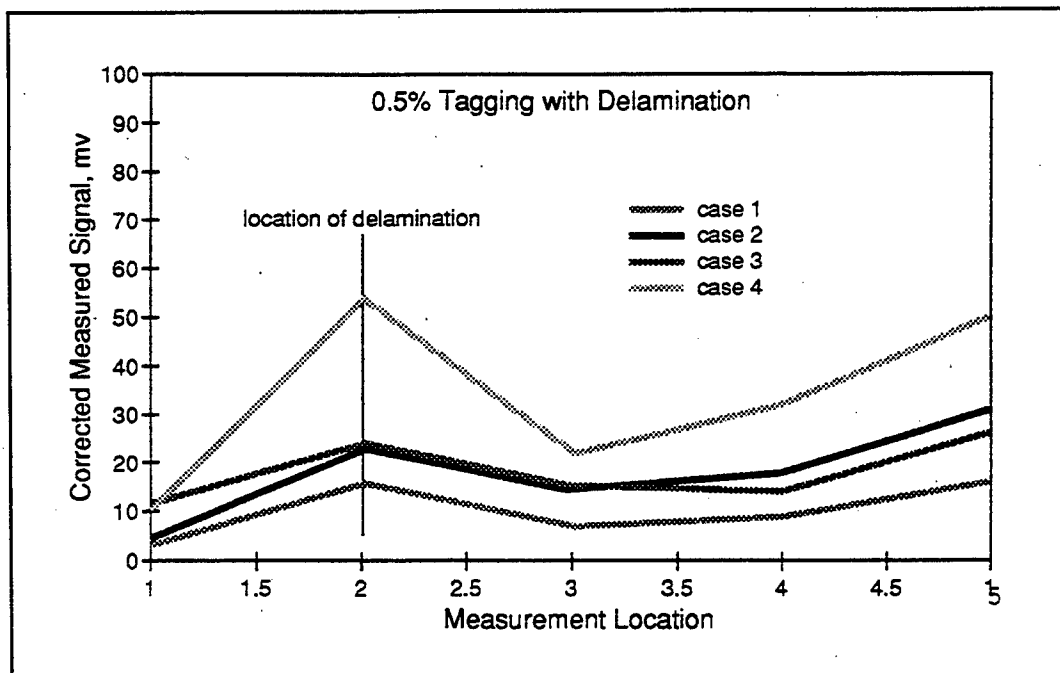
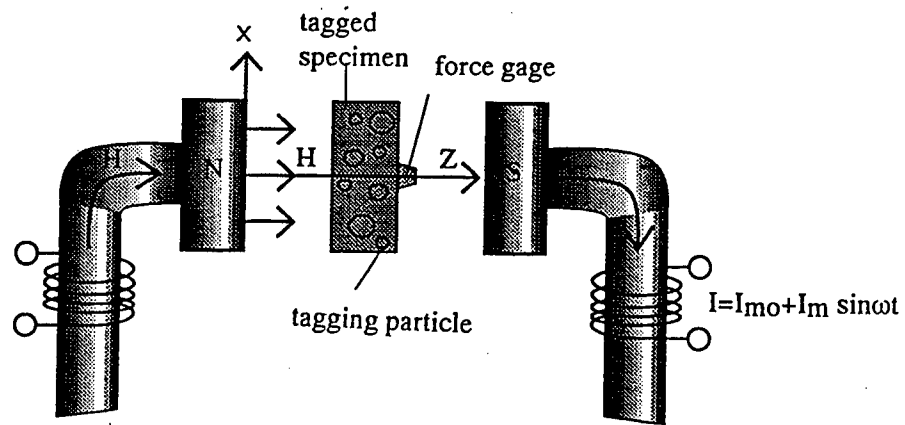
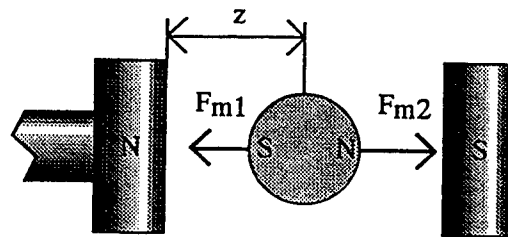


Figure 22. Experimental results obtained using magnetostrictive particle tagging.



(a)



(b)

Figure 23. Experimental set-up for active tagging with ferromagnet particles and magnetic excitation.

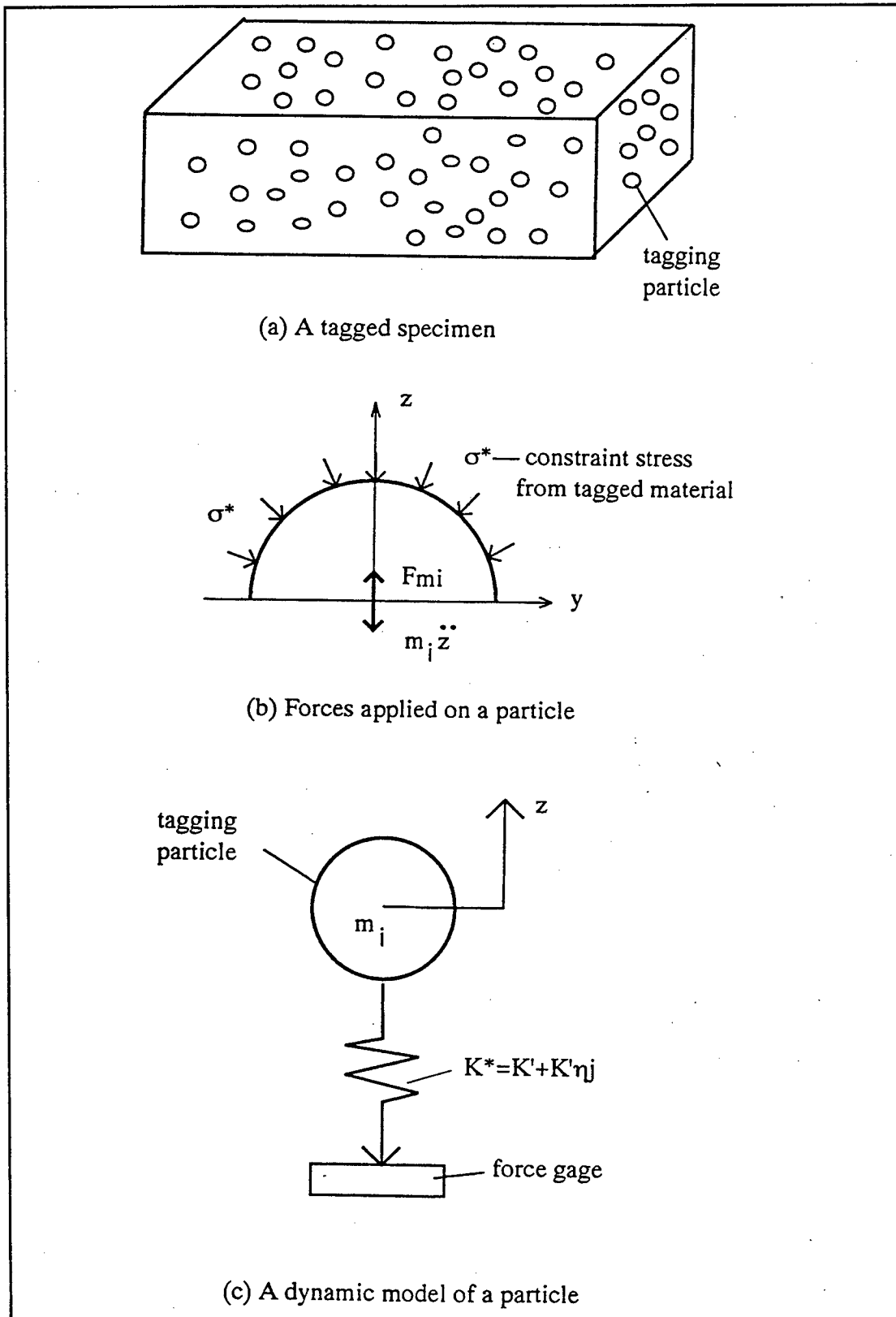


Figure 24. Schematic drawing showing a dynamic model for ferromagnetic particle tagging.

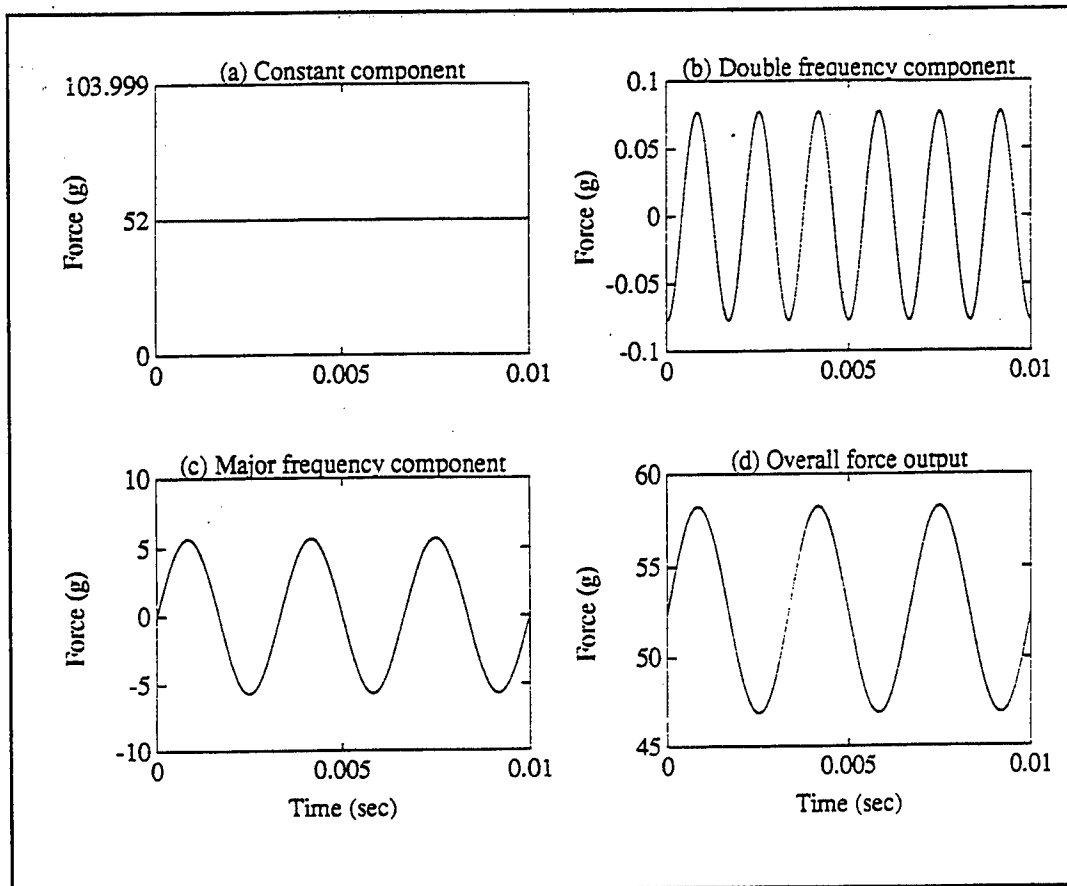


Figure 25. Numerical results showing the three structural excitation force components.

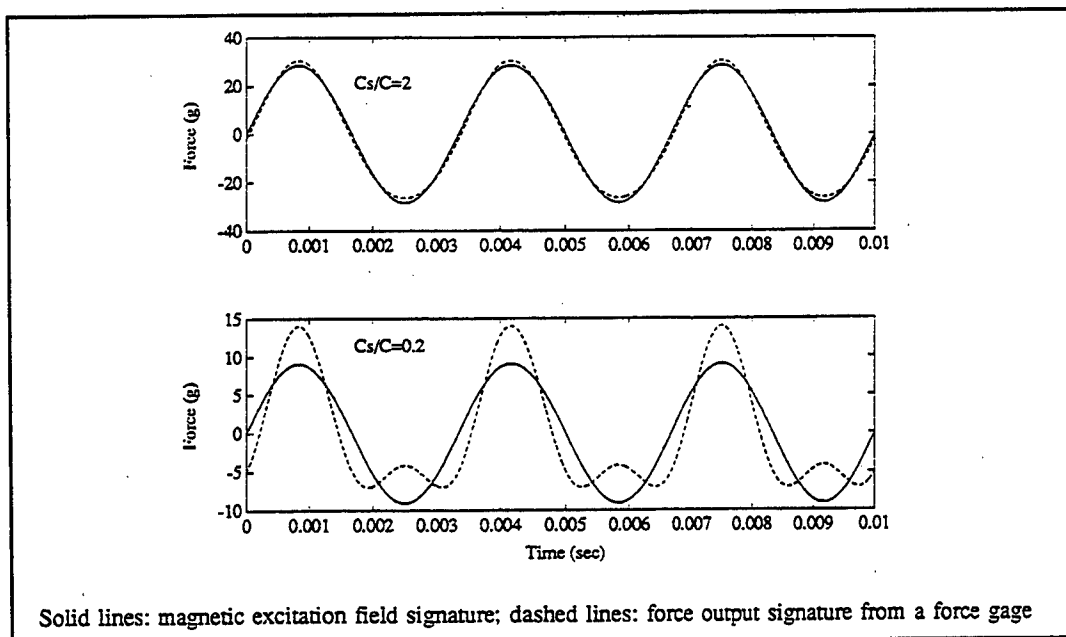


Figure 26. Numerical results show that a high value of C_s/C can suppress the signature distortion caused by the second harmonic excitation.

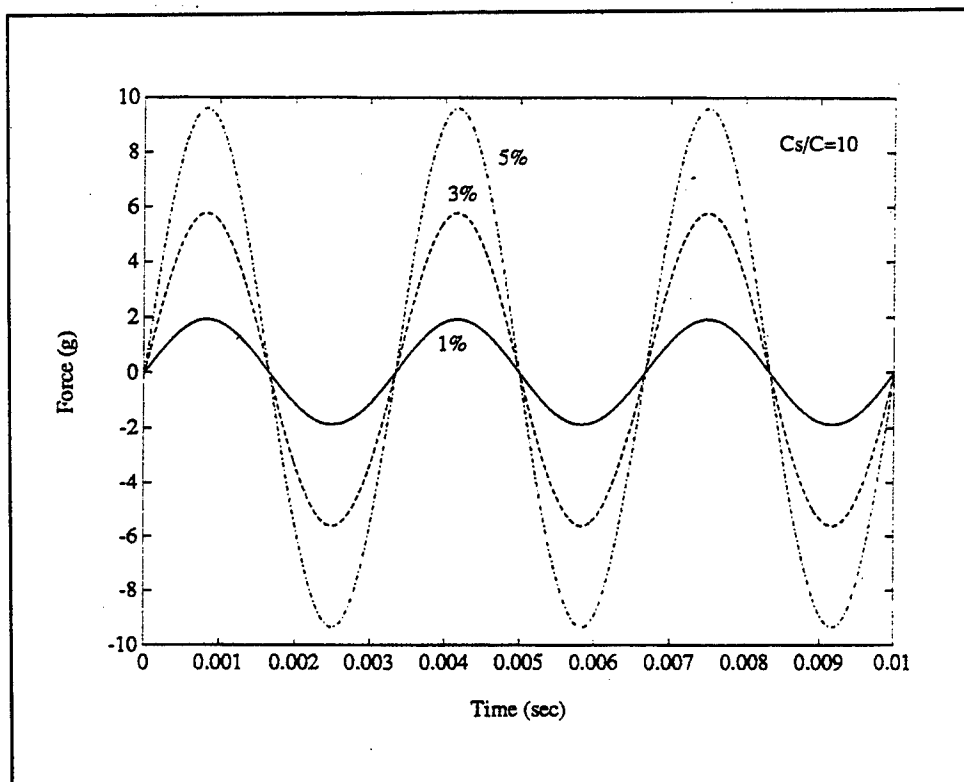


Figure 27. Numerical results show that the force response is proportional to the embedded particle contents.

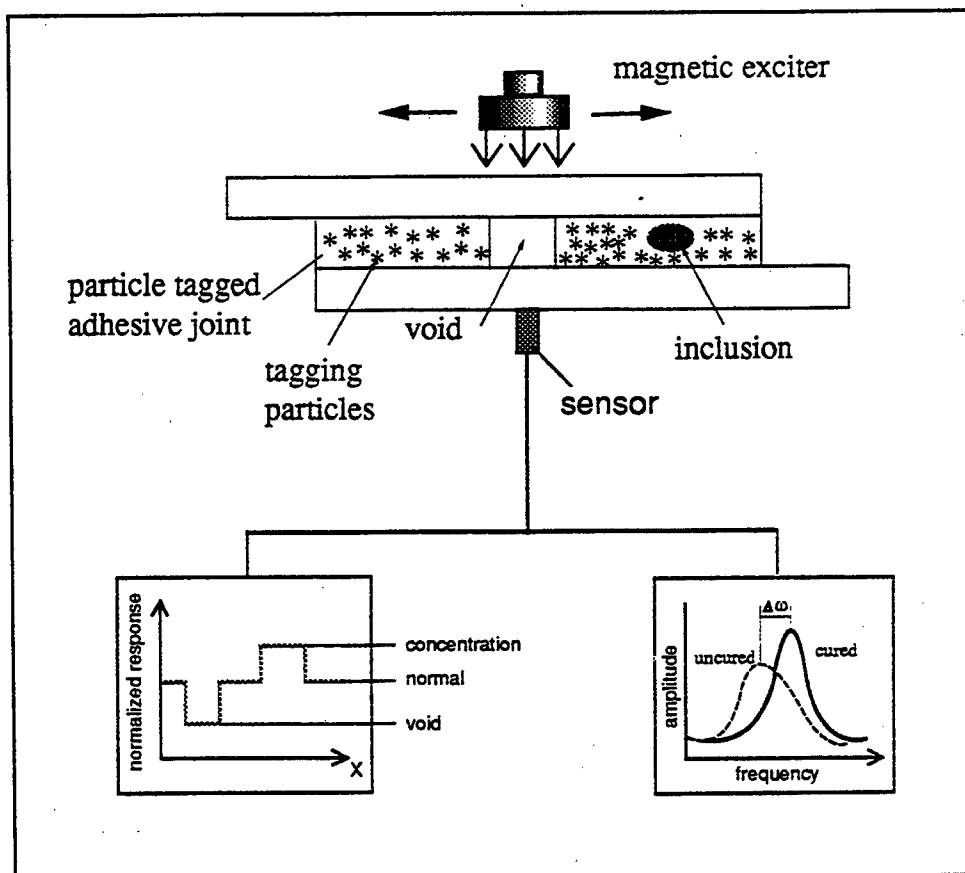


Figure 28. The active tagging particle technique in inspecting the bonding integrity of an adhesive joint.

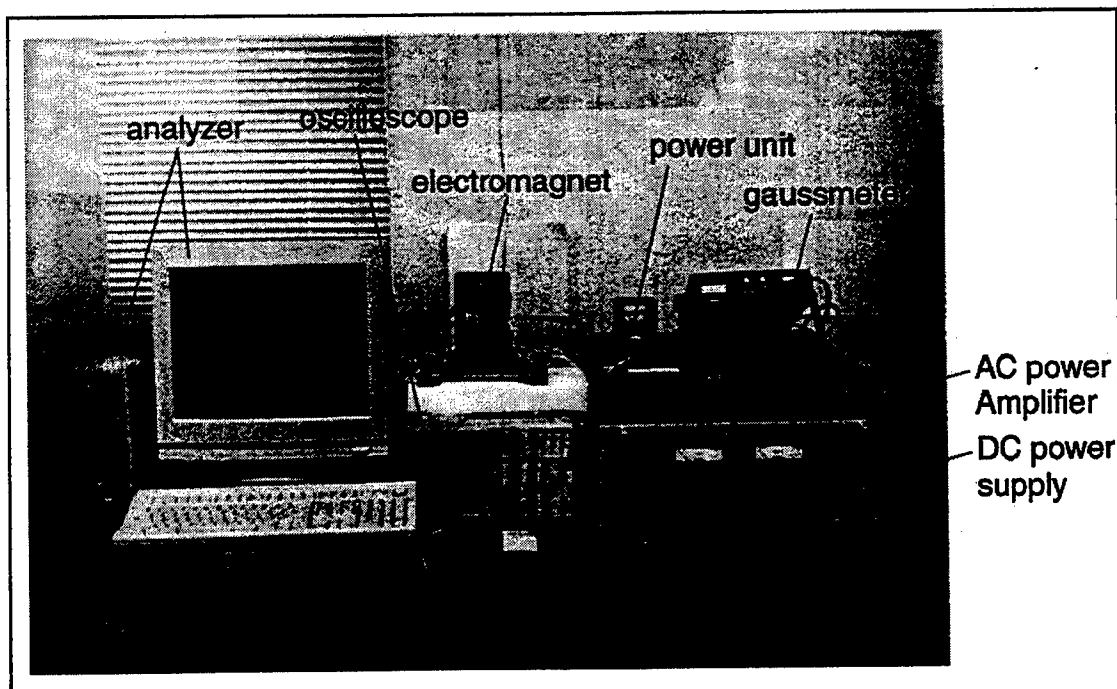


Figure 29. The experimental configuration used to measure the dynamic response of the specimen using magnetic excitation.

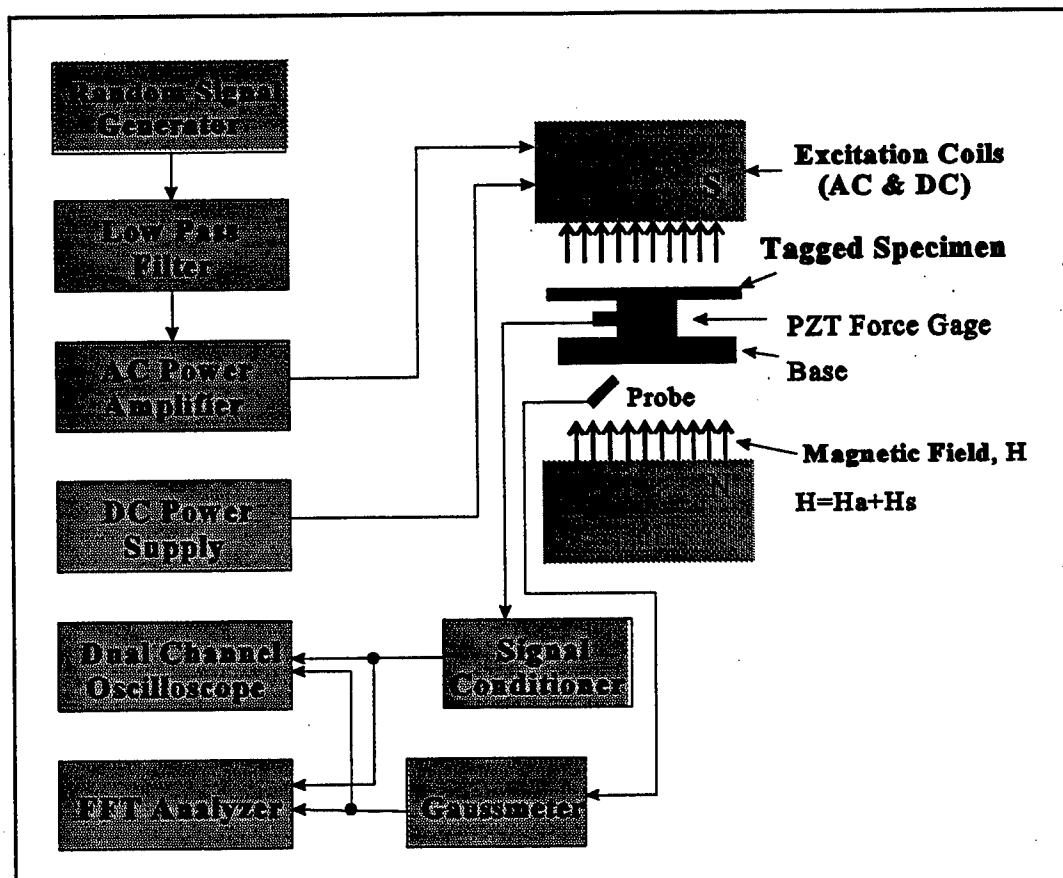


Figure 30. Experimental set-up used to test the dynamic response of the specimen using magnetic excitation.

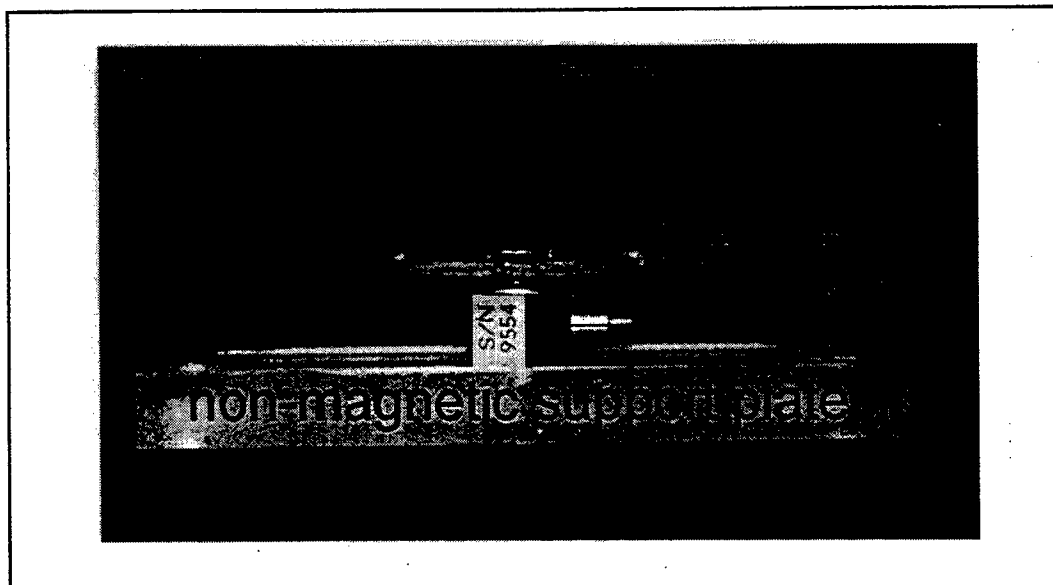


Figure 31. Illustration of the connections between a test specimen and a force gage.

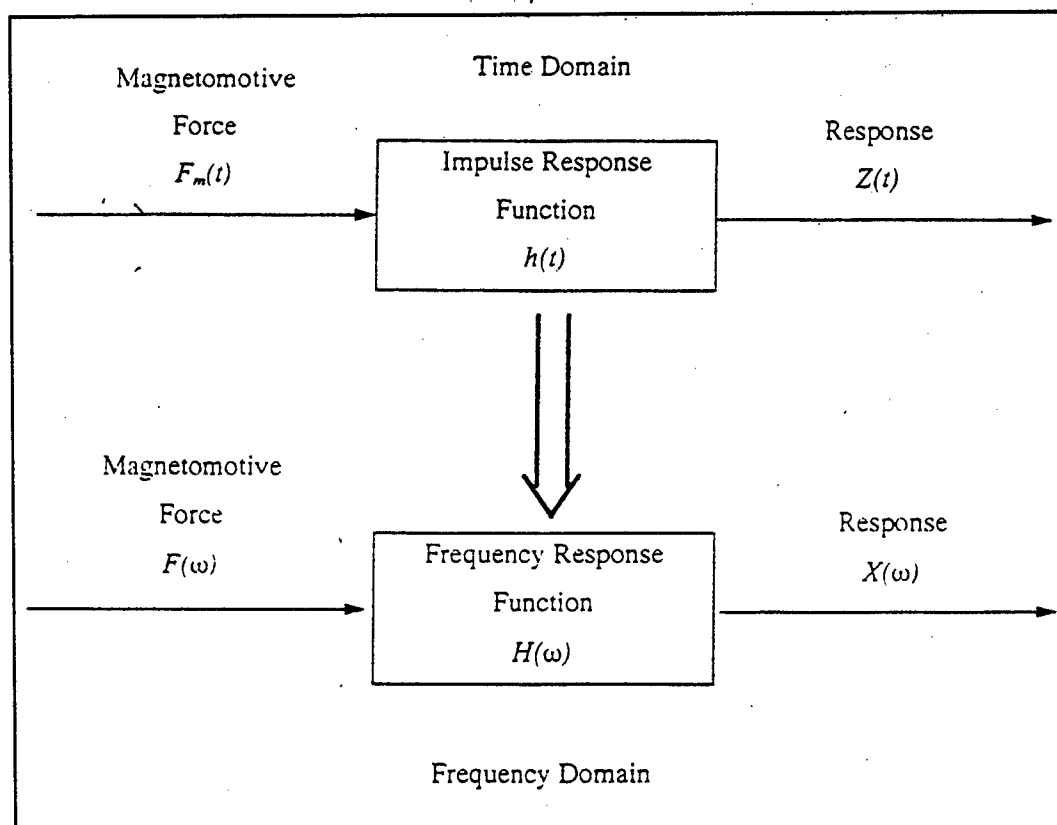


Figure 32. Transfer function of time domain to frequency domain transform.

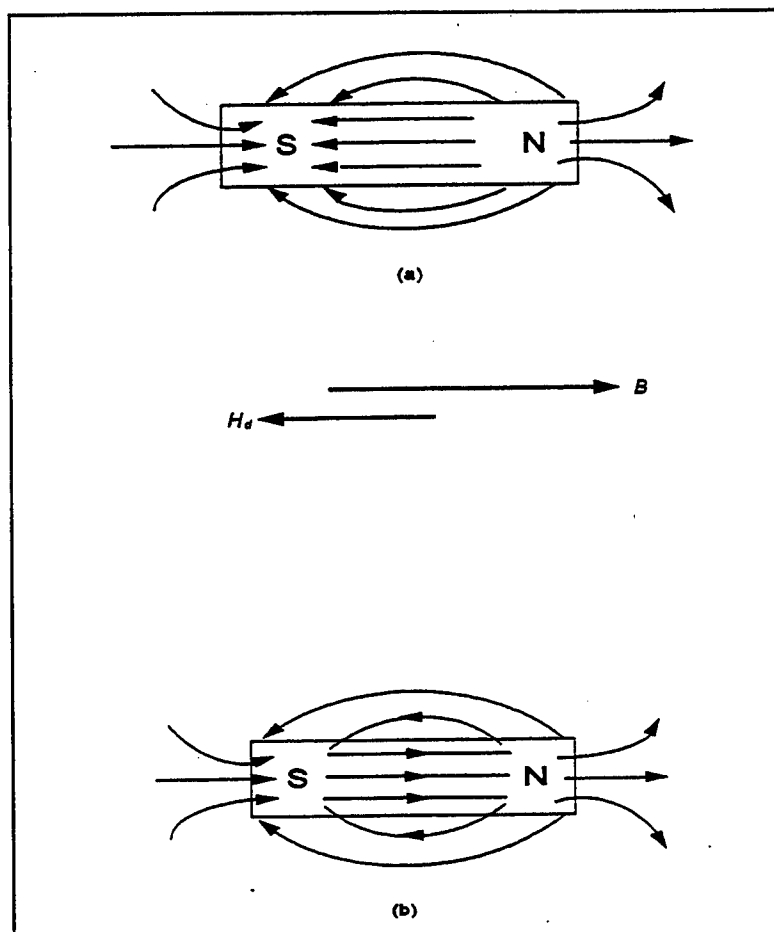


Figure 33. Schematic drawing showing magnetic fields of a bar magnet in zero applied field: (a) magnetic intensity, H , field, and (b) magnetic flux density, B , field. The vectors in the center magnet indicate the values of these quantities at the center of the magnet.

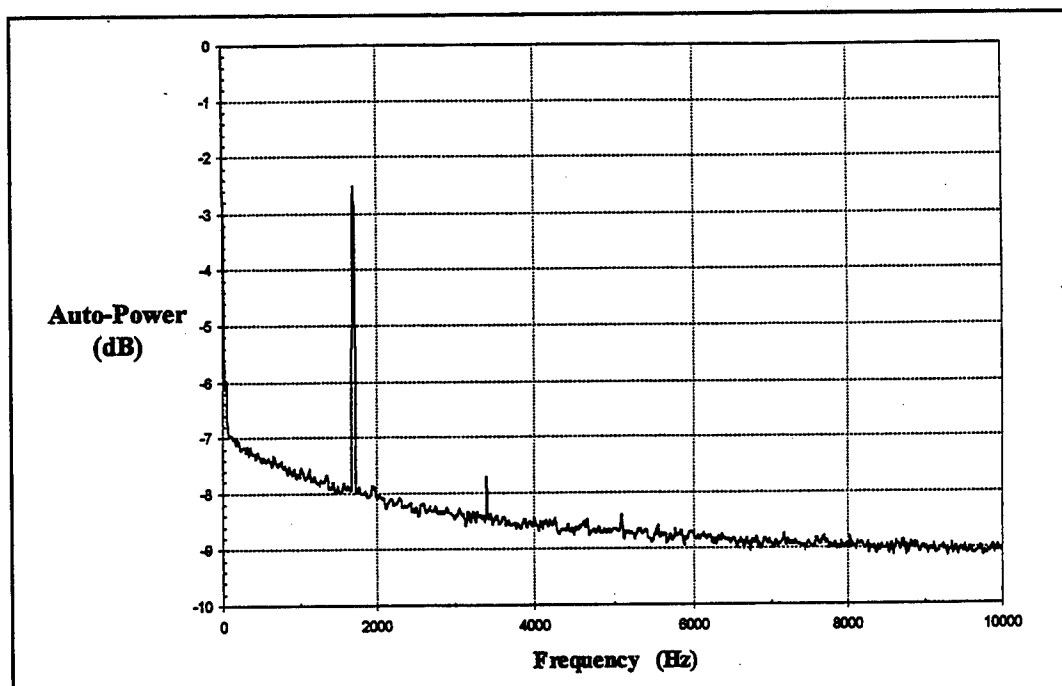


Figure 34. Power spectrum analysis of magnetomotive force for active tagging with ferromagnetic particles.

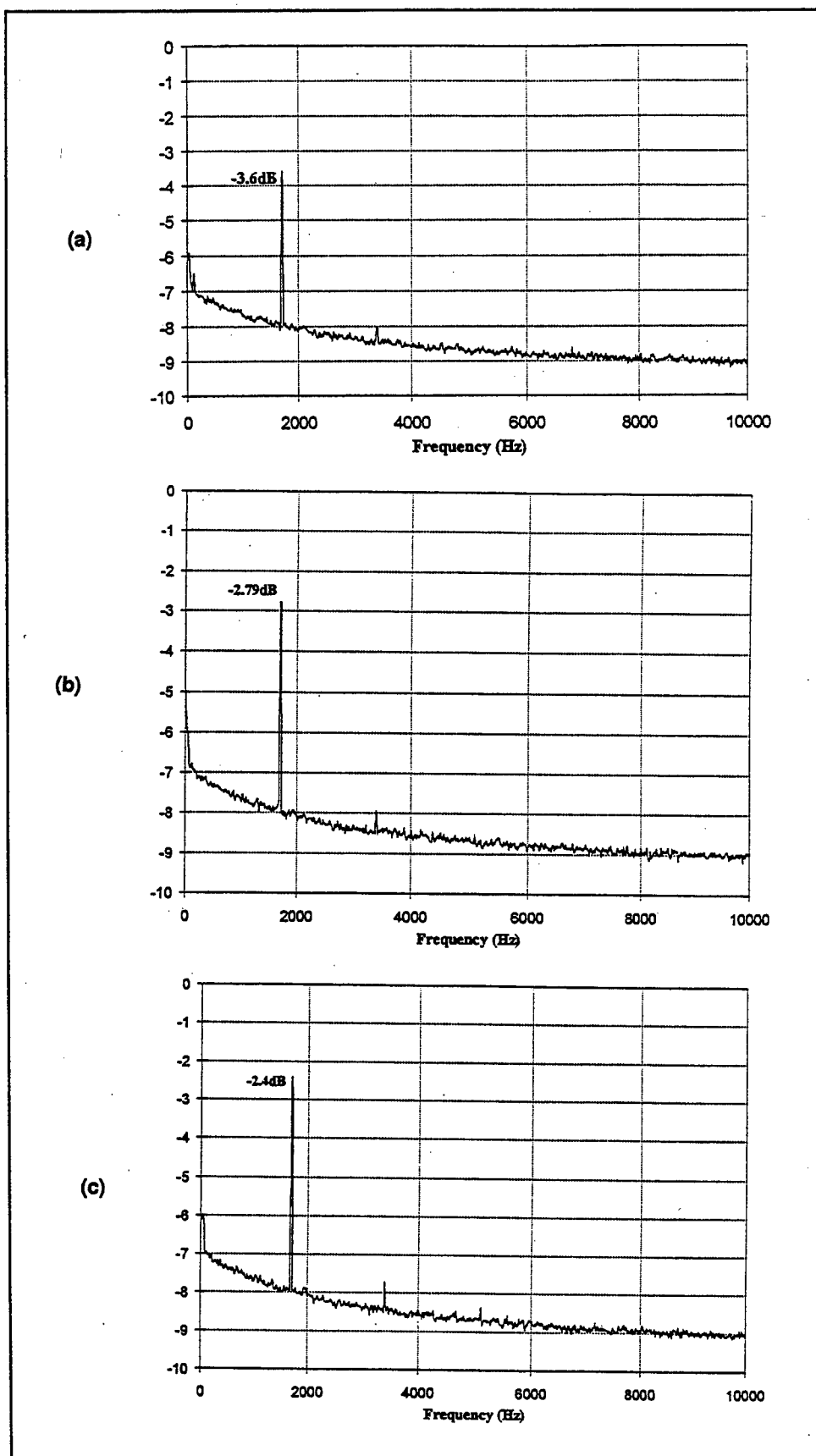


Figure 35. Output power spectrum of the frequency response of (a) 3% magnetite tagging specimen; (b) 5% MnZn ferrite tagging specimen; (c) 8% MnZn ferrite tagging specimen.

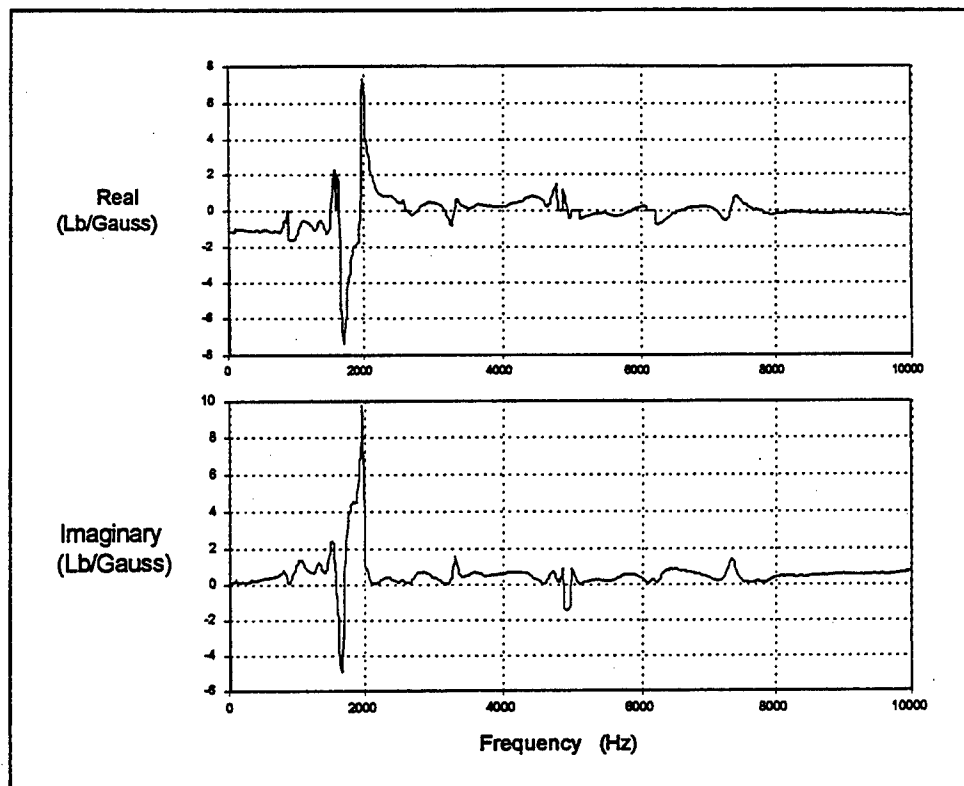


Figure 36. Frequency response function of polymer composite tagged with 8% MnZn ferrite subjected to magnetic excitation.

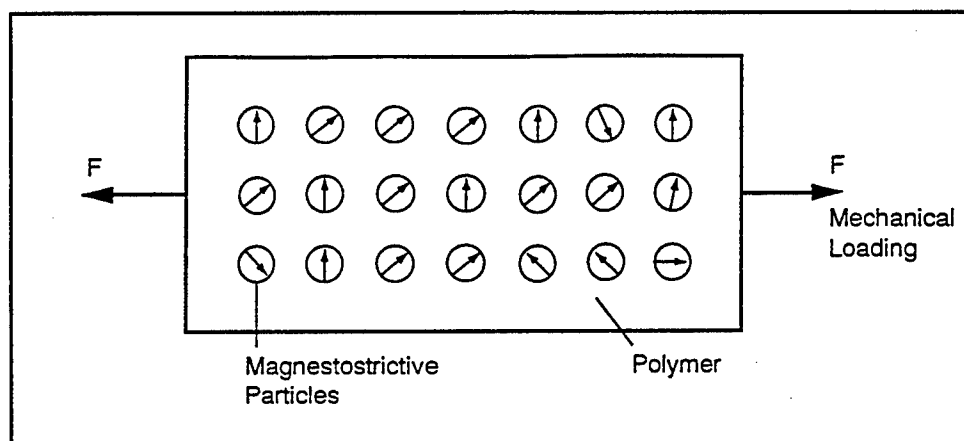


Figure 37. Magnetostrictive particle tagged specimen stressed by mechanical loading.

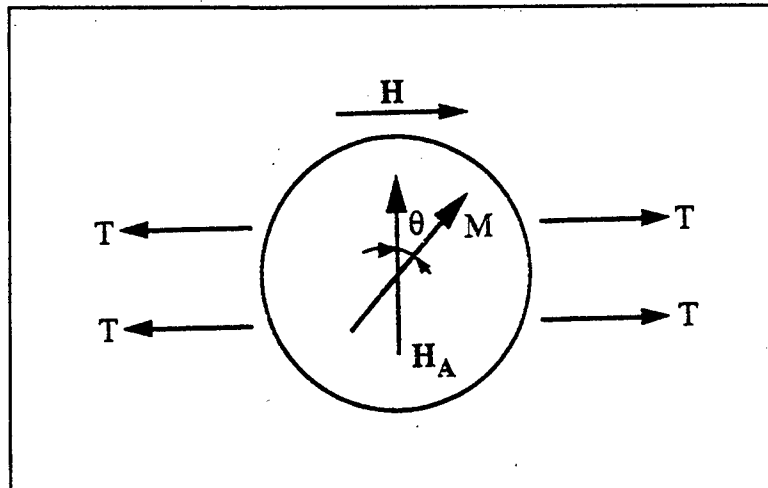


Figure 38. Schematic illustration of a single domain of a magnetostrictive particle.

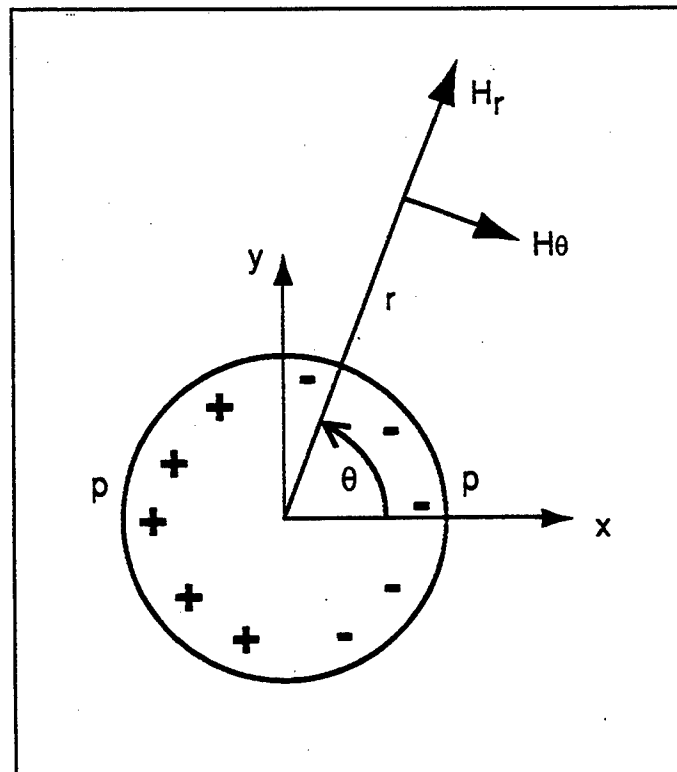


Figure 39. Schematic illustration of the magnetic induction outside a magnetic dipole.

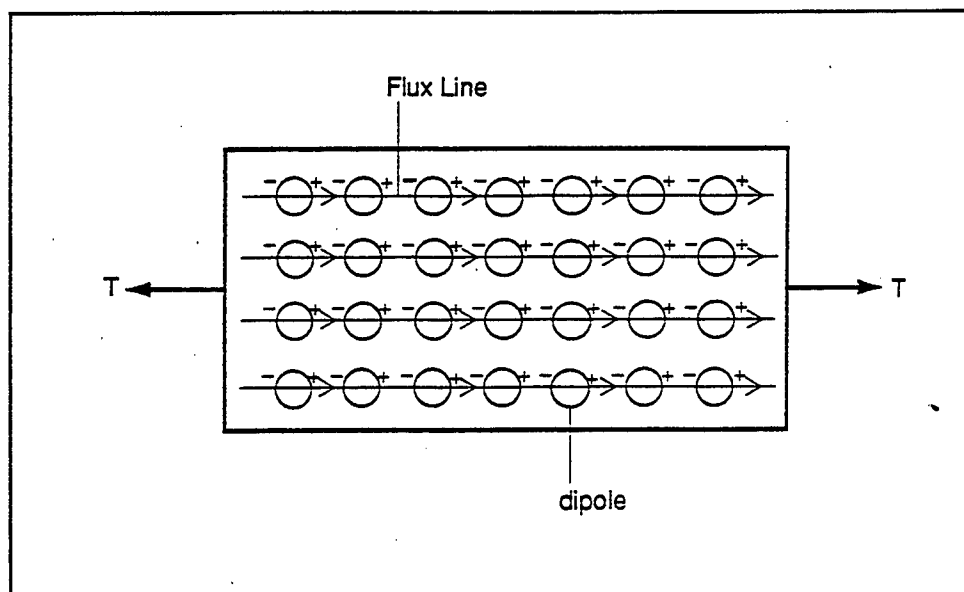


Figure 40. Schematic drawing showing the flux lines due to the attraction between unlike poles under mechanical loading.

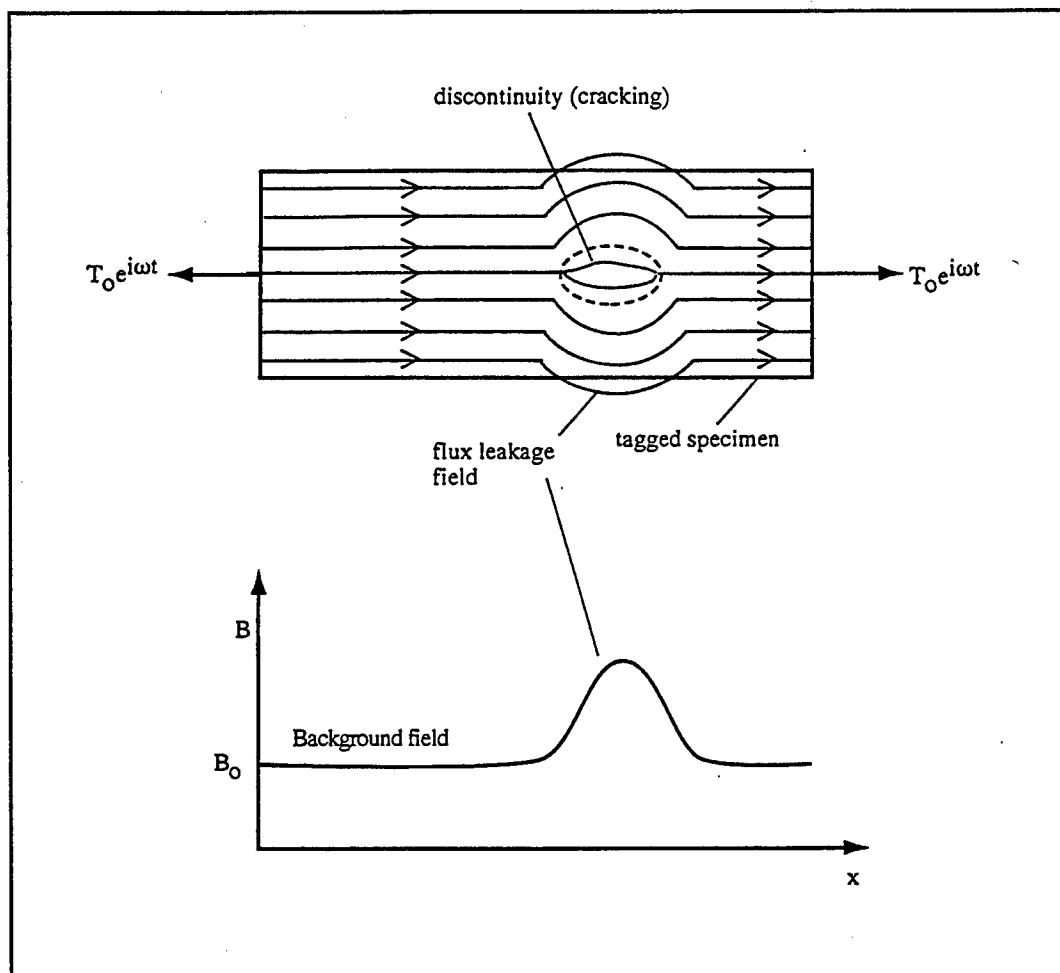


Figure 41. Schematic drawing showing a surface magnetic flux leakage due to a residual induction of a discontinuity.

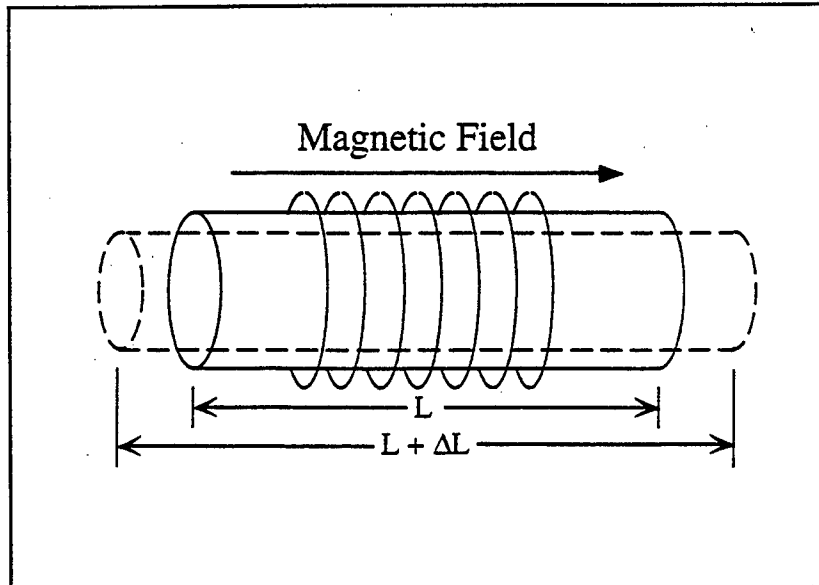


Figure 42. Magnetostriction effect.

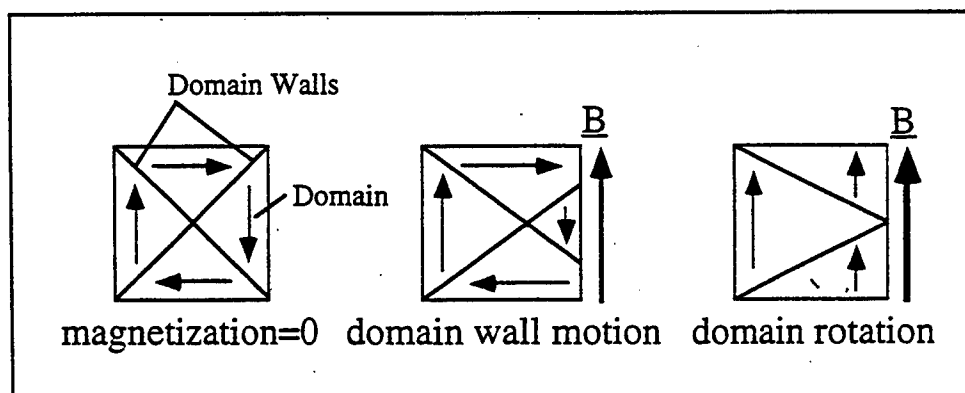


Figure 43. Magnetic domains.

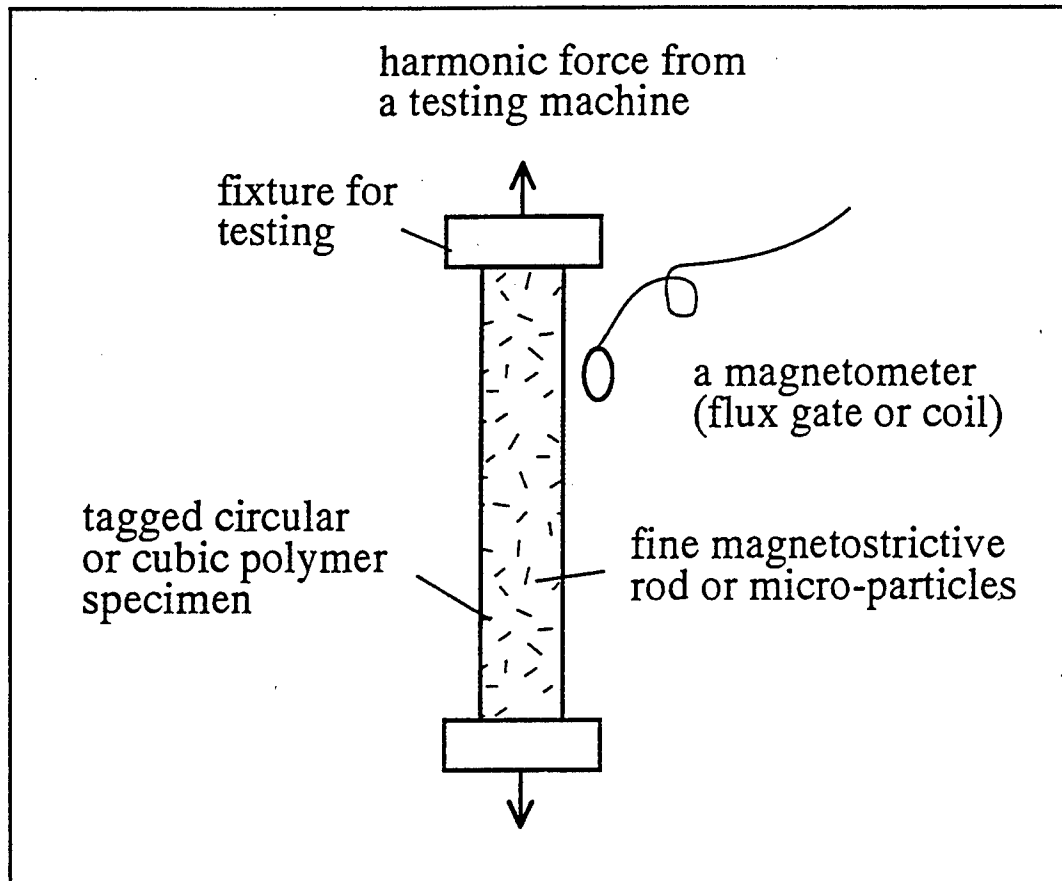


Figure 44. Schematic drawing showing the magnetostrictive tagged specimen experimental set-up.

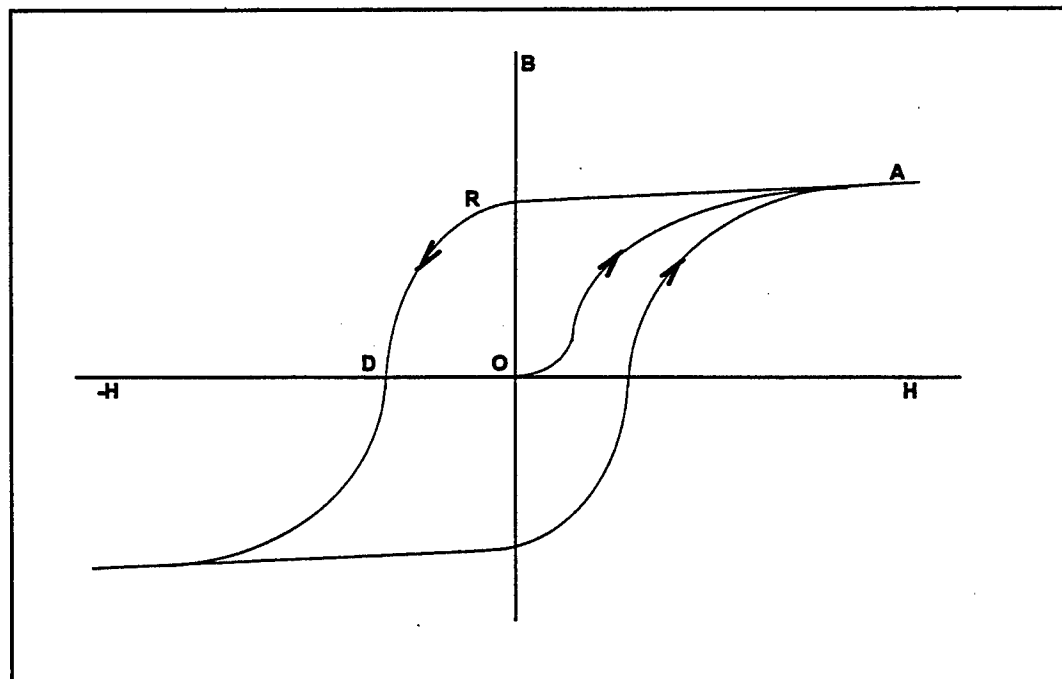


Figure 45. Schematic drawing showing a hysteresis loop in the magnetostriction of magnetostrictive material.

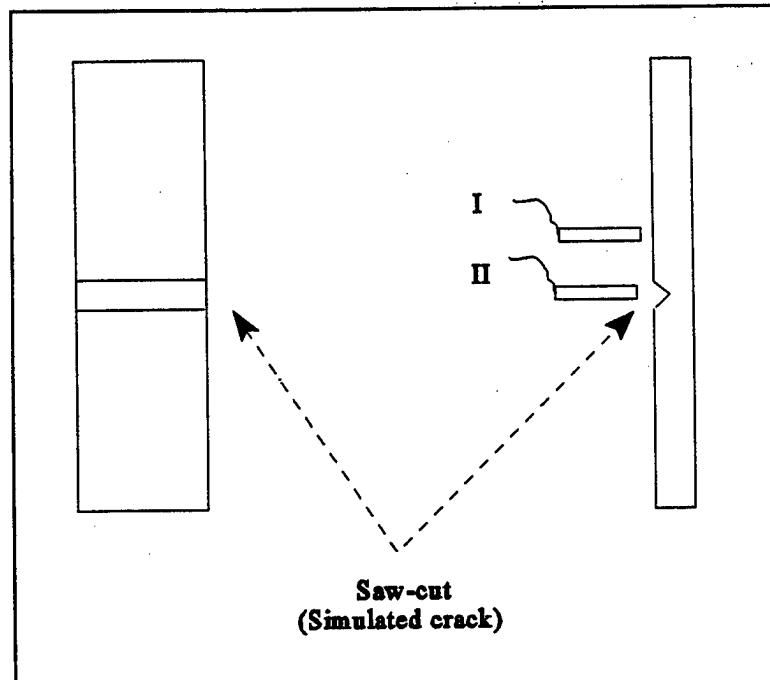


Figure 46. Schematic drawing showing a saw-cut crack on specimen B, where A and B are the locations of a gaussmeter probe to pick up the crack-free signal and the crack signal, respectively.

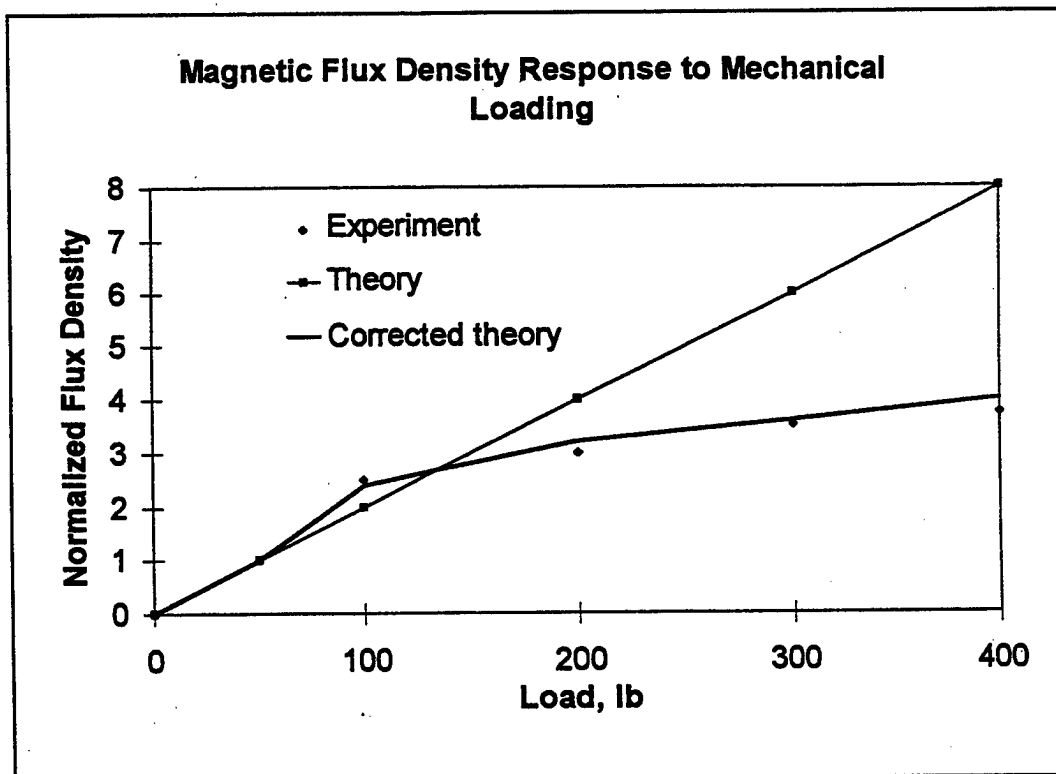


Figure 47. Test results of specimen A with the magnetostrictive active tagging method for experimental validation of the theoretical model.

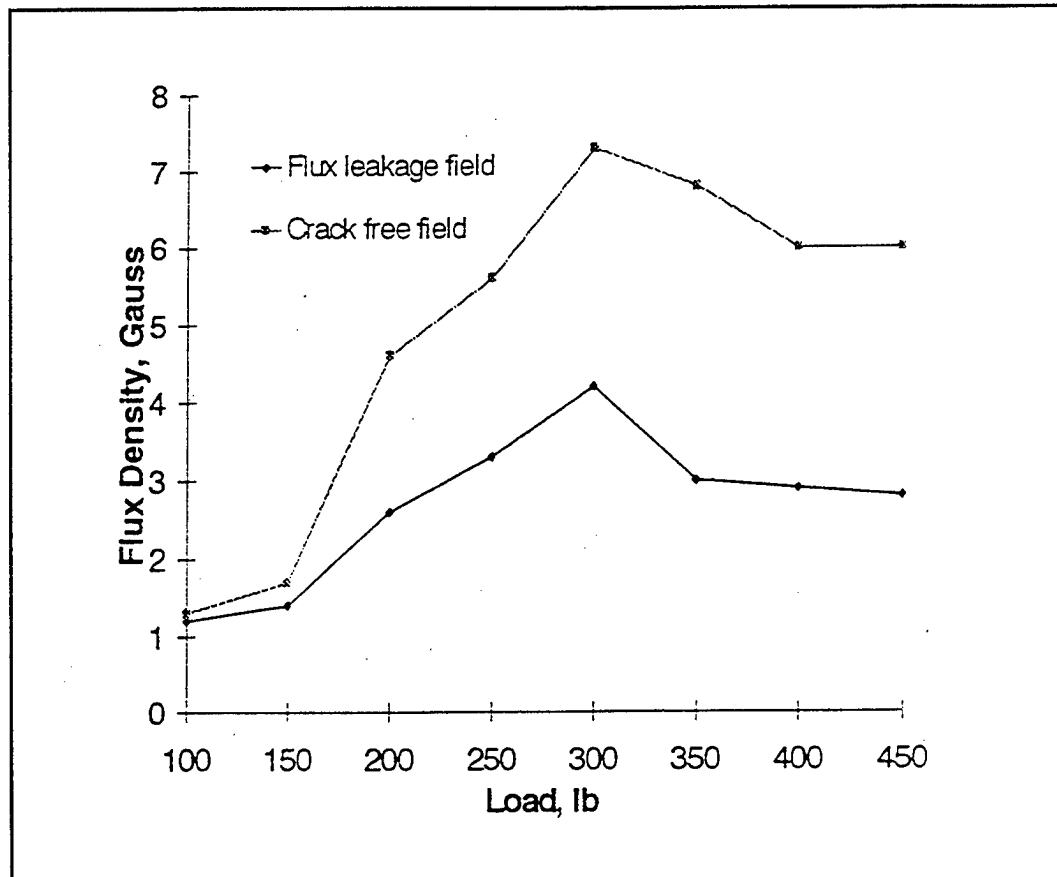


Figure 48. Test results of specimen B with the magnetostrictive active tagging method for defect detection.

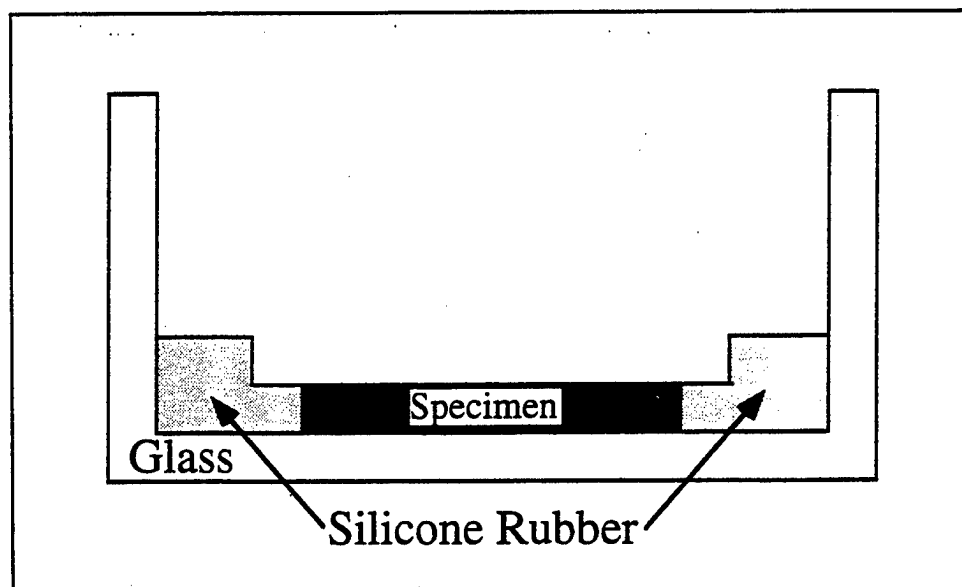


Figure 49. Glass/silicone rubber mold used for unreinforced specimens.

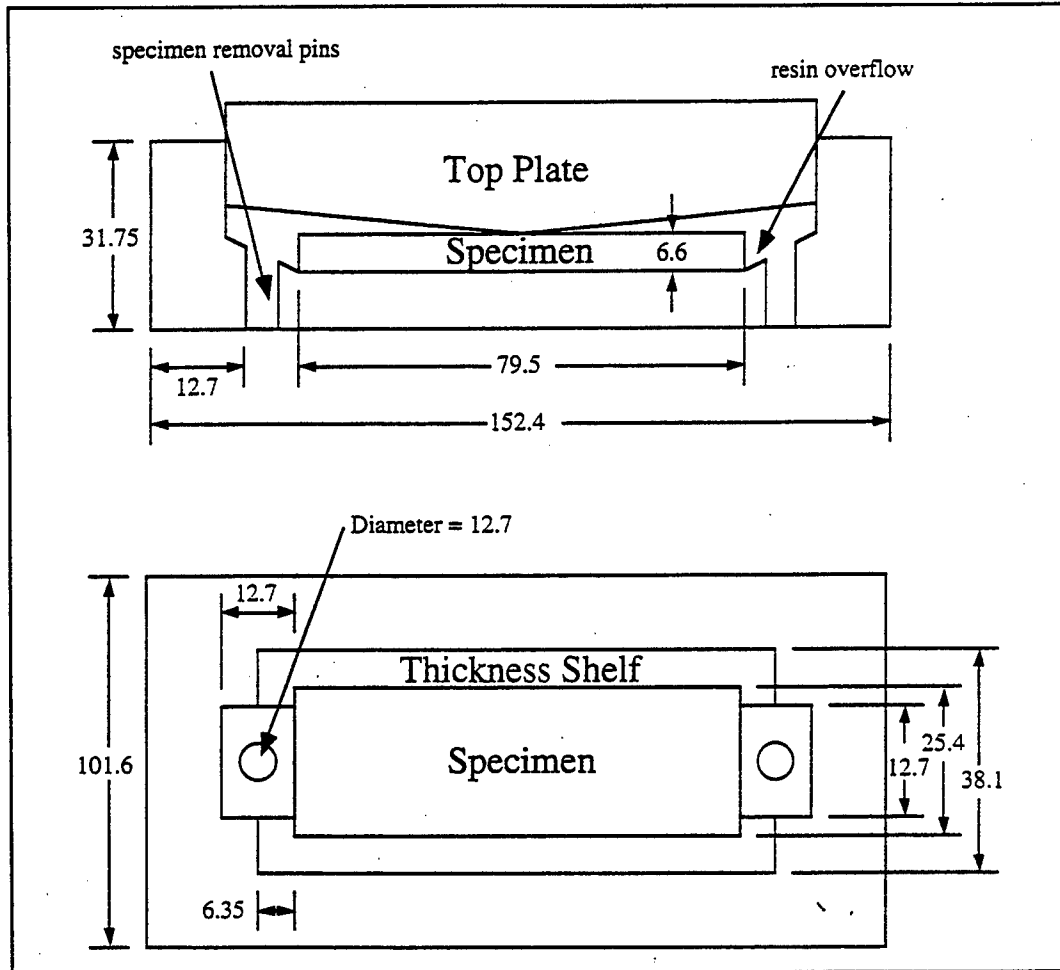


Figure 50. Plexiglas mold used for reinforced specimens (all dimensions in mm).

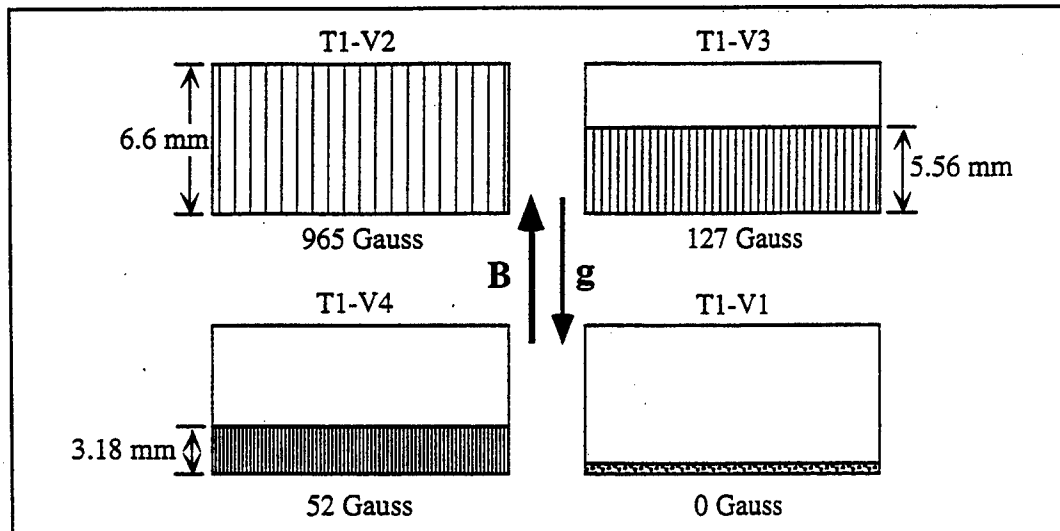


Figure 51. Schematic representation of micrographs M1-M4.

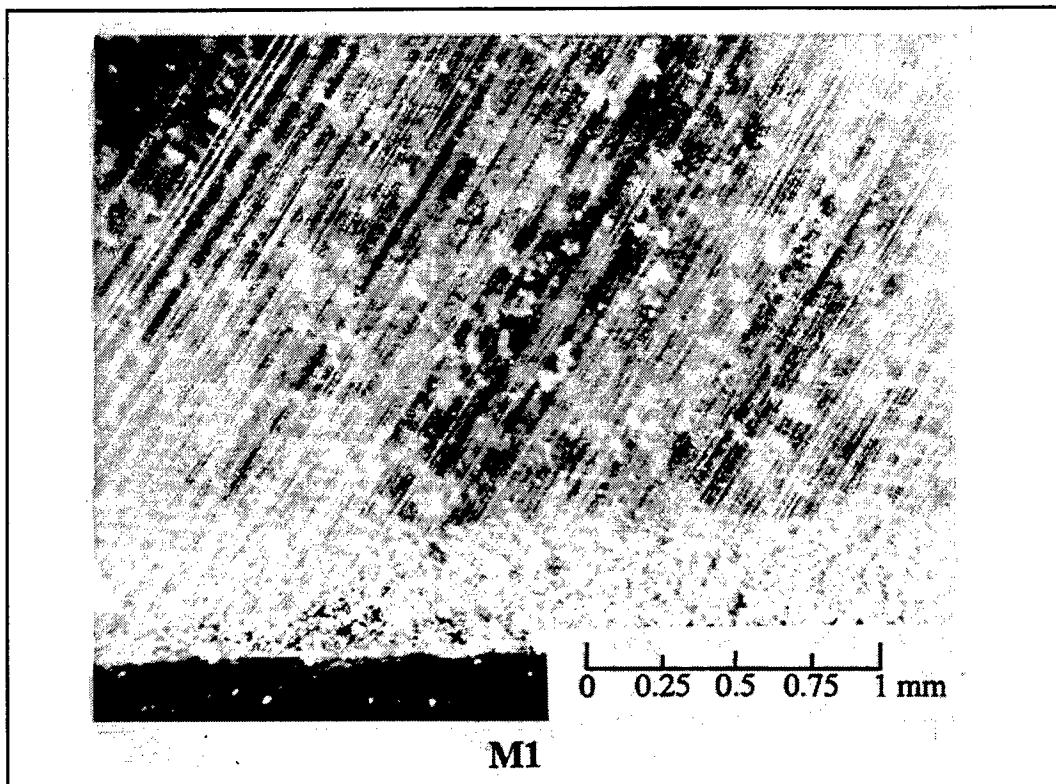


Figure 52. Terfenol-D "chaining" observed in a vinyl-ester polymer (no magnetic field, 40X).

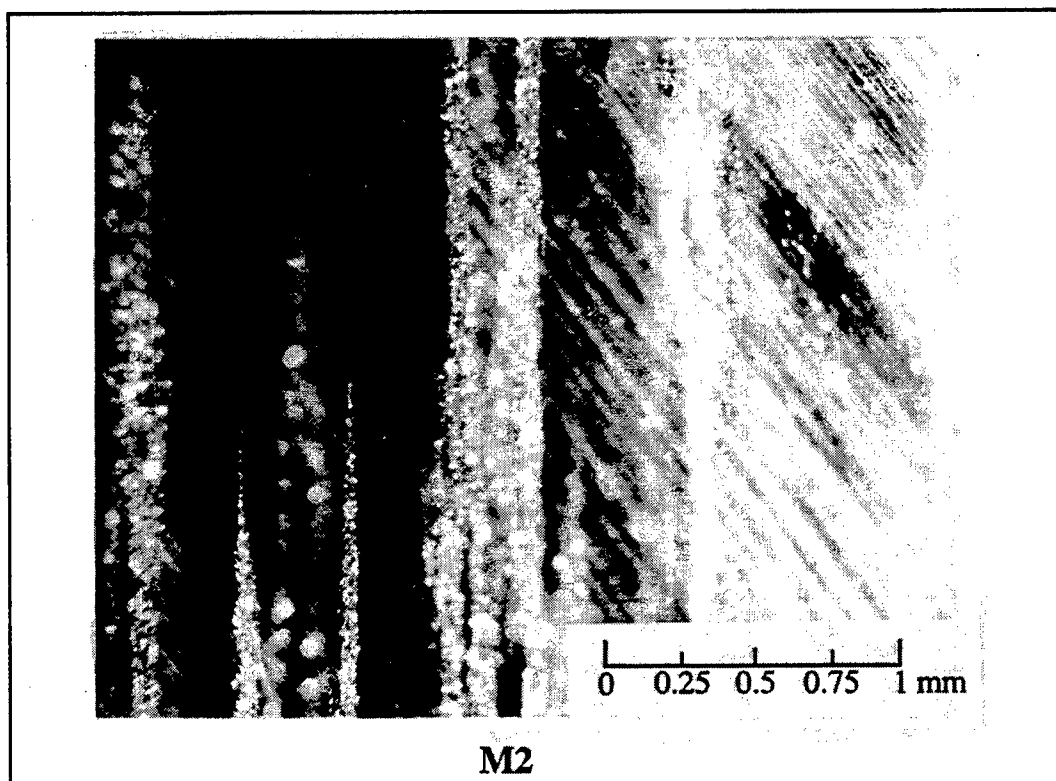


Figure 53. Significant terfenol-D "chaining" observed in a vinyl-ester polymer (965 Gauss magnetic field, 40X).

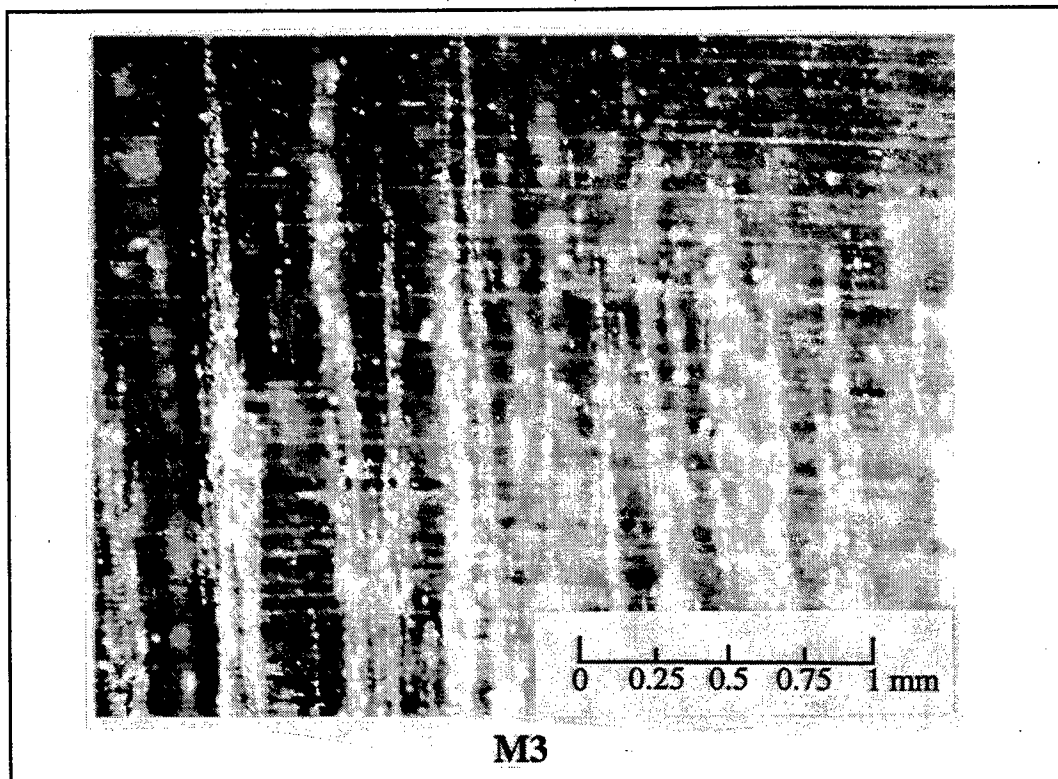


Figure 54. Terfenol-D "chaining" observed in a vinyl-ester polymer (127 Gauss magnetic field, 40X).

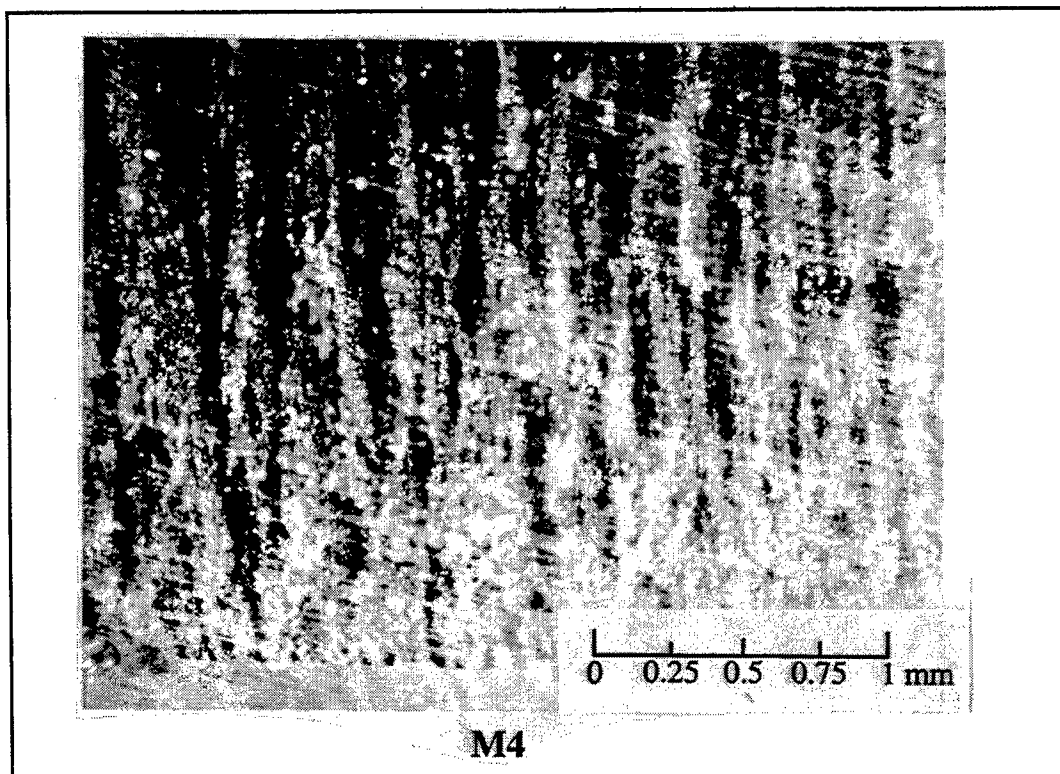


Figure 55. Sparse terfenol-D "chaining" observed in a vinyl-ester polymer (52 Gauss magnetic field, 40X).

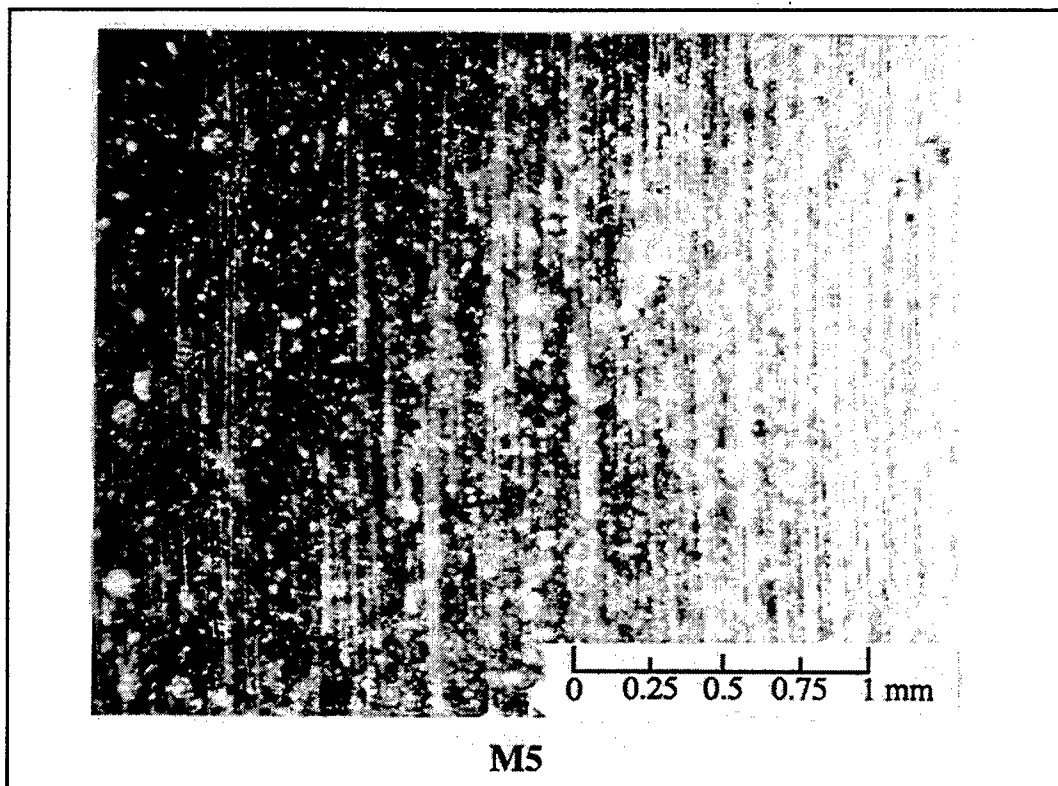


Figure 56. Uniform terfenol-D distribution is achieved by adding the particles to a partially gelled vinyl-ester polymer (no magnetic field, 40X).

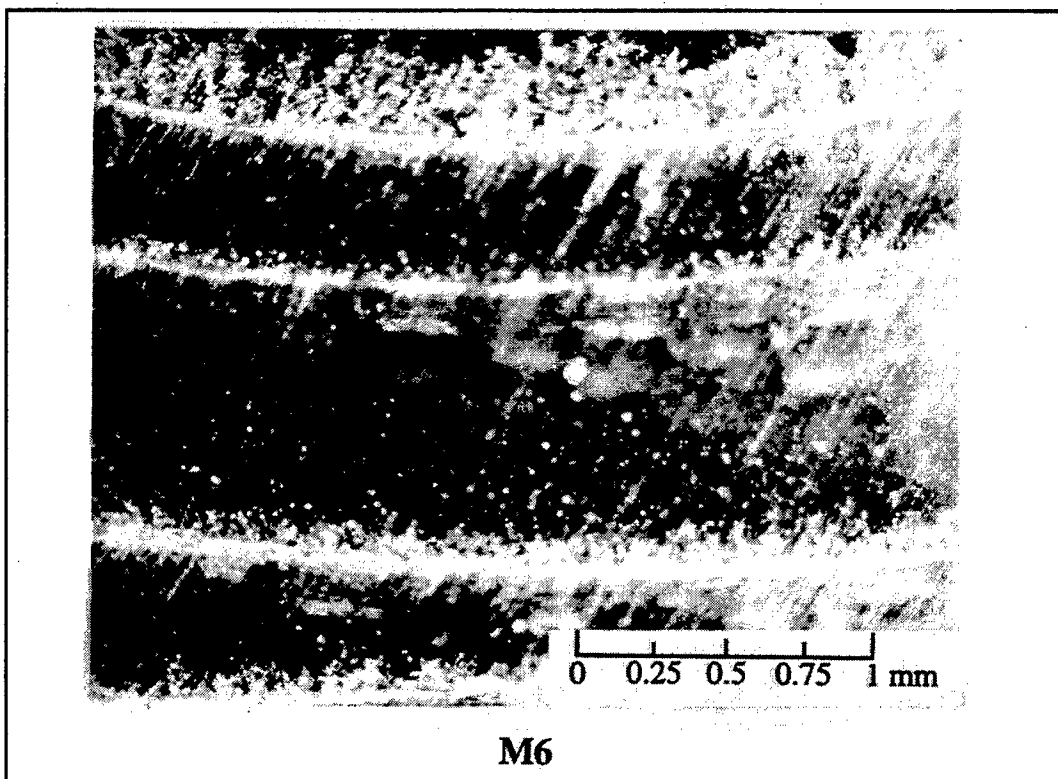


Figure 57. Terfenol-D particles settling in a glass/vinyl-ester composite (no magnetic field, 40X).

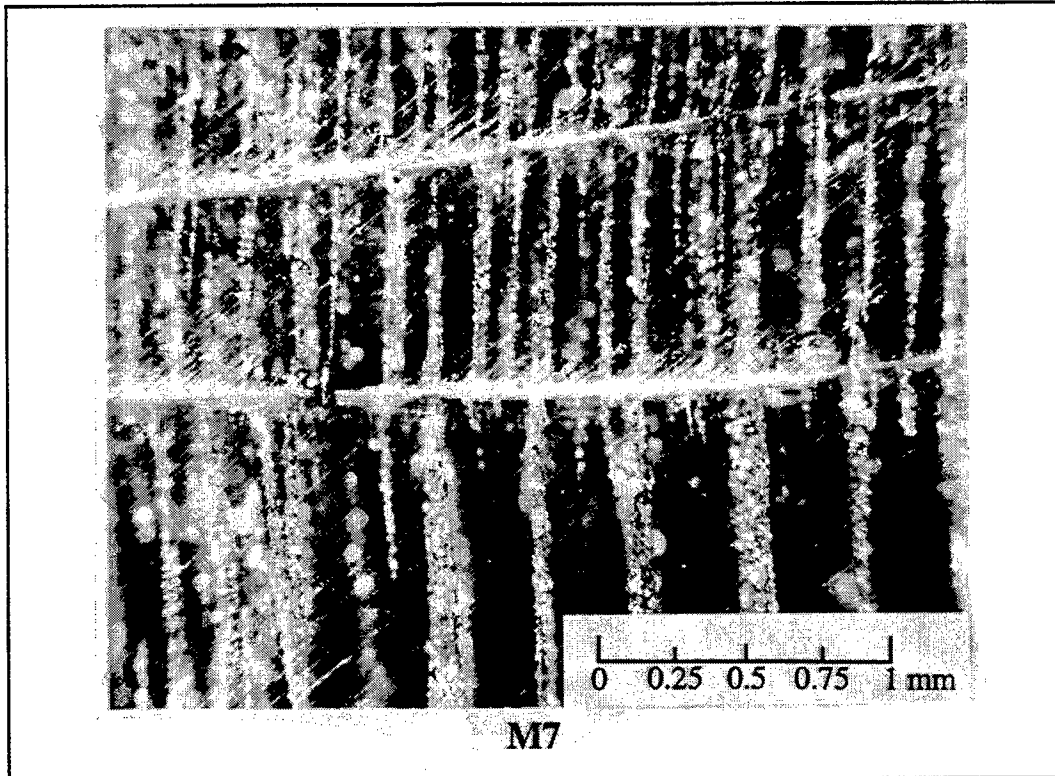


Figure 58. Significant terfenol-D "chaining" observed in a glass/vinyl-ester composite (965 Gauss magnetic field, 40X).

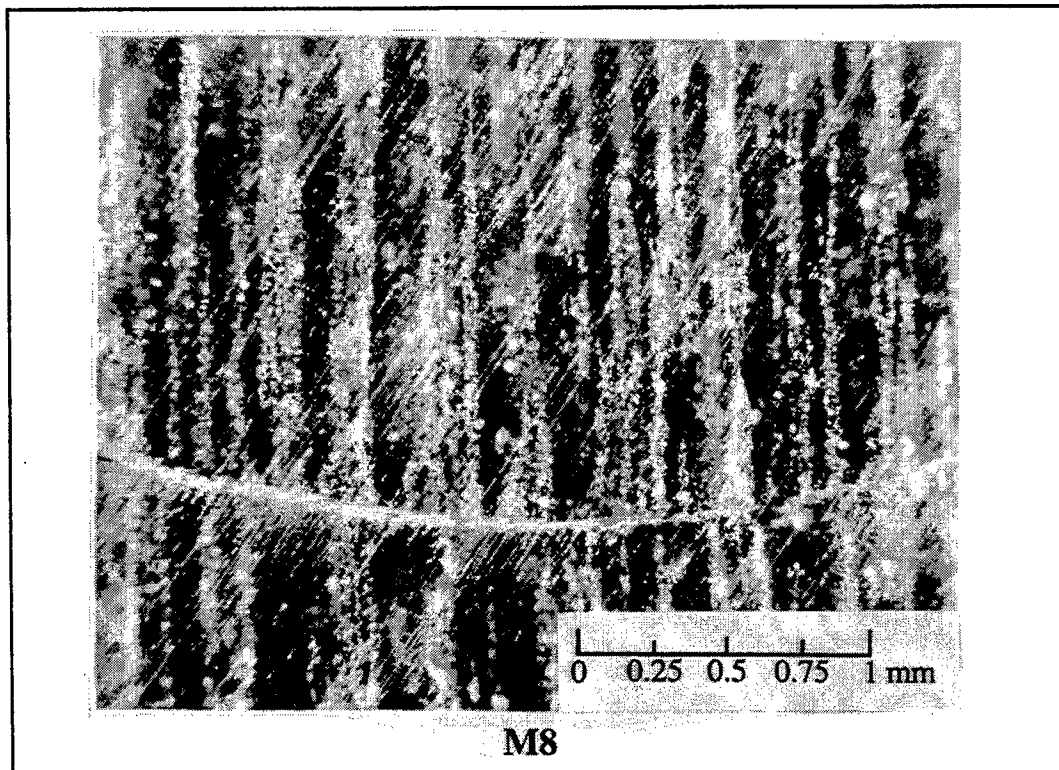


Figure 59. Terfenol-D "chaining" observed in a glass/vinyl-ester composite (127 Gauss magnetic field, 40X).

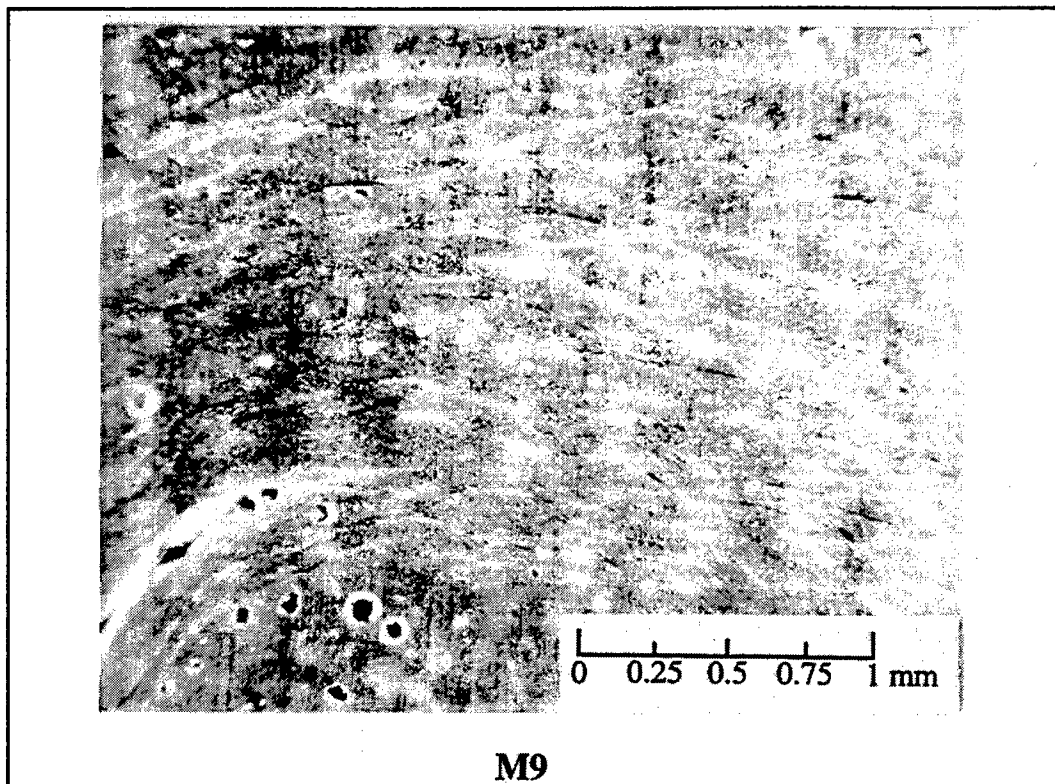


Figure 60. Processing issues affect terfenol-D distribution in a partially gelled (6 minute gel time) glass/vinyl-ester composite (no magnetic field, 40X).

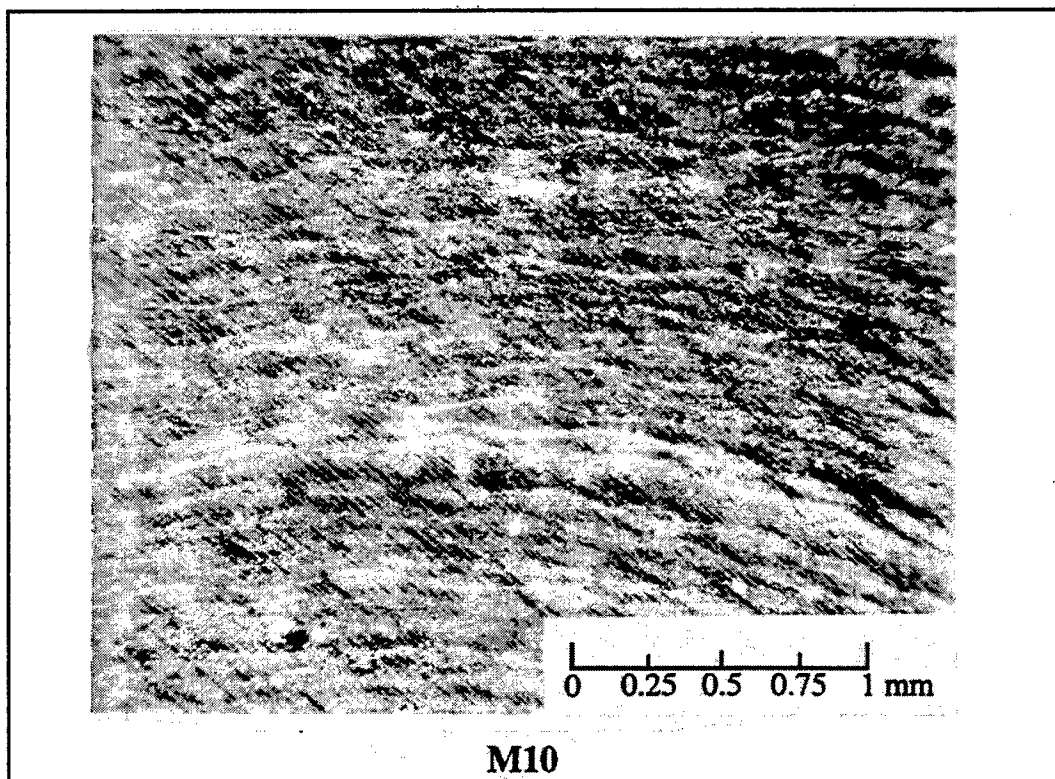


Figure 61. Uniform terfenol-D distribution is achieved by adding the particles to a partially gelled (15 minute gel time) glass/vinyl-ester composite (no magnetic field, 40X).

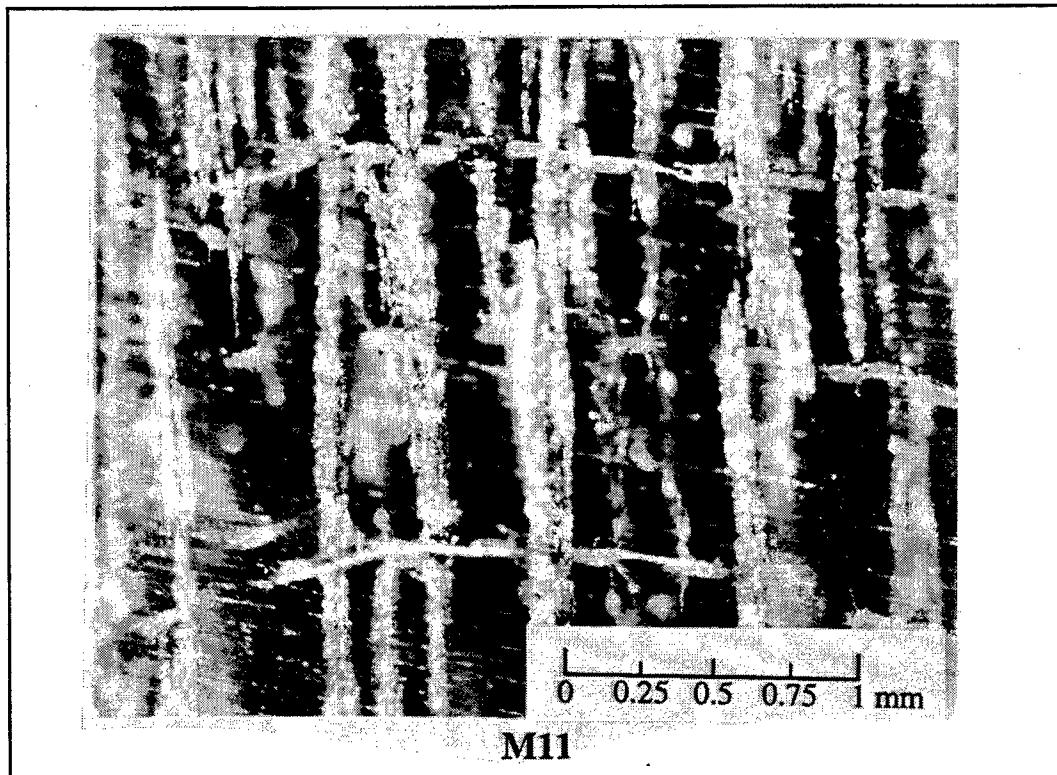


Figure 62. Terfenol-D "chaining" observed in a glass/vinyl-ester composite (965 Gauss magnetic field, 40X).

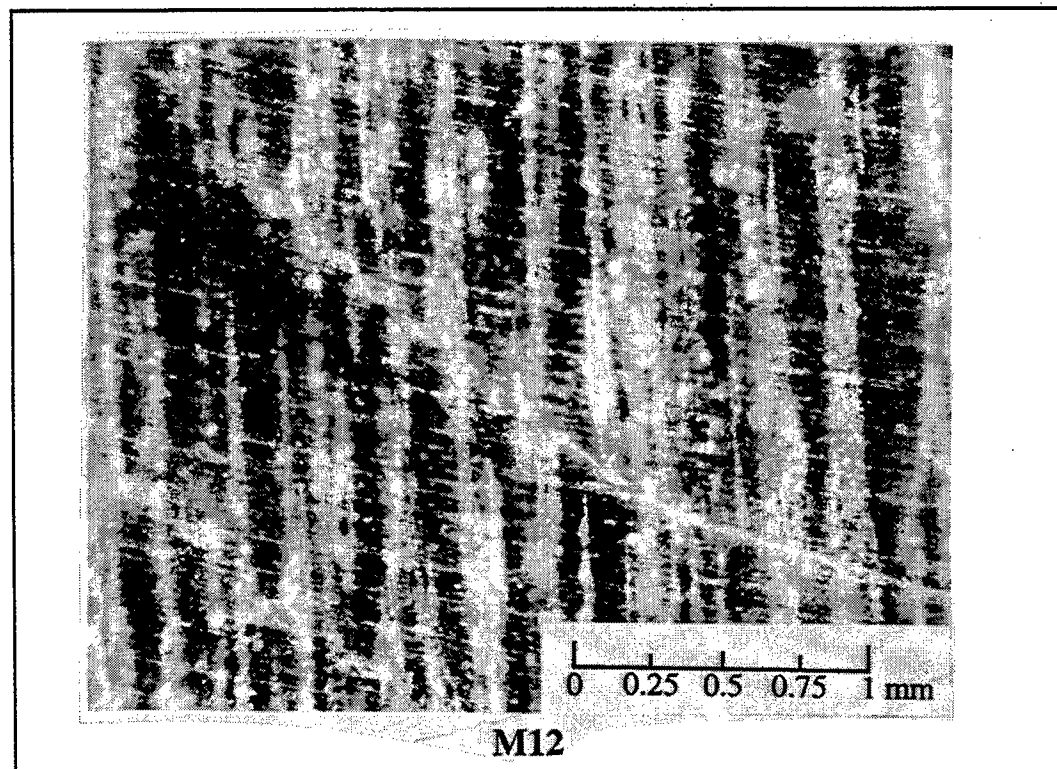


Figure 63. Terfenol-D "chaining" observed in a glass/vinyl-ester composite (127 Gauss magnetic field, 40X).

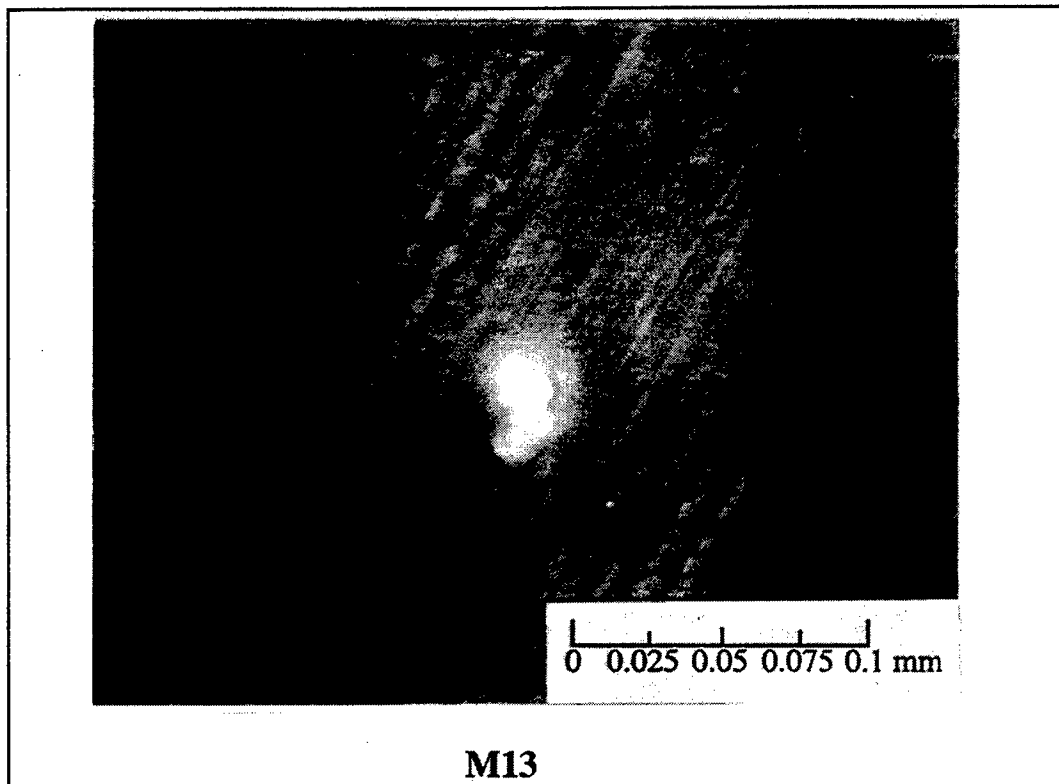


Figure 64. Single terfenol-D particle (<45mm) embedded in a glass/vinyl-ester composite (the absence of radial cracks or debonds shows that a good interface has developed between tag and polymer, 400X).

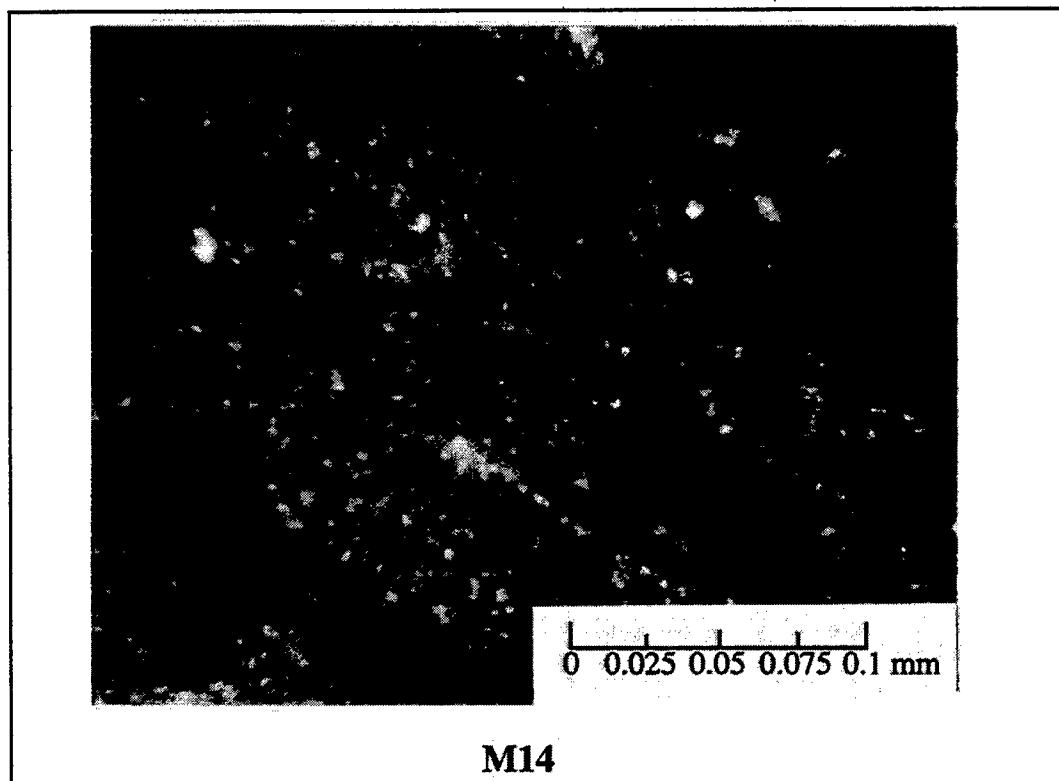


Figure 65. Terfenol-D particles (<100mm) interacting with glass fibers in a glass/vinyl-ester composite (400X).

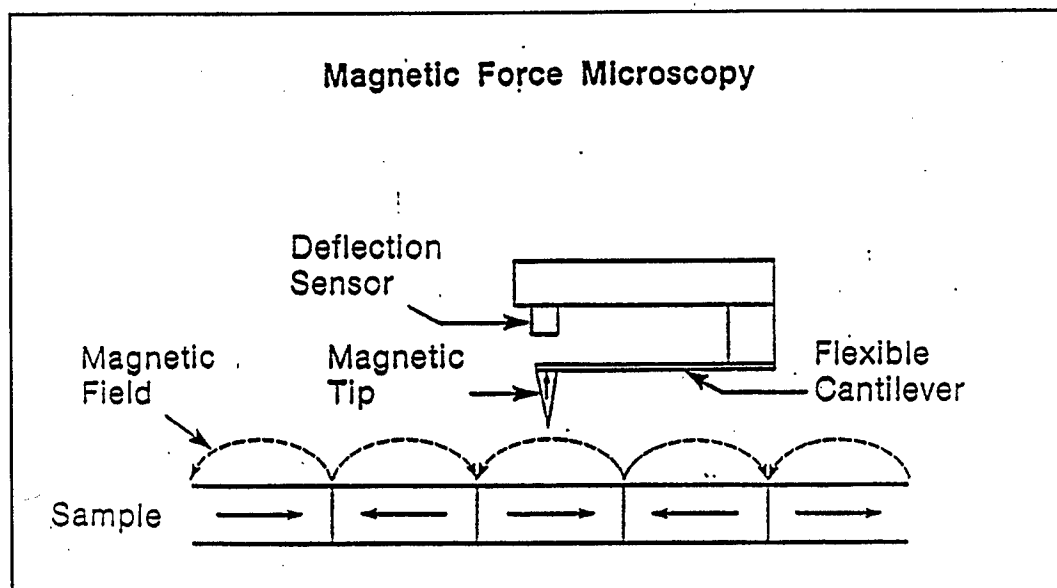


Figure 66. Principles of Magnetic Force Microscopy (MFM).

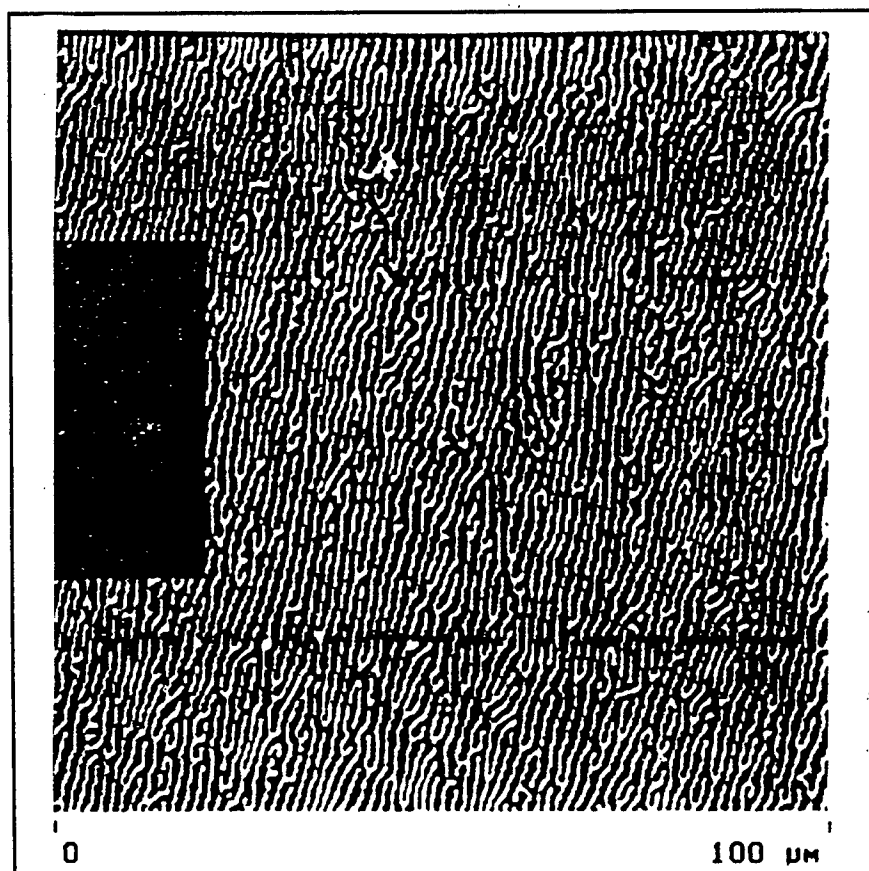


Figure 67. MFM image showing the domain structure of a 0.8 μ thick amorphous terfenol-D film grown on Si/SiO₂ (Su et al., 1995).

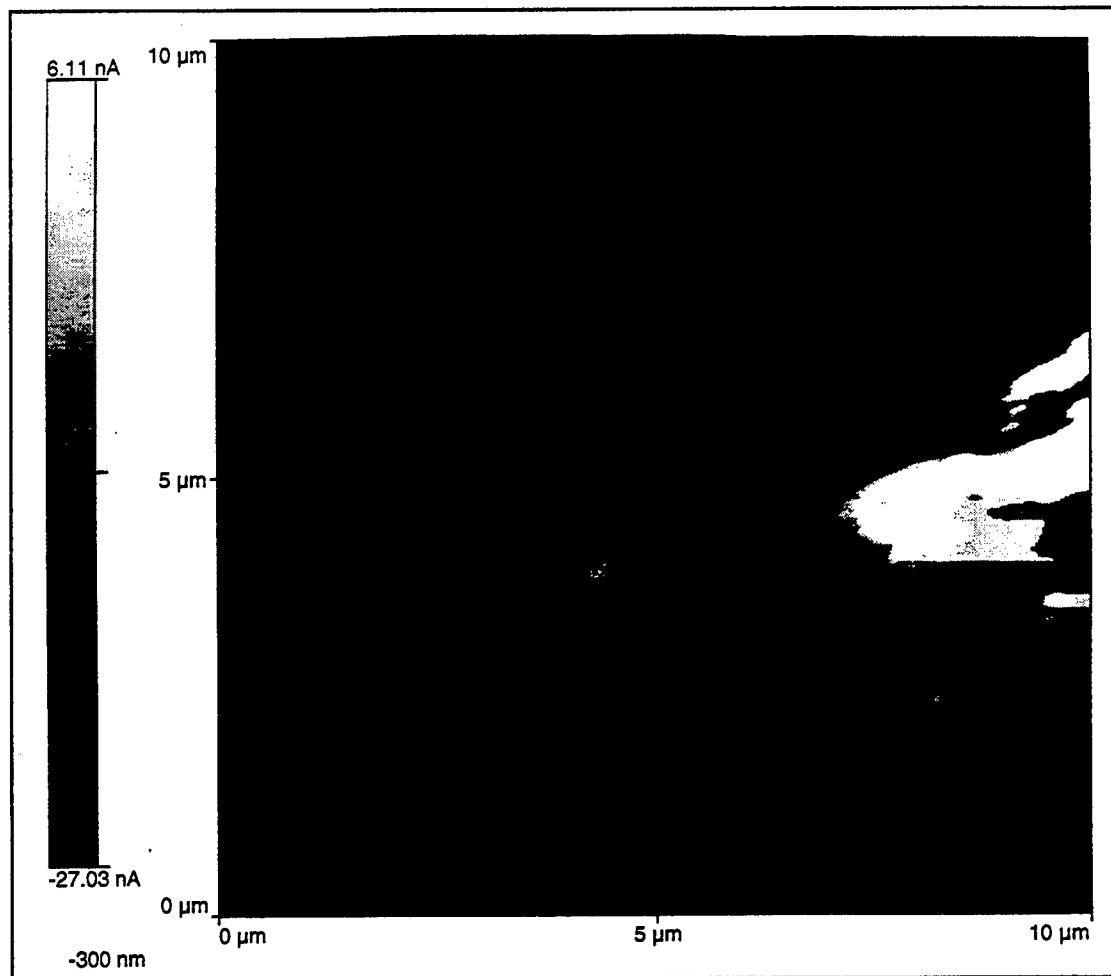


Figure 68. MFM image of a specimen cured under 52 Gauss field in a direction perpendicular to the image. No postcure field was applied to the specimen. The terfenol particle appears as a white region in the middle-right portion of the image. No magnetic domain features can be detected.

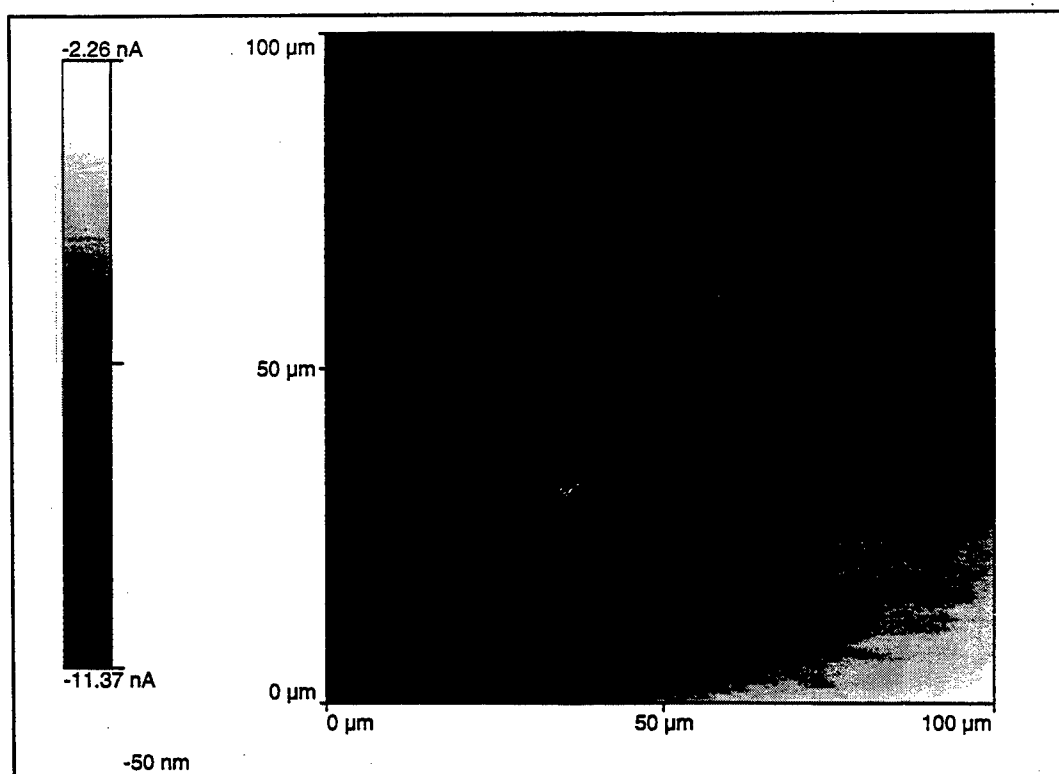


Figure 69. MFM image of a specimen cured under 965 Gauss field in a direction perpendicular to the image. No postcure field was applied to the specimen. The terfenol particle extends from the lower-right corner to about half way across the diagonal of the image. Some magnetic domain features are detectable with a gradual shading across the particle and faint lines radiating out from the lower-right corner.

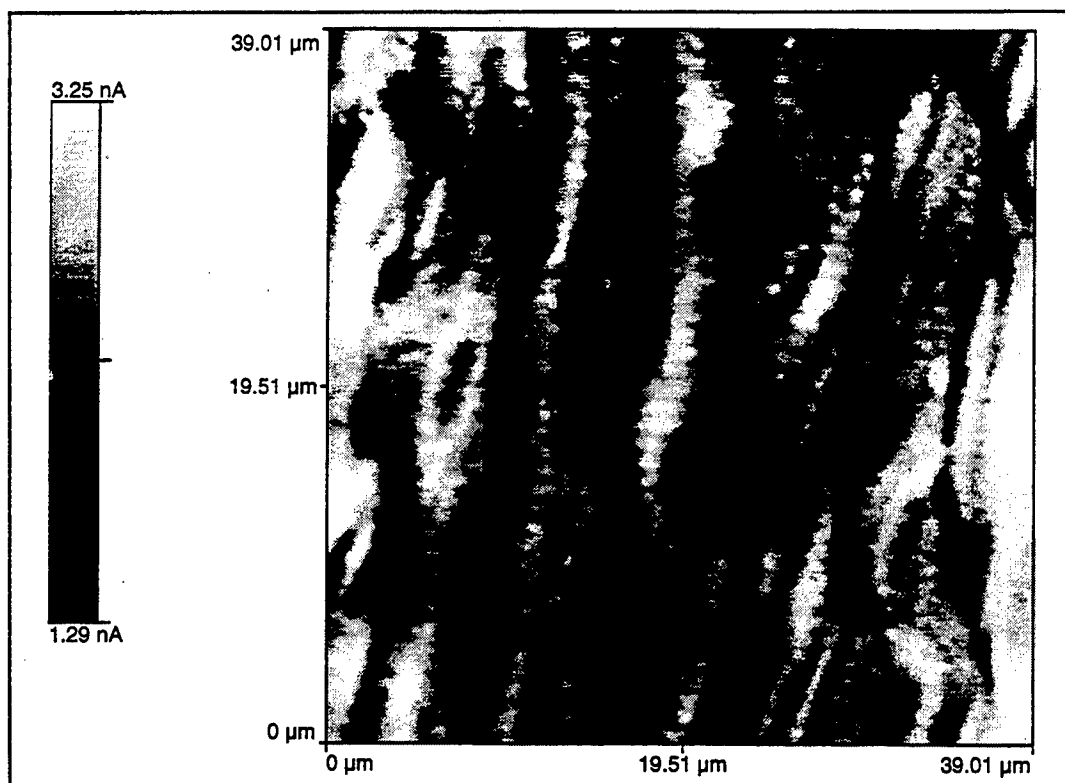


Figure 70. MFM image of a specimen cured under 52 Gauss field in a direction perpendicular to the image. A postcure field of 1307 Gauss was applied to the specimen for 30 minutes, again in a direction perpendicular to the image. The entire image is the central portion of a terfenol particle. Now distinct magnetic domains are present, primarily in a vertical orientation to the image.

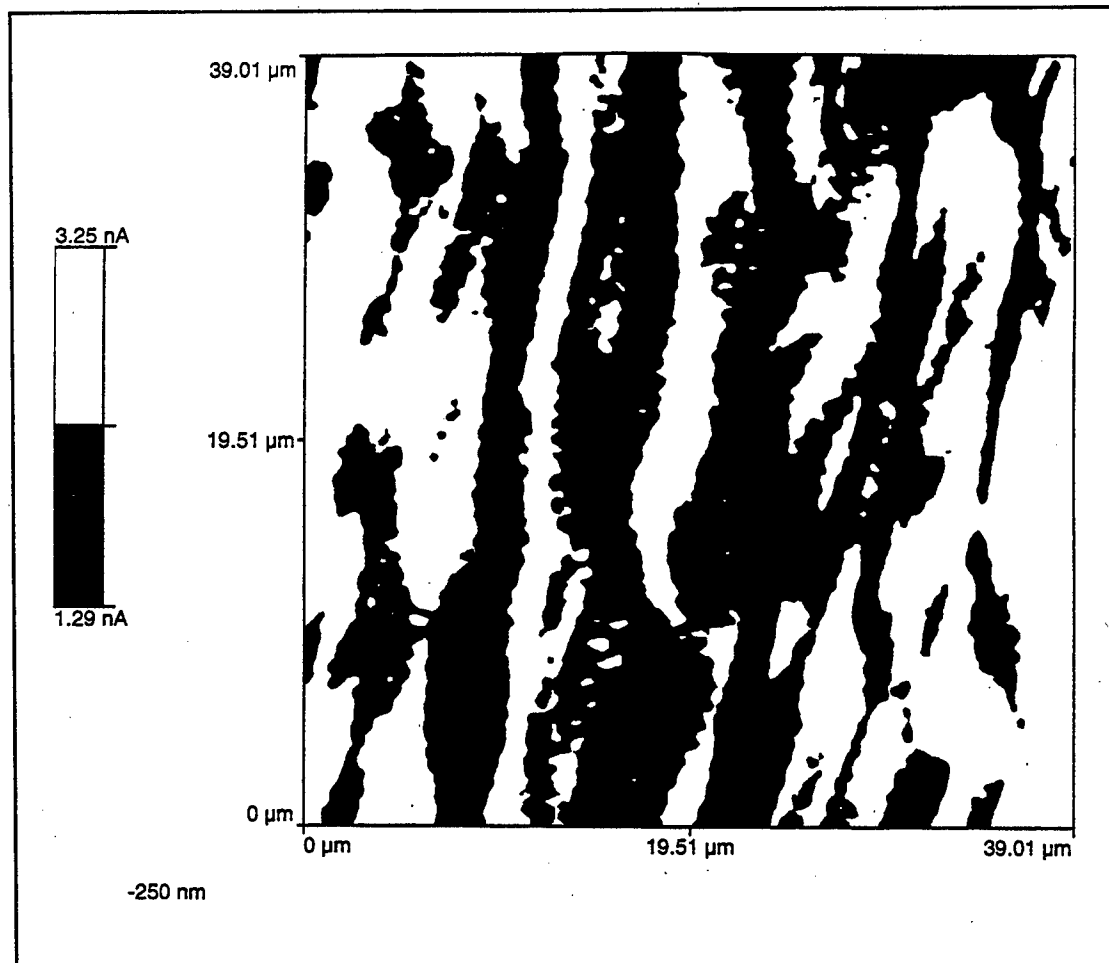


Figure 71. Same as Figure 70 with increased contrast to differentiate the domain walls.

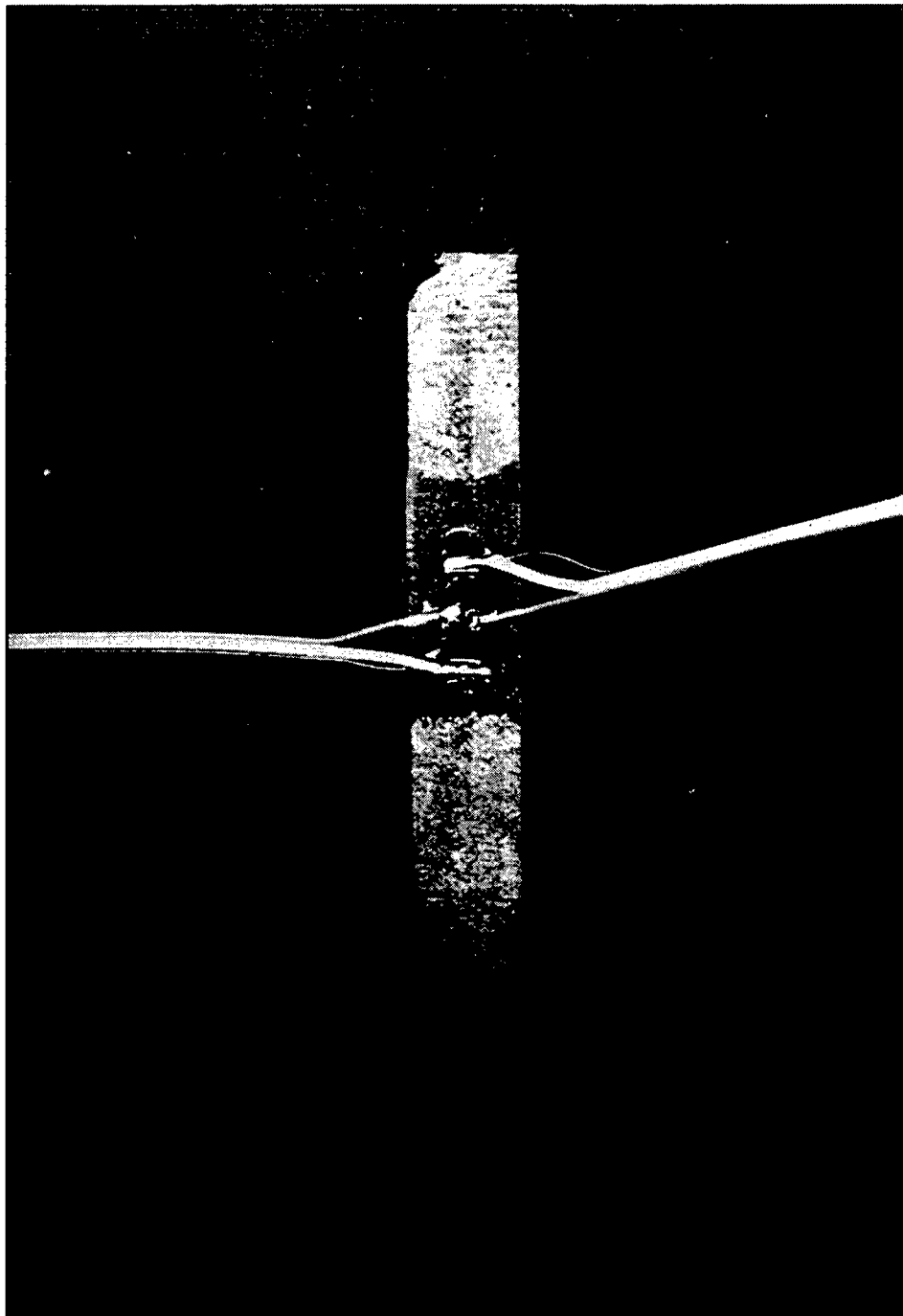


Figure 72. Typical terfenol tagged polyester specimen after strain gaging.

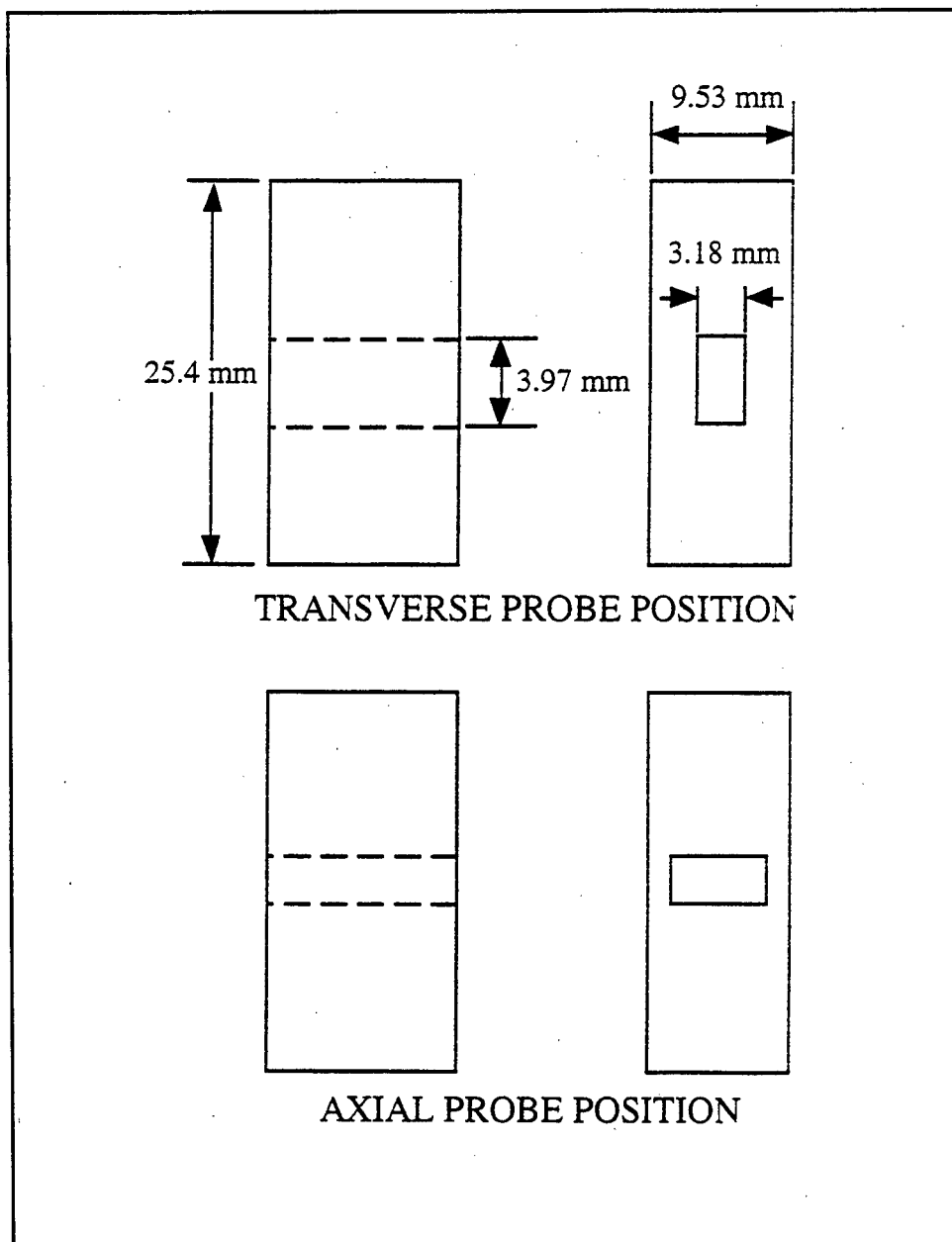


Figure 73. Transverse and axial probe guides.

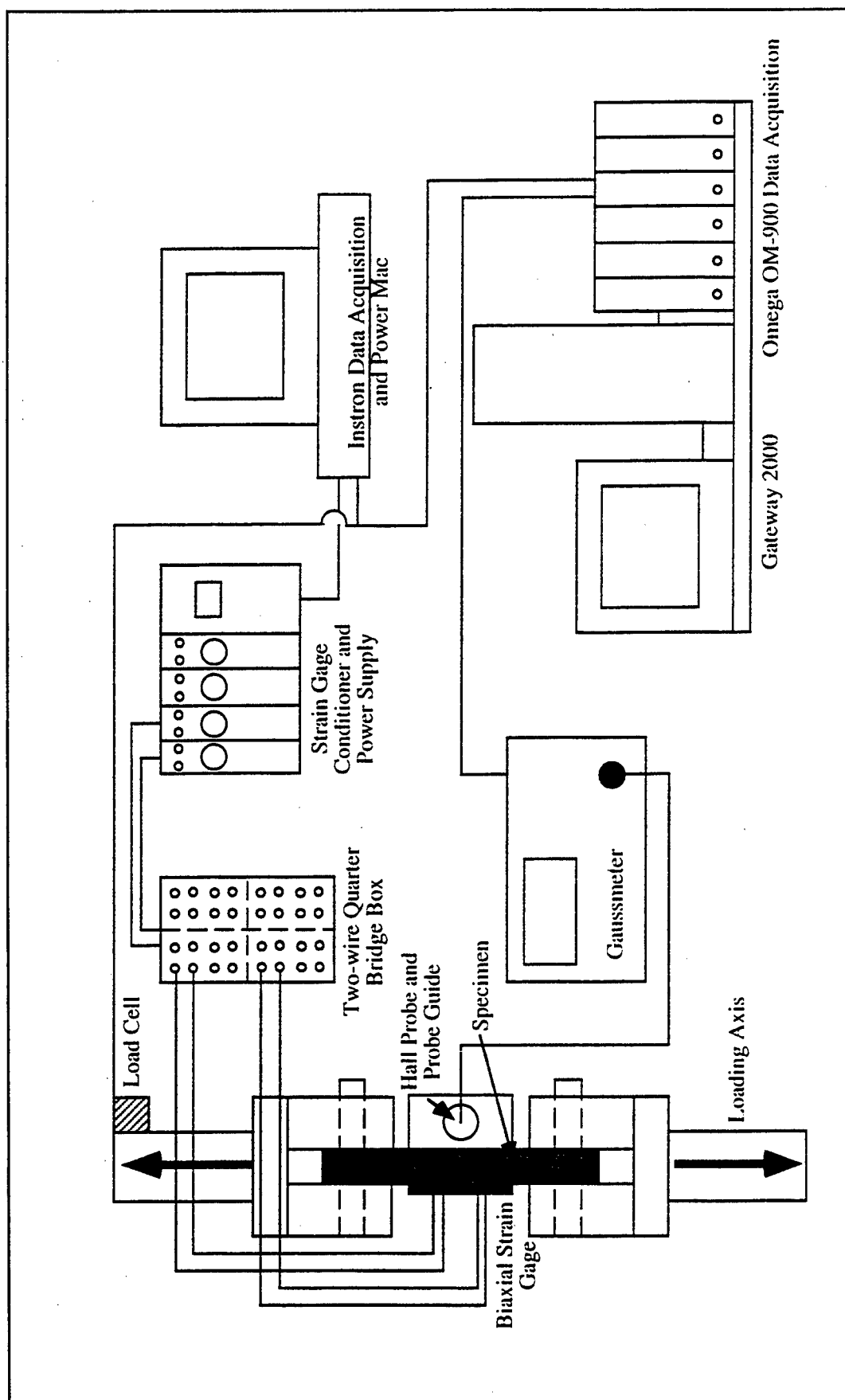


Figure 74. Mechanical loading experimental set-up.

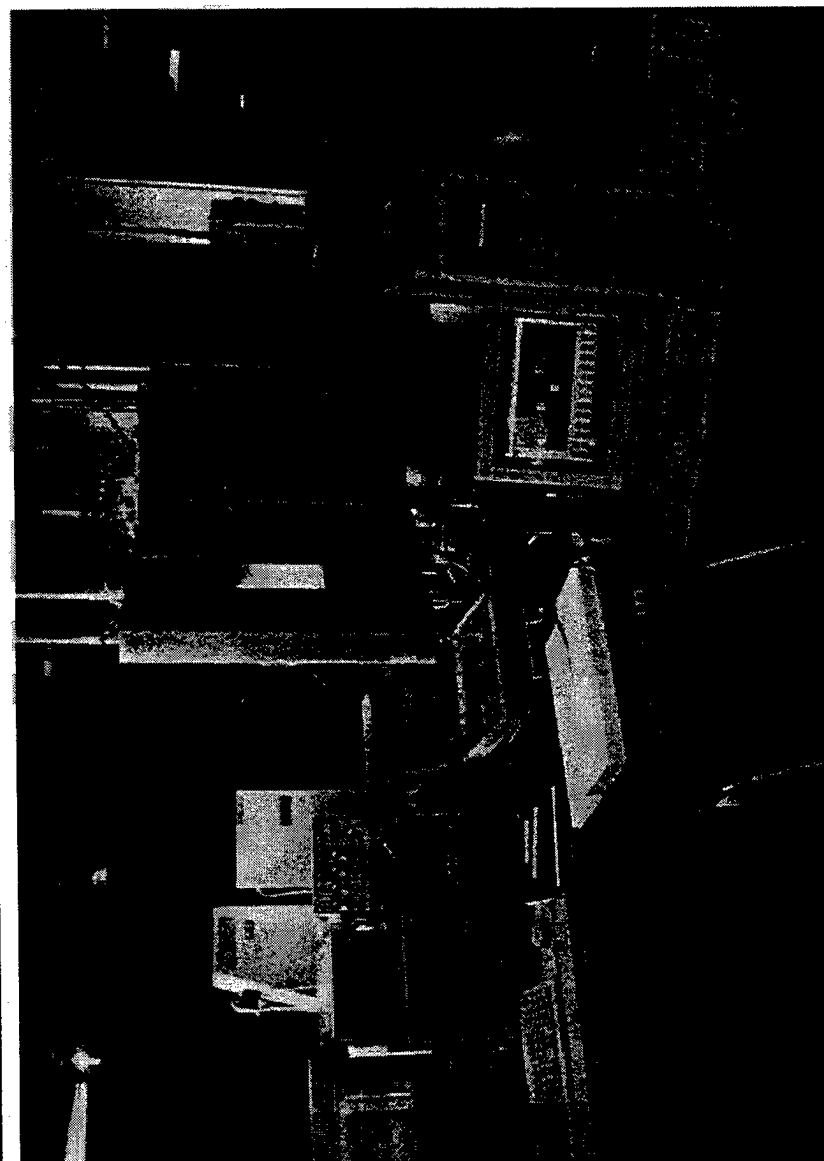


Figure 75. Photograph of mechanical loading experimental set-up.

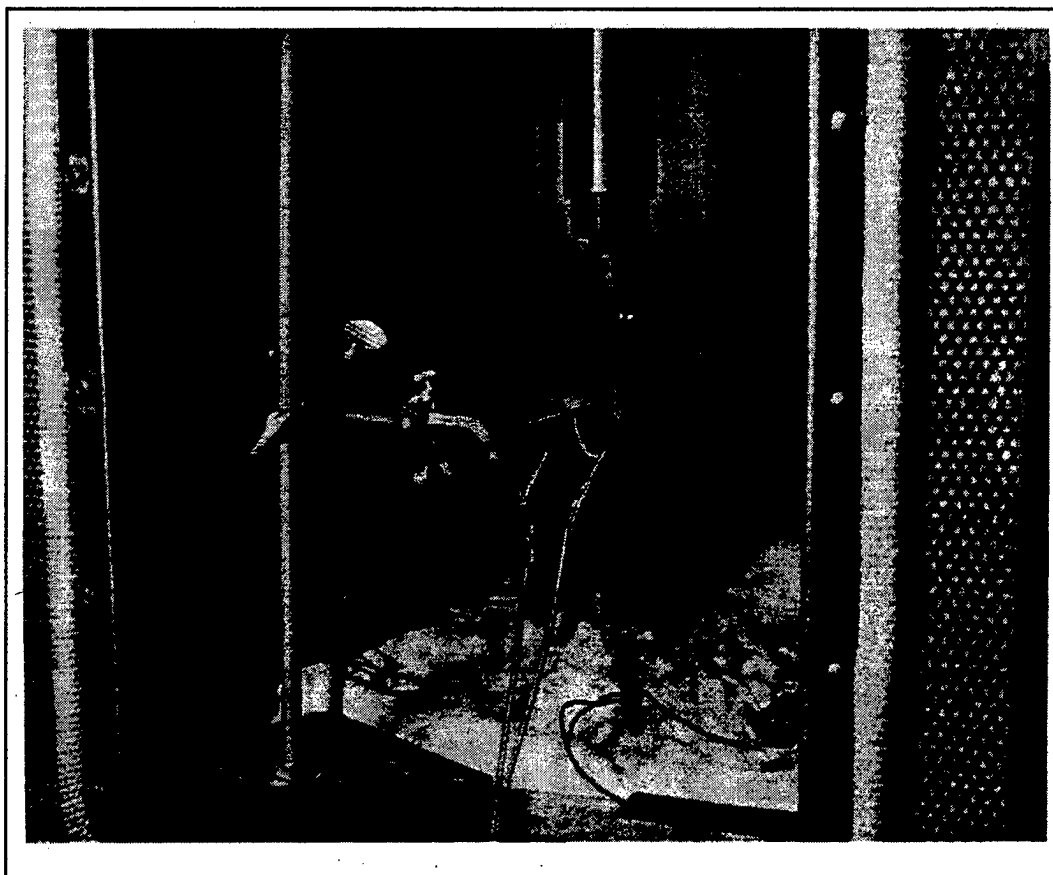


Figure 76. Specimen loaded in mechanical grips at the start of a test. The Gauss probe is supported by a clamp and stand while the tip of the probe is housed in the plexiglas template next to the specimen surface.

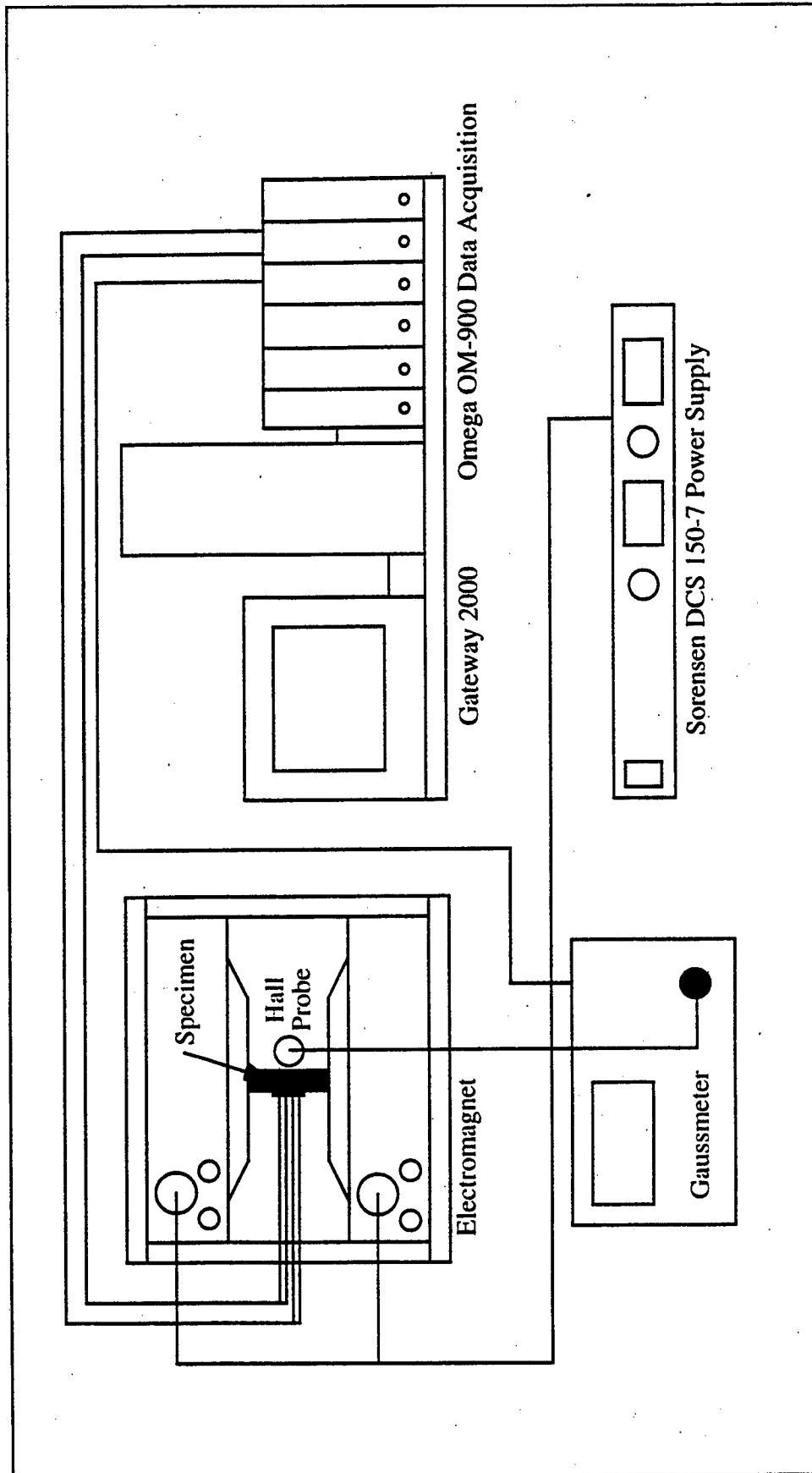


Figure 77. Magnetic field loading experimental test set-up.



Figure 78. Magnetic loading experiment test set-up. Specimen is placed in the central core of the electromagnet and magnetic field lines are oriented along the length of the specimen.

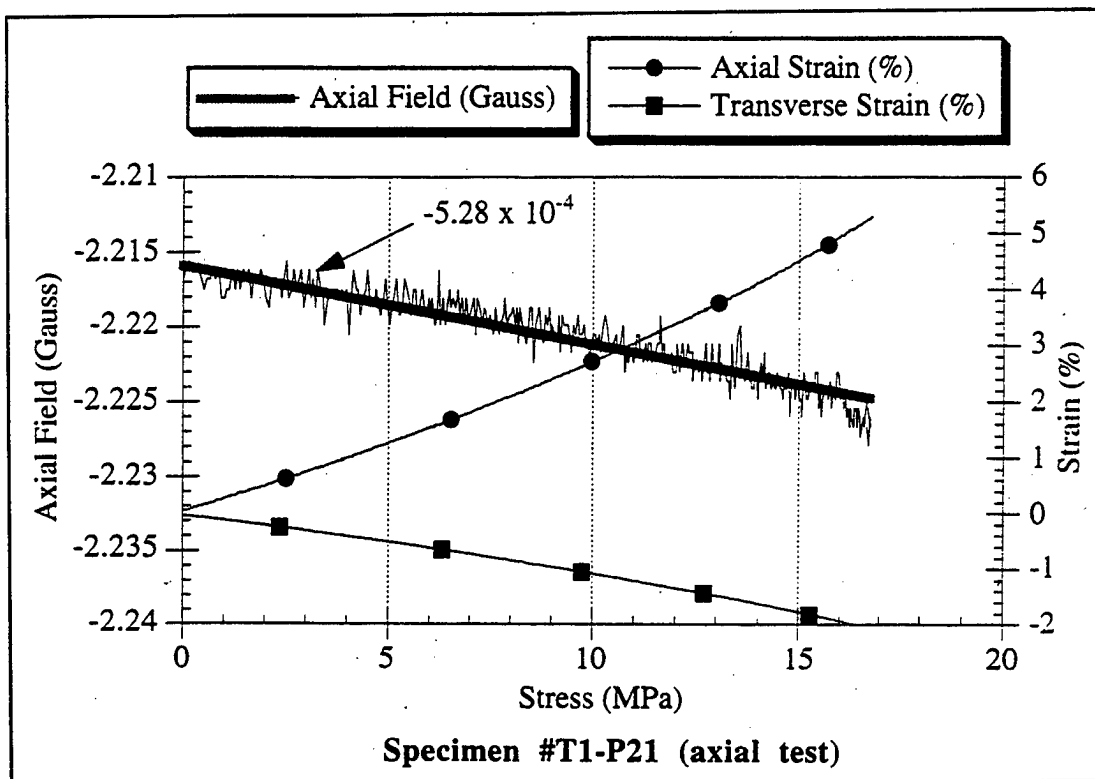


Figure 79. Typical axial field response curve [series D, specimen T1-P21].

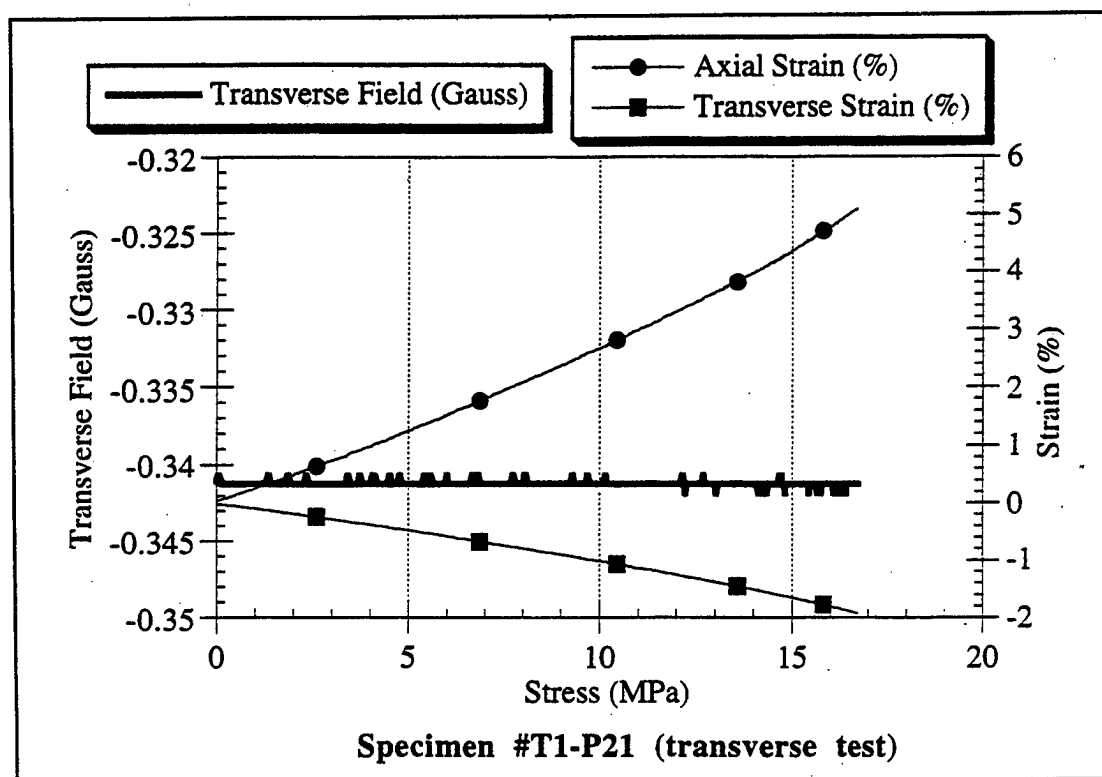


Figure 80. Typical transverse field response curve [series D, specimen T1-P21].

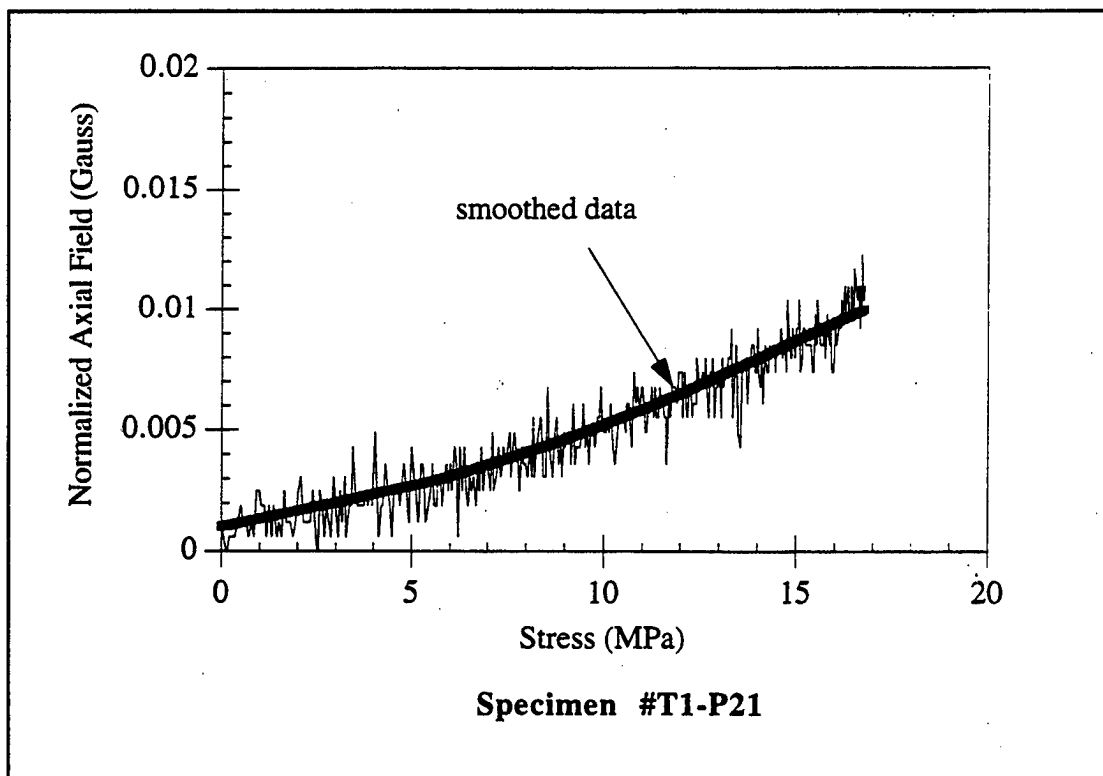


Figure 81. Normalized and smoothed data for specimen T1-P21.

Series	Filler	Matrix	Tag Vol. Fraction	Tag Size (μ)	Magnetic Field (G)
D	terfenol-D	polyester	1	45,75,100	None
F	terfenol-D	polyester	0.5	45,75,100	None
G	terfenol-D	polyester	2	45,75,100	None
H	terfenol-D	polyester	4	45,75,100	None

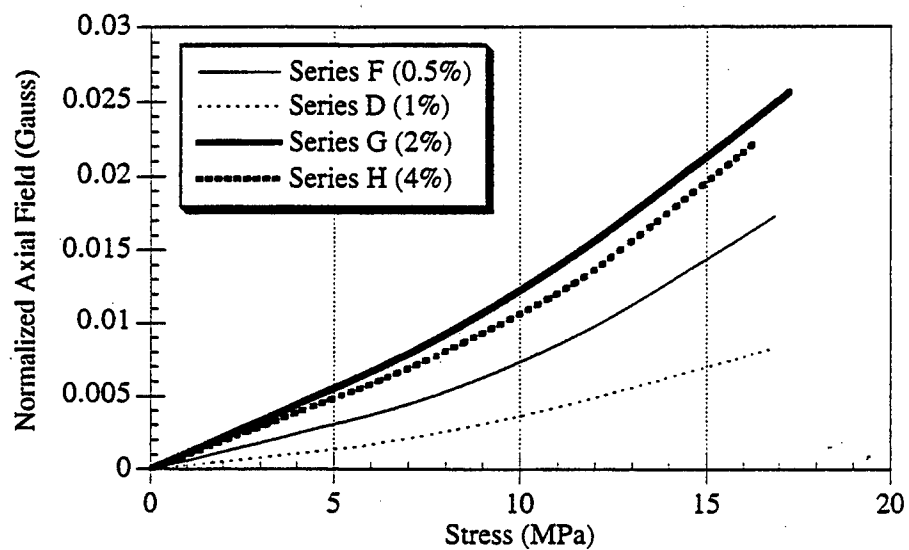


Figure 82. Effect of tag volume fraction on axial response curves.

Series	Filler	Matrix	Tag Vol. Fraction	Tag Size (μ)	Magnetic Field (G)
A	terfenol-D	polyester	1	45	None
B	terfenol-D	polyester	1	75	None
C	terfenol-D	polyester	1	105	None
D	terfenol-D	polyester	1	45, 75, 105	None
E	terfenol-D	polyester	1	45, 75	None

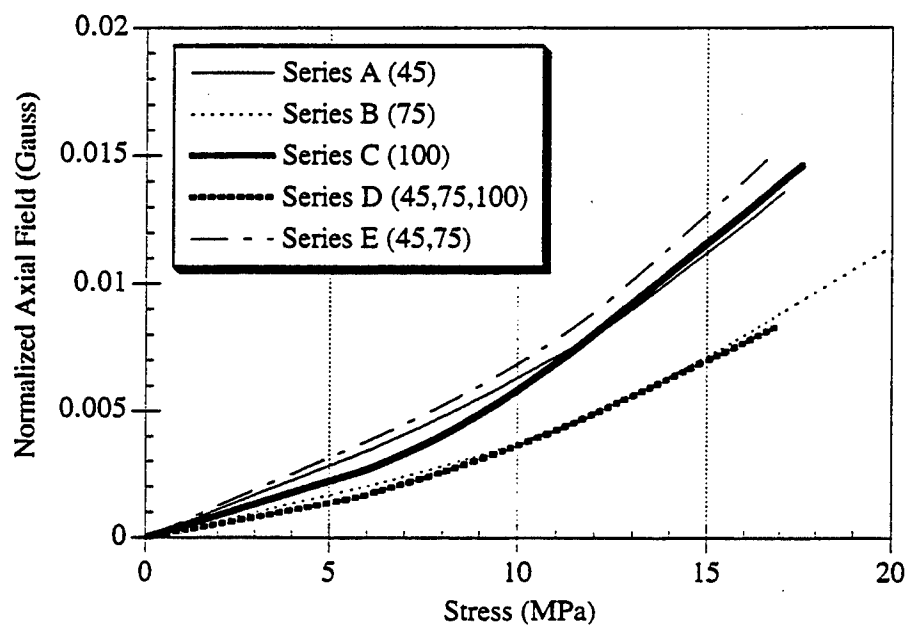


Figure 83. Effect of tag size on axial response curve.

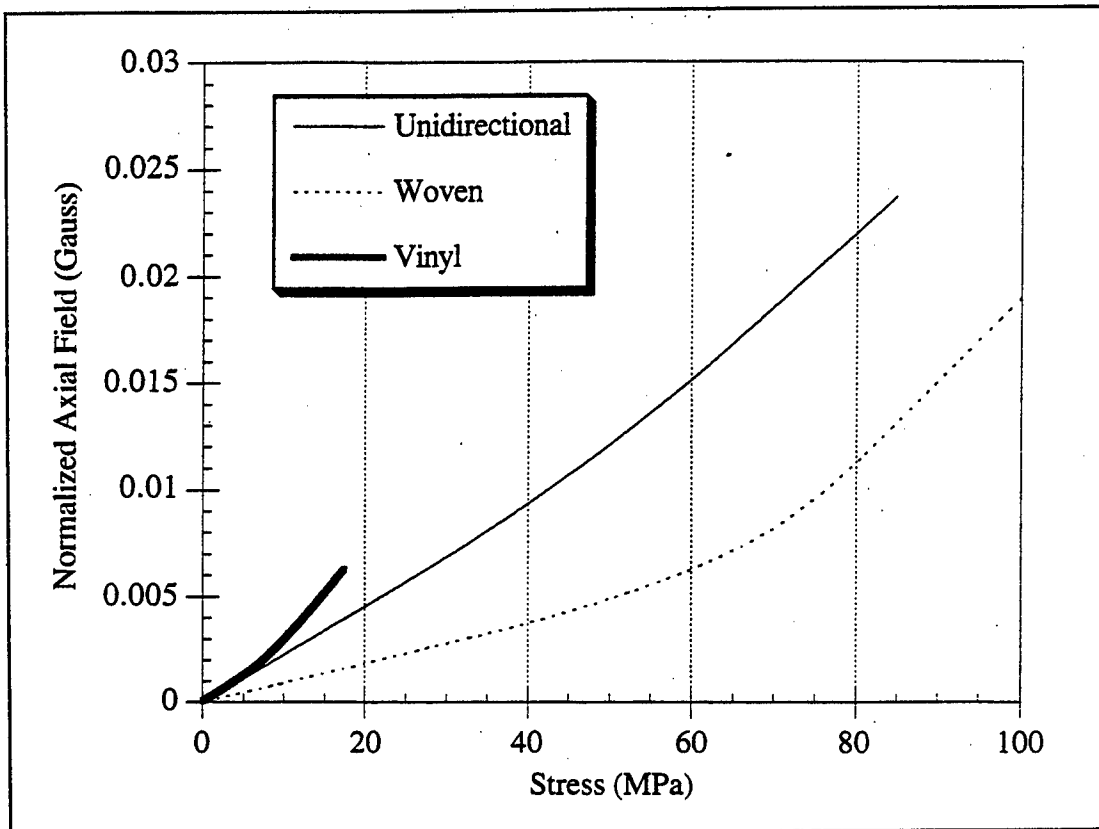


Figure 84. Effect of glass reinforcement on axial response curves.

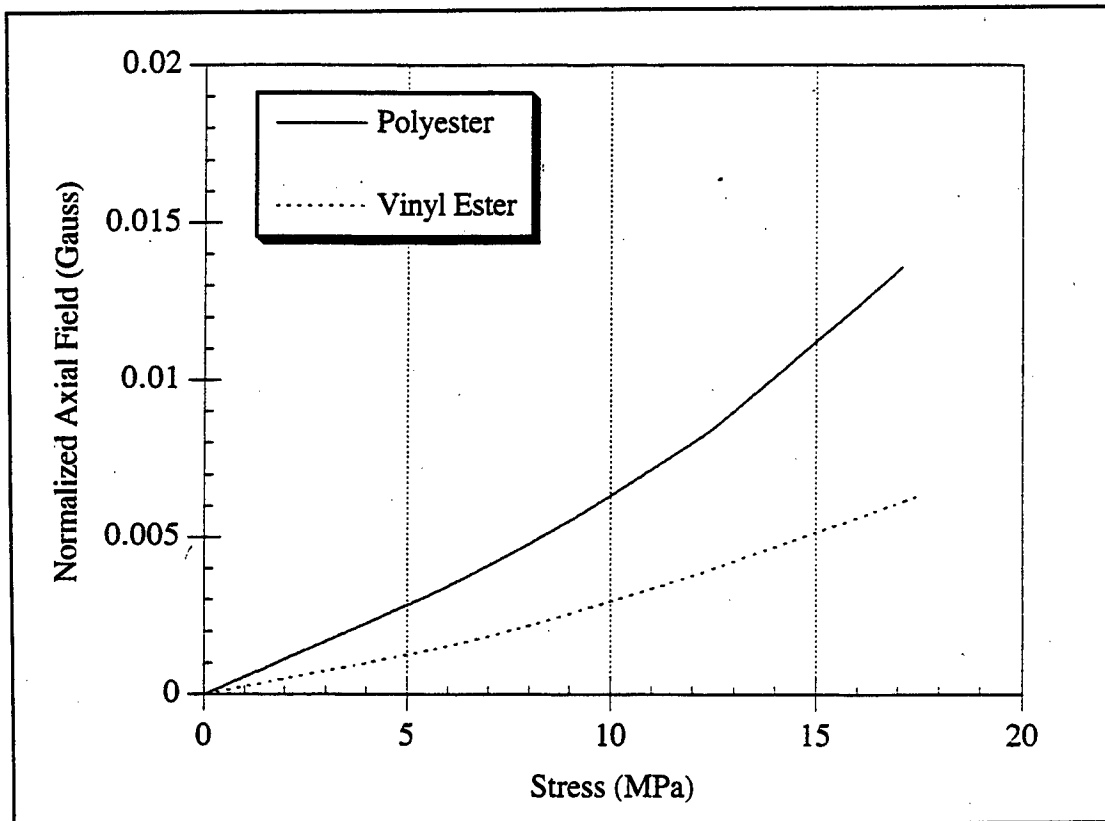


Figure 85. Effect of matrix material on axial response curves.

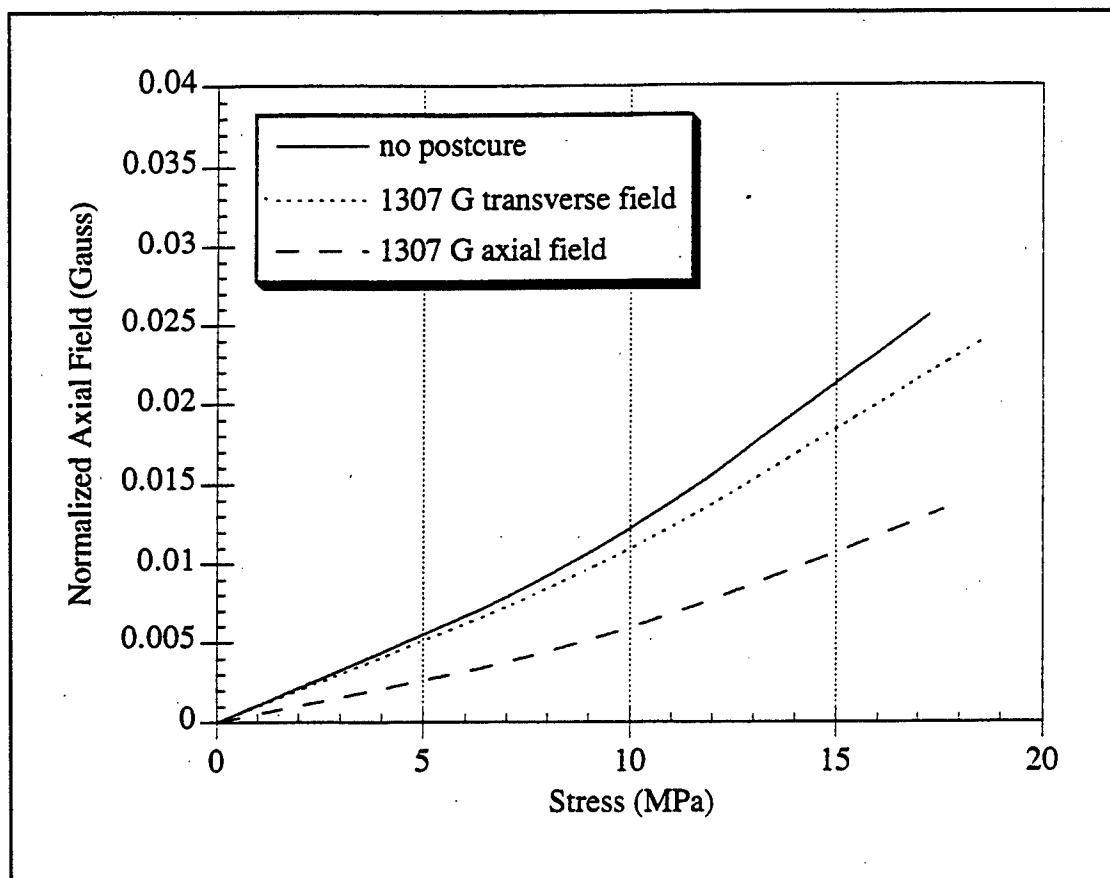


Figure 86. Series G axial field response curves.

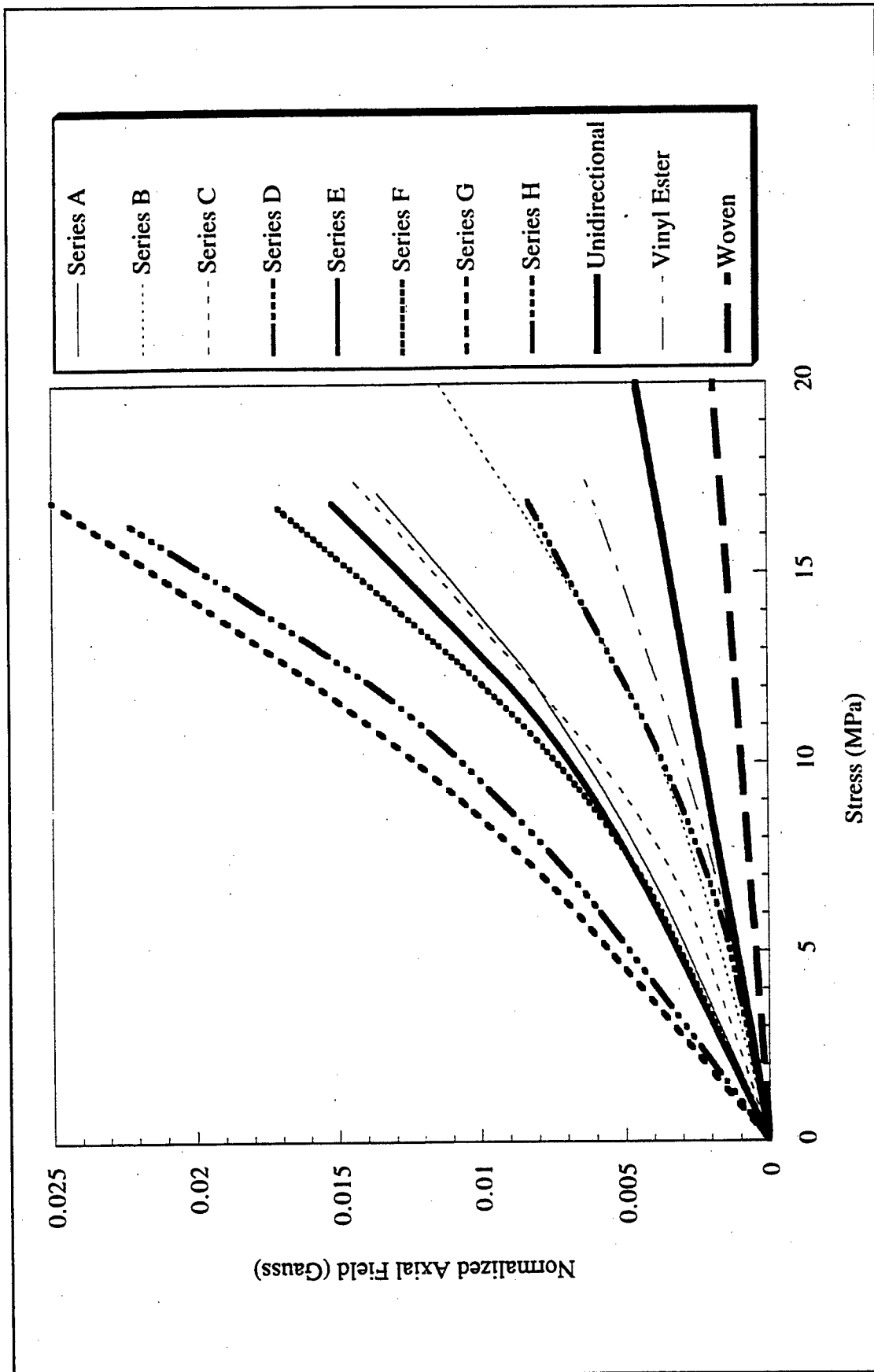


Figure 87. Data summary for mechanical loading studies.

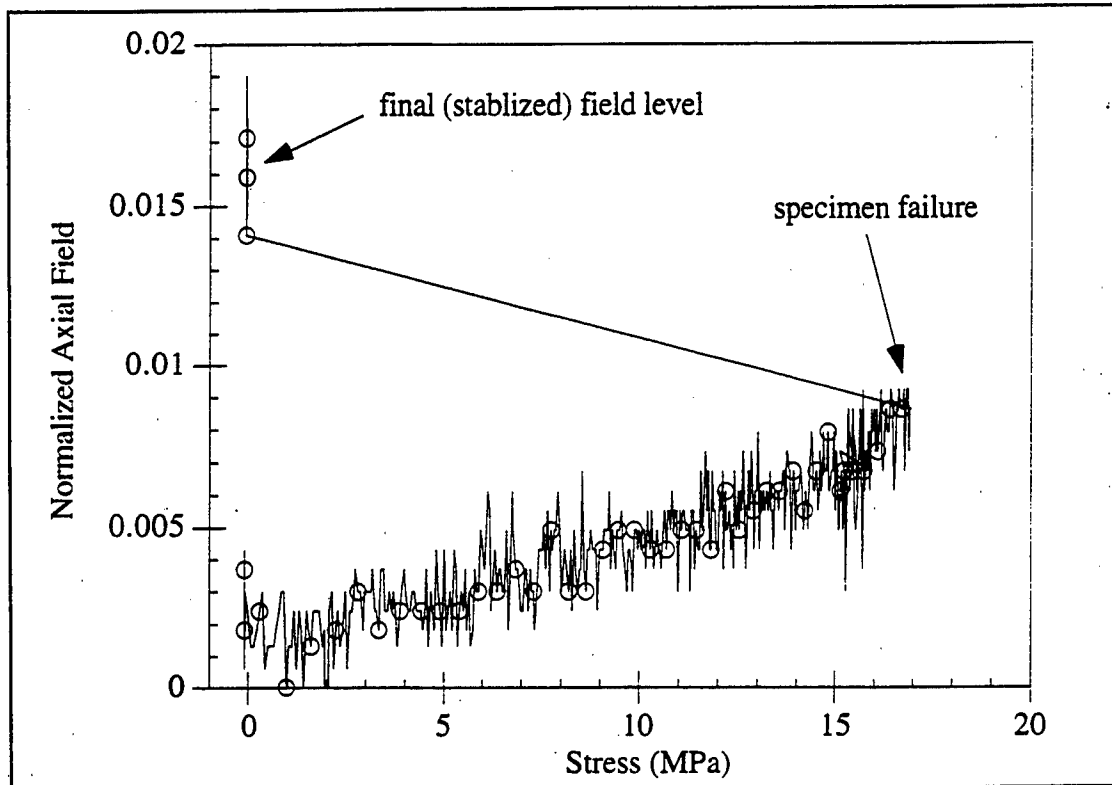


Figure 88. Series B (specimen #T1-P9) showing residual axial field response after specimen failure.

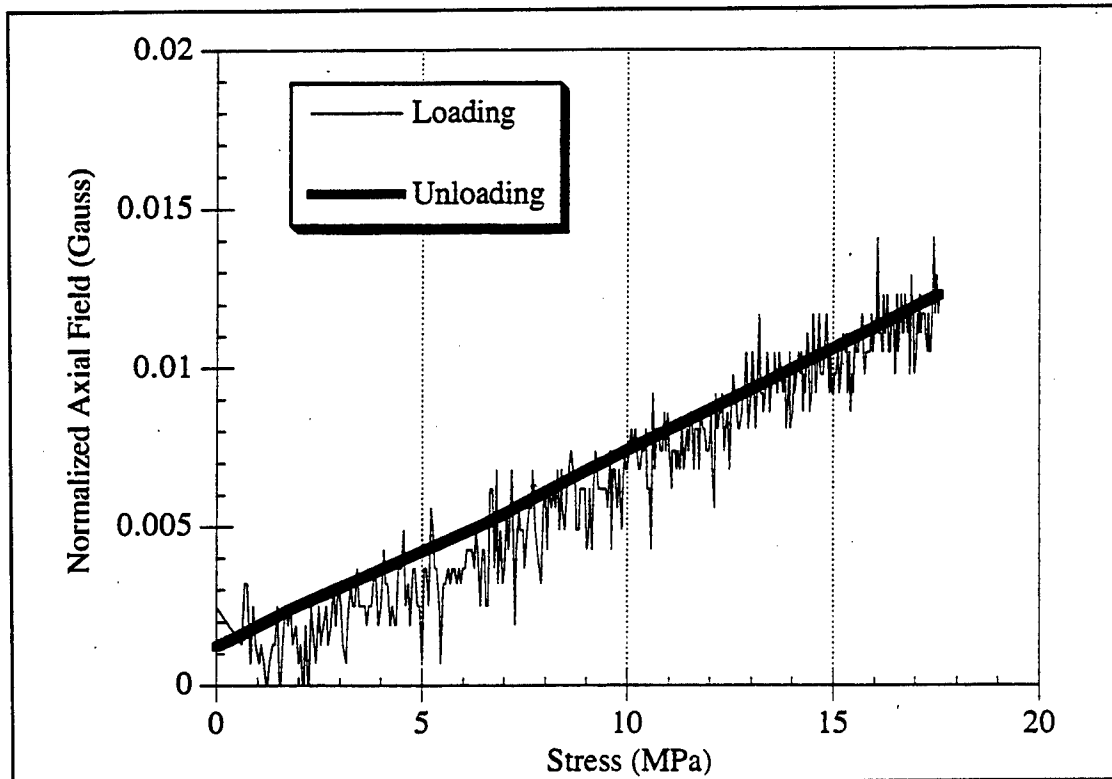


Figure 89. Normal loading-unloading curves showing no residual axial field response [series G, specimen #T1-P16].

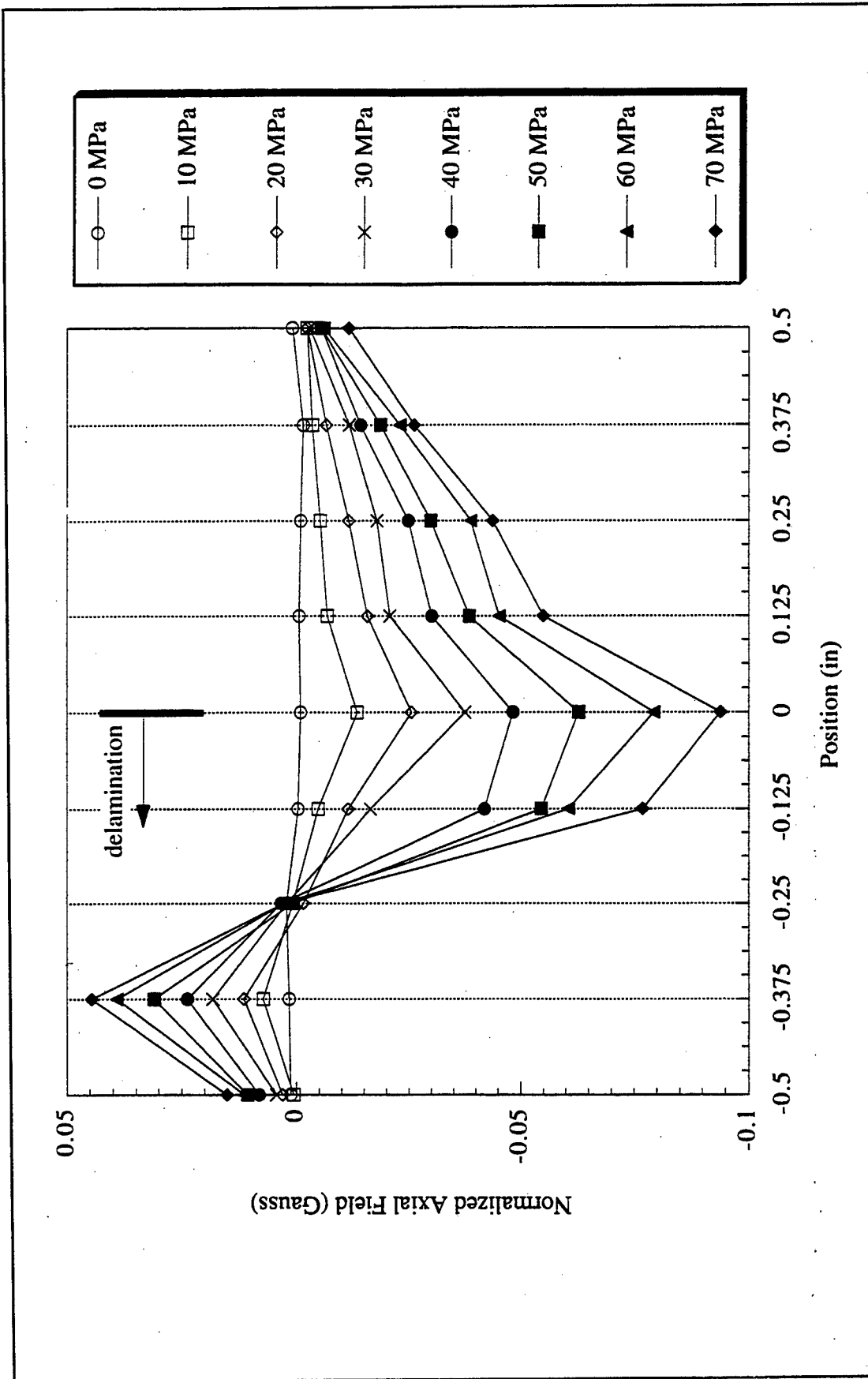


Figure 90. Axial field distribution along the length of the delamination [0=edge, <0 inside the delam].

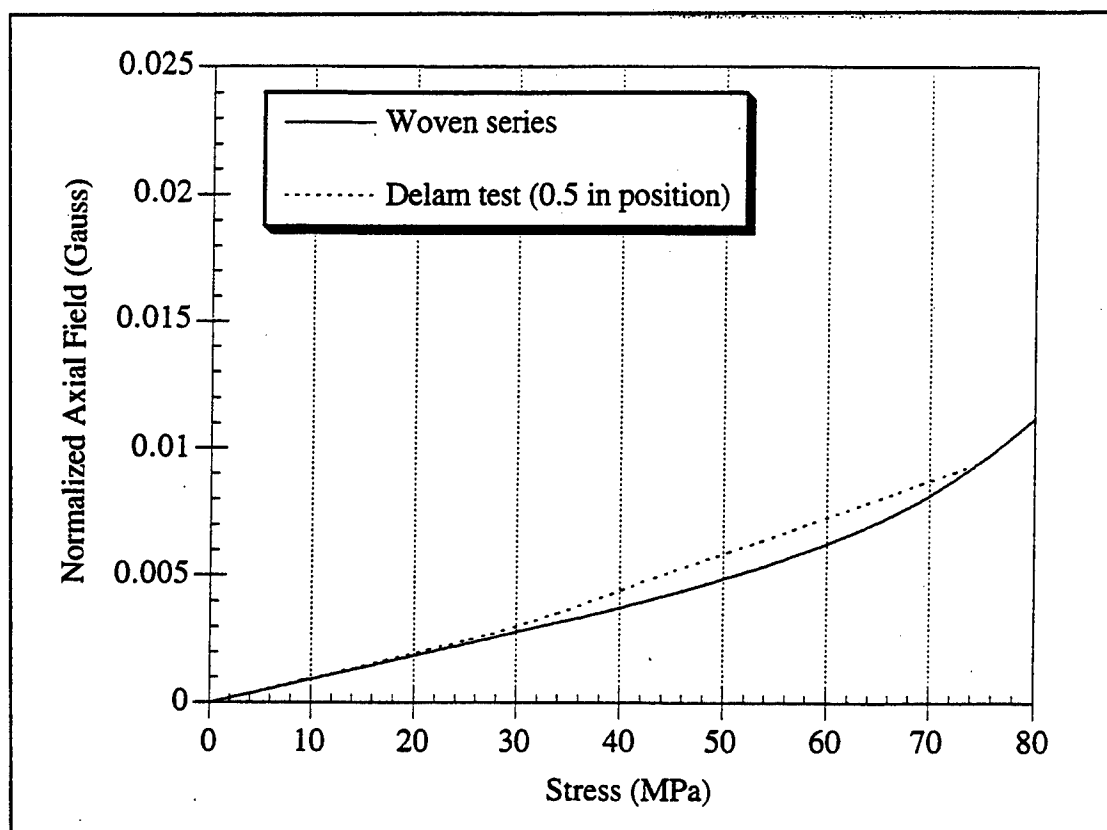


Figure 91. Loading curves for woven glass/vinyl ester series specimens and the delamination specimen at a position far from the edge of the delamination.

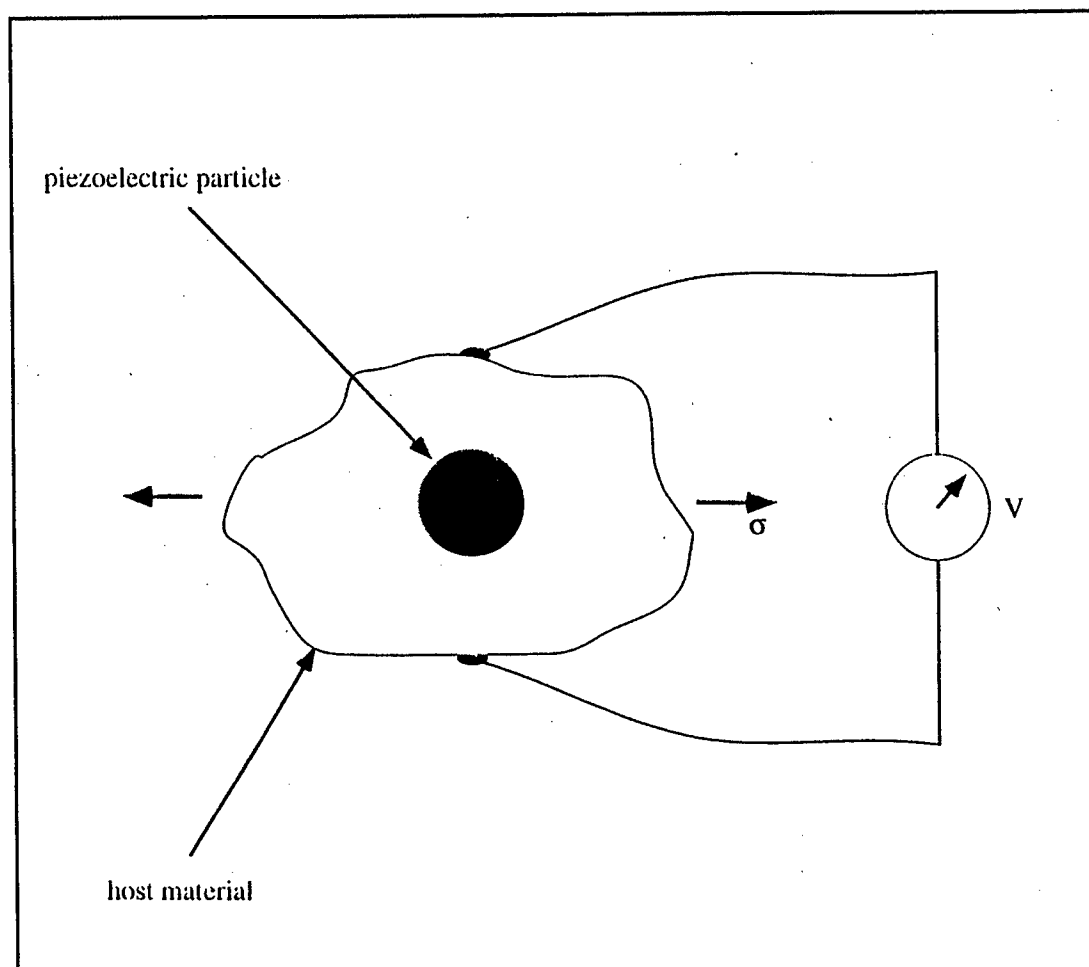


Figure 92. Piezoelectric tagged 0-3 composite material.

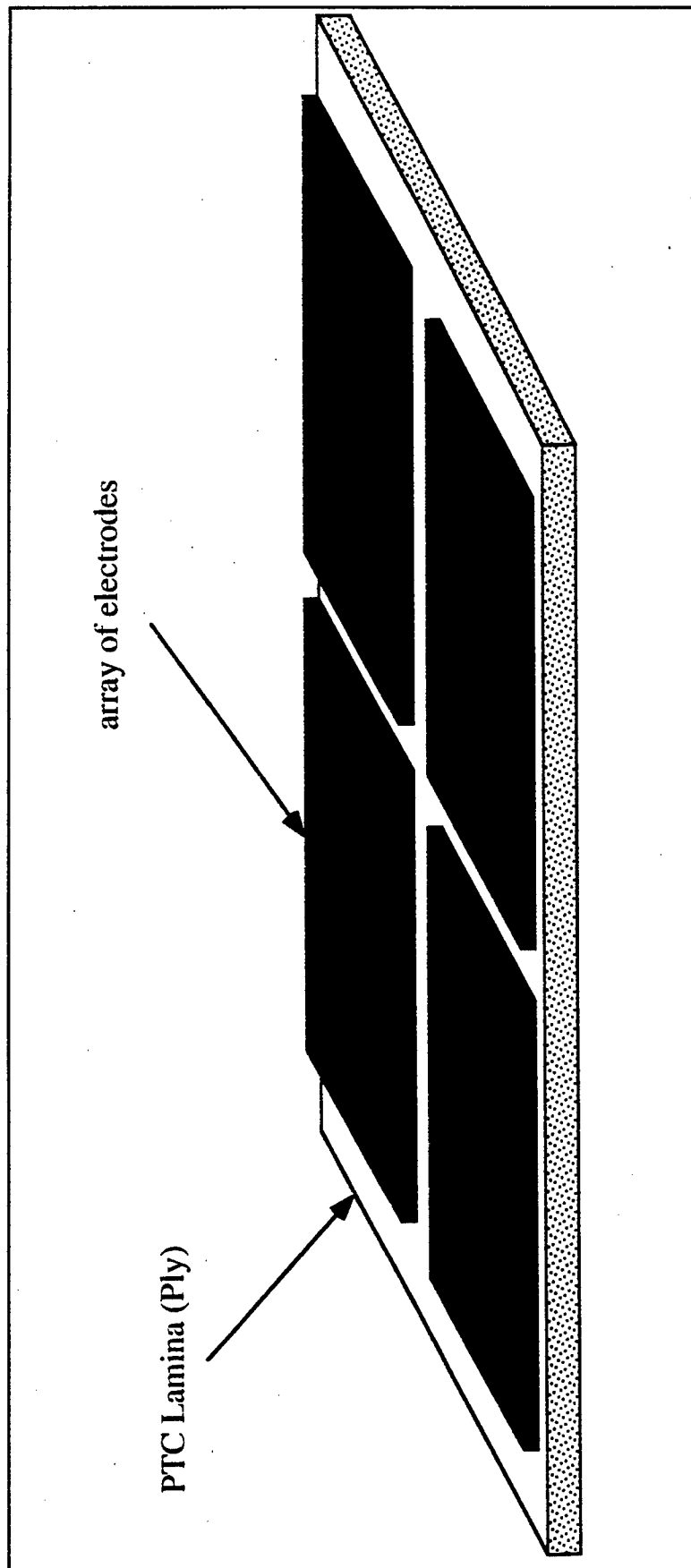


Figure 93. Laminated electrode interrogation method.

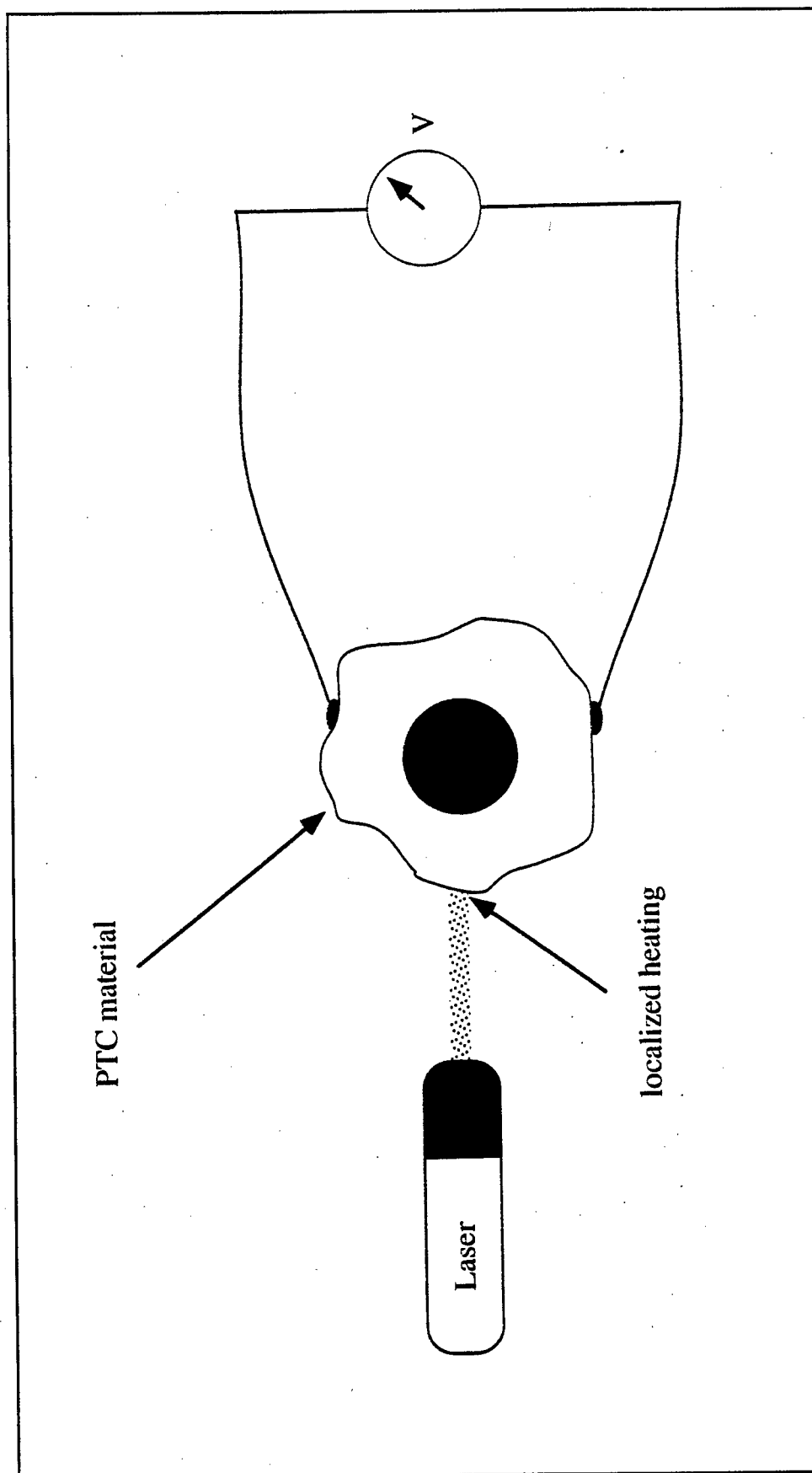


Figure 94. Laser excitation Interrogation method.

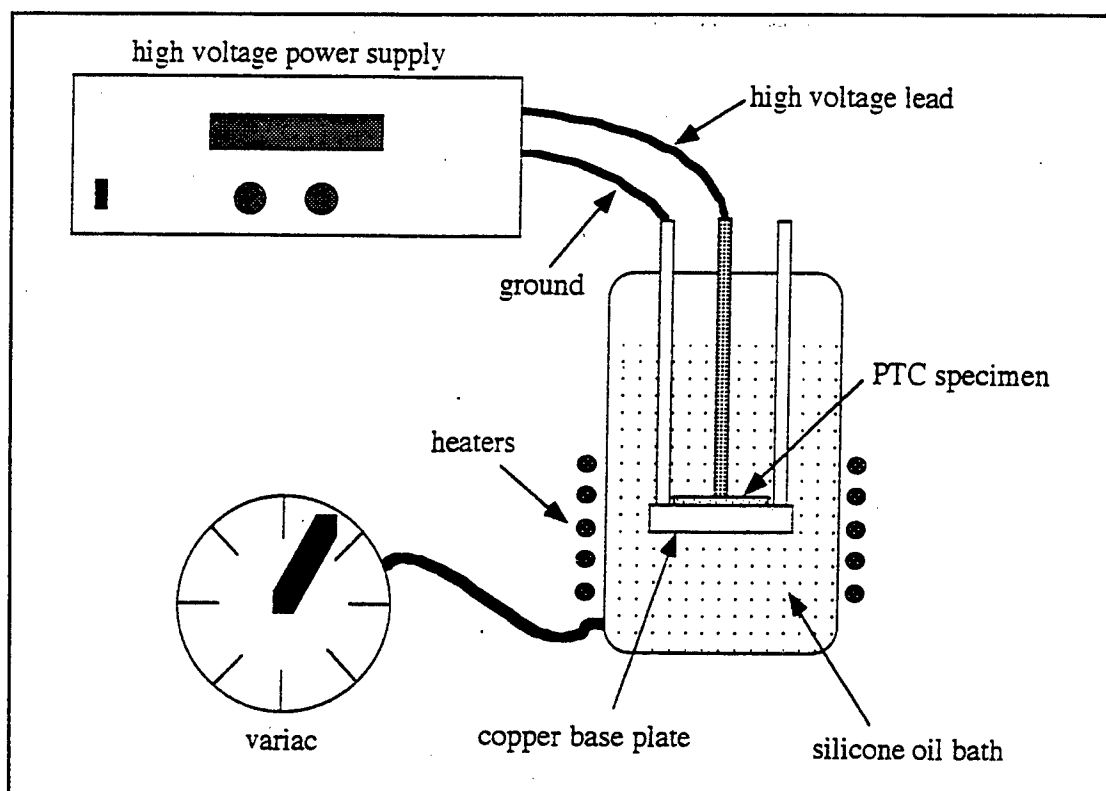


Figure 95. Poling apparatus used in the experiments.

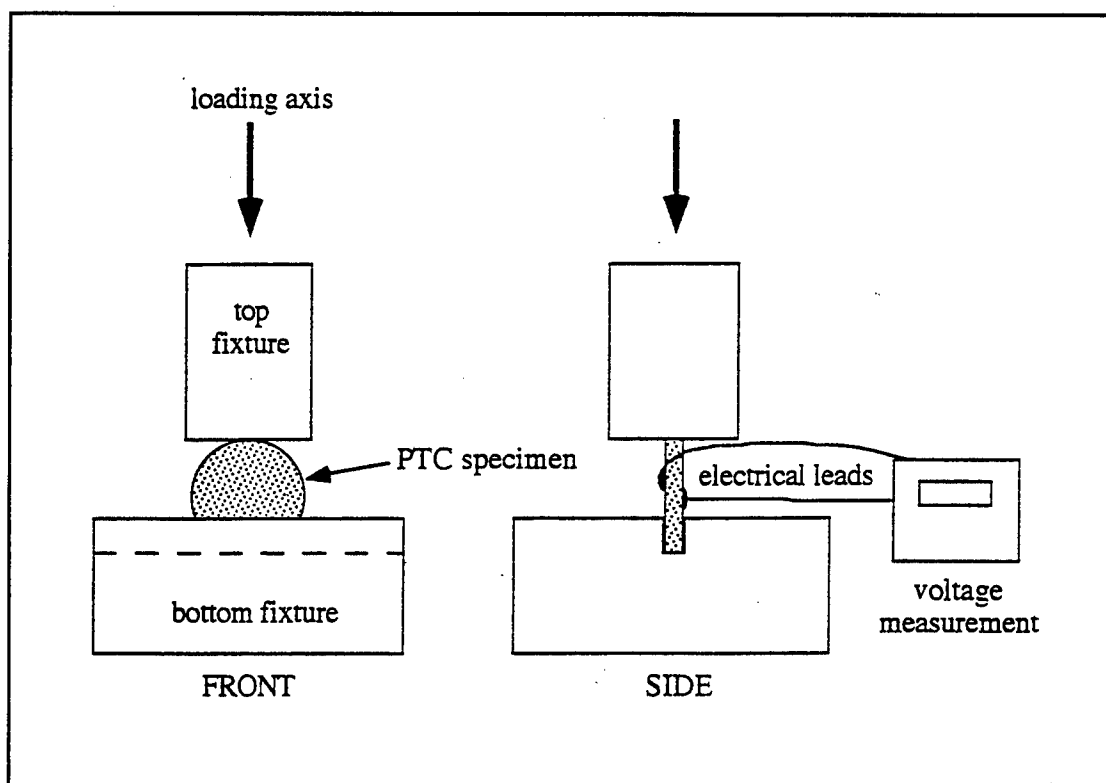


Figure 96. Diametral compression test set-up for PTC specimens.

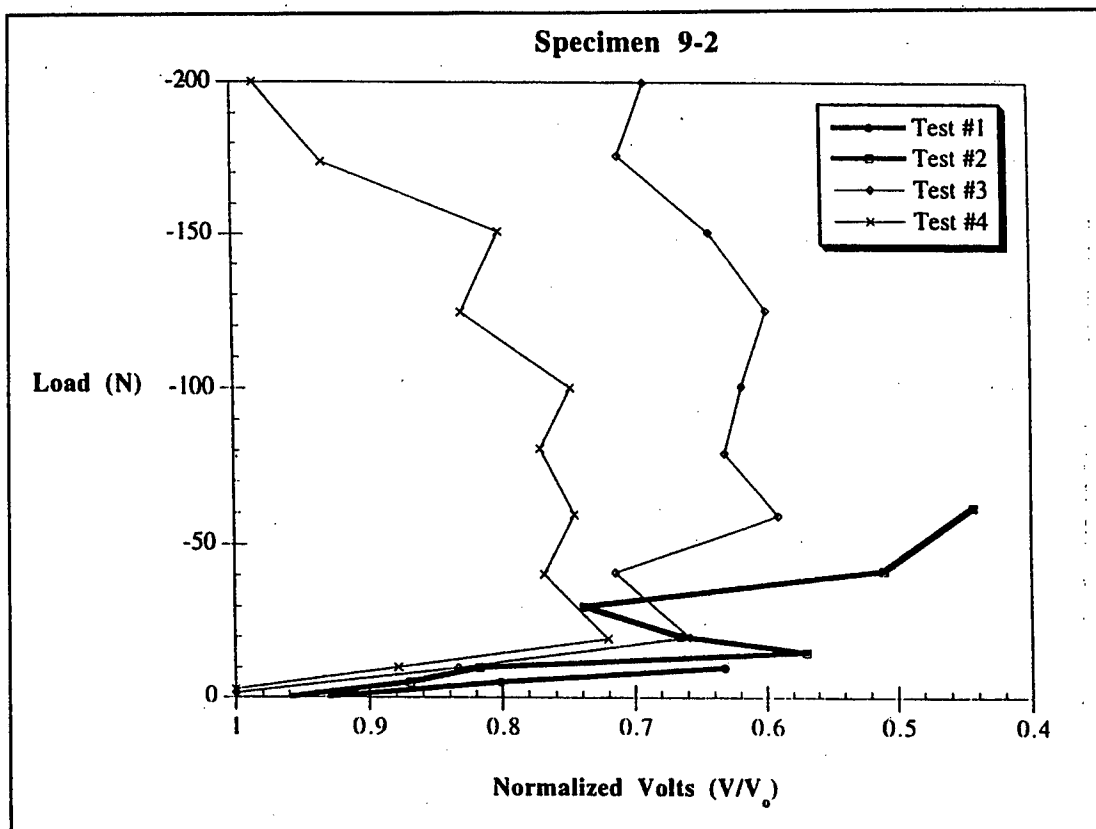


Figure 97. Summary plot of normalized voltage versus applied load.

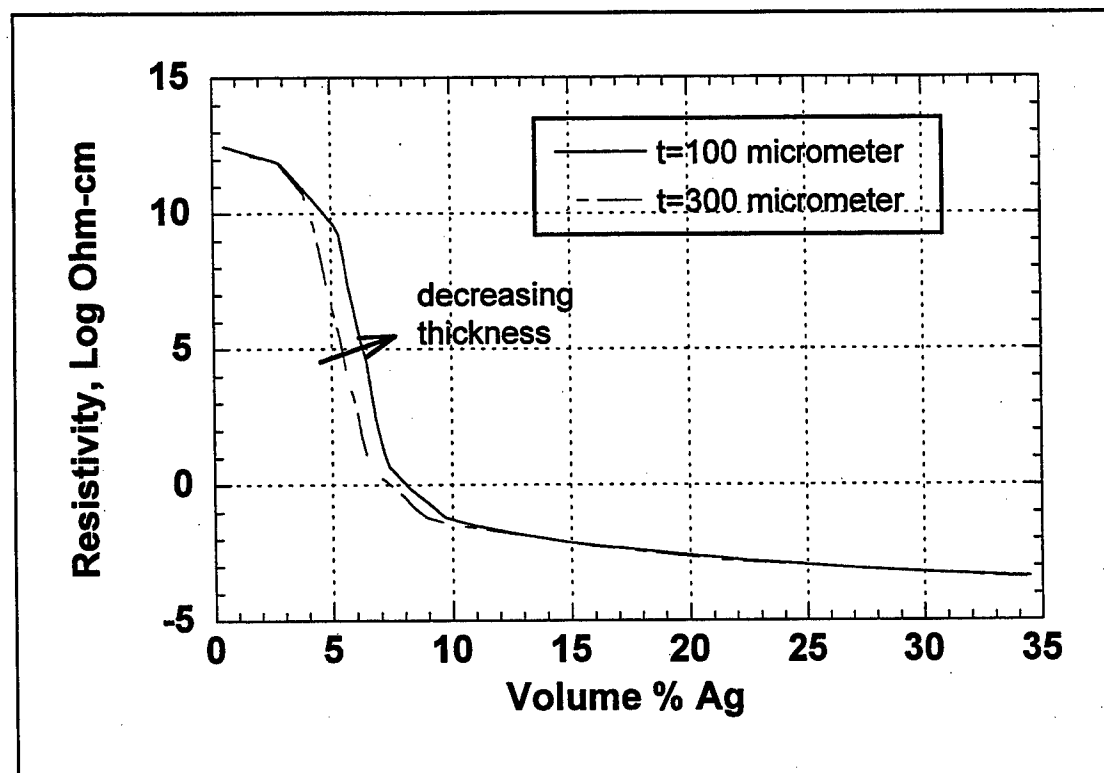


Figure 98. Percolation curves for $0.5\mu\text{m}$ Ag powder-filled silicone rubber composites (Rushau et al., 1992).

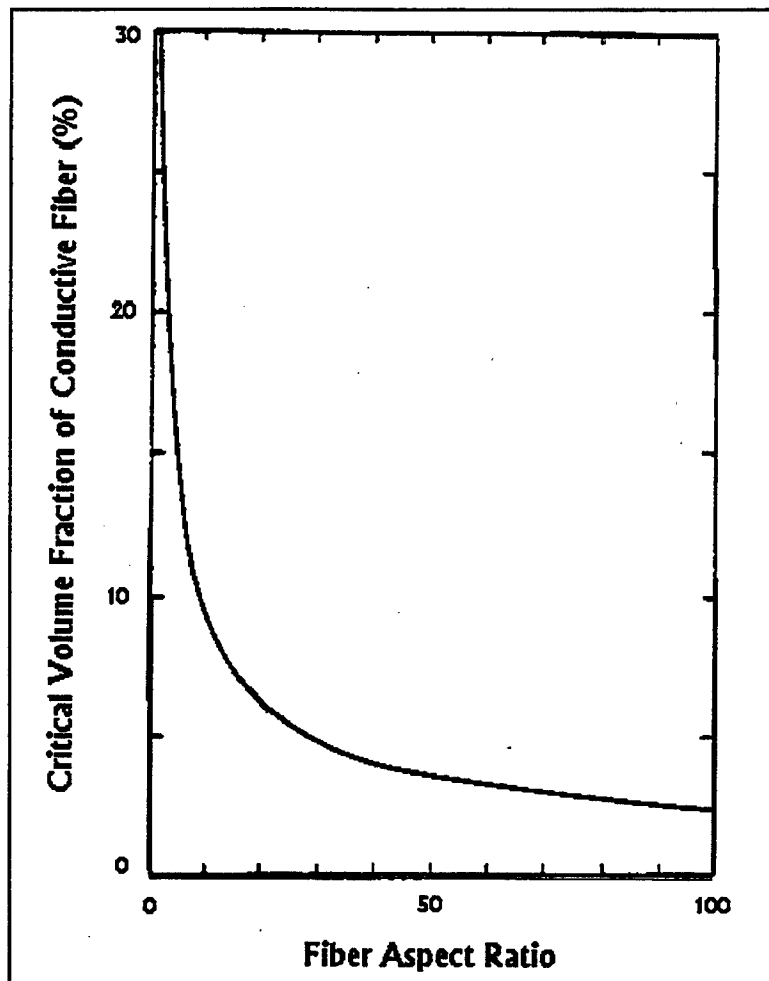


Figure 99. Critical volume fraction for electrical conductivity as a function of fiber aspect ratio.

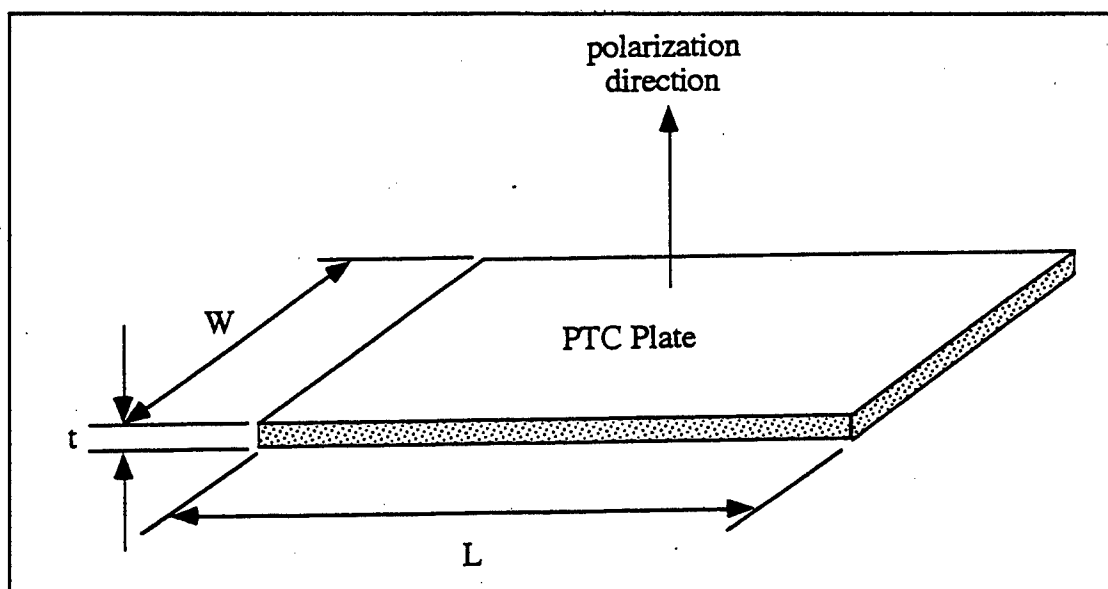


Figure 100. Geometry of a PTC plate.

Table 1. Parameters of the typical specimens in the experiments.

	Ferromagnetic Particles	Epoxy
Weight(g)/Weight ratio(%)	0.05/3	1.60
	0.08/5	1.50
	1.6/15	10.8
	2.6/25	10.5
Density (kg/m ³)	8000	1100
Diameter (μm)	5-20	N/A

Table 2. Comparison of test results and Finite Element calculation results.

	Test Results (Hz)	FE Results (Hz)	Errors (%)
Mode 1	925	927.7	0.3
Mode 2	*	1098.3	N/A
Mode 3	1550	1478.8	-4.6
Mode 4	2275	2113.9	-7.1
Mode 5	2850	3052	7.1
Mode 6	3525	3686.7	4.6
* It is difficult to excite this mode in the test.			

Table 3. Parameters of tagging particles and polymer.

	Iron Ferrite	MnZn Ferrite	HTP-402 Polyester Resin
Size	<5(mm)	<1.5 (mm)	36x32x2(mm ³)
Mass Density(ρ)(Kg/m ³)	5200	5160	1080
Weight Ratio(Δw)	3%	5%,8%	
Shape Factor(α)	3	3	

Table 4. Parameters of the coils and the yoke.

	dc coils	ac coils	Yoke
Turns (N)	100	100	
Length (l) (m)	0.05	0.05	
Radius (a) (m)	0.02	0.03	
Current (I) (A)	5	1	
Susceptibility (χ)			250
Distance (Z) (m)			0.005
Distance (L) (m)			0.03
Demagnetization factor (N_d)			0.1

Table 5. Equipment list.

Name	Brand	Model	Manufacturer
Analyzer	ZONIC+AND	4000	Zonic Corp, Milforio, OH
Power amplifier	Com-Tech	400	Crown Internat'l, Inc. Elhart, IN
DC power supply	Hewlett-Packard	HP6268B	Hewlett-Packard Co., Palo Alto, CA
Gaussmeter	Walker	MG-5D	Walker Scientific, Inc., Worcester, MA
Power unit	PCB	480C06	PCB Piezotronics, Inc., Depew, NY
Force gage	PCB	208M100	PCB Piezotronics, Inc., Depew, NY
Oscilloscope	JDR	2000	
Magnetic exciter	N/A	N/A	
Material test system	MTS	810	MTS Systems Corp., Eden Prairie, MN

Table 6. Comparison of test data and predicted values for ferromagnetic active tagging.

	Q_{01}/Q_{02} $f=1.7\text{kHz}$	ϕ_{01} $f=1.7\text{kHz}$	ϕ_{02} $f=1.7\text{kHz}$
Test Data	1.59×10^5	-37.7°	-27.8°
Predicted Value	1.39×10^5	-27.4°	-6.43°
Difference %	12.6	27.2	-77.0

Table 7. Parameters of a tagged circular beam made of Shell Epon 828 resin.

mass density ρ (kg/m ³)	radius r (m)	length L (m)	local stressed area Δv (m ³)	average distance at a point Q, \bar{r} (m)
1100	0.002	0.2	$\pi \times 0.002^2 \times 0.004$	0.003

Table 8. Parameters of Terfenol-D particles.

Mass Density ρ (kg/m ³)	Radius r (m)	Piezomagnetic Constant, d (m/A)	Weight ratio ΔW (wt%)	Permeability in Free Space, μ_r (m)
9,250	2×10^{-6}	1.5×10^{-8}	1	1.16×10^{-5}

Table 9. Comparison of test results and predicted values of specimen A with magnetostrictive tagging particles.

Load (lb)	Stress (lb/in²)	Measured Normalized Flux Density	Predicted Normalized Flux Density	Difference %
50	621.9	1	1	
100	1243.8	2.5	2	20
200	2487.6	3	4	33
300	3731.3	3.5	6	71
400	4975.1	3.75	8	113

Table 10. Comparison of signals of flux leakage field and crack-free field of specimen B with magnetostrictive tagging particles.

Load (lb)	Stress (lb/in²)	Flux leakage field (gauss)	Crack-free field (gauss)	Difference %
100	1035.2	1.2	1.3	0.1
150	1552.8	1.4	1.7	0.3
200	2070.4	2.6	4.6	2
250	2588.0	3.3	5.6	2.3
300	3105.6	4.2	7.3	3.1
350	3623.2	3.0	6.8	3.8
400	4140.8	2.9	6.0	3.1
450	4658.4	2.8	6.0	3.2

Table 11. Mixing ratios for matrix resins.

	Polyester [6 minutes]	Vinyl ester [60 minutes]	Vinyl ester [15 minutes]
Cobalt Naphthenate	1.33%	0.4%	0.7%
Dimethylaniline	1.25%	0.05%	0.15%
MEKP	0.3%	1.25%	2.5%

Table 12. Materials used in this study.

Material	Type	Supplier
Magnetostrictive powder	Terfenol-D	Etrema Products, Inc. & USACERL, Ames, IA
Magnetite	Fe ₃ O ₄	Aldrich Chemical Co., Milwaukee, WI
Matrix (polyester)	Polylite 31610-05	Reichhold Chemicals, Inc., Research Triangle Park, NC
Matrix (vinyl ester)	31347-00	Reichhold Chemicals, Inc. Research Triangle Park, NC
Catalyst	N, N-Dimethylaniline	Sigma Chemical Co., St. Louis, MO
Catalyst	Cobalt Naphthenate	Sigma Chemical Co., St. Louis, MO
Initiator	Superox (R) 709	Reichhold Chemicals, Inc.
Glass reinforcement (woven)	2113	Clark-Schwebel, Inc., Anderson, SC
Glass reinforcement (pseudo-unidirectional)	1297	Clark-Schwebel, Inc. Anderson, SC

Table 13. Polishing routine for microscopy samples.

Grit	Time (min.)
<i>Carbimet SiC abrasive discs, 8 inch, plain backed</i>	
180	4
320	3
600	2
2400	2
<i>Chemomet I polishing cloth, 8 inch, PSA backed</i>	
~ 0.05 mm	2

Table 14. Equipment used in mechanical loading experiment.

Hydraulic Loading Frame	Instron Model 1331
Load Frame Control	Instron 8500 Control System, Canton, MA
Load Cell	Instron, 100 kN
Load Frame Computer	Power Mac 7100/80 with National Instruments LabView, Austin, TX
Strain Gage Conditioners	Measurements Group Model 2120, Raleigh, NC
Data Acquisition System	Omega OM-900 Series, Stamford, CT (912 General Voltage Input Module)
Data Acquisition System Computer	Gateway 2000 (386) with Labtech Notebook Pro
Digital Gaussmeter	F. W. Bell Model 9500, Orlando, FL
Transverse Hall Probe	F. W. Bell Model TF99-0608

Table 15. Results of magnetite specimen tensile tests.

Specimen Series	Average Failure Load (kN)	Average Ultimate Strength (MPa)
M1-P Series	1.484	24.80
M10-P Series	1.390	23.20
M1-V Series	1.975	33.14
M10-V Series	1.306	21.85
M1WV Series	7.212	123.88
M1UV Series	6.346	110.51

Table 16. Specimens for volume fraction study.

Series	Filler	Matrix	Tag Vol. Fraction	Tag Size (m)	Magnetic Field (G)
D	Terfenol-D	polyester	1	45,75,100	None
F	Terfenol-D	polyester	0.5	45,75,100	None
G	Terfenol-D	polyester	2	45,75,100	None
H	Terfenol-D	polyester	4	45,75,100	None

Table 17. Specimens for tag size study.

Series	Filler	Matrix	Tag Vol. Fraction	Tag Size (m)	Magnetic Field (G)
A	Terfenol-D	polyester	1	45	None
B	Terfenol-D	polyester	1	75	None
C	Terfenol-D	polyester	1	105	None
D	Terfenol-D	polyester	1	45, 75, 105	None
E	Terfenol-D	polyester	1	45,75	None

Table 18. Piezoelectric voltage constants for several materials.

Material	g_{33} ($\times 10^{-3}$ Vm/N)	g_{31} ($\times 10^{-3}$ Vm/N)
PZT-4	24.9	-10.6
PZT-5A	24.8	-11.4
PZT-5H	19.7	-9.1
PZT-7A	41	-16
PZT-7D	21	-9.6
PN-2	32	--

Table 19. Properties of PZT-5A-169G (24 h after poling).

Property	Value
K_{33}^T	1841
DF	0.0131
Q_M	92
r (g/cm ³)	7.82
d_{33} (x 10 ⁻¹² m/V)	384.0
d_{31} (x 10 ⁻¹² m/V)	168.2
g_{33} (x 10 ⁻³ Vm/N)	23.6
g_{31} (x 10 ⁻³ Vm/N)	10.3
E_{11}^E (GPa)	68.0
E_{11}^D (GPa)	77.1
S_{11}^E (TPa ⁻¹)	14.7
S_{11}^D (TPa ⁻¹)	13.0

Table 20. Materials used in this study.

Material	Type	Supplier
Piezoelectric ceramic	PZT-5A-169G	Morgan Matroc, Inc.
Matrix	polyester	Bondo Corp.
Graphite reinforcement	AS-4 fiber	Hercules Corp.
Glass reinforcement	E-type fiber	Bondo Corp.

Table 21. Piezoelectric tagged composite specimens manufactured.

Volume Fraction					
Group	Resin	Piezo Powder	Graphite Powder	Glass Fiber	Note
1	50	50	--	--	0-3 system
2	70	30	--	--	0-3 system
3	90	10	--	--	0-3 system
4	48.5	50	1.5	--	0-3 system [graphite loaded]
5	68.5	30	1.5	--	0-3 system [graphite loaded]
6	88.5	10	1.5	--	0-3 system [graphite loaded]
7	58.5	30	1.5	10	0-3 system [glass+graphite reinforced]
8	38.5	30	1.5	30	0-3 system [glass+graphite reinforced]
9	60	30	--	10	0-3 system [glass-reinforced]
10	65	30	--	5	0-3 system [glass-reinforced]
11	45	50	5	--	0-3 system [graphite loaded]
12	47	50	3	--	0-3 system [graphite loaded]
13	94	6	--	--	1-3 system [20 rods]
14	97	3	--	--	1-3 system [10 rods]
15	99	1	--	--	1-3 system [3 rods]

Table 22. Poling conditions for PTC specimens.

Group	Spec. #	Voltage* (V)	Current (mA)	Temp. (°C)	Note	Group	Spec. #	Voltage* (V)	Current (mA)	Temp. (°C)	Note
1	1	6000	0.044	105		8	1	5000	0.035	96	
	2	46	2.772	95	1		2	160	2.770	95	
	3	6000	0.083	94			3	5000	0.062	94	
	4	6000	0.035	93		9	1	5300	0.089	95	
2	1	6000	0.071	95			2	5000	0.064	95	
	2	6000	0.061	95			3	6000	0.103	94	
	3	5000	0.081	93			4	5000	0.100	95	
	4	5000	0.063	94		10	1	6500	0.015	94	
3	1	6000	0.000	91			2	8000	0.050	96	
	2	5500	0.000	93			3	7500	0.035	94	
	3	6000	0.033	96			4	6000	0.004	91	
	4	5500	0.000	94		11	1	165	2.771	99	2
	5	5000	0.000	95			2	230	2.771	95	2
4	1	3500	0.017	94			3	179	2.770	94	2
	2	6000	0.096	94			4	2000	0.017	95	
	3	6000	0.091	93			5	218	2.770	96	2
		6000	0.015	94		12	1	180	2.769	93	2
5	1	6000	0.017	95			2	5000	0.005	96	
	2	5000	0.057	93			3	5500	0.001	93	
	3	5500	0.050	94			4	4000	0.006	93	
	4	5500	0.046	97			5	246	2.770	94	2
6	1	6000	0.001	97		13	1	9000	0.125	100	
	2	8000	0.034	99	3		2	7000	0.021	95	
	3	6700	0.002	99			3	7000	0.015	95	
	4	7000	0.017	108		14	1	6000	0.050	95	
	5	6500	0.020	106				5000	0.001	92	
7	1	5500	0.045	95				5500	0.021	97	
	2	5500	0.069	94		15	1	7500	0.005	102	
	3	3000	0.012	94			2	7000	0.035	95	
	4	54	2.771	95	2		3	7700	0.047	100	
							4	7500	0.038	98	

* conditions held for 5 minutes for each specimen
note #1: short circuit
note #2: short circuit (graphite induced)
note #3: discharged at end of poling

References

- Adly, A.A., I.D. Mayergoyz, and A. Bergqvist, "Preisach Modeling of Magnetostrictive Hysteresis," *Journal of Applied Physics*, vol 69, no 8 (1991) pp 5777-5779.
- Bagdassaryan, G.E., and E.A. Danoyan, "Mathematical Modeling of the Vibrations of Two-Layer Magnetostrictive Plates," *Izv. AN SSSR. Mekhanika Tverdogo Tela*, vol 27, no 3 (1992), pp 87-94.
- Benbouzid, M., G. Reyne, and G. Meunier, "Nonlinear Finite Element Modeling of Giant Magnetostriction," *IEEE Trans. of Magnetism*, vol 29, no 6 (1993), pp 2467-2469.
- Bergqvist, A., and G. Engdahl, "A Stress-Dependent Magnetic Preisach Hysteresis Model," *IEEE Trans. of Magnetism*, vol 27, no 6 (1991), pp 4796-4798.
- Bray, D.E., and R.K. Stanley, *Nondestructive Evaluation: a Tool for Design, Manufacturing, and Service* (McGraw-Hill, 1989).
- Brown, R.L., "Methods of Evaluating and Inspecting Adhesively Bonded Joints and Structures Adapted for Such Evaluation and Inspection," *U.S. Patent*, no 3,351,760 (November 1967).
- Buzdugan, G., *Vibration Measurement* (Martinus Nijhoff Publishers, 1986), p 261.
- Carman, G.P. and M. Mitrovic, "Nonlinear constitutive relations for magnetostrictive materials with applications to 1-D problems," *Journal of Intelligent Material Systems and Structures*, vol 6, no 5 (September 1995).
- Carmona, F., F. Barreau, P. Delhaes, and R. Conet, *J. Phys. Lett.*, 41, 1980, p L531.
- Carmona, F., R. Conet, and P. Delhaes, *Journal of Applied Physics*, vol 61 (1987), p 2550.

- Cheng, D.K., *Field and Wave Electromagnetics* (Addison-Wesley Publishing, 1989), pp 225-293.
- Civil Engineering Research Foundation (CERF), *Setting a National Agenda for the Civil Engineering Profession*, Volume 1: Final Report (CERF, August 1991).
- Clark, A.E., *Ferromagnetic Materials: A Handbook on the Properties of Magnetically Ordered Substances*, vol. 1 (North-Holland Publishing Co., 1980), pp 565+.
- Clark, A.E., M.L. Spano, and H.T. Savage, 1983, "Effect of stress on the magnetostriction and magnetization of rare earth alloys," *IEEE Trans. of Magnetics*, vol 19, no 5 (1983).
- Clark, A.E., J.D. Verhoven, O.D. McMasters, and E.D. Gibson, "Magnetostriction in Twinned [112] Crystals of $Tb_{.27}Dy_{.73}Fe_2$," *IEEE Trans. of Magnetics*, vol 22 (1986), pp 973-975.
- Clark, W.G., Jr., and W.R. Junker, "System and Method for Qualitatively Inspecting Adhesive Joints and Other Materials," *U.S. Patent*, no 4,944,185 (July 1990).
- Clark, W.G., Jr., R.K. Sadhir, and W.R. Junker, "Tagged Adhesives for Improved Electromagnetic Inspection," *Materials Evaluation*, vol 48 (January 1990), pp 60-64.
- Clark, W.G., Jr., and R.E. Shannon, "Tagging Lets You Test the Untestable," *Advanced Materials and Processes*, vol 137, no 4 (1990), pp 59-60+.
- Clark, W.G., Jr., *Materials Reliability: Material Tagging for Improved Inspection and Process Control*, Technical Report [TR] 91-1TEO-TAGGS-P1 (Westinghouse Science and Technology Center, 1991), pp 1-20.
- Clark, W.G., Jr., "Magnetic Tagging for Improved Material Diagnostics," *Proceedings of Recent Advances in Adaptive and Sensory Materials and Their Applications* (April 1992), pp 274-284.
- Cullity, B.D., *Introduction to Magnetic Materials* (Addison-Wesley Publishing, 1972).
- De Bondt, S., L. Froyen, and A. Deruyttere, *Journal of Materials Science*, vol 27 (1992), p 1983.

Dietz, P.W., and A.H. Sharbaugh, "NonDestructive Detection of Voids in Plastic Materials," *U.S. Patent*, no 4,620,145 (October 1986).

Dry, C., "Passive Smart Materials for Sensing and Actuation," *Proceedings of Recent Advances in Adaptive and Sensory Materials and Their Applications* (April 1992), pp 207-222.

Engdahl, G., and L. Svensson, "Simulation of the Magnetostrictive Performance of Terfenol-D in Mechanical Devices," *Journal of Applied Physics*, vol 63, no 8 (1988), pp 3924-3926.

Engdahl, G., and L. Kvarnsjö, "A Time Dependent Radially Resolved Simulation Model of 'Giant' Magnetostrictive Materials," *Mechanical Modeling of New Electromagnetic Materials* (International Union of Theoretical and Applied Mechanics [IUTAM] April 1990), pp 131-138.

Ewins, D.J., *Modal Testing: Theory and Practice* (Research Studies Press, 1984).

Fuhr, P.L., D.R. Huston, P.J. Kajenski, and T.P. Ambrose, "Performance and Health Monitoring of the Stafford Medical Building Using Embedded Sensors," *Smart Material Structures*, (January 1992), pp 63-68.

Goddard Space Flight Center, "Metal-Filled Adhesives Amenable to X-ray Inspection," *NASA Tech Briefs*, October 1994.

Hathaway, K.B., and A.E. Clark, "Magnetostrictive Materials," *MRS Bulletin*, vol 18 (April 1993), pp 34-41.

Hermansen, R.D., T.H. Sutherland and R. Predmore, 1990, "Method of Bonding Metals with a Radio-Opaque Adhesive/Sealant for Void Detection and Product Made," *U.S. Patent*, no 4,940,633 (July 1990).

Hossack, J.A., and B. A. Auld, ONR Final Technical Report, Stanford University, July 1992.

Jang, B.Z., H.B. Hsieh, and M.D. Shelby, "Real Time Cure Monitoring and Control of Composite Fabrication Using Nondestructive Dynamic Mechanical Methods," *Nondestructive Evaluation of Materials* (September 1989), pp 377-383.

Jackson, J.D., *Classical Electrodynamics* (John Wiley & Sons, 1962), pp 132-168.

- Jiles, D.C., and J.B. Thielke, "Modeling of the Combined Effects of Stress and Anisotropy on the Magnetostriction of $Tb_3Dy_7Fe_2$," *IEEE Trans. of Magnetism*, vol 27, no 6 (1991), pp 5352-5354.
- Kim, P., and U. Meier, "CFRP Cables for Large Structures," *Proceedings of Advanced Composites Materials in Civil Engineering Structures* (American Society of Civil Engineers [ASCE], January 1991).
- Kvarnsjö, L., and G. Engdahl, "Nonlinear 2-D Transient Modeling of Terfenol-D Rods," *IEEE Trans. of Magnetism*, vol 27, no 6 (1991), pp 5349-5351.
- Lee, P.K., "Method of Tagging with Color-Coded Micro-Particles," *U.S. Patent*, no 4,053,433 (October 1977).
- Li, M.X., W.Z. Ding, and J.M. Chen, "Principles of an Acoustic Impedance Method for Detection and Location of NonBonds in Adhesive-Bonded Multi-Layered Joints," *NDT International*, vol 15, no 6 (June 1982), pp 137-142.
- Livesay, R.G., "Method of Tagging with Micro-Particles," *U.S. Patent*, no 3,772,200 (November 1973).
- Livesay, R.G. "Tagging Explosives with Organic Micro-Particles," *U.S. Patent*, no 3,897,284 (July 1975).
- Maeda, N., "Computer Simulation of Magnetic Particle Behavior," *Materials Evaluation*, vol 51, no 2 (February 1993), pp 290-293.
- McConnell, V.P., "Can Composites Rebuild America's Infrastructure?" *Advanced Composites*, vol 7, no 6 (November/ December 1992), pp 22-31.
- McLachlan, D.S., M. Blaszkiewicz, and R.E. Newnham, *Journal of the American Ceramic Society*, vol 73 (1990), p 2187.
- Meier, U., "Carbon Fiber-Reinforced Polymers: Modern Materials in Bridge Engineering," *Reprint from Structural Engineering International* (January 1992), pp 1-7.
- Meirovitch, L., *Elements of Vibration Analysis* (McGraw-Hill, 1986).

- Mermelstein, M.D., "Coupled Mode Analysis for Magnetoelastic Amorphous Metal Sensors," *IEEE Transactions on Magnetics*, vol 22, no 5 (September 1986), pp 442-444.
- Mitrovic, M., M. Robert, and G. Carman, "Magnetostrictive Composite Material Systems Analytical/Experimental," *Proceedings of the American Society for Composites Tenth Technical Conference* (American Society for Composites [ASC] 1995), pp 85-94.
- Newnham, R.E., "Molecular Mechanisms in Smart Materials," *MRS Bulletin*, May 1997, pp. 20-30.
- Newnham, R.E., A. Safari, G. Sa-gong, and J. Giniewicz. 1984 *Ultrasonics Symposium* (Institute of Electrical and Electronics Engineers [IEEE] November 1984), pp 501-506.
- Rao, N.N., *Elements of Engineering Electromagnetics, 2nd Ed.* (Prentice-Hall, 1987), pp 97-98.
- Rogers, C.A., D.K. Barker., K.D. Bennett, and R.H. Wynn, Jr., "Demonstration of a Smart Material with Embedded Actuators and Sensors for Active Control," *Proceedings of SPIE's International Symposium on Fiber Optics, Optoelectronics, and Laser Applications in Science and Engineering* (International Society for Optical Engineering [SPIE], September 1988), pp 90-105.
- Rogers, C.A., S.W. Zhou, and Z. Chaudhry. "A State-of-the-Art Report: An Embedded Particle Tagging Technique for In-Field Nondestructive Evaluation," *USACERL Report*, Contract DACA88-94-D-0021-0001a, November 1994.
- Rogers, C.A., S.W. Zhou, and Z. Chaudhry. "Concepts for Active Tagging of Reinforced Composites for In-process and In-field Nondestructive Evaluation," *USACERL Report*, Contract DACA88-94-D-0021-0001b, March 1995.
- Rogers, C.A., Z. Chen, and V. Giurgiutiu. "Results of the Active Tagging Experiments with Ferromagnetic and Magnetostrictive Sensors," *USACERL Report*, Contract DACA88-94-D-0021-0002, February 1996.
- Ruschau, G.R., S. Yoshikawa, and R.E. Newnham *42nd Electronic Components and Technology Conference* (Institute of Electrical and Electronics Engineers [IEEE] May 1992), pp 481-486.

- Ryan, F.M., and P.C. Handke, "Phosphor Combination and Method, Particularly Adapted for Use with Explosives, for Providing a Distinctive Information Label," *U.S. Patent*, no 3,772,099 (November 1973).
- Ryan, F.M., and P.C. Handke, "Phosphor Combination and Method, Particularly Adapted for Use with Explosives, for Providing a Distinctive Information Label," *U.S. Patent*, re 29,334 (August 1977).
- Ryan, F.M., and P.C. Handke, "Tagged Particles Which are Easily Detected by Luminescent Response, or Magnetic Pickup, or Both," *U.S. Patent*, no 4,131,064 (December 1978).
- Ryan, F.M., and W. Vodoklys, "Combination of Band-Type and Line-Type Emission Phosphors with Explosive," *U.S. Patent*, no 3,967,990 (July 1976).
- Savage, H.T., R. Abbundi, and A.E. Clark, "Permeability, Magnetomechanical Coupling and Magnetostriction in Grain-Oriented Rare Earth-Iron Alloys," *Journal of Applied Physics*, vol 50, no 3 (March 1979), pp 1674-1676.
- Shaffer, R.D., "Eddy Current Testing, Today and Tomorrow," *Materials Evaluation*, vol 52, no 1 (January 1994), pp 28-32.
- Silimon, D.D., "Passive Tagging for Composite Identification," *Research Report*, CIMSS, Virginia Polytechnic Institute and state University (August 1994), pp 1-12.
- Stauffer, D., *Introduction to Percolation Theory* (Taylor and Francis, 1985).
- Strong, A.B., *Fundamentals of Composites Manufacturing: Materials, Methods, and Applications* (Society of Manufacturing Engineers, 1989).
- Su, Q., Y. Zheng, A. Roytburd, and M. Wuttig, "Substrate Stress Controlled Magnetic Domains in Amorphous Terfenol-D Films," *Applied Physics Letters*, vol 66, no 18 (1995), pp 2424-2426.
- Sun, F.P., C. Liang, C.A. Rogers, C.A., and L. Vick, "Magnetic Activation of Embedded Sensory Particles in Active Tagging Interrogation of Adhesive Bonding," *Proceedings of the 1993 SPIE Conference on Smart Structures and Materials* (International Society for Optical Engineering [SPIE], February 1993), pp 400-409.

- Taya, M. and N. Ueda, *Journal of Engineering Materials and Technology (ASME)*, vol 109 (1987), p 252.
- Tsai, S.W., and H.T. Hahn, *Introduction to Composite Materials* Technomic Publishing, Westport, Conn., 1980.
- Valleau, A.R., "Eddy Current NonDestructive Testing of Graphite Composite Materials," *Materials Evaluation*, vol 48, no 2 (February 1990), pp 230-239.
- White, S.R., "Smart Tagged Composites using Piezoelectric Particles," *Proceedings of the 1995 SPIE Conference on Smart Structures and Materials* (International Society for Optical Engineering [SPIE], March 1995).
- White, S.R., "Concepts for Interrogating Shape Memory Alloy (SMA) and Piezoelectric Tagged Polymer Composites," *USACERL Report*, Contract DACA88-94-M-0603, September 1995.
- White, S.R., and R.A. Albers, "Magnetostrictive Tagging of Composites for Structural Health Monitoring," *USACERL Report*, Contract DACA88-95-D-0004-0001, February 1996.
- White, S.R., N.R. Sottos, P.H. Guebelle, A.J. Hegeman, and D. Jung "Concepts for Producing Self-Repairing Polymeric Composites," *USACERL Report*, Contract DACA88-95-D-0004-0002, February 1996.
- Zallen, R., *The Physics of Amorphous Solids* (Wiley Interscience, 1983).
- Zhou, S.W., C. Liang, C.A. Rogers, F.P. Sun et al., "An In-Situ Sensory Technique for In-Service Monitoring—Measurement of the Complex Young's Modulus of Polymers," *Proceedings of the 1993 SPIE Conference on Smart Structures and Materials* (International Society for Optical Engineering [SPIE], February 1993), pp 14-23.
- Zhou, S.W., Z. Chaudhry, C.A. Rogers, and R. Quattrone, "Review of Embedded Particle Tagging Methods for NDE of Composite Materials and Structures," *Proceedings of the 1995 SPIE Conference on Smart Structures and Materials* (International Society for Optical Engineering [SPIE], February 1995).
- Zhou, S.W., Z. Chaudhry, C.A. Rogers, and R. Quattrone, "An Active Particle Tagging Method Using Magnetic Excitation for Material Diagnostics," *Proceedings of the 36th Structures, Structural Dynamics, and Materials*

Conference (American Institute of Aeronautics and Astronautics [AIAA], April 1995)

Taya, M. and N. Ueda, *Journal of Engineering Materials and Technology (ASME)*, vol 109 (1987), p 252.

Tsai, S.W., and H.T. Hahn, *Introduction to Composite Materials* Technomic Publishing, Westport, Conn., 1980.

Valleau, A.R., "Eddy Current NonDestructive Testing of Graphite Composite Materials," *Materials Evaluation*, vol 48, no 2 (February 1990), pp 230-239.

White, S.R., "Smart Tagged Composites using Piezoelectric Particles," *Proceedings of the 1995 SPIE Conference on Smart Structures and Materials* (International Society for Optical Engineering [SPIE], March 1995).

White, S.R., "Concepts for Interrogating Shape Memory Alloy (SMA) and Piezoelectric Tagged Polymer Composites," *USACERL Report*, Contract DACA88-94-M-0603, September 1995.

White, S.R., and R.A. Albers, "Magnetostrictive Tagging of Composites for Structural Health Monitoring," *USACERL Report*, Contract DACA88-95-D-0004-0001, February 1996.

White, S.R., N.R. Sottos, P.H. Guebelle, A.J. Hegeman, and D. Jung "Concepts for Producing Self-Repairing Polymeric Composites," *USACERL Report*, Contract DACA88-95-D-0004-0002, February 1996.

Zallen, R., *The Physics of Amorphous Solids* (Wiley Interscience, 1983).

Zhou, S.W., C. Liang, C.A. Rogers, F.P. Sun et al., "An In-Situ Sensory Technique for In-Service Monitoring—Measurement of the Complex Young's Modulus of Polymers," *Proceedings of the 1993 SPIE Conference on Smart Structures and Materials* (International Society for Optical Engineering [SPIE], February 1993), pp 14-23.

Zhou, S.W., Z. Chaudhry, C.A. Rogers, and R. Quattrone, "Review of Embedded Particle Tagging Methods for NDE of Composite Materials and Structures," *Proceedings of the 1995 SPIE Conference on Smart Structures and Materials* (International Society for Optical Engineering [SPIE], February 1995).

Zhou, S.W., Z. Chaudhry, C.A. Rogers, and R. Quattrone, "An Active Particle Tagging Method Using Magnetic Excitation for Material Diagnostics," *Proceedings of the 36th Structures, Structural Dynamics, and Materials*

USACERL DISTRIBUTION

Chief of Engineers

ATTN: CEHEC-IM-LH (2)

ATTN: CEHEC-IM-LP (2)

ATTN: CECC-R

ATTN: CEMP-E

ATTN: CEMP-ET

ATTN: CERD-L

ATTN: CERD-M

Defense Tech Info Center 22304

ATTN: DTIC-O (2)

21

(+ 13)

3/98